Synthetic and Photophysical Studies on Bright and Long-Lived Phosphorescent Ruthenium(II) Complexes Based on Arylborane-Appended Ligands

Atsushi Nakagawa

Graduate School of Chemical Sciences and Engineering

HOKKAIDO UNIVERSITY (**2018**)

CONTENTS

Chapter 1: Introduction

1-1: Emissive Transition Metal Complexes

Emissive transition metal complexes represented by polypyridyl ruthenium(II) complexes,[1,2] cyclometalated iridium(III) complexes[3–6] and so forth[7–22] have attracted much attention due to their versatile emission properties. Although some complexes exhibit fluorescence[23–26] from the relevant singlet excited states (S_1) to the electronic ground states (S_0) similar to organic compounds such as anthracene, the most distinguished characteristics of a transition metal complex is the phosphorescence transition from the triplet excited state (T_1), produced by intersystem crossing (ISC) from S_1 through spin–orbit coupling originated from the heavy atom effects by a metal center as shown in Scheme 1-1. In such a complex, the intrinsically spin-forbidden T_1–S_0 phosphorescence transition is partially allowed by mixing between the electronic wave functions of S_1 and T_1 through spin–orbit coupling[7] and, thus, the phosphorescence from the complex can be observed even at room temperature, in contrast to the ordinary organic compounds whose phosphorescence is not typically available at room temperature.

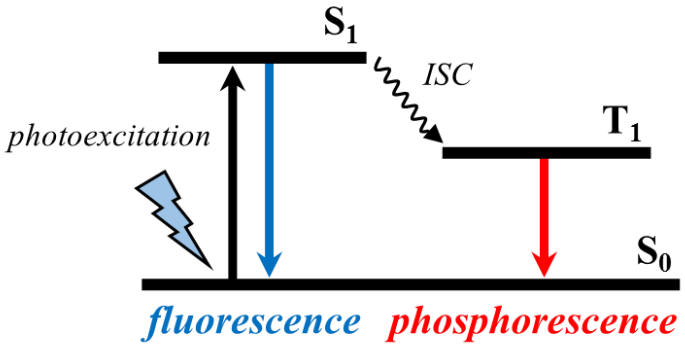

Scheme 1-1. Energy diagram for the excited-state processes.

Transition metal complexes exhibit a variety of the electronic transitions arisen from the metal-centered (e.g., d–d and f–f), ligand-centered (e.g., π–π* and intraligand charge transfer (ILCT)[8,9]), metal–ligand (e.g., metal-to-ligand CT (MLCT)[1,2] and ligand-to-metal CT (LMCT)[10,11]) and ligand–ligand interactions (e.g., ligand-to-ligand CT (LLCT)[12,13]). Since the electronic transition features of a complex are controllable by a combination of a metal center and a ligand structure, phosphorescent complexes having a d^6-,[1–6,15–19] d^8-[8,9,12,13,17,18] or d^{10}-metal ion(s)[10,19–22] have been extensively synthesized as exemplified in Chart 1-1. As an outstanding example, the *facial* isomer of tris(2-phenylpyridinato)iridium(III) (*fac*-[Ir(ppy)$_3$]) reported by Watts *et al.* in 1985[3] shows efficient green phosphorescence, and it has been utilized in a practical device of organic light-emitting diodes (OLEDs) in 1999.[27] After the report, various phosphorescent iridium(III) complexes (e.g., *mer*-*N*,*N*-[Ir(HFP)$_2$(pic)][5] and *mer*-*N*,*N*-[Ir(btp)$_2$(acac)][6] in Chart 1-1) have been developed aiming at the applications to OLEDs to achieve broad and visible emission from blue to red.

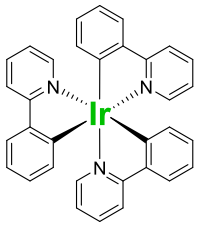

fac-[Ir(ppy)$_3$] [3]

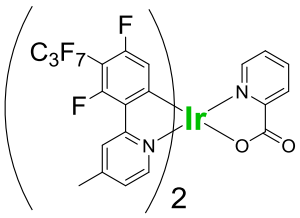

mer-*N*,*N*-[Ir(HFP)$_2$(pic)] [5]

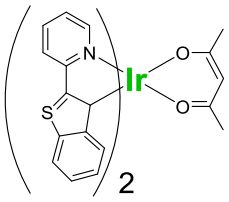

mer-*N*,*N*-[Ir(btp)$_2$(acac)] [6]

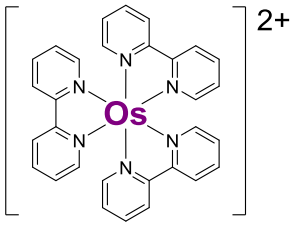

[Os(bpy)$_3$]$^{2+}$ [14]

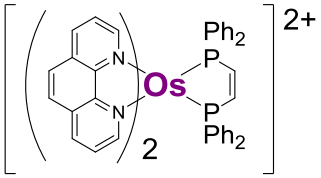

[Os(phen)$_2$(dppene)]$^{2+}$ [15]

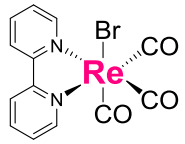

fac-[Re(bpy)(CO)$_3$Br] [16]

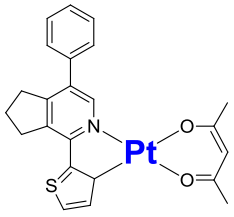

[Pt(s1-thpy)(acac)] [17]

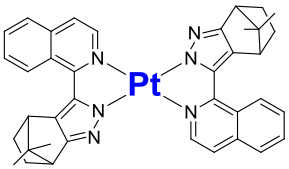

[Pt(1-iqdz)$_2$] [18]

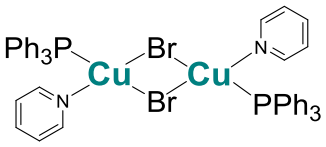

[Cu$_2$Br$_2$(PPh$_3$)(py)] [19]

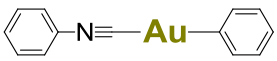

[(PhNC)Au(Ph)] [21]

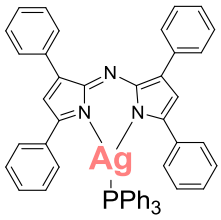

[Ag(tpa-dipy)(PPh$_3$)] [22]

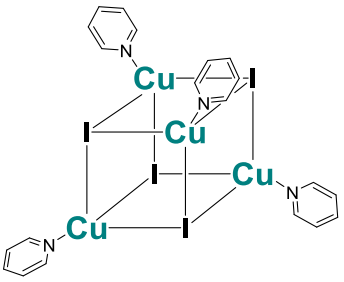

[Cu$_4$I$_4$(py)$_4$] [20]

Chart 1-1. Chemical structures of phosphorescent transition metal complexes.

In addition to the emission properties of a complex itself, environmental responses of photoluminescence is also important characteristics.[28–36] A typical example is a d^8 platinum(II) complex possessing a square-planar geometry. Although polypyridyl platinum(II) complexes such as *cis*-(2,2'-bipyridine)dicyanidoplatinum(II) (*cis*-[Pt(bpy)$(CN)_2$]),[28] whose structure is shown in Figure 1-1, are nonemissive in diluted solutions, the complexes in a condensed phase often exhibit the characteristic emissions arisen from platinum–platinum interactions.[28–30] In the case of *cis*-[Pt(bpy)$(CN)_2$], dimerization of the complex in the ground state and resulting higher-energy dσ*-orbital give rises to metal–metal-to-ligand CT (MMLCT) absorption and the relevant emission even at room temperature. Since such bimolecular interactions hugely depend on the intermolecular distance, the emission from the complex is varied as functions of the surrounding environments such as temperature[32,33] and vapor. [34–36]

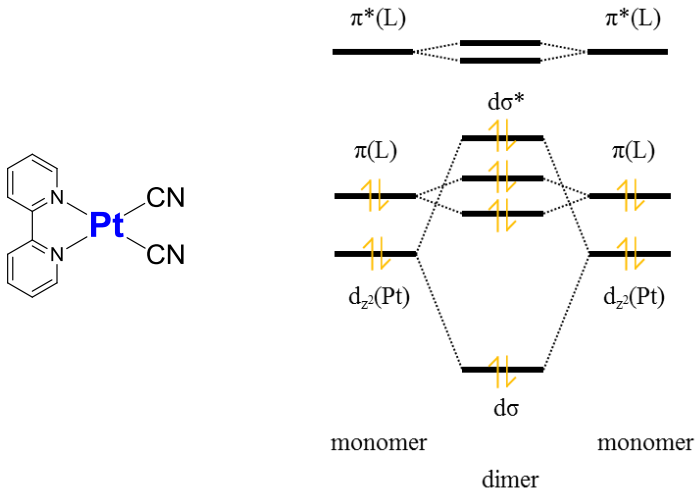

Figure 1-1. Chemical structure and molecular-orbital diagram of *cis*-[Pt(bpy)$(CN)_2$].[28]

Emissive transition metal complexes are applicable to light-emitting materials,[12–14,37–40] sensing for surrounding environments (e.g., heavy metal

atom/ion,[41–44] pH[45,46] and vapor[34–36]), bio-imaging[47,48] and so forth[49–51] and, therefore, various attractive examples have been hitherto reported. However, most of them are based on the structure–property relation since the photophysical properties of a transition metal complex are dependent on many structural factors such as nature of a metal center and a ligand as well as a coordination geometry. Furthermore, such complexes often show complicated photophysical behaviors arisen from multiple factors: intra- and inter-molecular interactions, multiple-component emission, and different spin characters between the absorption and emission transitions. Owing to such complicacies, theoretical aspects into the photophysical properties of phosphorescent transition metal complexes are not sufficient enough in the present stage of the investigations in spite of well-documented fluorescent compounds.[52,53]

1-2: Polypyridyl Ruthenium(II) Complexes

Polypyridyl ruthenium(II) complexes represented by tris(2,2'-bipyridine)-ruthenium(II) ($[Ru(bpy)_3]^{2+}$ in Figure 1-2) are one of the most extensively studied metal complexes. $[Ru(bpy)_3]^{2+}$ was first synthesized by Burstall in 1936.[54] After the report on the emission from $[Ru(bpy)_3]^{2+}$ at 77 K in 1959,[55] the origin of the lowest-energy excited state (i.e., phosphorescent or fluorescent and d–d or MLCT transition) had been actively discussed until 1970's[55–63] and, currently, the triplet MLCT (^{3}MLCT) model reported by Harrigan *et al.* in 1973[63] is widely accepted on the basis of three thermally-equilibrated levels analysis for the temperature dependence of the emission lifetimes (τ_{em}) below 77 K. In addition to the ligand-centered $\pi\pi^*$ absorption band, $[Ru(bpy)_3]^{2+}$ exhibits an intense and broad MLCT absorption band in >400 nm. The singlet MLCT (^{1}MLCT) excited state produced by photoexcitation is converted to the ^{3}MLCT excited

state *via* ISC (~15 fs in water[64]) followed by thermal relaxation (~20 ps in water[65]) and, then, the complex shows room-temperature phosphorescence. The emission from $[Ru(bpy)_3]^{2+}$ is temperature-dependent owing to a contribution of the triplet dd excited (^{3}dd*) state to thermal deactivation from the ^{3}MLCT excited state (see Figure 1-2) as revealed by Watts *et al.* in 1976.[66] Furthermore, later than 1980's, the photophysical processes of ruthenium(II) complexes have been extensively studied based on the energy gap dependence of the nonradiative decay rate constant,[67] solvent effects on both absorption and emission[68,69] and so forth.[70–74] Since there are further numerous experimental and theoretical reports on polypyridyl ruthenium(II) complexes, these complexes play important roles in current coordination photochemistry and are ideal targets for understanding the photophysical process of phosphorescent transition metal complexes. Furthermore, the visible absorption and emission of polypyridyl ruthenium(II) complexes enable utilizations of the complexes for not only fundamental studies but also a variety of photochemical applications in sensing[75–79] and light-emitting materials[80,81], artificial photosynthesis[82–85], and so forth.[86–89] In particular, the complexes are often employed as photosensitizers owing to their intense MLCT absorption, long-lived excited state (~1 μs) and high stabilities in the multiple redox states.

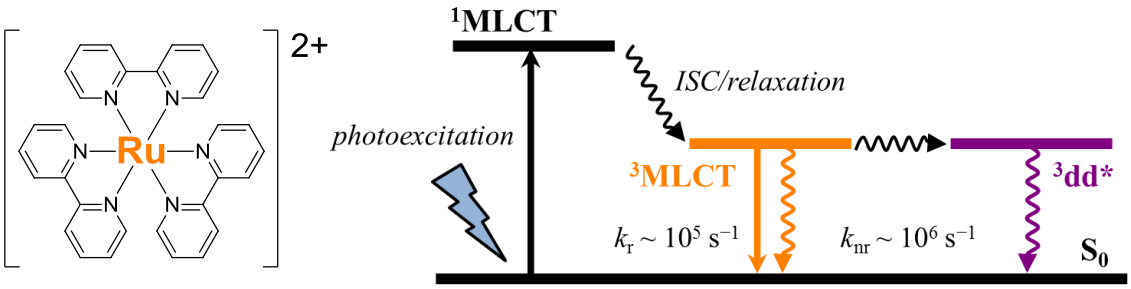

Figure 1-2. Chemical structure and photophysical processes of $[Ru(bpy)_3]^{2+}$.

Although polypyridyl ruthenium(II) complexes show obvious phosphorescence from the ^{3}MLCT excited states even at room temperature, the emission quantum yields (Φ_{em}) are not necessarily high among other phosphorescent transition metal complexes. As an example, the Φ_{em} value of $[Ru(bpy)_3]^{2+}$ is 0.095 in deaerated CH_3CN at 298 K,[90] whereas that of *fac*-$[Ir(ppy)_3]$ is 0.92 under similar conditions.[91] The highest Φ_{em} value among those of polypyridyl ruthenium(II) complexes was reported by Hahn *et al.* for a dendritic tris(4,7-diphenyl-1,10-phenanthroline)ruthenium(II) ($[Ru(dpp)_3]^{2+}$) derivative with the value being 0.41 in CH_3OH, which was achieved by encapsulation of the $[Ru(dpp)_3]^{2+}$ core in oligo(ethyleneglycol) units.[92] However, most of the Φ_{em} values of polypyridyl ruthenium(II) complexes are still less than 0.1[93] and, therefore, development of highly-emissive polypyridyl ruthenium(II) complexes is of primary importance. Since the Φ_{em} value of a complex is determined primarily by the relation $\Phi_{em} = k_r/(k_r + k_{nr})$ where k_r and k_{nr} are the radiative and nonradiative decay rate constants, respectively, the simplest approach to enhance the emission efficiency is an increase in k_r and a decrease in k_{nr}. However, the k_{nr} value of a polypyridyl ruthenium(II) complex is typically 10-times larger than k_r owing to a large contribution of nonradiative decay *via* the ^{3}dd* state as described above,[66] and such large k_{nr} impedes a development of a highly-emissive polypyridyl ruthenium(II) complex. Furthermore, a control of k_r has been scarcely conducted due to its experimental difficulties. On the basis of these research backgrounds, a systematic study on the spectroscopic and photophysical properties of polypyridyl ruthenium(II) complexes is absolutely required to obtain a new synthetic strategy for an enhancement of the emission efficiency of the complex.

1-3: Triarylborane Derivatives

An electrically-neutral organoborane derivative possesses a planar sp^2-hybridized structure and the vacant p-orbital on the boron atom (p(B)), which differs from the relevant derivatives of carbon, nitrogen and other typical element compounds as shown in Figure 1-3. In spite of the fascinating electronic structures of tricoordinated organoborane derivatives, they are not stable in air or solution due to the presence of p(B) and, therefore, subtle molecular designs to protect p(B) sterically by bulky substituents are required.

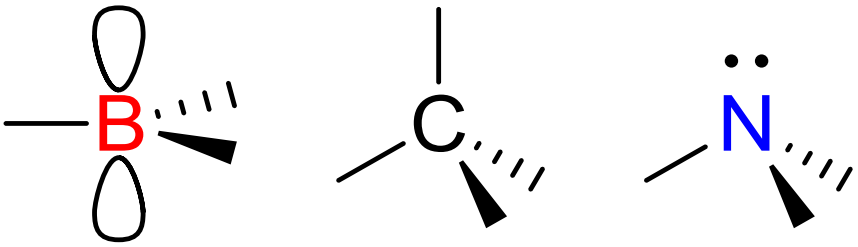

Figure 1-3. Chemical and electronic structures of electrically-neutral boron, carbon and nitrogen derivatives.

Triarylborane compounds, which are electrically-neutral organoborane derivatives possessing three aryl groups, act as powerful electron-acceptors and show characteristic spectroscopic/photophysical properties owing to the presence of p(B).[94–103] In 1966, Ramsey reported the spectroscopic properties of a series of triarylborane derivatives having various π-electron chromophores (phenyl, tolyl, mesityl, or naphthyl group) and demonstrated a linear dependence of the absorption energy on the ionization potential of the aryl group.[94] After the report by Ramsey, synthetic works on triarylborane derivatives have been frequently reported, whereas the number of the reports on their spectroscopic properties is limited. In 2000, Yamaguchi *et al.* reported

that tri(9-anthryl)borane (TAB in Figure 1-4) showed broad and intense absorption at around 470 nm (band I) in tetrahydrofuran (THF) at room temperature, in addition to the band similar to the ππ* band of anthracene in 330–380 nm (band II).[95] Furthermore, TAB exhibits room-temperature fluorescence whose band ranging in 480–650 nm is broad, structureless and red-shifted largely compared to that of anthracene (380–480 nm) as shown in Figure 1-4. According to the theoretical calculations on TAB by Yamaguchi *et al.*, band I is ascribed to the charge-transfer transition from the π-orbital of the anthryl group (highest-energy occupied molecular orbital (HOMO)) to p(B) (lowest-energy unoccupied molecular orbital (LUMO)): π(aryl)–p(B) CT. On the basis of the report, Kitamura *et al.* have investigated the solvent dependences of the absorption/fluorescence spectra[96] and the electro-absorption/fluorescence of TAB,[97] and revealed experimentally that these spectroscopic features are derived from π(aryl)–p(B) CT. The results demonstrated that p(B) in a triarylborane derivative plays an essential role in its spectroscopic and excited-state properties. Furthermore, owing to the presence of the electron-accepting p(B) and bulky aryl groups, a small Lewis base (e.g., fluoride or cyanide ion) can bind p(B) selectively, and the absorption/fluorescence spectra of a triarylborane derivative change drastically upon binding with the Lewis base.[98–100]

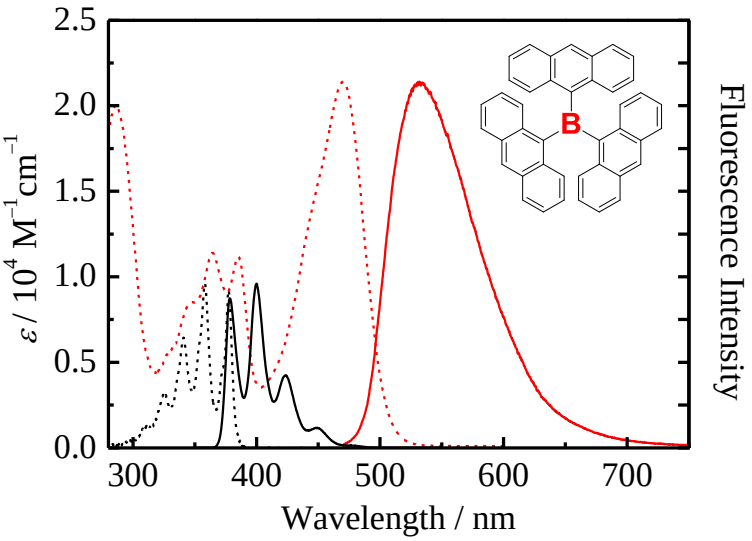

Figure 1-4. Absorption (broken curves) and fluorescence (solid curves) spectra of TAB (red) and anthracene (black) in THF. Inset: chemical structure of TAB.

A choice of the aryl groups would result in further characteristics of the spectroscopic and photophysical properties of a triarylborane derivative. Therefore, a variety of triarylborane derivatives have been hitherto reported aiming at anion sensors,[98–100] ion/electron conduction materials,[104–108] light-emitting materials[109–111] and so forth.[112–115] For examples, Kitamura *et al.* have reported that a triarylborane derivative connecting the boron atom with electron-donating *N*,*N*-dimethylaminophenyl groups *via* triple bonds (TMAB in Chart 1-2), which is synthesized by Yamaguchi *et al.* in 2000,[116] shows huge fluorescent solvatochromism from blue to red and possesses the extremely large electric dipole moment in the singlet excited state (~60 D (1 D = 3.34×10^{-30} Cm)).[117] A cross-shaped triarylborane derivative (BNPhB in Chart 1-2) reported by Zhao *et al.* shows extremely intense emission (Φ_{em} = 0.98 or 0.43 in toluene or THF, respectively), and its emission color drastically changes from yellow to blue by adding a fluoride ion in THF.[118] Interestingly, BNPhB is sensitive to a fluoride ion even in a poly(methyl methacrylate) film. Furthermore, Saito *et al.* reported a triarylborane

derivative in which a boron atom was sit in a fully-fused polycyclic π-conjugated skeleton (ThAB in Chart 1-2).[119] In a pyridine/THF mixture (1/15, v/v), ThAB shows unique thermochromic behaviors due to the temperature-dependent Lewis acidity and resulting ligation/dissociation of pyridine with ThAB.

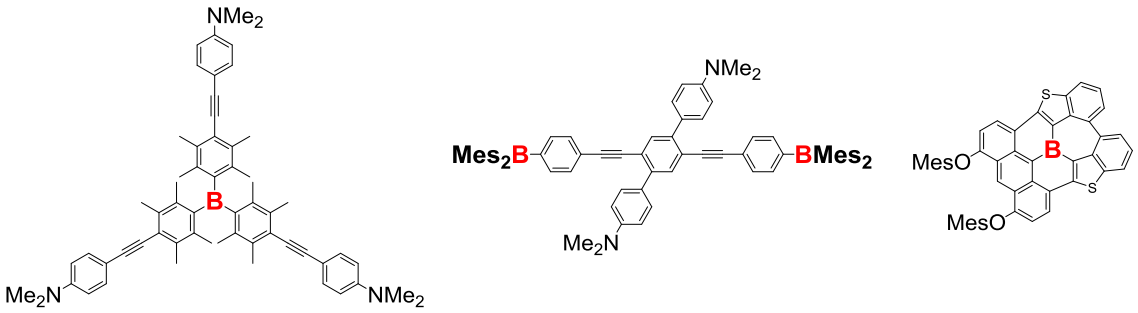

TMAB [116,117] BNPhB [118] ThAB [119]

Chart 1-2. Chemical structures of triarylborane derivatives.

1-4: Transition Metal Complexes Having Arylborane Units

The spectroscopic and photophysical properties of an MLCT-type transition metal complex are highly dependent on the electronic structures of the ligand(s). Therefore, chemical decorations of a complex by a triarylborane unit(s) would be a fascinating choice to control the excited-state characteristics of the complex. In a transition metal complex possessing a triarylborane-appended ligand, the π(aryl)–p(B) CT transition in the triarylborane moiety is expected to synergistically participate in the MLCT transition in the metal-complex moiety and, as a result, the complex will show intriguing spectroscopic and excited-state properties. In 2006, Kitamura *et al.* have reported that the platinum(II) complex having a 4'-{*p*-(dimesityl)borylphenyl}-2,2':6',2''-terpyridine ligand ($[Pt(Btpy)Cl]^+$ in Chart 1-3), the first arylborane–transition metal complex, exhibits the emission in $CHCl_3$ at room temperature (Φ_{em} = 0.011), in

contrast to nonluminescent nature of an unsubstituted reference complex ($[Pt(tpy)Cl]^+$ (tpy = 2,2':6',2"-terpyridine)) in solution at room temperature.[120] Later on, several research groups have reported transition metal complexes (platinum(II),[121–126] iridium(III),[91,127–130] ruthenium(II),[131–133] copper(I),[121] and so on[134–138]) bearing an arylborane unit(s) on ligand(s). Wang *et al.* reported that $[Cu(Bnpa)(PPh_3)_2]^+$ in Chart 1-3 showed extremely intense emission in the crystalline phase (Φ_{em} = 0.88), in which the MLCT excited state was stabilized in energy than the ligand-centered excited state by an introduction of a (dimesityl)boryl group to the periphery of the ligand.[121] Furthermore, Kitamura *et al.* reported the cyclometalated iridium(III) complex having (dimesityl)boryl groups (*fac*-$[Ir(Bppy)_3]$ in Chart 1-3) also showed the large molar absorption coefficient ($\varepsilon = 5.8 \times 10^4$ $M^{-1}cm^{-1}$ (M = mol/dm^3) at 379 nm in THF) and brilliant green emission (Φ_{em} = 1.0).[91] Since density functional theory (DFT) calculations suggested that HOMO and LUMO of *fac*-$[Ir(Bppy)_3]$ are localized on the iridium and boron atoms, respectively, the excited state of the complex was assigned to metal-to-boron CT (MBCT) in character. In the excited states of arylborane–transition metal complexes, π(aryl)–p(B) CT in the triarylborane moiety synergistically interacts with the MLCT in the metal-complex moiety owing to the electron-withdrawing ability of the triarylborane unit and, thus, such synergistic MLCT/π(aryl)–p(B) CT interactions influence greatly the excited-state characteristics of the complex such as excited-state switching and an enhanced transition dipole moment.

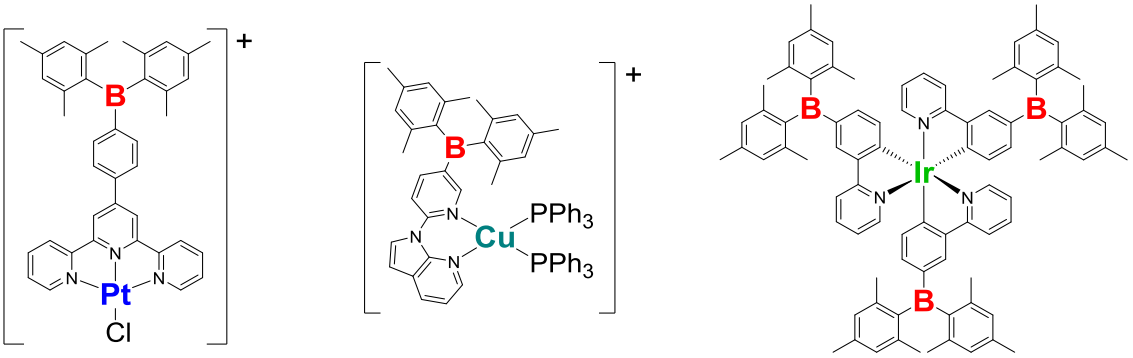

[Pt(Btpy)Cl]$^{+}$ [120] [Cu(Bnpa)(PPh$_3$)$_2$]$^{+}$ [121] *fac*-[Ir(Bppy)$_3$] [91]

Chart 1-3. Chemical structures of arylborane–transition metal complexes.

As remarkable examples of arylborane–ruthenium(II) complexes, Sakuda *et al.* reported [Ru(phen)$_3$]$^{2+}$ (phen = 1,10-phenanthroline) derivatives bound to an arylborane unit by a triple bond at the 4- or 5-position of the phen ligand (4RuB or 5RuB, respectively; in Chart 1-4). The MLCT absorption band of 4RuB (λ_{abs} = 473 nm and ε_{473} = 2.6 × 10^4 M^{-1}cm^{-1} in CH$_3$CN) was lower in energy and more intense than that of [Ru(phen)$_3$]$^{2+}$ (λ_{abs} = 445 nm and ε_{445} = 1.7 × 10^4 M^{-1}cm^{-1}). Furthermore, both 4RuB and 5RuB show low-energy, intense and long-lived emission in CH$_3$CN (λ_{em} = 681 nm, Φ_{em} = 0.11 and τ_{em} = 12 μs for 4RuB, λ_{em} = 607 nm, Φ_{em} = 0.11 and τ_{em} = 1.2 μs for 5RuB) compared to [Ru(phen)$_3$]$^{2+}$ (λ_{em} = 599 nm, Φ_{em} = 0.045 and τ_{em} = 0.42 μs).[131] Such low-energy and long-lived emission from 4RuB or 5RuB was explained by stabilization of the emitting excited state by the strong synergistic MLCT/π(aryl)–p(B) CT interactions and subsequent decrease in the contribution of the nonemitting ^{3}dd* states to excited-state decay. An introduction of the arylborane unit to the 4-position of a phen ligand influenced more largely on the absorption and emission properties of the complex than that to the 5-position of phen, suggesting more effective interactions between MLCT and π(aryl)–p(B) CT in 4RuB. These results demonstrate that an

introduction of the arylborane unit(s) to a polypyridyl ruthenium(II) complex greatly affects the spectroscopic/photophysical properties of the complex and that molecular design to maximize the synergistic MLCT/π(aryl)–p(B) CT interactions is very important.

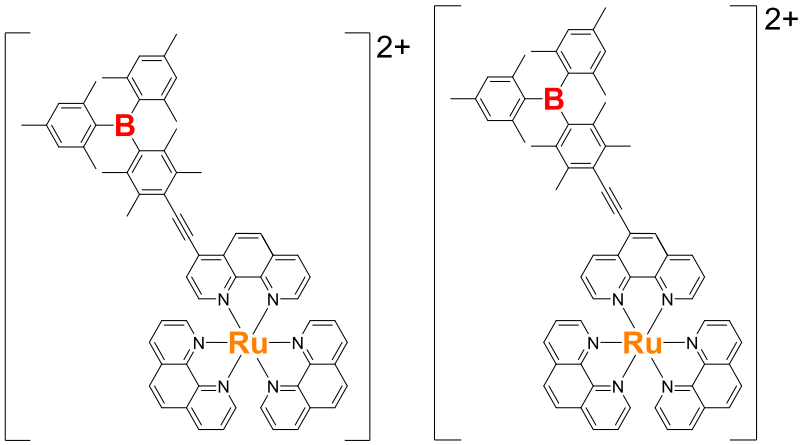

Chart 1-4. Chemical structures of 4RuB and 5RuB.[131]

1-5: Purposes and Contents of the Thesis

As described in the preceding sections, theoretical aspects into the photophysical properties of phosphorescent transition metal complexes are not sufficient enough in the present stage of the investigations and polypyridyl ruthenium(II) complexes are ideal targets of the relevant study. Furthermore, the emission quantum yields of ruthenium(II) complexes hitherto reported are still low and the development of highly-emissive polypyridyl ruthenium(II) complexes is of primary importance. Owing to the presence of the vacant p-orbital on the boron atom (p(B)) in a triarylborane, a class of transition metal complexes having a triarylborane group(s) in the periphery of the ligand(s) shows fascinating excited-state properties, characterized by the synergistic interactions between MLCT in the metal-complex moiety and

π(aryl)–p(B) CT in the triarylborane group: synergistic MLCT/π(aryl)–p(B) CT.[131] Therefore, further understanding of the arylborane effects on the spectroscopic and photophysical properties of the complexes are of primary importance.

The present study targets the synthetic modulation of the spectroscopic and photophysical properties of polypyridyl ruthenium(II) complexes by an introduction of an arylborane unit(s). On the basis of the systematic studies on ruthenium(II) complexes by varying the diimine- and ancillary-ligand structures and the number of the arylborane unit in the diimine-ligand(s), the spectroscopic and photophysical properties of the complexes are discussed in detail. Although the phosphorescent process is affected by the degrees of mixing between S_1 and T_1 characters, intense emission from arylborane–ruthenium(II) complexes should be explained by theoretical aspects such as the Strickler–Berg relation[53] which demonstrates a positive correlation between absorption and emission properties. Such a relation is scarcely studied for phosphorescent compounds, despite the relation is widely accepted for fluorescent organic compounds. Therefore, the total understanding of the Strickler–Berg relation and mixing between S_1 and T_1 characters in a transition metal complexes will provide the new synthetic strategy for bright (i.e., large absorption and emission efficiencies) and long-lived emissive transition metal complexes. In the arylborane–ruthenium(II) complexes, a (dimesityl)borylduryletheynyl (DBDE) group is employed as an arylborane unit since the DBDE group is chemically-stable owing to the presence of the bulky methyl groups in the mesityl and durylene moieties and, the ethynylene moiety would maximize the synergistic MLCT/π(aryl)–p(B) CT interactions by reducing the dihedral angle between the durylene and diimine-ligand moieties. A DBDE group(s) was introduced to the 4 and/or 4'-position(s) of bpy or 4,7-positions of phen to realize effective MLCT/π(aryl)–

p(B) CT interactions originated from the linear arrangement between the dipole moments of the MLCT (i.e., Ru–N bond) and π(aryl)–p(B) CT transitions (i.e., durylene–B bond) as demonstrated by more effective MLCT/π(aryl)–p(B) CT interactions in 4RuB relative to those in 5RuB.

The thesis consists of five chapters as described briefly below.

In Chapter 1, the research background and purpose of the thesis are described. As the key aspects into the present study, the examples of emissive transition metal complexes, polypyridyl ruthenium(II) complexes, triarylborane derivatives and transition metal complexes having an arylborane unit(s) are overviewed. As the theoretical back ground for designing bright and long-lived emissive ruthenium(II) complexes, the Strickler–Berg relation for a fluorescence transition of a molecule and the role of excited singlet–triplet mixing for a phosphorescence transition in a transition metal complex are also introduced briefly in this chapter.

In Chapter 2, the synthesis and the electrochemical, spectroscopic, and photophysical properties of a series of the novel $[Ru(bpy)_3]^{2+}$ derivatives having multiple arylborane units ($[Ru(B_2bpy)_n(bpy)_{3-n}]^{2+}$ (**2a**: n = 3, **2b**: n = 2, **2c**: n = 1) and $[Ru(Bbpy)_n(bpy)_{3-n}]^{2+}$ (**2a'**: n = 3, **2b'**: n = 2, **2c'**: n = 1): for the structures, see Chart 1-5) are described. The complexes, **2a**–**c** and **2a'**–**c'**, showed intense absorption and intense/long-lived emission due to the synergistic MLCT/π(aryl)–p(B) CT interactions. Furthermore, the Φ_{em} values of **2a**–**c** and **2a'**–**c'** increased with an increase in n for both **2a**–**c** and **2a'**–**c'** series. In particular, **2a** showed extremely intense emission with Φ_{em} = 0.43. One of the important findings of the study is the increase in the ε_{MLCT} values of **2a**–**2c** and **2a'**–**c'** with that in n, and the increase in ε_{MLCT} of the complex brings about

an increase in k_r. The positive correlations between k_r and ε_{MLCT} observed for **2a**–**2c** and **2a'**–**c'** resemble with the Strickler–Berg relation for the fluorescence transition of a molecule. These results are essentially due to the synergistic MLCT/π(aryl)–p(B) CT interactions in the emitting excited states of **2a**–**c** and **2a'**–**c'**, as demonstrated by the electrochemical, spectroscopic/photophysical, and time-dependent DFT (TD-DFT) calculation studies.

In Chapter 3, the synthesis and the spectroscopic/photophysical properties of a novel homoleptic ruthenium(II) complex having DBDE groups at the 4- and 7-positions of the phen ligands in $[Ru(phen)_3]^{2+}$ ($[Ru(B_2phen)_3]^{2+}$: **3a**, see structure in Chart 1-5) were described in special references to the diimine ligand structure effects on the properties by comparing the data on **3a** with those on **2a**. Since **3a** shows simultaneously intense visible absorption, high Φ_{em}, and long τ_{em}, the diimine-ligand structure in a complex is one of the important factors to characterize the synergistic MLCT/π(aryl)–p(B) CT interactions of the complexes.

In Chapter 4, the synthesis and the spectroscopic/photophysical properties of novel heteroleptic arylborane–ruthenium(II) complexes having a series of ancillary ligands L' ($[Ru(B_2bpy)L'_2]^{2+}$: **4dpbpy** (L' = 4,4'-ph_2-bpy), **4dmbpy** (L' = 4,4'-me_2-bpy), **4dpphen** (L' = 4,7-ph_2-phen), **4dmphen** (L' = 4,7-me_2-phen), **4phen** (L' = phen): see Chart 1-5) were described focusing on the ancillary-ligand effects on the properties. The MLCT absorption/emission energies of $[Ru(B_2bpy)L'_2]^{2+}$ is shown to be manipulated synthetically by the electron donating ability of the ancillary ligand(s). As the results of *T*-dependences of the emission lifetimes and Strickler–Berg-type analysis, furthermore, it is revealed that the photophysical properties of $[Ru(B_2bpy)L'_2]^{2+}$ can be also manipulated by the choice of an ancillary-ligand in the complex.

In Chapter 5, the principal conclusions and future perspective of the study are summarized.

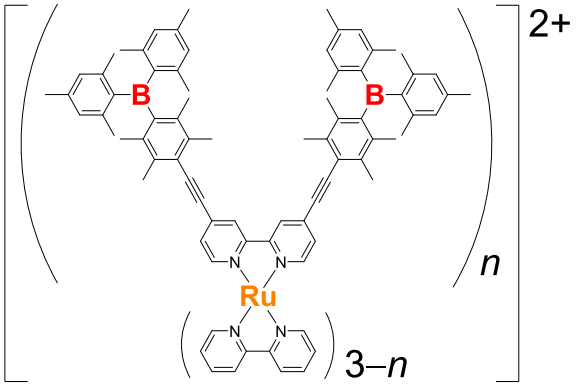

2a–c (*n* = 3–1)

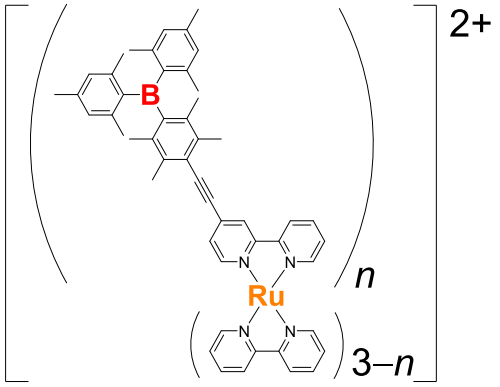

2a'–c' (*n* = 3–1)

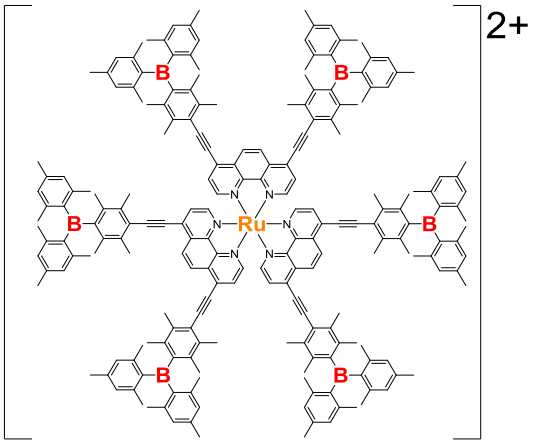

3a

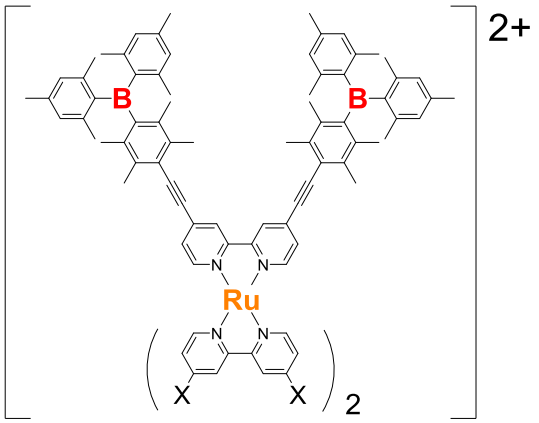

4dpbpy (-X = -C_6H_5),
4dmbpy (-X = -CH_3)

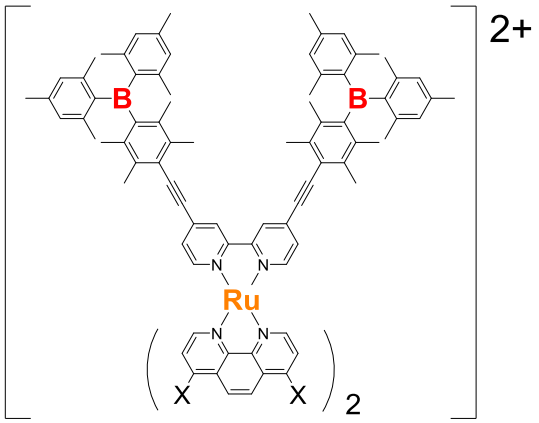

4dpphen (-X = -C_6H_5),
4dmphen (-X = -CH_3),
4phen (-X = -H)

Chart 1-5. Chemical structures and abbreviations of the arylborane–ruthenium(II) complexes developed in this thesis.

1-5: References

[1] Thompson, D.W.; Ito, A.; Meyer. T. J. $[Ru(bpy)_3]^{2+}$* and Other Remarkable Metal-to-Ligand Charge Transfer (MLCT) Excited States. *Pure Appl. Chem.* **2013**, *85*, 1257–1305.

[2] Kalyanasundaram, K. Photophysics, Photochemistry and Solar Energy Conversion with Tris(bipyridyl)ruthenium(II) and its Analogs. *Coord. Chem. Rev.* **1982**, *46*, 159–244.

[3] King, K. A.; Spellane, P. J.; Watts, R. J. Excited-State Properties of a Triply Ortho-Metalated Iridium(III) Complex. *J. Am. Chem. Soc.* **1985**, *107*, 1431–1432.

[4] You, Y.; Park, S. Y. Phosphorescent Iridium(III) Complexes: Toward High Phosphorescence Quantum Efficiency through Ligand Control. *Dalton Trans.* **2009**, *8*, 1267–1282.

[5] Kim, J.; Han, S.; Yang, K.; Kwon, S.; Kim, J.; Kim, Y. Highly Efficient Deep-Blue Phosphorescence from Heptafluoropropyl-Substituted Iridium Complexes. *Chem. Commun.* **2015**, *51*, 58–61.

[6] Adachi, C.; Baldo, M. A.; Forresta, S. R.; Lamansky, S.; Thompson, M. E.; Kwong, R. C. High-Efficiency Red Electrophosphorescence Devices. *Appl. Phys. Lett.* **2001**, *78*, 1622–1624.

[7] Yersin, H.; Rausch, A. F.; Czerwieniec, R.; Hofbeck, T.; Fischer, T. The Triplet State of Organo-Transition Metal Compounds. Triplet Harvesting and Singlet Harvesting for Efficient OLEDs. *Coord. Chem. Rev.* **2011**, *255*, 2622–2652.

[8] Liu, R.; Li, Y.; Li, Y.; Zhu, H.; Sun, W. Photophysics and Nonlinear Absorption of Cyclometalated 4,6-Diphenyl-2,2'-Bipyridyl Platinum(II) Complexes with Different Acetylide Ligands. *J. Phys. Chem. A* **2010**, *114*, 12639–12645.

[9] Shao, P.; Li, Y.; Yi, J.; Pritchett, T. M.; Sun, W. Cyclometalated Platinum(II) 6-Phenyl-4-(9,9-Dihexylfluoren-2-yl)-2,2'-Bipyridine Complexes: Synthesis, Photophysics, and Nonlinear Absorption. *Inorg. Chem.* **2010**, *49*, 4507–4517.

[10] Guyon, F.; Hameau, A.; Khatyr, A.; Knorr, M.; Amrouche, H.; Fortin, A.; Harvey, P. D.; Strohmann, C.; Ndiaye, A. L.; Huch, V.; Veith, M.; Avarvari, N. Syntheses, Structures, and Photophysical Properties of Mono- and Dinuclear Sulfur-Rich Gold(I) Complexes. *Inorg. Chem.* **2008**, *47*, 7483–7492.

[11] Krogh-Jespersen, K.; Stibrany, R. T.; John, E.; Westbrook, J. D.; Emge, T. J.; Clarke, M. J.; Potenza, J. A.; Schugar, H. J. Solid-State Changes in Ligand-to-Metal Charge-Transfer Spectra of $(NH_3)_5Ru^{III}$(2,4-Dihydroxybenzoate) and $(NH_3)_5Ru^{III}$(Xanthine) Chromophores. *Inorg. Chem.* **2008**, *47*, 9813–9827.

[12] Shavaleev, N. M.; Davies, E. S.; Adams, H.; Best, J.; Weinstein, J. A. Platinum(II) Diimine Complexes with Catecholate Ligands Bearing Imide Electron-Acceptor Groups: Synthesis, Crystal Structures, (Spectro) Electrochemical and EPR studies, and Electronic Structure. *Inorg. Chem.* **2008**, 47, 1532–1547.

[13] Bi, D.; Feng, Y.; Zhao, Q.; Wang, H.; Zhu, Y.; Bao, X.; Fan, H.; Yu, L.; Yang, Q.; Qiu, D. Synthesis, Crystal Structure, Photophysical Property and Metal Ion-Binding Behavior of a Cyclometalated Platinum(II) Terpyridylacetylide with Efficient π-Conjugation Degree. *RSC Adv.* **2017**, *7*, 46980–46988.

[14] Ito, A.; Knight, T. E.; Stewart, D. J.; Brennaman, M. K.; Meyer, T. J. Rigid Medium Effects on Photophysical Properties of MLCT Excited States of Polypyridyl Os(II) Complexes in Polymerized Poly(ethylene glycol)dimethacrylate Monoliths. *J. Phys. Chem. A* **2014**, *118*, 10326–10332.

[15] Caspar, J. V.; Kober, E. M.; Sullivan, B. P.; Meyer, T. J. Application of the Energy Gap Law to the Decay of Charge-Transfer Excited States. *J. Am. Chem. Soc.* **1982**, *104*, 630–632.

[16] Sacksteder, L.; Zipp, A. P.; Brown, E. A.; Streich, J.; Demas, J. N.; DeGraff, B. A. Luminescence Studies of Pyridine α-Diimine Rhenium(I) Tricarbonyl Complexes. *Inorg. Chem.* **1990**, *29*, 4335–4340.

[17] Kozhevnikov, D. N.; Kozhevnikov, V. N.; Ustinova, M. M.; Santoro, A.; Bruce, D. W.; Koenig B.; Czerwieniec, R.; Fischer, T.; Zabel, M.; Yersin, H. Synthesis of Cyclometallated Platinum Complexes with Substituted Thienylpyridines and Detailed Characterization of Their Luminescence Properties. *Inorg. Chem.* **2009**, *48*, 4179–4189.

[18] Chang, S.; Kavitha, J.; Hung, J.; Chi, Y.; Cheng, Y.; Li, E. Y.; Chou, P.; Lee, G.; Carty, A. J. Luminescent Platinum(II) Complexes Containing Isoquinolinylindazolate Ligands: Synthetic Reaction Pathway and Photophysical Properties. *Inorg. Chem.* **2007**, *46*, 7064–7074.

[19] Araki, H.; Tsuge, K.; Sasaki, Y.; Ishizaka, S.; Kitamura, N. Luminescence Ranging from Red to Blue: A Series of Copper(I)-Halide Complexes Having Rhombic $\{Cu_2(\mu\text{-}X)_2\}$ (X = Br and I) Units with *N*-Heteroaromatic Ligands. *Inorg. Chem.* **2005**, *44*, 9667–9675.

[20] Ford, P.C.; Cariati, E.; Bourassa, J. Photoluminescence Properties of Multinuclear Copper(I) Compounds. *Chem. Rev.* **1999**, *99*, 3625–3647.

[21] Ito, H.; Muromoto, M.; Kurenuma, S.; Ishizaka, S.; Kitamura, N.; Sato, H.; Seki, T. Mechanical Stimulation and Solid Seeding Trigger Single-Crystal-to-Single-Crystal Molecular Domino Transformations. *Nat.*

Commun. **2013**, *4*, 2009.

[22] Teets, T. S.; Partyka, D. V.; Esswein, A. J.; Updegraff III, J. B.; Zeller, M.; Hunter, A. D.; Gray, T. G. Luminescent, Three-Coordinate Azadipyrromethene Complexes of d^{10} Copper, Silver, and Gold. *Inorg. Chem.* **2007**, *46*, 6218–6220.

[23] Chia, Y. Y.; Tay, M. G. An Insight into Fluorescent Transition Metal Complexes. *Dalton Trans.* **2014**, *43*, 13159–13168.

[24] Armaroli, N. Photoactive Mono- and Polynuclear Cu(I)–Phenanthrolines. A Viable Alternative to Ru(II)–Polypyridines?. *Chem. Soc. Rev.* **2001**, *30*, 113–124.

[25] Cuttell, D. G.; Kuang, S.; Fanwick, P. E.; McMillin, D. R.; Walton, R. A. Simple Cu(I) Complexes with Unprecedented Excited-State Lifetimes. *J. Am. Chem. Soc.* **2002**, *124*, 6–7.

[26] Czerwieniec, R.; Leitl, M. J.; Homeier, H. H. H.; Yersin, H. Cu(I) Complexes - Thermally Activated Delayed Fluorescence. Photophysical Approach and Material Design. *Coord. Chem. Rev.* **2016**, *325*, 2–28.

[27] Baldo, M. A.; Lamansky, S.; Burrows, P. E.; Thomson, M. E.; Forrest, S. R. Very High-Efficiency Green Organic Light-Emitting Devices Based on Electrophosphorescence. *Appl. Phys. Lett.* **1999**, *75*, 4–6.

[28] Kato, M.; Kosuge, C.; Morii, K.; Ahn, J. S.; Kitagawa, H.; Mitani, T.; Matsushita, M.; Kato, T.; Yano, S.; Kimura, M. Luminescence Properties and Crystal Structures of Dicyano(diimine)platinum(II) Complexes Controlled by Pt···Pt and π-π Interactions. *Inorg. Chem.* **1999**, *38*, 1638–1641.

[29] Lai, S.; Lam, H.; Lu, W.; Cheung, K.; Che, C. Observation of Low-Energy Metal−Metal-to-Ligand Charge Transfer Absorption and Emission: Electronic Spectroscopy of Cyclometalated Platinum(II) Complexes with Isocyanide Ligands.

Organometallics **2002**, *21*, 226–234.

[30] Field, J. S.; Haines, R. J.; Ledwaba, L. P.; McGuire, R. Jr.; Munro, O. Q.; Low, M. R.; McMillin, D. R. Synthesis, Electrochemistry and Luminescence of $[Pt\{4'\text{-}(R)trpy\}(CN)]^+$ (R = Ph, *o*-$CH_3C_6H_4$, *o*-ClC_6H_4 or *o*-$CF_3C_6H_4$; trpy = 2,2':6',2''-Terpyridine): Crystal Structure of $[Pt\{4'\text{-}(Ph)trpy\}(CN)]BF_4 \cdot CH_3CN$. *Dalton Trans.* **2007**, *2*, 192–199.

[31] Ku, H.; Tong, B.; Chi, Y.; Kao, H.; Yeh, C.; Chang, C.; Lee, G. Luminescent Pt(II) Complexes Bearing Dual Isoquinolinyl Pyrazolates: Fundamentals and Applications. *Dalton Trans.* **2015**, *44*, 8552–8563.

[32] Karakus, C.; Fischer, L. H.; Schmeding, S.; Hummel, J.; Risch, N.; Schaeferling, M.; Holder, E. Oxygen and Temperature Sensitivity of Blue to Green to Yellow Light-Emitting Pt(II) Complexes. *Dalton Trans.* **2012**, *41*, 9623–9632.

[33] Han, M.; Tian, Y.; Yuan, Z.; Zhu, L.; Ma, B. A Phosphorescent Molecular "Butterfly" that Undergoes a Photoinduced Structural Change Allowing Temperature Sensing and White Emission. *Angew. Chem. Int. Ed.* **2014**, *53*, 10908–10912.

[34] Kitani, N.; Kuwamura, N.; Tsuji, T.; Tsuge, K.; Konno, T. Water-Molecule-Driven Vapochromic Behavior of a Mononuclear Platinum(II) System with Mixed Bipyridine and Thioglucose. *Inorg. Chem.* **2014**, *53*, 1949–1951.

[35] Han, A.; Du, P.; Sun, Z.; Wu, H.; Jia, H.; Zhang, R.; Liang, Z.; Cao, R.; Eisenberg. R. Reversible Mechanochromic Luminescence at Room Temperature in Cationic Platinum(II) Terpyridyl Complexes. *Inorg. Chem.* **2014**, *53*, 3338–3344.

[36] Shigeta, Y.; Kobayashi, A.; Ohba, T.; Yoshida, M.; Matsumoto, T.; Chang, H.;

Kato, M. Shape-Memory Platinum(II) Complexes: Intelligent Vapor-History Sensor with ON–OFF Switching Function. *Chem.–Eur. J.* **2016**, *22*, 2682–2690.

[37] Baldo, M. A.; O'Brien, D. F.; You, Y.; Shoustikov, A.; Sibley, A.; Thompson, M. E.; Forrest, S. R. Highly Efficient Phosphorescent Emission from Organic Electroluminescent Devices. *Nature* **1998**, *395*, 151–154.

[38] Yang, X.; Zhou, G.; Wong, W. Functionalization of Phosphorescent Emitters and their Host Materials by Main-Group Elements for Phosphorescent Organic Light-Emitting Devices. *Chem. Soc. Rev.* **2015**, *44*, 8484–8575.

[39] Liao, K.; Hsu, C.; Chi, Y.; Hsu, M.; Wu, S.; Chang, C.; Liu, S.; Lee, G.; Chou, P.; Hu, Y.; Robertson, N. Pt(II) Metal Complexes Tailored with a Newly Designed Spiro-Arranged Tetradentate Ligand; Harnessing of Charge-Transfer Phosphorescence and Fabrication of Sky Blue and White OLEDs. *Inorg. Chem.* **2015**, *54*, 4029–4038.

[40] Ma, D.; Zhang, C.; Qiu, Y.; Duan, L. Highly Efficient Blue-Green Organic Light-Emitting Diodes Achieved by Controlling the Anionic Migration of Cationic Iridium(III) Complexes. *J. Mater. Chem. C* **2016**, *4*, 5731–5738.

[41] Carraway, E. R.; Demas, J. N.; DeGraff, B. A.; Bacon, J. R. Photophysics and Photochemistry of Oxygen Sensors Based on Luminescent Transition-Metal Complexes. *Anal. Chem.* **1991**, *63*, 337–342.

[42] McDonagh, C.; MacCraith, B. D.; McEvoy, A. K. Tailoring of Sol−Gel Films for Optical Sensing of Oxygen in Gas and Aqueous Phase. *Anal. Chem.* **1998**, *70*, 45–50.

[43] Anzenbacher, P. Jr.; Tyson, D. S.; Jursíková, K.; Castellano, F. N. Luminescence Lifetime-Based Sensor for Cyanide and Related Anions. *J. Am. Chem. Soc.* **2002**,

124, 6232–6233.

[44] Liu, Z.; He, W.; Guo, Z. Metal Coordination in Photoluminescent Sensing. *Chem. Soc. Rev.* **2013**, *42*, 1568–1600.

[45] Cattaneo, M.; Fagalde, F.; Katz, N. E.; Borsarelli, C. D.; Parella, T. pH-Induced Luminescence Changes of Chromophore-Quencher Tricarbonylpolypyridylrhenium(I) Complexes with 4-Pyridinealdazine. *Eur. J. Inorg. Chem.* **2007**, *34*, 5323–5332.

[46] Walsh, J. J.; Zeng, Q.; Forster, R. J.; Keyes, T. E. Highly Luminescent Ru(II) Metallopolymers: Photonic and Redox Properties in Solution and as Thin Films. *Photochem. Photobiol. Sci.* **2012**, *11*, 1547–1557.

[47] Ma, D.; He, H.; Leung, K.; Chan, D. S.; Leung, C. Bioactive Luminescent Transition-Metal Complexes for Biomedical Applications. *Angew. Chem. Int. Ed.* **2013**, *52*, 7666–7682.

[48] Septiadi, D.; Aliprandi, A.; Mauro, M.; De Cola, L. Bio-Imaging with Neutral Luminescent Pt(II) Complexes Showing Metal···Metal Interactions. *RSC Adv.* **2014**, *4*, 25709–25718.

[49] Wang, S.; Zeman IV, C. J.; Jiang, J.; Pan, Z.; Schanze, K. S. Intercalation of Alkynylplatinum(II) Terpyridine Complexes into a Helical Poly(phenylene ethynylene) Sulfonate: Application to Protein Sensing. *ACS Appl. Mater. Interfaces* **2017**, *9*, 33461–33469.

[50] Pashaei, B.; Shahroosvand, H.; Abbasi, P. Transition Metal Complex Redox Shuttles for Dye-Sensitized Solar Cells. *RSC Adv.* **2015**, *5*, 94814–94848.

[51] Loeblein, M.; Bruno, A.; Loh, G. C.; Bolker, A.; Saguy, C.; Antila, L.; Tsang, S. H.; Teo, E. H. T. Investigation of Electronic Band Structure and Charge Transfer

Mechanism of Oxidized Three-Dimensional Graphene as Metal-Free Anodes Material for Dye Sensitized Solar Cell Application. *Chem. Phys. Lett.* **2017**, 685, 442–450.

[52] Turro, N. J. *Modern Molecular Photochemistry*. Benjamin/Cummings Publishing, Menlo Park, **1978**.

[53] Strickler, S. J.; Berg, R. A. Relationship between Absorption Intensity and Fluorescence Lifetime of Molecules. *J. Chem. Phys.* **1962**, *37*, 814–822.

[54] Burstall, F. H. Optical Activity Dependent on Co-ordinated Bivalent Ruthenium. *J. Chem. Soc.* **1936**, 173–175.

[55] Paris, J. P.; Brandt, W. W. Charge Transfer Luminescence of a Ruthenium(II) Chelate. *J. Am. Chem. Soc.* **1959**, *81*, 5001–5002.

[56] Crosby, G. A.; Perkins, W. G.; Klassen, D. M. Luminescence from Transition-Metal Complexes: Tris(2,2'-bipyridine)- and Tris(1,10-phenanthroline) ruthenium(II). *J. Chem. Phys.* **1965**, *43*, 1498–1503.

[57] Palmer, R. A.; Piper, T. S. 2,2'-Bipyridine Complexes. I. Polarized Crystal Spectra of Tris(2,2'-bipyridine)copper(II), -nickel(II), -cobalt(II), -iron(II), and -ruthenium(II). *Inorg. Chem.* **1966**, *5*, 864–878.

[58] Klassen, David M.; Crosby, Glenn A. Spectroscopic Studies of Ruthenium(II) Complexes. Assignment of the Luminescence. *J. Chem. Phys.* **1968**, *48*, 1853–1858.

[59] Demas, J. N.; Crosby, G. A. The Multiplicity of the Emitting State of Ruthenium(II) Complexes. *J. Mol. Spectrosc.* **1968**, *26*, 72–77.

[60] Lytle, F. E.; Hercules, D. M. Luminescence of Tris(2,2'-bipyridine)ruthenium(II) Dichloride. *J. Am. Chem. Soc.* **1969**, *91*, 253–257.

[61] Crosby, G. A.; Demas, J. N. Quantum Efficiencies on Transition Metal Complexes. II. Charge-Transfer Luminescence. *J. Am. Chem. Soc.* **1971**, *93*, 2841–2847.

[62] Fujita, I.; Kobayashi, H. Luminescence Polarization of the Tris(2,2'-bipyridine) ruthenium(II) Complex. *Inorg. Chem.* **1973**, *12*, 2758–2762.

[63] Harrigan, R. W.; Crosby, G. A. Symmetry Assignments of the Lowest CT Excited States of Ruthenium (II) Complexes via a Proposed Electronic Coupling Model *J. Chem. Phys.* **1973**, *59*, 3468–3476.

[64] Cannizzo, A.; Van Mourik, F.; Gawelda, W.; Zgrablic, G.; Bressler, C.; Chergui, M. Broadband Femtosecond Fluorescence Spectroscopy of $[Ru(bpy)_3]^{2+}$. *Angew. Chem. Int. Ed.* **2006**, *45*, 3174–3176.

[65] Cooley, L. F.; Bergquist, P.; Kelley, D. F. Determination of Exciton Hopping Rates in Ruthenium(II) Tris(bipyridine) Complexes by Picosecond Polarized Absorption Spectroscopy. *J. Am. Chem. Soc.* **1990**, *112*, 2612–2617.

[66] Van Houten, J.; Watts, R. J. Temperature Dependence of the Photophysical and Photochemical Properties of the Tris(2,2'-bipyridyl)ruthenium(II) Ion in Aqueous Solution. *J. Am. Chem. Soc.* **1976**, *98*, 4853–4858.

[67] Caspar, J. V.; Meyer, T. J. Photochemistry of MLCT Excited States. Effect of Nonchromophoric Ligand Variations on Photophysical Properties in the Series cis-$Ru(bpy)_2L_2^{2+}$. *Inorg. Chem.* **1983**, *22*, 2444–2453.

[68] Caspar, J. V.; Meyer, T. J. Photochemistry of $Ru(bpy)_3^{2+}$. Solvent Effects. *J. Am. Chem. Soc.* **1983**, *105*, 5583–5590.

[69] Chen, P.; Meyer, T. J. Medium Effects on Charge Transfer in Metal Complexes. *Chem. Rev.* **1998**, *98*, 1439-1477.

[70] Kober, E. M.; Meyer, T. J. An Electronic Structural Model for the Emitting MLCT Excited States of $Ru(bpy)_3^{2+}$ and $Os(bpy)_3^{2+}$. *Inorg. Chem.* **1984**, *23*, 3877–3886.

[71] Lumpkin, R. S.; Kober, E. M.; Worl, L. A.; Murtaza, Z.; Meyer, T. J. Metal-to-Ligand Charge-Transfer (MLCT) Photochemistry: Experimental Evidence for the Participation of a Higher Lying MLCT State in Polypyridyl Complexes of Ruthenium(II) and Osmium(II). *J. Phys. Chem.* **1990**, *94*, 239–243.

[72] Treadway, J. A.; Loeb, B.; Lopez, R.; Anderson, P. A.; Keene, F. R.; Meyer, T. J. Effect of Delocalization and Rigidity in the Acceptor Ligand on MLCT Excited-State Decay. *Inorg. Chem.* **1996**, *35*, 2242–2246.

[73] Kestell, J. D.; Williams, Z. L.; Stultz, L. K.; Claude, J. P. Medium Dependence of Intramolecular Vibrational Modes Coupled to MLCT Transitions in Metal Polypyridyl Complexes. *J. Phys. Chem. A* **2002**, *106*, 5768–5778.

[74] Ito, A.; Meyer, T. J. The Golden Rule. Application for Fun and Profit in Electron Transfer, Energy Transfer, and Excited-State Decay. *Phys. Chem. Chem. Phys.* **2012**, *14*, 13731–13745.

[75] Hartmann, P.; Leiner, M. J. P.; Lippitsch, M. E. Luminescence Quenching Behavior of an Oxygen Sensor Based on a Ru(II) Complex Dissolved in Polystyrene. *Anal. Chem.* **1995**, *67*, 88–93.

[76] Klimant, I.; Wolfbeis, O. S. Oxygen-Sensitive Luminescent Materials Based on Silicone-Soluble Ruthenium Diimine Complexes. *Anal. Chem.* **1995**, *67*, 3160–3166.

[77] Delaney, J. L.; Hogan, C. F.; Tian, J.; Shen, W. Electrogenerated Chemiluminescence Detection in Paper-Based Microfluidic Sensors. *Anal. Chem.*

2011, *83*, 1300–1306.

[78] Juris, A.; Balzani, V.; Barigelletti, F.; Campagna, S.; Belser, P.; von Zelewsky, A. Ru(II) Polypyridine Complexes: Photophysics, Photochemistry, Electrochemistry, and Chemiluminescence. *Coord. Chem. Rev.* **1988**, *84*, 85–277.

[79] Czioska, S.; Chen, Z. Electrogenerated Chemiluminescence of the Tris(2,2'-bipyridine)ruthenium(II)/Aliphatic Amine System: A Universal Effect of Perchlorate Salts. *RSC Adv.* **2016**, *6*, 6583–6588.

[80] Hu, Y.; Maclennan, A.; Sham, T. K. Electronic Structure and Optical Luminescence Studies of Ru Based OLED Compounds. *J. Lumin.* **2015**, *166*, 143–147.

[81] Mahenderkar, N. K.; Chen, Q.; Liu, Y.; Duchild, A. R.; Hofheins, S.; Chason, E.; Switzer, J. A. Epitaxial Lift-off of Electrodeposited Single-Crystal Gold Foils for Flexible Electronics. *Science*, **2017**, *355*, 1203–1206.

[82] Schwarz, P.; Bossmann, S.; Guldner, A.; Duerr, H. A Combined Investigation of Four Colloids for Artificial Photosynthesis by Scanning Electron Microscopy, Quasielastic Light Scattering, and Bis-heteroleptic Styrene-Attached Ruthenium Complexes, Adsorbed at the water/colloid Interface. *Langmuir* **1994**, *10*, 4483–4497.

[83] Sun, L.; Hammarstrom, L.; Akermark, B.; Styring, S. Towards Artificial Photosynthesis: Ruthenium-Manganese Chemistry for Energy Production. *Chem. Soc. Rev.* **2001**, *30*, 36–49.

[84] Yamazaki, Y.; Takeda, H.; Ishitani, O. Photocatalytic Reduction of CO_2 Using Metal Complexes. *Photochem. Photobiol. C* **2015**, *25*, 106–137.

[85] Kuramochi, Y.; Fukaya, K.; Yoshida, M.; Ishida, H.

trans-(Cl)-[Ru(5,5'-diamide-2,2'-bipyridine)$(CO)_2Cl_2$]: Synthesis, Structure, and Photocatalytic CO_2 Reduction Activity. *Chem. –Eur. J.* **2015**, *21*, 10049–10060.

[86] O'Regan, B.; Grätzel, M. A Low-cost, High-Efficiency Solar Cell Based on Dye-Sensitized Colloidal TiO_2 Films. *Nature* **1991**, *353*, 737–740.

[87] Polander, Lauren E.; Yella, Aswani; Curchod, Basile F. E.; Ashari Astani, Negar; Teuscher, Joel; Scopelliti, Rosario; Gao, Peng; Mathew, Simon; Moser, Jacques-E.; Tavernelli, Ivano; Rothlisberger, U.; Grätzel, M.; Nazeeruddin, M. K.; Frey, J. *Angew. Chem. Int. Ed.* **2013**, *52*, 8731–8735.

[88] Dong, Y.; Wei, L.; Fan, R.; Yang, Y.; Wang, P. Influence of Anchoring Group Numbers in an Efficient Pyridine-Anchor Co-Adsorbent of Pyridinecarboxaldimine Substituted Aminonaphthalene on the Performance of N719 Sensitized Solar Cells. *RSC Adv.* **2016**, *6*, 39972–39981.

[89] Lu, T.; Li, W.; Bai, F.; Jia, R.; Chen, J.; Zhang, H. Anionic Ancillary Ligands in Cyclometalated Ru(II) Complex Sensitizers Improve Photovoltaic Efficiency of Dye-Sensitized Solar Cells: Insights from Theoretical Investigations. *J. Mater. Chem. A* **2017**, *5*, 15567–15577.

[90] Suzuki, K.; Kobayashi, A.; Kaneko, S.; Takehira, K.; Yoshihara, T.; Ishida, H.; Shiina, Y.; Oishi, S.; Tobita, S. Reevaluation of Absolute Luminescence Quantum Yields of Standard Solutions Using a Spectrometer with an Integrating Sphere and a Back-Thinned CCD Detector. *Phys. Chem. Chem. Phys.* **2009**, *11*, 9850–9860.

[91] Ito, A.; Hirokawa, T.; Sakuda, E.; Kitamura, N. Bright Green-phosphorescence from Metal-to-Boron Charge-transfer Excited State of a Novel Cyclometalated Iridium(III) Complex. *Chem. Lett.* **2011**, *40*, 34–36.

[92] Hahn, U.; Luelf, H.; Winkler, H. D .F.;Schalley, C. A.; Vçgtle, F.; De Cola, L.

Encapsulation of Luminescent Homoleptic $[Ru(dpp)_3]^{2+}$-Type Chromophores within an Amphiphilic Dendritic Environment. *Chem.–Eur. J.* **2012**, *18*, 15424–15432.

[93] Montalti, M.; Credi, A.; Prodi, L.; Teresa, M. *Handbook of Photochemistry*, *3rd ed.*, CRC Press, Boca Raton, **2006**.

[94] Ramsey, B. G. Charge-Transfer States in Boranes and Carbonium Ions. Their Ultraviolet Spectra. *J. Phys. Chem.* **1966**, *70*, 611–618.

[95] Yamaguchi, S.; Akiyama, S.; Tamao, K. Tri-9-anthrylborane and Its Derivatives: New Boron-Containing π-Electron Systems with Divergently Extended π-Conjugation through Boron. *J. Am. Chem. Soc.* **2000**, *122*, 6335–6336.

[96] Kitamura, N.; Sakuda, E. Spectroscopic and Excited-State Properties of Tri-9-anthrylborane I: Solvent Polarity Effects. *J. Phys. Chem. A* **2005**, *109*, 7429–7434.

[97] Kitamura, N.; Sakuda, E.; Yoshizawa, T.; Iimori, T.; Ohta, N. Spectroscopic and Excited-State Properties of Tri-9-anthrylborane II: Electroabsorption and Electrofluorescence Spectra. *J. Phys. Chem. A* **2005**, *109*, 7435–7441.

[98] Yamaguchi, S.; Akiyama, S.; Tamao, K. Colorimetric Fluoride Ion Sensing by Boron-Containing π-Electron Systems. *J. Am. Chem. Soc.* **2001**, *123*, 11372–11375.

[99] Kubo, Y.; Yamamoto, M.; Ikeda, M.; Takeuchi, M.; Shinkai, S.; Yamaguchi, S.; Tamao, K. A Colorimetric and Ratiometric Fluorescent Chemosensor with Three Emission Changes. Fluoride Ion Sensing by a Triarylborane-Porphyrin Conjugate. *Angew. Chem. Int. Ed.* **2003**, *42*, 2036–2040.

[100] Parab, K.; Venkatasubbaiah, K.; Jaekle, F. Luminescent Triarylborane-

Functionalized Polystyrene: Synthesis, Photophysical Characterization, and Anion-Binding Studies. *J. Am. Chem. Soc.* **2006**, *128*, 12879–12885.

[101] Sakuda, E.; Tsuge, K.; Sasaki, Y.; Kitamura, N. Spectroscopic and Excited-State Properties of Tri-9-anthrylborane III: Crystal and Spectroscopic Polymorphisms. *J. Phys. Chem. B* **2005**, *109*, 22326–22331.

[102] Kitamura, N.; Sakuda, E.; Iwahashi, Y.; Tsuge, K.; Sasaki, Y.; Ishizaka, S. Linkage-Structure Dependences of the Spectroscopic and Photophysical Properties of Anthracene Derivatives: Tri(9-anthryl)benzene and Tri(9-anthryl)borane. *J. Photochem. Photobiol. A: Chem.* **2009**, *207*, 102–108.

[103] Ito, A.; Kawanishi, K.; Sakuda, E.; Kitamura, N. Synthetic Control of Spectroscopic and Photophysical Properties of Triarylborane Derivatives Having Peripheral Electron-Donating Groups. *Chem.–Eur. J.* **2014**, *20*, 3940–3953.

[104] Matsumi, N.; Sugai, K.; Ohno, H. Selective Ion Transport in Organoboron Polymer Electrolytes Bearing a Mesitylboron Unit. *Macromolecules* **2002**, *35*, 5731–5733.

[105] Matsumi, N.; Sugai, K.; Ohno, H. Ion Conductive Characteristics of Alkylborane Type and Boric Ester Type Polymer Electrolytes Derived from Mesitylborane. *Macromolecules*, **2003**, *36*, 2321–2326.

[106] Matsumi, N.; Mizumo, T.; Ohno, H. Single Ion Conductive Characteristics of Poly(organoboron halide)-Imidazole Complex. *Polym. Bull.* **2004**, *51*, 389–394.

[107] Mengel, A. K. C.; He, B.; Wenger, O. S. A Triarylamine-Triarylborane Dyad with a Photochromic Dithienylethene Bridge. *J. Org. Chem.* **2012**, *77*, 6545–6552.

[108] Matsumi, N.; Naka, K.; Chujo, Y. Poly(p-phenylene-borane)s. Novel Organoboron π-Conjugated Polymers via Grignard Reagent. *J. Am. Chem. Soc.*

1998, *120*, 10776–10777.

[109] Jia, W.; Song, D.; Wang, S. Blue Luminescent Three-Coordinate Organoboron Compounds with a 2,2'-Dipyridylamino Functional Group. *J. Org. Chem.* **2003**, *68*, 701–705.

[110] Qin, Y.; Kiburu, I.; Shah, S.; Jaekle, F. Synthesis and Characterization of Organoboron Quinolate Polymers with Tunable Luminescence Properties. *Macromolecules* **2006**, *39*, 9041–9048.

[111] Nagata, Y.; Chujo, Y. Main-Chain-Type *N*,*N*'-Chelate Organoboron Aminoquinolate Polymers: Synthesis, Luminescence, and Energy Transfer Behavior. *Macromolecules* **2008**, *41*, 3488–3492.

[112] Hayek, A.; Nicoud, J.; Bolze, F.; Bourgogne, C.; Baldeck, P. L. Boron-Containing Two-Photon-Absorbing Chromophores: Electronic Interaction through the Cyclodiborazane Core. *Angew. Chem. Int. Ed.* **2006**, *45*, 6466–6469.

[113] Branger, C.; Lequan, M.; Lequan, R. M.; Large, M.; Kajzar, F. Polyurethanes Containing Boron Chromophores as Sidechains for Nonlinear Optics. *Chem. Phys. Lett.* **1997**, *272*, 265–270.

[114] Entwistle, C. D.; Marder, T. B. Applications of Three-Coordinate Organoboron Compounds and Polymers in Optoelectronics. *Chem. Mater*. **2004**, *16*, 4574–4585.

[115] Jäkle, F. Advances in the Synthesis of Organoborane Polymers for Optical, Electronic, and Sensory Applications. *Chem. Rev.* **2010**, *110*, 3985–4022.

[116] Yamaguchi, S.; Shirasaka, T.; Tamao, K. Tridurylboranes Extended by Three Arylethynyl Groups as a New Family of Boron-Based π-Electron Systems. *Org. Lett.* **2000**, *2*, 4129–4132.

[117] Sakuda, E.; Ando, Y.; Ito, A.; Kitamura, N. Extremely Large Dipole Moment in the Excited Singlet State of Tris{[*p*-(*N*,*N*-dimethylamino)-phenylethynyl]duryl}borane. *J. Phys. Chem. A* **2010**, *114*, 9144–9150.

[118] Zhao, Y.; Pan, H.; Fu, G.; Lin, J.; Zhao, C. A Highly Emissive Cruciform Triarylborane as a Ratiometric and Solid State Fluorescence Sensor for Fluoride Ions. *Tetrahedron Lett.* **2011**, *52*, 3832–3835.

[119] Saito, S.; Matsuo, K.; Yamaguchi, S. Polycyclic π-Electron System with Boron at Its Center. *J. Am. Chem. Soc.* **2012**, *134*, 9130–9133.

[120] Sakuda, E.; Funahashi, A.; Kitamura, N. Synthesis and Spectroscopic Properties of Platinum(II) Terpyridine Complexes Having an Arylborane Charge Transfer Unit. *Inorg. Chem.* **2006**, *45*, 10670–10677.

[121] Zhao, S.–B.; McCormick, T.; Wang, S. Ambient-Temperature Metal-to-Ligand Charge-Transfer Phosphorescence Facilitated by Triarylboron: Bnpa and Its Metal Complexes. *Inorg. Chem.* **2007**, *46*, 10965–10967.

[122] Sun, Y.; Ross, N.; Zhao, S.–B.; Huszarik, K.; Jia, W.–L.; Wang, R.–Y.; Macartney, D.; Wang, S. Enhancing Electron Accepting Ability of Triarylboron via π-Conjugation with 2,2'-Bipy and Metal Chelation: 5,5'-Bis($BMes_2$)-2,2'-bipy and Its Metal Complexes. *J. Am. Chem. Soc.* **2007**, *129*, 7510–7511.

[123] Sun, Y.; Wang, S. Conjugated Triarylboryl Donor–Acceptor Systems Supported by 2,2'-Bipyridine: Metal Chelation Impact on Intraligand Charger Transfer Emission, Electron Accepting Ability, and "Turn-on" Fluoride Sensing. *Inorg. Chem.* **2009**, *48*, 3755–3767.

[124] Hudson, Z. M.; Zhao, S.–B.; Wang, R. Y.; Wang, S. Switchable Ambient-Temperature Singlet-Triplet Dual Emission in Nonconjugated

Donor-Acceptor Triarylboron-Pt Complexes. *Chem.–Eur. J.* **2009**, *15*, 6131–6137.

[125] Rao, Y.–L.; Wang, S. Impact of Constitutional Isomers of ($BMes_2$)phenylpyridine on Structure, Stability, Phosphorescence, and Lewis Acidity of Mononuclear and Dinuclear Pt(II) Complexes. *Inorg. Chem.* **2009**, *48*, 7698–7713.

[126] Sun, Y.; Wang, S. Extending π-Conjugation of Triarylborons with a 2,2-Bpy Core: Impact of Donor−Acceptor Geometry on Luminescence, Anion Sensing, and Metal Ion Binding *Inorg. Chem.* **2010**, *49*, 4394–4404.

[127] Zhou, G.; Ho, C.–L.; Wong, W.–Y.; Wang, Q.; Ma, D.; Wang, L.; Lin, Z.; Marder, T. B.; Beeby, A. Manipulating Charge-Transfer Character with Electron-Withdrawing Main-Group Moieties for the Color Tuning of Iridium Electrophosphors. *Adv. Funct. Mater.* **2008**, *18*, 499–511.

[128] You, Y.; Park, S. Y. A Phosphorescent Ir(III) Complex for Selective Fluoride Ion Sensing with a High Signal-to-Noise Ratio. *Adv. Mater.* **2008**, *20*, 3820–3826.

[129] Zhao, Q.; Li, F.; Liu, S.; Yu, M.; Liu, Z.; Yi, T.; Huang, C. Highly Selective Phosphorescent Chemosensor for Fluoride Based on an Iridium(III) Complex Containing Arylborane Units. *Inorg. Chem.* **2008**, *47*, 9256–9264.

[130] Lin, W.; Tan, Q.; Liang, H.; Zhang, K. Y. Liu, S.; Jiang, R.; Hu, R.; Xu, W.; Zhao, Q.; Huang, W. Phosphorescence Switch and Logic Gate of Iridium(III) Complexes Containing a Triarylboron Moiety Triggered by Fluoride and an Electric Field. *J. Mater. Chem. C* **2015**, *3*, 1883–1887.

[131] Sakuda, E.; Ando, Y.; Ito, A.; Kitamura, N. Long-Lived and Temperature-Independent Emission from a Novel Ruthenium(II) Complex Having an Arylborane Charge-Transfer Unit. *Inorg. Chem.* **2011**, *50*, 1603–1613

[132] Wade, C. R.; Gabbaï, F. P. Cyanide Anion Binding by a Triarylborane at the Outer Rim of a Cyclometalated Ruthenium(II) Cationic Complex. *Inorg. Chem.* **2010**, *49*, 714–720.

[133] Sun, Y.; Hudson, Z. M. Rao, Y.; Wang, S. Tuning and Switching MLCT Phosphorescence of $[Ru(bpy)_3]^{2+}$ Complexes with Triarylboranes and Anions *Inorg. Chem.* **2011**, *50*, 3373–3378.

[134] Ito, A.; Kang, Y.; Sakuda, E.; Kitamura, N. Photophysical and Photoredox Characteristics of a Novel Tricarbonyl Rhenium(I) Complex Having an Arylborane-Appended Aromatic Diimine Ligand. *Inorg. Chem.* **2012**, *51*, 7722–7732.

[135] Kang, Y.; Ito, A.; Sakuda, E.; Kitamura, N. Diimine Ligand Structure Effects on Photophysical Properties of Tricarbonyl Rhenium(I) Complexes Having Arylborane Charge Transfer Units. *J. Photochem. Photobiol. A: Chem.* **2015**, *313*, 107–116.

[136] Kang, Y.; Ito, A.; Sakuda, E.; Kitamura, N. Characteristic Spectroscopic and Photophysical Properties of Tricarbonyl Rhenium(I) Complexes Having Multiple Arylborane Charge Transfer Units. *Bull. Chem. Soc. Jpn.* **2017**, *90*, 574–585.

[137] Smith, L. F.; Blight, B. A.; Park, H.–J.; Wang, S. Sensitizing Tb(III) and Eu(III) Emission with Triarylboron Functionalized 1,3-Diketonato Ligands. *Inorg. Chem.* **2014**, *53*, 8036–8044.

[138] Park, H.–J.; Ko, S.–B.; Wyman, I. W.; Wang, S. Selective Sensitization of Eu(III) and Tb(III) Emission with Triarylboron-Functionalized Dipicolinic Acids. *Inorg. Chem.* **2014**, *53*, 9751–9760.

Chapter 2: Spectroscopic and Photophysical Properties of Tris(2,2'-bipyridyl)ruthenium(II) Complexes Having Multiple Arylborane Units

2-1: Introduction

This study targets the synthetic modulation of the spectroscopic and photophysical properties of polypyridyl ruthenium(II) complexes by focusing on a triarylborane substituent(s) in the periphery of the diimine ligand(s). Owing to the presence of the vacant p-orbital on the boron atom (p(B)) in a triarylborane, a class of transition metal complexes having a triarylborane group(s) in the periphery of the ligand(s) shows fascinating excited-state properties, characterized by the synergistic interactions between MLCT in the transition metal complex and π(aryl)–p(B) CT in the triarylborane group: synergistic MLCT/π(aryl)–p(B) CT.[1–6] As a typical example, a $[Ru(phen)_3]^{2+}$ (phen = 1,10-phenathroline) derivative having a (dimesityl)borylduryl-ethynyl (DBDE) group at the 4- (4RuB) or 5-position of one of the three phen ligands (5RuB) shows intense MLCT absorption/emission and long-lived excited state compared to $[Ru(phen)_3]^{2+}$[2] as described in Chapter 1. Since a triarylborane unit is one of the fascinating choices for chemical decoration of transition metal complexes, further understanding of arylborane effects on the spectroscopic and photophysical properties of the complexes are of primary importance toward the molecular design for future photofunctional materials.

In this chapter, the synthesis and the electrochemical, spectroscopic, and photophysical properties of a series of novel $[Ru(bpy)_3]^{2+}$ (bpy = 2,2'-bipyridine) derivatives having multiple arylborane units ($[Ru(B_2bpy)_n(bpy)_{3-n}]^{2+}$ (**2a**: n = 3, **2b**: n

= 2, **2c**: n = 1; B_2bpy = 4,4'-$(DBDE)_2$-bpy) and $[Ru(Bbpy)_n(bpy)_{3-n}]^{2+}$ (**2a'**: n = 3, **2b'**: n = 2, **2c'**: n = 1; Bbpy = 4-DBDE-bpy), see Chart 2-1) are described. On the basis of a systematic control of the number of the arylborane unit in a ligand and/or complex, the intra- and inter-ligand electronic interactions between the arylborane units in the ground- and excited-state complex as well as the electronic interactions between the $[Ru(bpy)_3]^{2+}$ and arylborane moieties were evaluated in detail. It is worth emphasizing that, although a variety of the transition metal complexes bearing a triarylborane-appended ligand have been reported[1–20] as mentioned in Chapter 1, the complex having multiple arylborane-substituted polypyridyl ligands (i.e., multiple borane centers in multiple ligands in a complex) has never been reported. Therefore, the present works are worth conducting in detail for further advances in the relevant researches.

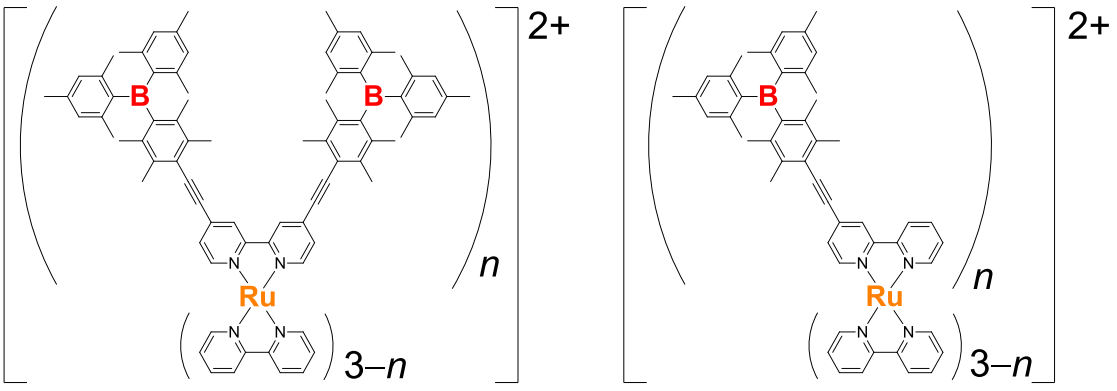

2a–**c** (n = 3–1) **2a'**–**c'** (n = 3–1)

Chart 2-1. Chemical structures of **2a**–**c** and **2a'**–**c'**.

2-2: Experiments and Methodologies

2-2-1: Synthesis

The synthetic routes to **2a**–**c** and **2a'**–**c'** are shown in Scheme 2-1. A

hexafluorophosphate (PF_6^-) ion was used as the counterions of the complexes since the PF_6^- salt of $[RuL_3]^{2+}$ (L = diimine) is highly soluble in polar organic solvents.

All of the complexes were successfully synthesized by the palladium-catalyzed Sonogashira–Hagihara cross-coupling reactions between (ethynylduryl)dimesitylborane (EDDB) and the relevant bromo-substituted precursor complexes, $[Ru(4,4'\text{-}Br_2\text{-}bpy)_n(bpy)_{3-n}](PF_6)_2$ or $[Ru(4\text{-}Br\text{-}bpy)_n(bpy)_{3-n}](PF_6)_2$ (n = 1–3; 4,4'-Br_2-bpy = 4,4'-dibromo-2,2'-bipyridine, 4-Br-bpy = 4-bromo-2,2'-bipyridine), similar to the synthetic procedures for 4RuB.[2] The spectroscopic and photophysical purities of the complexes were confirmed by single-exponential emission decay in CH_3CN at 298 K in addition to the typical characterization methods described later. The enantiomers and diastereomers (Δ-/Λ- isomers around a ruthenium(II) ion and a boron atom) of **2a**–**c** and **2a'**–**c'** were not separated since the emission decay curves could be analyzed by single-exponential functions. The results demonstrate that, even if the isomers of the complexes are present, they do not affect their photophysical properties of the complexes. While it is expected that **2a'** and **2b'** also possess *facial*/*meridional* isomers as suggested by the complicated proton signals of the pyridine rings in the ^{1}H-NMR spectra, they have not been separated due to the same reason with that mention above.

EDDB was prepared according to the literature.[4] All of other chemicals were purchased from Wako Pure Chemical Ind. Ltd., Kanto Chemical Co. Inc., or Tokyo Chemical Ind. Co. Ltd. and used as supplied. $[Ru(bpy)_3](PF_6)_2$ as a reference complex was prepared by adding a saturated aqueous ammonium hexafluorophosphate solution (NH_4PF_4(aq)) to an aqueous solution of $[Ru(bpy)_3]Cl_2$ (Sigma–Aldrich Co. LLC). Column chromatography was carried out by using an aluminum oxide 90 standardized

(Merck, Al_2O_3), GE Healthcare Sephadex LH-20 or Recycling Preparative HPLC (Japan Analytical Industry Company, LC-9201) with a JAIGEL-1H gel-permeation chromatography (GPC) column equipped with UV-3740 UV/Vis and RI-50s RI detectors. ^1H NMR spectra were recorded on a JEOL JME-EX270 FT-NMR system (270 MHz). The chemical shifts of the spectra determined in CD_3CN were given in ppm, with tetramethylsilane being an internal standard (0.00 pm). Electrospray ionization (ESI) mass spectra were recorded on a Waters micromass ZQ spectrometer. Elemental analyses were conducted in the Instrumental Analysis Division, Equipment Management Center, Creative Research Institution, Hokkaido University.

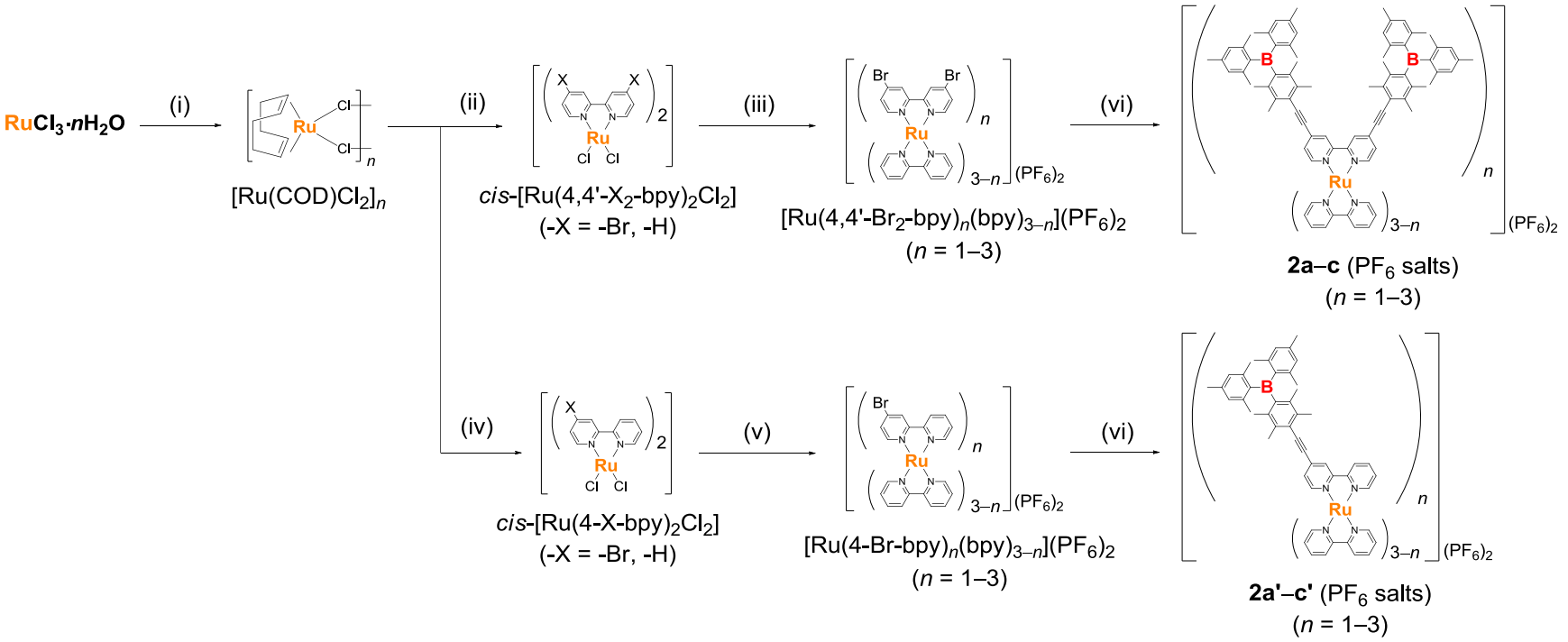

Scheme 2-1. Synthetic routes for the PF_6^- salts of the complexes: (i) 1,5-cyclooctadiene, ethanol, 80ºC, 45 h, (ii) 4,4'-Br_2-bpy or bpy, *o*-dichlorobenzene, 160ºC, 2 h, (iii) 4,4'-Br_2-bpy or bpy, ethanol/water, 80ºC, 5 h, (iv) 4-Br-bpy or bpy, *o*-dichlorobenzene, 160ºC, 2 h, (v) 4-Br-bpy or bpy, ethanol/water, 80ºC, 5 h, (vi) EDDB, $Pd(PPh_3)_2Cl_2$, CuI, NEt_3, CH_3CN/THF, 50ºC, 4 h.

Synthesis of Dichlorido(1,5-cyclooctadiene)ruthenium(II) ([Ru(COD)Cl_2]$_n$). The synthesis was performed by the reported procedures with some modifications.[21] 1,5-Cyclooctadiene (COD, 12 mL, 97 mmol) was added to a suspension of $RuCl_3 \cdot nH_2O$ (2.0 g, 7.7 mmol) in ethanol (50 mL). The mixture was heated at reflux temperature (80ºC) for 45 h and, then, allowed to cool to room temperature. The resulting precipitates were collected by filtration, and washed with ethanol (30 mL × 2), affording [Ru(COD)Cl_2]$_n$ as brown powders (2.2 g, 100%). This compound was used in the following step without any purification and identification.

Synthesis of *cis*-Dichloridobis(4,4'-dibromo-2,2'-bipyridine)ruthenium(II) (*cis*-[Ru(4,4'-Br_2-bpy)$_2Cl_2$]). The synthesis was performed by the reported procedures with some modifications.[22] A suspension of [Ru(COD)Cl_2]$_n$ (100 mg, 0.36 mmol on the basis of the ruthenium atom) and 4,4'-Br_2-bpy (220 mg, 0.72 mmol) in *o*-dichlorobenzene (10 mL) was heated at reflux temperature (160ºC) for 2 h. After cooling the suspension, the reaction mixture was added into diethyl ether (60 mL) and stirred for 30 minutes. The resulting precipitates were collected by filtration, affording *cis*-[Ru(4,4'-Br_2-bpy)$_2Cl_2$] as black powders (260 mg, 92%). This compound was used in the following step without any purification and identification.

Synthesis of *cis*-Bis(2,2'-bipyridine)dichloridoruthenium(II) (*cis*-[Ru(bpy)$_2Cl_2$]). The complex was synthesized similar to the synthesis of *cis*-[Ru(4,4'-Br_2-bpy)$_2Cl_2$] by heating a suspension of [Ru(COD)Cl_2]$_n$ (150 mg, 0.53 mmol) and bpy (170 mg, 1.1 mmol) in *o*-dichlorobenzene (10 mL), giving *cis*-[Ru(bpy)$_2Cl_2$] as black powders (210 mg, 81%). This compound was used in the following step without any purification and

identification.

Synthesis of *cis*-Bis(4-bromo-2,2'-bipyridine)dichloridoruthenium(II) (*cis*-[Ru-(4-Br-bpy)$_2$Cl$_2$]). The complex was synthesized similar to the synthesis of *cis*-[Ru(4,4'-Br$_2$-bpy)$_2$Cl$_2$] by heating a suspension of [Ru(COD)Cl$_2$]$_n$ (100 mg, 0.36 mmol) and 4-Br-bpy (170 mg, 0.72 mmol) in *o*-dichlorobenzene (10 mL), giving *cis*-[Ru(4-Br-bpy)$_2$Cl$_2$] as black powders (180 mg, 78%). This compound was used in the following step without any purification and identification.

Synthesis of Tris(4,4'-dibromo-2,2'-bipyridine)ruthenium(II) Bis(hexafluoro-phosphate) ([Ru(4,4'-Br$_2$-bpy)$_3$](PF$_6$)$_2$). The synthesis was performed by the reported procedures with some modifications.[23] A suspension of *cis*-[Ru(4,4'-Br$_2$-bpy)$_2$Cl$_2$] (94 mg, 0.12 mmol) and 4,4'-Br$_2$-bpy (110 mg, 0.35 mmol) in 120 mL of an ethanol/water mixture (1/1, v/v) was heated at 80°C for 5 h. After cooling to room temperature, ethanol was removed under reduced pressure. The insoluble residues were removed by filtration, and an excess amount of an NH_4PF_6(aq) solution was added to the filtrate. The resulting precipitates were collected and purified by column chromatography (Al_2O_3, $CH_3CN/CHCl_3$ (1/1, v/v)). The crude product was dissolved in a minimum amount of acetone and, then, an excess amount of *n*-hexane was added dropwise to the solution, giving [Ru(4,4'-Br$_2$-bpy)$_3$](PF$_6$)$_2$ as red powders (110 mg, 69%). ^{1}H NMR (270 MHz, CD_3CN, TMS) δ/ppm 8.73 (6H, d, J = 1.9 Hz, 3,3'-Ar-H of 4,4'-Br$_2$-bpy), 7.63 (2H, d, J = 2.4 Hz, 6,6'-Ar-H of 4,4'-Br$_2$-bpy), 7.61 (4H, d, J = 2.4 Hz, 6,6'-Ar-H of 4,4'-Br$_2$-bpy), 7.55 (4H, s, 5,5'-Ar-H of 4,4'-Br$_2$-bpy), 7.53 (2H, s, 5,5'-Ar-H of 4,4'-Br$_2$-bpy); MS (ESI) m/z 521.8 (calcd for $[M-2PF_6]^{2+}$ ($C_{30}H_{18}N_6Br_6Ru$): 521.5).

Synthesis of (2,2'-Bipyridine)bis(4,4'-dibromo-2,2'-bipyridine)ruthenium(II) Bis(hexafluorophosphate) ([Ru(4,4'-Br_2-bpy)$_2$(bpy)](PF_6)$_2$). The complex was synthesized similar to the synthesis of [Ru(4,4'-Br_2-bpy)$_3$](PF_6)$_2$ by heating a suspension of *cis*-[Ru(4,4'-Br_2-bpy)$_2Cl_2$] (100 mg, 0.13 mmol) and bpy (39 mg, 0.25 mmol) in 120 mL of an ethanol/water mixture (1/1, v/v), giving [Ru(4,4'-Br_2-bpy)$_2$-(bpy)](PF_6)$_2$ as red powders (79 mg, 51%). ^{1}H NMR (270 MHz, CD_3CN) δ/ppm 8.73 (4H, s, 3,3'-Ar-H of 4,4'-Br_2-bpy), 8.48 (2H, d, J = 7.9 Hz, 3,3'-Ar-H of bpy), 8.12–8.02 (2H, *m*, 4,4'-Ar-H of bpy), 7.71 (2H, d, 6,6'-Ar-H of 4,4'-Br_2-bpy), 7.64–7.55 (6H, *m*, 5,5',6,6'-Ar-H of 4,4'-Br_2-bpy and 6,6'-Ar-H of bpy), 7.49 (6H, d, J = 6.2 Hz, 5,5'-Ar-H of 4,4'-Br_2-bpy), 7.44–7.37 (6H, *m*, 5,5'-Ar-H of bpy)); MS (ESI) m/z 443.0 (calcd for $[M-2PF_6]^{2+}$ ($C_{30}H_{20}N_6Br_4Ru$): 442.6).

Synthesis of Bis(2,2'-bipyridine)(4,4'-dibromo-2,2'-bipyridine)ruthenium(II) Bis(hexafluorophosphate) ([Ru(4,4'-Br_2-bpy)(bpy)$_2$](PF_6)$_2$). The complex was synthesized similar to the synthesis of [Ru(4,4'-Br_2-bpy)$_3$](PF_6)$_2$ by heating a suspension of *cis*-[Ru(bpy)$_2Cl_2$] (100 mg, 0.21 mmol) and 4,4'-Br_2-bpy (130 mg, 0.41 mmol) in 220 mL of an ethanol/water mixture (1/1, v/v), giving [Ru(4,4'-Br_2-bpy)-(bpy)$_2$](PF_6)$_2$ as red powders (140 mg, 67%). ^{1}H NMR (270 MHz, CD_3CN) δ/ppm 8.74 (2H, s, 3,3'-Ar-H of 4,4'-Br_2-bpy)), 8.49 (4H, d, J = 8.2 Hz, 3,3'-Ar-H of bpy), 8.11–8.01 (4H, *m*, 4,4'-Ar-H of bpy), 7.75 (2H, d, J = 5.6 Hz, 6,6'-Ar-H of bpy), 7.67 (2H, d, J = 5.7 Hz, 6,6'-Ar-H of bpy), 7.60–7.53 (4H, *m*, 5,5',6,6'-Ar-H of 4,4'-Br_2-bpy)), 7.45–7.35 (4H, *m*, 5,5'-Ar-H of bpy)); MS (ESI) m/z 363.6 (calcd for $[M-2PF_6]^{2+}$ ($C_{30}H_{22}N_6Br_2Ru$): 363.7).

Synthesis of Tris(4-bromo-2,2'-bipyridine)ruthenium(II) Bis(hexafluorophosphate) ([Ru(4-Br-bpy)$_3$](PF$_6$)$_2$). The complex was synthesized similar to the synthesis of [Ru(4,4'-Br$_2$-bpy)$_3$](PF$_6$)$_2$ by heating a suspension of *cis*-[Ru(4-Br-bpy)$_2$-Cl$_2$] (120 mg, 0.19 mmol) and 4-Br-bpy (88 mg, 0.37 mmol) in 200 mL of an ethanol/water mixture (1/1, v/v), giving [Ru(4-Br-bpy)$_3$](PF$_6$)$_2$ as red powders (120 mg, 58%). ^{1}H NMR (270 MHz, CD$_3$CN, TMS) δ/ppm 8.72 (3H, s, 3-Ar-H of 4-Br-bpy), 8.50 (3H, d, J = 8.2 Hz, 3'-Ar-H of 4-Br-bpy), 8.08 (3H, t, J = 8.4 Hz, 4'-Ar-H of 4-Br-bpy), 7.81–7.67 (4H, *m*, 6,6'-Ar-H of 4-Br-bpy), 7.62–7.56 (4H, *m*, 5,5',6,6-Ar-H of 4-Br-bpy), 7.51–7.40 (4H, *m*, 5,5'-Ar-H of 4-Br-bpy); MS (ESI) m/z 403.0 (calcd for [M−2PF$_6$]$^{2+}$ (C$_{30}$H$_{21}$N$_6$Br$_3$Ru): 403.2).

Synthesis of (2,2'-Bipyridine)bis(4-bromo-2,2'-bipyridine)ruthenium(II) Bis(hexafluorophosphate) ([Ru(4-Br-bpy)$_2$(bpy)](PF$_6$)$_2$). The complex was synthesized similar to the synthesis of [Ru(4,4'-Br$_2$-bpy)$_3$](PF$_6$)$_2$ by heating a suspension of *cis*-[Ru(4-Br-bpy)$_2$Cl$_2$] (54 mg, 0.084 mmol) and bpy (36 mg, 0.23 mmol) in 60 mL of an ethanol/water mixture (1/1, v/v), giving [Ru(4-Br-bpy)$_2$(bpy)](PF$_6$)$_2$ as red powders (42 mg, 49%). ^{1}H NMR (270 MHz, CD$_3$CN, TMS) δ/ppm 8.72 (2H, s, 3,3'-Ar-H of 4-Br-bpy), 8.50 (4H, d, J = 7.6 Hz, 3,3'-Ar-H of bpy), 8.12–8.02 (4H, *m*, 4,4'-Ar-H of bpy and 4'-Ar-H of 4-Br-bpy), 7.82–7.64 (5H, *m*, 6,6'-Ar-H of bpy and 6,6'-Ar-H of 4-Br-bpy), 7.48–7.40 (3H, *m*, 5,5',6'-Ar-H of 4-Br-bpy), 7.46–7.36 (4H, *m*, 5,5'-Ar-H of 4-Br-bpy and 5,5'-Ar-H of bpy); MS (ESI) m/z 363.7 (calcd for [M−2PF$_6$]$^{2+}$ (C$_{30}$H$_{22}$N$_6$Br$_2$Ru): 363.7).

Synthesis of Bis(2,2'-bipyridine)(4-bromo-2,2'-bipyridine)ruthenium(II) Bis-

(hexafluorophosphate) ([Ru(4-Br-bpy)(bpy)$_2$](PF$_6$)$_2$). The complex was synthesized similar to the synthesis of [Ru(4,4'-Br$_2$-bpy)$_3$](PF$_6$)$_2$ by heating a suspension of *cis*-[Ru(bpy)$_2$Cl$_2$] (67 mg, 0.14 mmol) and 4-Br-bpy (65 mg, 0.28 mmol) in 150 mL of an ethanol/water mixture (1/1, v/v), giving [Ru(4-Br-bpy)$_2$(bpy)](PF$_6$)$_2$ as red powders (120 mg, 93%). ^{1}H NMR (270 MHz, CD$_3$CN, TMS) δ/ppm 8.73 (1H, s, 3,3'-Ar-H of 4-Br-bpy), 8.50 (5H, d, J = 7.6 Hz, 3,3'-Ar-H of 4-Br-bpy and 3,3'-Ar-H of bpy), 8.12–8.01 (5H, *m*, 4,4'-Ar-H of bpy and 4'-Ar-H of 4-Br-bpy), 7.80–7.67 (5H, *m*, 6,6'-Ar-H of bpy and 6,6'-Ar-H of 4-Br-bpy), 7.59–7.54 (2H, *m*, 5',6'-Ar-H of 4-Br-bpy), 7.46–7.35 (5H, *m*, 5,5'-Ar-H of 4-Br-bpy and 5,5'-Ar-H of bpy); MS (ESI) m/z 324.1 (calcd for [M−2PF$_6$]$^{2+}$ (C$_{30}$H$_{23}$N$_6$BrRu): 324.3).

Synthesis of Tris[4,4'-bis{(dimesitylboryl)durylethynyl}-2,2'-bipyridine]-ruthenium(II) Bis(hexafluorophosphate) (2a(PF$_6$)$_2$). An oven-dried Schlenk tube was evacuated and filled subsequently with an argon gas. [Ru(4,4'-Br$_2$-bpy)$_3$](PF$_6$)$_2$ (41 mg, 0.031 mmol), CuI (1.7 mg, 0.0089 mmol), and dichloridobis(triphenylphosphine)-palladium(II) (Pd(PPh$_3$)$_2$Cl$_2$, 2.3 mg, 0.0033 mmol) were added to the tube and, then, the tube was evacuated and filled with an argon gas again. An argon-gas purged CH$_3$CN/triethylamine (NEt$_3$) mixture (1.0 mL/0.40 mL) was added to the reaction tube, and the resulting suspension was stirred at room temperature for 20 min. A tetrahydrofuran (THF) solution (5.5 mL) of EDDB (110 mg, 0.27 mmol) was then added dropwise to the reaction mixture. The mixture was stirred at 50ºC for 4 h under argon-gas atmosphere and, then, allowed to cool to room temperature. The insoluble residues were removed by filtration through Celite® (No. 500), and the filtrate was evaporated to dryness. The crude product was dissolved in a minimum amount of

acetone, and the solution was added dropwise to an excess amount of *n*-hexane, giving red precipitates. After repeating the reprecipitation procedures three times, purifications by column chromatography (LH-20, CH_3CN/ethanol (1/1, v/v)) followed by preparative HPLC (GPC, chloroform) afforded **2a**$(PF_6)_2$ as red powders (53 mg, 52%). ^{1}H NMR (270 MHz, CD_3CN, TMS) δ/ppm 8.72 (6H, s, 3,3'-Ar-H of B_2bpy), 7.74 (6H, d, J = 5.9 Hz, 6,6'-Ar-H of B_2bpy), 7.53 (6H, dd, J = 1.5, 5.9 Hz, 5,5'-Ar-H of B_2bpy), 6.80 (24H, s, Ar-H of mes), 2.44 (36H, s, CH_3, *m*-positions of duryl groups), 2.24 (36H, s, CH_3, *o*-positions of duryl groups), 2.01 (36H, s, CH_3, *p*-positions of mes groups), 1.94 (72H, s, CH_3 *o*-positions of mes groups); MS (ESI) m/z 1498.4 (calcd for $[M-2PF_6]^{2+}$ ($C_{210}H_{222}N_6B_6Ru$): 1497.9). Elemental analysis calcd (%) for $C_{210}H_{222}N_6B_6RuP_2F_{12}\cdot 1.5CHCl_3$: C 73.31, H 6.50, N 2.43; found: C 73.40, H 6.39, N 2.47.

Synthesis of (2,2'-Bipyridine)bis[4,4'-bis{(dimesitylboryl)durylethynyl}-2,2'-bipyridine]ruthenium(II) Bis(hexafluorophosphate) (2b$(PF_6)_2$). The complex was synthesized similar to the synthesis of **2a**$(PF_6)_2$ by reacting [Ru(4,4'-Br_2-bpy)$_2$-(bpy)]$(PF_6)_2$ (39 mg, 0.033 mmol), CuI (2.0 mg, 0.010 mmol), $Pd(PPh_3)_2Cl_2$ (2.7 mg, 0.0038 mmol) in CH_3CN/NEt_3 (1.1 mL/0.50 mL) and a THF solution (4.0 mL) of EDDB (81 mg, 0.20 mmol), giving **2b**$(PF_6)_2$ as red powders (49 mg, 61%). Similar workup and purification procedures with those for **2a**$(PF_6)_2$ gave the pure product. ^{1}H NMR (270 MHz, CD_3CN) δ/ppm 8.70 (4H, d, J = 1.4 Hz, 3,3'-Ar-H of B_2bpy), 8.54 (2H, d, J = 8.2 Hz, 3,3'-Ar-H of bpy), 8.11 (2H, td, J = 1.4, 8.0 Hz, 4,4'-Ar-H of bpy), 7.83–7.79 (4H, *m*, 6,6'-Ar-H of B_2bpy), 7.71 (2H, d, J = 6.0 Hz, 6,6'-Ar-H of bpy), 7.53–7.44 (6H, *m*, 5,5'-Ar-H of bpy and 5,5'-Ar-H of B_2bpy), 6.80 (16H, s, Ar-H of

mes), 2.44 (24H, s, CH_3, *m*-positions of duryl groups), 2.24 (24H, s, CH_3, *o*-positions of duryl groups), 2.02 (24H, s, CH_3, *p*-positions of mes groups), 1.94 (48H, s, CH_3, *o*-positions of mes groups); MS (ESI) m/z 1093.4 (calcd for $[M-2PF_6]^{2+}$ ($C_{150}H_{156}N_6B_4Ru$): 1093.6). Elemental analysis calcd (%) for $C_{150}H_{156}N_6B_4RuP_2F_{12}\cdot 2CHCl_3$: C 67.22, H 5.86, N 3.09; found: C 67.28, H 5.79, N 3.18.

Synthesis of Bis(2,2'-bipyridine)[4,4'-bis{(dimesitylboryl)durylethynyl}-2,2'-bipyridine]ruthenium(II) Bis(hexafluorophosphate) (2c(PF_6)$_2$). The complex was synthesized similar to the synthesis of **2a**$(PF_6)_2$ by reacting [Ru(4,4'-Br_2-bpy)-$(bpy)_2$]$(PF_6)_2$ (51 mg, 0.051 mmol), CuI (2.8 mg, 0.015 mmol), $Pd(PPh_3)_2Cl_2$ (2.5 mg, 0.0036 mmol) in CH_3CN/NEt_3 (1.6 mL/0.7 mL) and a THF solution (3.0 mL) of EDDB (60 mg, 0.15 mmol), giving **2c**$(PF_6)_2$ as red powders (67 mg, 78%). Similar workup and purification procedures with those for **2a**$(PF_6)_2$ gave the pure product. ^{1}H NMR (270 MHz, CD_3CN) δ/ppm 8.69 (2H, d, J = 1.4 Hz, 3,3'-Ar-H of B_2bpy)), 8.53 (4H, d, J = 8.2 Hz, 3,3'-Ar-H of bpy), 8.08 (4H, *m*, 4,4'-Ar-H of bpy), 7.82 (2H, dd, J = 1.4, 4.8 Hz, 6,6'-Ar-H of B_2bpy), 7.72 (4H, d, J = 5.7 Hz, 6,6'-Ar-H of bpy), 7.56–7.38 (6H, *m*, 5,5'-Ar-H of bpy and 5,5'-Ar-H of B_2bpy)), 6.80 (8H, s, Ar-H of mes), 2.44 (12H, s, CH_3, *m*-positions of duryl groups), 2.25 (12H, s, CH_3, *o*-positions of duryl groups), 2.02 (12H, s, CH_3, *p*-positions of mes groups), 1.94 (24H, s, CH_3, *o*-positions of mes groups); MS (ESI) m/z 689.3 (calcd for $[M-2PF_6]^{2+}$ ($C_{90}H_{90}N_6B_2Ru$): 689.3). Elemental analysis calcd (%) for $C_{90}H_{90}N_6B_2RuP_2F_{12}\cdot 0.8CHCl_3$: C 61.83, H 5.19, N 4.76; found: C 61.97, H 5.17, N 4.76.

Synthesis of Tris[4-{(dimesitylboryl)durylethynyl}-2,2'-bipyridine]ruthenium(II) Bis(hexafluorophosphate) (2a'(PF$_6$)$_2$). The complex was synthesized similar to the synthesis of **2a**(PF$_6$)$_2$ by reacting [Ru(4-Br-bpy)$_3$](PF$_6$)$_2$ (60 mg, 0.055 mmol), CuI (3.0 mg, 0.016 mmol), Pd(PPh$_3$)$_2$Cl$_2$ (4.5 mg, 0.011 mmol) in CH$_3$CN/NEt$_3$ (1.8 mL/0.70 mL) and a THF solution (5.0 mL) of EDDB (100 mg, 0.25 mmol), giving **2a'**(PF$_6$)$_2$ as red powders (50 mg, 51%). Similar workup and purification procedures with those for **2a**(PF$_6$)$_2$ gave the pure product. ^{1}H NMR (270 MHz, CD$_3$CN, TMS) δ/ppm 8.62–8.59 (6H, *m*, 3,3'-Ar-H of Bbpy), 8.10–8.08 (3H, *m*, 4-Ar-H of Bbpy), 7.81–7.69 (6H, *m*, 5,5'-Ar-H of Bbpy), 7.50–7.45 (6H, *m*, 6,6'-Ar-H of Bbpy), 6.80 (12H, s, Ar-H of mes), 2.44 (18H, s, CH$_3$, *m*-positions of duryl groups), 2.25 (18H, s, CH$_3$, *o*-positions of duryl groups), 2.02 (18H, s, CH$_3$, *p*-positions of mes groups), 1.93 (36H, s, CH$_3$, *o*-positions of mes groups); MS (ESI) m/z 891.2 (calcd for [M−2PF$_6$]$^{2+}$ (C$_{120}$H$_{123}$N$_6$B$_3$Ru): 891.5). Elemental analysis calcd (%) for C$_{120}$H$_{123}$N$_6$B$_3$RuP$_2$F$_{12}$·1.1CHCl$_3$: C 65.99, H 5.68, N 3.81; found: C 65.95, H 5.68, N 3.80.

Synthesis of (2,2'-Bipyridine)bis[4-{(dimesitylboryl)durylethynyl}-2,2'-bipyridine]ruthenium(II) Bis(hexafluorophosphate) (2b'(PF$_6$)$_2$). The complex was synthesized similar to the synthesis of **2a**(PF$_6$)$_2$ by reacting [Ru(4-Br-bpy)$_2$(bpy)](PF$_6$)$_2$ (40 mg, 0.039 mmol), CuI (1.3 mg, 0.0068 mmol), Pd(PPh$_3$)$_2$Cl$_2$ (2.1 mg, 0.0030 mmol) in CH$_3$CN/NEt$_3$ (1.3 mL/0.60 mL) and a THF solution (2.4 mL) of EDDB (48 mg, 0.12 mmol), giving **2b'**(PF$_6$)$_2$ as red powders (43 mg, 67%). Similar workup and purification procedures with those for **2a**(PF$_6$)$_2$ gave the pure product. ^{1}H NMR (270 MHz, CD$_3$CN, TMS) δ/ppm 8.61–8.50 (6H, *m*, 3,3'-Ar-H of bpy and 3,3'-Ar-H of

Bbpy), 8.11–8.05 (4H, *m*, 4,4'-Ar-H of bpy and 4'-Ar-H of Bbpy), 7.82–7.68 (6H, *m*, 6,6'-Ar-H of bpy and 6,6'-Ar-H of Bbpy), 7.48–7.40 (6H, *m*, 5,5'-Ar-H of bpy and 5,5'-Ar-H of Bbpy), 6.81 (8H, s, Ar-H of mes), 2.44(12H, s, CH_3, *m*-positions of duryl groups), 2.25 (12H, s, CH_3, *o*-positions of duryl groups), 2.02 (12H, s, CH_3, *p*-positions of mes groups), 1.94 (24H, s, CH_3, *o*-positions of mes groups); MS (ESI) m/z 689.2 (calcd for $[M-2PF_6]^{2+}$ ($C_{90}H_{90}N_6B_2Ru$): 689.3). Elemental analysis calcd (%) for $C_{90}H_{90}N_6B_2RuP_2F_{12}\cdot 1.4CHCl_3$: C 59.81, H 5.02, N 4.58; found: C 59.74, H 4.97, N 4.76.

Synthesis of Bis(2,2'-bipyridine)[4-{(dimesitylboryl)durylethynyl}-2,2'-bipyridine]ruthenium(II) Bis(hexafluorophosphate) (2c'(PF_6)$_2$). The complex was synthesized similar to the synthesis of **2a**(PF_6)$_2$ by reacting [Ru(4-Br-bpy)(bpy)$_2$](PF_6)$_2$ (100 mg, 0.11 mmol), CuI (3.3 mg, 0.017 mmol), $Pd(PPh_3)_2Cl_2$ (5.6 mg, 0.0080 mmol) in CH_3CN/NEt_3 (3.5 mL/1.4 mL) and a THF solution (3.3 mL) of EDDB (66 mg, 0.16 mmol), giving **2c'**(PF_6)$_2$ as red powders (57 mg, 41%). Similar workup and purification procedures with those for **2a**(PF_6)$_2$ gave the pure product. ^{1}H NMR (270 MHz, CD_3CN, TMS) δ/ppm 8.59 (2H, s, 3,3'-Ar-H of Bbpy), 8.52–8.46 (4H, d, J = 8.1 Hz, 3,3'-Ar-H of bpy), 8.11–8.02 (5H, *m*, 4,4'-Ar-H of bpy and 4'-Ar-H of Bbpy), 7.82–7.67 (6H, *m*, 6,6'-Ar-H of bpy and 6,6'-Ar-H of Bbpy), 7.47–7.37 (6H, *m*, 5,5'-Ar-H of bpy and 5,5'-Ar-H of Bbpy), 6.80 (4H, s, Ar-H of mes), 2.43(6H, s, CH_3, *m*-positions of duryl groups), 2.25 (6H, s, CH_3, *o*-positions of duryl groups), 2.02 (6H, s, CH_3, *p*-positions of mes groups), 1.94 (12H, s, CH_3, *o*-positions of mes groups); MS (ESI) m/z 486.7 (calcd for $[M-2PF_6]^{2+}$ ($C_{60}H_{57}N_6BRu$): 487.2). Elemental analysis calcd (%) for $C_{60}H_{57}N_6BRuP_2F_{12}\cdot CHCl_3$: C 52.96, H 4.23, N 6.08; found: C 53.00, H

4.27, N 6.18.

2-2-2: Electrochemical Measurements

Cyclic and differential pulse voltammetries of the complexes in *N*,*N*-dimethylformamide (DMF, for nonaqueous titrimetry, Kanto Chemical Co., Inc.) were conducted by using a BAS ALS-701D electrochemical analyzer with a three-electrode system using glassy carbon working, Pt auxiliary, and Ag/Ag^+ reference electrodes. A small amount of ferrocene (Fc) was added to sample solutions as an internal standard for the redox potentials. Tetra-*n*-butylammonium hexafluorophosphate ($TBAPF_6$, 0.1 M), purified by recrystallizations from ethanol three times, was used as a supporting electrolyte. The concentration of a complex was set ~0.5 mM. Measurements were conducted at 25±2°C, and sample solutions were deaerated by purging an argon-gas stream over 20 min prior to measurements. The potential sweep rate was 100 mV/s in cyclic voltammetry, and the differential pulse voltammetry was conducted with 50 mV height pulses (0.06 s duration) being stepped by 4 mV intervals (2.0 s interval between the two pulses).

2-2-3: Spectroscopic and Photophysical Measurements at Room Temperature

Spectroscopic-grade (Wako Pure Chemical Ind. Ltd.) or Luminasol® (Dojindo Molecular Technologies, Inc.) CH_3CN was used for absorption or emission measurements, respectively, without further purification. The absorption spectra of the complexes were measured by using a Hitachi U-3900H spectrophotometer. The corrected emission spectra of the complexes were measured by using a Hamamatsu PMA-11 multichannel photodetector (excitation wavelength = 355 nm). The emission

intensity at each wavelength was corrected for the system spectral response so that the vertical axis of a spectrum corresponds to the photon number at each wavelength. The absolute emission quantum yields of the complexes were measured by a Hamamatsu C9920-02 system equipped with an integrating sphere and a PMA-12 red-sensitive multichannel photodetector (excitation wavelength = 400 nm).[24,25] Emission decay profiles of the complexes were measured by using a Hamamatsu C4334 streak camera as a photodetector at 355-nm excitation using a nanosecond Q-switched Nd:YAG laser (LOTIS TII, Ltd. LS-2137, fwhm ≈ 16–18 ns, repetition rate = 10 Hz) as a light source. For emission spectroscopy, the absorbance of a sample solution was set <0.05 at the excitation wavelength, and sample solutions were deaerated by purging an argon-gas stream over 30 min.

2-2-4: Temperature-Controlled Emission Measurements

The emission measurement system described in Section 2-2-3 was employed for temperature-controlled experiments.

For measurements in 250–330 K, propylene carbonate as a solvent was distilled prior to use.[26] The sample temperature was controlled by a liquid-N_2 cryostat (Oxford Instruments OptistatDN2 optical Dewar with a MercuryiTC temperature controller).

For measurements in 3.5–100 K, a poly(ethyleneglycol)dimethacrylate (PEG-DMA550, Scheme 2-2) polymerized monolith was used as a solid-state medium to minimize the intermolecular interactions between complexes.[27–30] A PEG-DMA550 liquid monomer (Sigma–Aldrich Co. LLC) was purified to remove the polymerization inhibitor (4-methoxyphenol) by passing through an alumina column by using acetone

as an eluent. Residual water/acetone were removed by evaporation under reduced pressure for over 2 h prior to use. Typically, the acetone solution (3 mL) of a complex whose absorbance was set ~0.1 at 355 nm and inhibitor-free liquid PEG-DMA550 (3 mL) was evaporated, and 1 wt% of 2,2'-azobis(2,4-dimethylvaleronitrile) (Wako Pure Chemical Ind., Ltd.) as a polymerization initiator was added. The solution was poured into a Pyrex® tube (diameter = 10 mm) and, then, heated at 50°C for 5 h under vacuum, yielding an optically-transparent PEG-DMA550 film. The sample temperature was controlled by a liquid-He cryostat (Oxford Instruments OptistatCF optical Dewar with an ITC503S temperature controller).

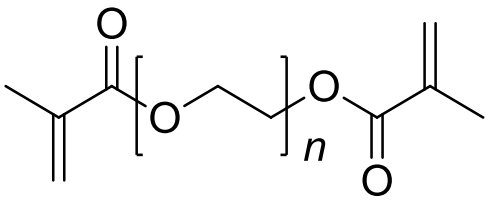

Chart 2-2. Chemical structure of PEG-DMA550 ($n \approx 9$).

2-2-5: Time-Dependent Density Functional Theory (TD-DFT) Calculations

Theoretical calculations for the complexes were conducted with Gaussian 09W[31] or 16W[32] software. The ground-state geometries of the complexes were optimized by using DFT with the B3LYP function.[33] The LanL2DZ16[34] and 6-31G(d,p)[35] basis sets were used to treat ruthenium and all other atoms, respectively. TD-DFT calculations were then performed to estimate the energies and oscillator strengths of the 10 lowest-energy singlet absorption transitions. All of the calculations were carried out as in acetonitrile by using a polarizable continuum model (PCM).[36] Kohn−Sham molecular orbitals (MOs) were plotted using GaussView 5.0[37] or 6.0.[38]

2-2-6: Franck–Condon Analyses of Emission Spectra at Room Temperature

The emission spectra of the complexes were simulated based on one-mode Franck–Condon analysis, given by eq. 2-1.[39,40]

$$I(\tilde{\nu}) = \sum_{v_M} \left(\frac{E_0 - v_M \hbar\omega_M}{E_0}\right)^3 \left(\frac{{S_M}^{v_M}}{v_M!}\right) \exp\left[-4\ln 2\left(\frac{\tilde{\nu} - E_0 + v_M \hbar\omega_M}{\Delta\tilde{\nu}_{0,1/2}}\right)^2\right]$$

(eq. 2-1)

In eq. 2-1, $I(\tilde{\nu})$ is the emission intensity at a given wavenumber (cm^{-1}) relative to that of the 0→0 emission transition. E_0 is the energy gap between the zeroth vibrational levels in the ground and emitting excited states, $\hbar\omega_M$ is the quantum spacing for the averaged medium-frequency vibrational mode, S_M is the electron–vibrational coupling constant or Huang–Rhys factor[41] reflecting the extent of the change in the normal coordinate of the average medium-frequency vibrational modes, and $\Delta\tilde{\nu}_{0,1/2}$ is the full width at half-maximum of an individual vibronic line in the emission spectrum. The photon numbers of the emission spectrum were corrected to a wavenumber scale by using the equation $I(\tilde{\nu}) = I(\lambda) \times \lambda^2$.[42] The parameters E_0, $\hbar\omega_M$, S_M, and $\Delta\tilde{\nu}_{0,1/2}$ were optimized with a least-squares minimization routine by using a Generalized Reduced Gradient (GRG2) algorithm.[43] The summation in eq. 2-1 was carried out over 11 vibrational levels (v_M: 0 → 10). The free-energy content of the triplet excited state (T_1) above the ground state (ΔG_{ES}), the inner- (λ_i) and outer-sphere reorganization energies (λ_o) were estimated by eqs. 2-2 and 2-3, respectively, with k_B and T being the Boltzmann constant and absolute temperature, respectively.[44,45]

$$\Delta G_{\mathrm{ES}} = E_0 + \lambda_{\mathrm{o}} = E_0 + \frac{\left(\Delta\tilde{\nu}_{0,1/2}\right)^2}{16 k_{\mathrm{B}} T \ln 2}$$

(eq. 2-2)

$$\lambda_{\mathrm{i}} = S_{\mathrm{M}} \hbar \omega_{\mathrm{M}}$$

(eq. 2-3)

2-3: Results and Discussion

2-3-1: Redox Potentials

Since the DBDE group(s) on the bpy ligand(s) in **2a**–**c** and **2a'**–**c'** would influence the redox potentials of the complexes due to the electron-accepting ability of p(B) in DBDE, the electrochemical properties of the complexes have been evaluated. The cyclic (CVs) and differential pulse voltammograms (DPVs) of **2a**–**c** and **2a'**–**c'** in DMF are shown in Figure 2-1, together with those of $[Ru(bpy)_3]^{2+}$ as a reference complex. The redox potentials of the complexes determined by the peak potentials of DPVs are summarized in Table 2-1. As seen in Figure 2-1 and Table 2-1, all of the complexes showed quasi-reversible oxidation waves responsible for the metal oxidation (E_{ox}) at +0.79–+0.85 V (vs. Fc/Fc^+, $E_{Fc/Fc+}$ = +0.634 V vs. Ag/AgCl in DMF containing 0.1-M $TBAPF_6$[46]). The oxidation potential of the complex was gradually shifted to the positive direction with an increase in the number of the DBDE group, indicative of a slight decrease in the electron density on the ruthenium(II) atom by the presence of the electron-withdrawing DBDE group(s). On the other hand, all of the complexes exhibited reversible or quasi-reversible multiple reduction waves originated from the ligand reductions. The first (E_{red1}), second (E_{red2}), and third reduction waves (E_{red3}) represent the sequential reductions of three bpy moieties in the complex. The $E_{red1,2,3}$ values of **2a**–**c** (E_{red1} = −1.46 to −1.52 V, E_{red2} = −1.61 to −1.83 V, and E_{red3} =

−1.83 to −2.06 V) and **2a'**–**c'** (E_{red1} = −1.57 to −1.63 V, E_{red2} = −1.73 to −1.87 V, and E_{red3} = −1.96 to −2.12 V) are more positive than the relevant values of $[Ru(bpy)_3]^{2+}$ (E_{red1} = −1.71 V, E_{red2} = −1.90 V, and E_{red3} = −2.16 V), demonstrating stabilization of the π*-orbital energies of the ligands in the complexes owing to the electron-withdrawing ability of the DBDE group. Furthermore, the increase in *n* from *n* = 0 (i.e., $[Ru(bpy)_3]^{2+}$) to *n* = 3 for the **2a**–**c** or **2a'**–**c'** series rendered a gradual positive shift of E_{red1} from −1.71 to −1.46 V or from −1.71 to −1.57 V, respectively. The results also demonstrate that, in addition to the stabilization of the π*-orbital energy by electron-withdrawing nature of the DBDE group(s), electron delocalization over the ligands also contributes to some extent to the $E_{red1,2,3}$ values. Furthermore, E_{red1} of the complexes having a B_2bpy ligand(s) (E_{red1} = −1.46 to −1.52 V for **2a**–**c**) are more positive than that of the relevant complexes having a Bbpy ligand(s) (E_{red1} = −1.57 to −1.63 V for **2a'**–**c'**). Since **2a**–**c** possess the extended π-electron systems *via* the two boron centers, the more positive E_{red1} values of the complexes relative to the corresponding values of **2a'**–**c'** are the reasonable consequence.

It is worth noting, furthermore, that one or two additional reduction wave(s) (E_{red4} and E_{red5}) other than $E_{red1,2,3}$ are observed for **2a'**–**c'** or **2a**–**c**, respectively. Since the reduction currents at E_{red4} and E_{red5} increase with increasing *n* and the E_{red4} value is almost independent of *n* at −2.34 to −2.38 V, the fourth reduction wave can be assigned to the simultaneous reduction of one DBDE group in each B_2bpy or Bbpy ligand(s) (i.e., 1–3 electron reduction) without an inter-ligand interaction. The fifth reduction wave, E_{red5}, observed for **2a**–**c** will be assigned to the reduction of the rest DBDE group(s), not reduced at E_{red4}. Since the E_{red1} value is shifted to the positive direction by the increase in *n* through delocalization of the electron among the ligands *via* p(B)

as mentioned above, E_{red4} and E_{red5} should show similar behaviors to E_{red1}. However, the E_{red4} and E_{red5} are almost independent of n, indicating that the electrostatic repulsion between the respective electrons also contributes to the $E_{red4,5}$ values.

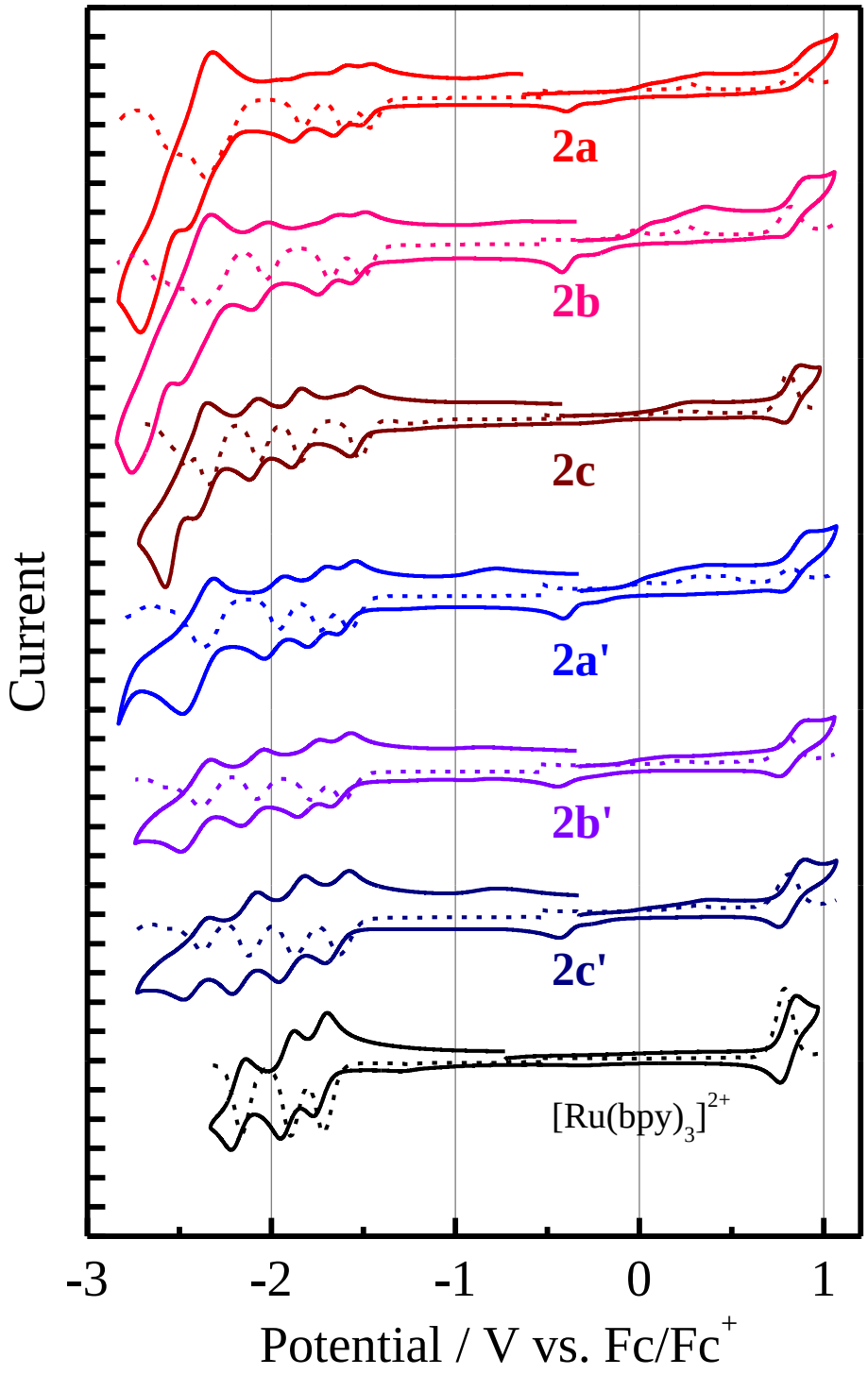

Figure 2-1. CVs (solid curves) and DPVs (broken curves) of **2a**–**c**, **2a'**–**c'** and $[Ru(bpy)_3]^{2+}$ in DMF containing 0.1-M $TBAPF_6$. The vertical-axis scale is 5 μA per division.

Table 2-1. Redox potentials of the complexes in DMF containing 0.1-M $TBAPF_6$.

Complex	Potential E / V vs. Fc/Fc^+ [a]					
	red5	red4	red3	red2	red1	ox
2a (n = 3)	−2.50	−2.35	−1.83	−1.61	−1.46	+0.85
2b (n = 2)	−2.52	−2.38	−2.03	−1.68	−1.51	+0.82
2c (n = 1)	−2.46	−2.34	−2.06	−1.83	−1.52	+0.81
2a' (n = 3)		−2.37	−1.96	−1.73	−1.57	+0.82
2b' (n = 2)		−2.38	−2.08	−1.78	−1.61	+0.81
2c' (n = 1)		−2.37	−2.12	−1.87	−1.63	+0.82
$[Ru(bpy)_3]^{2+}$			−2.16	−1.90	−1.71	+0.79

[a] The values were determined by the peak potentials of DPVs of the complexes.

The electrochemical behaviors of the complexes suggest that the highest-energy occupied MO (HOMO) and the lowest-energy unoccupied MO (LUMO) of the complex are determined primarily by the metal- and ligand-based molecular orbitals, respectively. To evaluate the detailed HOMOs and LUMOs, DFT calculations were carried out on **2c**, **2c'**, and $[Ru(bpy)_3]^{2+}$. The Kohn–Sham MOs are shown in Figure 2-2, whose details are also summarized in Tables 2-2–2-4. The HOMO of **2c** or **2c'** distributes mainly to the ruthenium(II) atom (~43%) and the B_2bpy or Bbpy ligand (~51%), while that of $[Ru(bpy)_3]^{2+}$ is localized on the ruthenium(II) atom (~84%). Furthermore, it is worth noting that, as shown in Figure 2-2, only one DBDE group contributes to HOMO of **2c** which is similar to that of **2c'**. Owing to such MO distributions, the HOMO energy of **2c** (−5.97 eV) is comparable with that of **2c'** (−5.97 eV).

The LUMOs of both **2c** and **2c'** are localized on the B_2bpy and Bbpy ligands (~71%), respectively, with slight distributions to the DBDE group(s) (18% for **2c** and 14% for **2c'**). These results will be explained by the extended π-electron systems in the

DBDE-appended ligands and electron-withdrawing nature of the arylborane unit(s). As seen in Figure 2-2, the two DBDE groups in **2c** contribute to the distribution in LUMO, while the HOMO distributes to one DBDE group in **2c**. Therefore, the LUMO energy of **2c** (−2.77 eV) is lower than those of **2c'** (−2.68 eV) and $[Ru(bpy)_3]^{2+}$ (−2.58 eV) and, thus, the first ligand-reduction potential shifts to the positive direction in the sequence **2c** (−1.52 V) > **2c'** (−1.63 V) > $[Ru(bpy)_3]^{2+}$ (−1.71 V) as seen in Scheme 2-2. Although the data on the DFT calculations are limited only for **2c** and **2c'** owing to the computational cost, it is expected that DFT calculations on other complexes having two or three DBDE-substituted ligands would also give similar results to those of the complexes, **2c** and **2c'**.

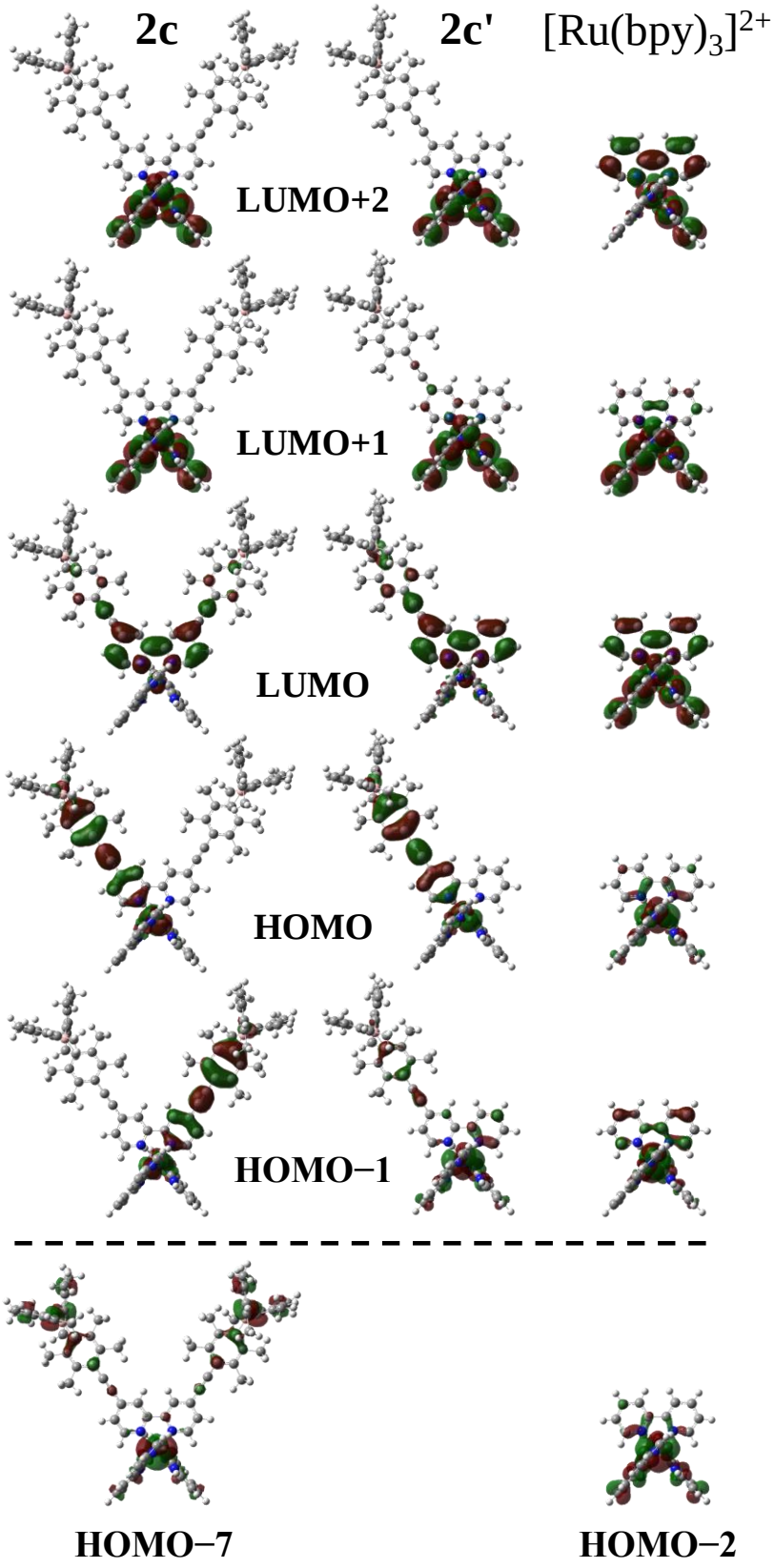

Figure 2-2. The Kohn–Sham MOs of **2c**, **2c'** and $[Ru(bpy)_3]^{2+}$ (contour = 0.02 eÅ^{-3}).

Table 2-2. Calculated molecular orbitals of **2c** in CH_3CN.

Molecular Orbital	Eigenvalue / Hartrees	MO Population / %						
		ruthenium	B_2bpy					bpy
			bpy	ethynyl	duryl	boron	mesityl	
LUMO+3	−0.08203	1.14	46.69	14.34	21.12	7.07	9.10	0.54
LUMO+2	−0.09107	7.20	1.02	0.03	0.01	0.00	0.00	91.74
LUMO+1	−0.09296	4.84	3.27	0.31	0.36	0.06	0.08	91.08
LUMO	−0.10186	5.19	70.47	7.91	8.03	1.00	1.44	5.96
HOMO	−0.21945	44.64	10.45	10.96	23.57	0.41	4.38	5.59
HOMO−1	−0.21950	38.31	10.77	12.70	27.39	0.48	5.08	5.27
HOMO−2	−0.22750	0.00	0.00	0.05	11.44	1.07	87.44	0.00
HOMO−3	−0.22760	0.00	0.00	0.05	11.66	1.09	87.20	0.00

Table 2-3. Calculated molecular orbitals of **2c'** in CH_3CN.

Molecular Orbital	Eigenvalue / Hartrees	MO Population / %						
		ruthenium	Bbpy					bpy
			bpy	ethynyl	duryl	boron	mesityl	
LUMO+3	−0.07544	0.97	58.56	5.87	12.57	7.26	9.82	4.95
LUMO+2	−0.09106	7.32	1.00	0.02	0.00	0.00	0.00	91.66
LUMO+1	−0.09314	5.12	6.33	0.55	0.63	0.11	0.14	87.12
LUMO	−0.09857	4.29	72.02	5.80	6.09	0.84	1.17	9.79
HOMO	−0.21947	41.77	10.59	11.74	25.39	0.44	4.67	5.40
HOMO−1	−0.22685	76.95	5.72	1.35	3.94	0.07	1.31	10.66
HOMO−2	−0.22752	0.05	0.01	0.05	11.41	1.07	87.40	0.01
HOMO−3	−0.23190	76.64	5.19	0.01	0.01	0.00	0.01	15.14

Table 2-4. Calculated molecular orbitals $[Ru(bpy)_3]^{2+}$ in CH_3CN.

Molecular Orbital	Eigenvalue / Hartrees	MO Population / %						
		ruthenium						bpy
LUMO+3	−0.06572	3.49						96.51
LUMO+2	−0.09111	7.31						92.69
LUMO+1	−0.09121	7.23						92.77
LUMO	−0.09473	1.74						98.26
HOMO	−0.22557	83.65						16.35
HOMO−1	−0.23181	79.58						20.42
HOMO−2	−0.23185	79.65						20.35
HOMO−3	−0.27019	0.42						99.58

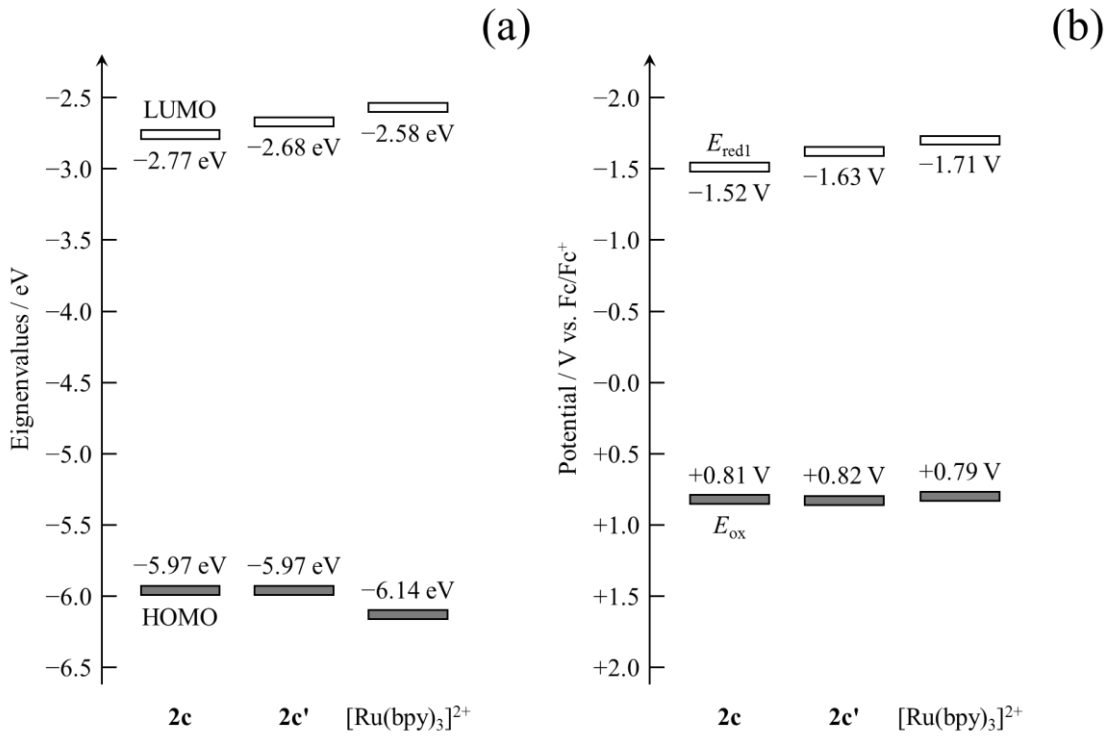

Scheme 2-2. Calculated HOMO/LUMO energies (a) and redox potentials (b) of **2c**, **2c'**, and $[Ru(bpy)_3]^{2+}$.

2-3-2: Absorption Spectra

Figure 2-3 shows the absorption spectra of the complexes in CH_3CN at 298 K. The absorption maximum wavelengths (λ_{abs}) and corresponding molar absorption coefficients (ε) are summarized in Table 2-5. Figure 2-3 demonstrates that, in addition to the relatively narrow and intense bands ($\varepsilon \geq 8 \times 10^4$ $M^{-1}cm^{-1}$) at around 290 nm ascribed to the $^1\pi\pi^*$ transitions in the bpy moieties, the complexes, **2a**–**c** and **2a'**–**c'**, show the characteristic absorption bands in 300–400 nm. Since the ε value of the band in 300–400 nm ($\varepsilon_{300–400}$) increases linearly with an increase in the number of the DBDE group in the complex (n_B, see Figure 2-4) and the spectral band shape resembles with that observed for a tricarbonyl rhenium(I) complex having a B_2bpy or Bbpy ligand,[5,6] the band observed for **2a**–**c** and **2a'**–**c'** in 300–400 nm can be assigned to the ligand-

centered (LC) absorption: superposition of the $^1\pi\pi^*$ transition in the durylethynyl-bpy moiety and the π(aryl)–p(B) CT transition in the B_2bpy or Bbpy ligand(s).

An introduction of the DBDE group(s) to the bpy ligand in $[Ru(bpy)_3]^{2+}$ also affected the ^{1}MLCT absorption band observed in $\lambda > 400$ nm. The complex having a B_2bpy or Bbpy ligand(s) showed a low-energy and intense ^{1}MLCT absorption compared to $[Ru(bpy)_3]^{2+}$. The low-energy shift of the ^{1}MLCT band relative to that of $[Ru(bpy)_3]^{2+}$ is reasonably explained by the stabilization of LUMO by the presence of the DBDE group(s) as suggested by the electrochemical data and DFT calculations. The relationship between the absorption and redox potentials of the complex can be evaluated by the plot between the MLCT absorption maximum energy (E_{abs}) and the difference in the redox potentials ($E_{ox} - E_{red1}$). The E_{abs} value of a $[RuL_3]^{2+}$-type complex (L = diimine ligand), in general, correlates proportionally to the ($E_{ox} - E_{red1}$) value as a measure of the energy difference between HOMO and LUMO.[47] In practice, Tazuke *et al.* have reported the linear relationship between E_{abs} and ($E_{ox} - E_{red1}$) for several $[RuL_3]^{2+}$ complexes as the data are shown in Figure 2-5.[47] It is worth noting that the data on **2a**–**c** and **2a'**–**c'** also fall on the proportional relationship between E_{abs} and ($E_{ox} - E_{red1}$) reported by Tazuke *et al.* as seen in Figure 2-5, with the slope value being ~1.08 eV/V (r = 0.9998). Since the effects of the DBDE group(s) on E_{red1} are much larger than those on E_{ox} as described before, the lower-energy MLCT absorption of **2a**–**c** and **2a'**–**c'** compared to that of $[Ru(bpy)_3]^{2+}$ is responsible for the stabilization of the π*(bpy)-orbital energy through the π(aryl)−p(B) CT interaction.

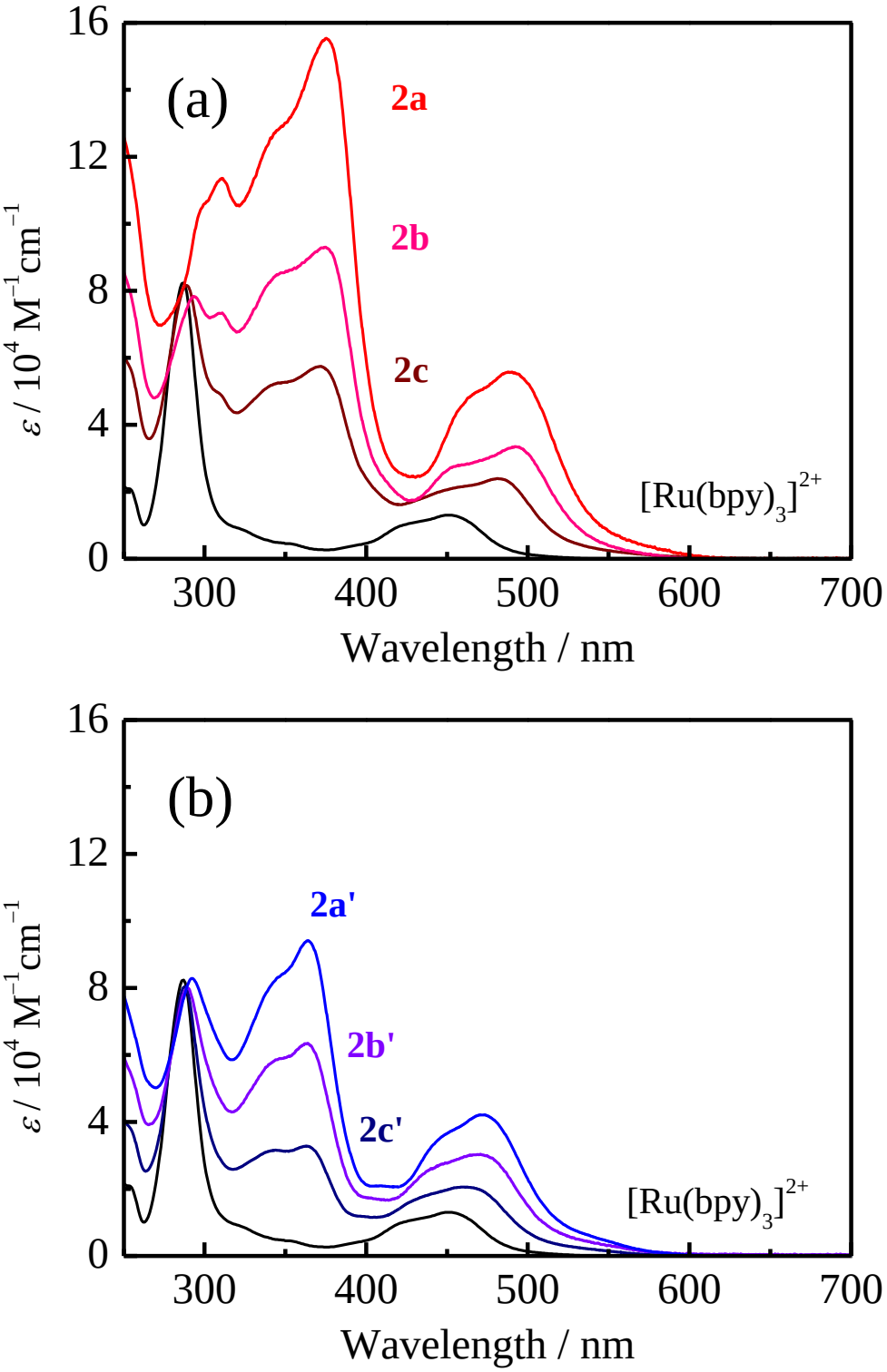

Figure 2-3. Absorption spectra of the complexes (**2a**–**c** (a) and **2a'**–**c'** (b)) in CH_3CN at 298 K.

Table 2-5. Absorption features of the complexes in CH_3CN at 298 K.

Complex	λ_{abs} / nm (ε / 10^4 $M^{-1}cm^{-1}$)		
2a (n = 3)	311 (11.4)	375 (15.5)	488 (5.6)
2b (n = 2)	294 (7.8)	375 (9.3)	492 (3.4)
2c (n = 1)	289 (8.2)	371 (5.7)	481 (2.4)
2a' (n = 3)	292 (8.3)	364 (9.4)	471 (4.2)
2b' (n = 2)	289 (8.0)	364 (6.3)	469 (3.0)
2c' (n = 1)	288 (8.0)	363 (3.3)	461 (2.1)
$[Ru(bpy)_3]^{2+}$	287 (8.2)		451 (1.3)

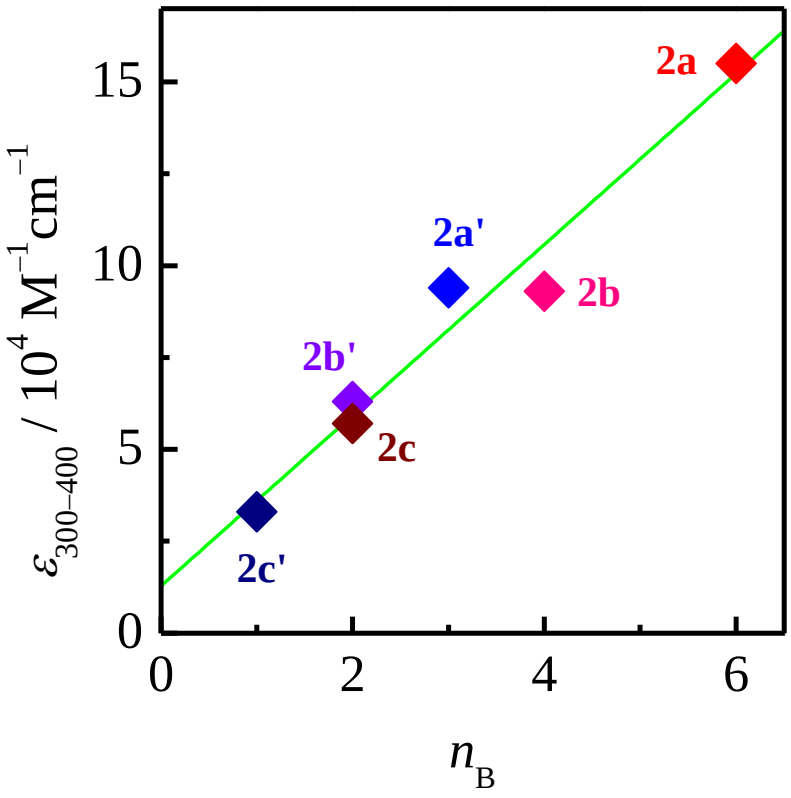

Figure 2-4. Relationship between $\varepsilon_{300-400}$ and n_B of **2a**–**c** and **2a'**–**c'**. The green line represents the linear regression for the plot.

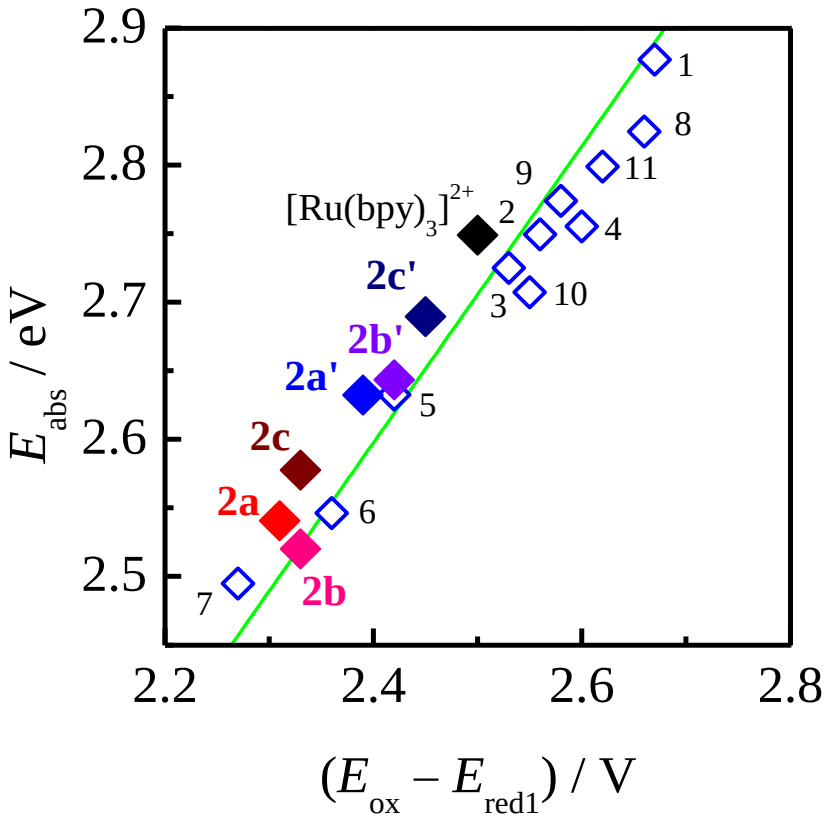

Figure 2-5. Relationship between the E_{abs} and (E_{ox} − E_{red1}) values of ruthenium(II) complexes. Blue open boxes represent the data on the $[RuL_3]^{2+}$ complexes reported by Tazuke *et al.* (L = 2-(2-pyridyl)pyrimidine (1), 4-methyl-2-(2-pyridyl)pyrimidine (2), 5-phenyl-2-(2-pyridyl)pyrimidine (3), 2,2'-bipyrimidine (4), 6-methyl-4-(2-pyridyl)-pyrimidine (5), 6-phenyl-4-(2-pyridyl)pyrimidine (6), 6,6'-dimethyl-4,4'-bipyrimidine (7), 2,2'-bipyrazine (8), 3,3'-bipyridazine (9), 4,4'-dimethyl-bpy (10), phen (11)) in CH_3CN at 298 K whose data were taken from [47]. The data on **2a**–**2c** and **2a'**–**2c'** are taken from Tables 2-1 and 2-5. The green line represents the linear regression between E_{abs} and (E_{ox} − E_{red1}), of which the intercept has been fixed at 0 eV.

The intense ^{1}MLCT absorption is an another important aspect into the spectroscopic properties of **2a**–**c** and **2a'**–**c'** not observed for those of $[Ru(bpy)_3]^{2+}$, and the ε value of the MLCT band (ε_{MLCT}) of the complex increases with an increase in n in $[Ru(B_2bpy)_n(bpy)_{3-n}]^{2+}$ or $[Ru(Bbpy)_n(bpy)_{3-n}]^{2+}$ (n = 0–3) as seen in Figure 2-3 and Table 2-5. Although an increase in the ε value of the LC band in 300–400 nm with n is the reasonable consequence, those in ε_{MLCT} of **2a**–**c** and **2a'**–**c'** are very extraordinary. Since the results similar to those of **2a**–**c** and **2a'**–**c'** have also been confirmed for 4RuB and 5RuB,[2] the enhancement of the ε(MLCT) values of **2a**–**c** and **2a'**–**c'** compared to that of $[Ru(bpy)_3]^{2+}$ is due essentially to the synergistic MLCT/ π(aryl)−p(B) CT interactions.

The oscillator strength of an absorption band (f) is proportional to the square of the absorption transition moment ($\vec{M}$) as given in eqs. 2-4 and 2-5.[45]

$$f \propto \int \varepsilon(\tilde{\nu})\, d\tilde{\nu} = \frac{2\pi N_A}{3000\hbar^2 c D_s \ln 10} \left|\vec{M}\right|^2 \qquad \text{(eq. 2-4)}$$

$$\left|\vec{M}\right| = \langle \Psi_{el,f} | e \sum_n \vec{r}_n | \Psi_{el,i} \rangle \langle \Psi_{vib,f} | \Psi_{vib,i} \rangle = |\vec{\mu}| \langle \Psi_{vib,f} | \Psi_{vib,i} \rangle \qquad \text{(eq. 2-5)}$$

In eq. 2-4, $\varepsilon(\tilde{\nu})$ is the molar absorption coefficient of a molecule at a given wavenumber (cm^{-1}), N_A is the Avogadro number, $\hbar$ is the reduced Planck constant, c is the speed of light, and D_s is the refractive index of a medium. In eq. 2-5, $\Psi_{el,f}$ and $\Psi_{el,i}$ are the electronic wave functions of the final and initial states for an absorption transition, respectively, and $e\sum_n \vec{r}_n$ represents the sum of the transition dipole moment in all of the electronic coordinates. $\Psi_{vib,f}$ and $\Psi_{vib,i}$ are the vibrational wave functions of the final and initial states for an absorption transition, respectively. The

presence of the DBDE group(s) in the bpy ligand(s) gives rise to the enhancement of the MLCT absorption transition dipole moment ($\vec{\mu}$) through charge transfer from the ruthenium atom to the peripheral DBDE group(s) as predicted from eqs. 2-4 and 2-5. Thus, the arylborane–ruthenium(II) complexes (i.e., **2a**–**c** and **2a'**–**c'**) show larger ε_{MLCT} than that of $[Ru(bpy)_3]^{2+}$. It is worth emphasizing that the ε_{MLCT} value of **2a**–**2c** ((2.4–5.6) × 10^4 $M^{-1}cm^{-1}$) for a given *n* is larger than the relevant value of **2a'**–**2c'** ((2.1–4.2) × 10^4 $M^{-1}cm^{-1}$): see Table 2-5. In particular, **2a** showed an extremely large ε value (ε_{488} = 5.6 × 10^4 $M^{-1}cm^{-1}$). It has been reported that the presence of multiple boron centers in a triarylborane brings about electron conjugation *via* p(B) in LUMO,[48,49] and this gives rise to a lower-energy spectral shift and enhancement of the ε value of the π(aryl)–p(B) CT absorption band of the derivative. In practice, the π(aryl)–p(B) CT absorption bands of **2a**–**c** (λ_{abs} = 371–375 nm) were shifted to the lower energy compared to those of **2a'**–**c'** (λ_{abs} = 363–364 nm). Such triarylborane effects (i.e., π(aryl)–p(B) CT effects) on the electronic structures would reflect on the MLCT absorption transition probabilities of **2a**–**c** and **2a'**–**c'**.

To reveal more details about the synergistic MLCT/π(aryl)–p(B) CT interactions, TD-DFT calculations were conducted for **2c**, **2c'**, and $[Ru(bpy)_3]^{2+}$. The calculated absorption transitions (energy and *f*) of the complexes are summarized in Figure 2-6 and Tables 2-6–2-8, and they are compared with the observed absorption spectra in Figure 2-3. To correct the overestimation of the transition energy calculated by TD-DFT,[36] the calculated absorption transitions shown in Figure 2-6 were shifted to the lower energy by 5%. As clearly seen in Figure 2-6, TD-DFT calculations explain very well the low-energy and intense MLCT absorption band observed for **2c** and **2c'** and, therefore, the present calculations are shown to be done properly. The data

demonstrate that the lowest-energy absorption of **2c** is the mixed HOMO−7 (20%)/ HOMO−1 (80%) → LUMO transitions at 494 nm (f = 0.082), while that of **2c'** is the mixed HOMO−1 (50%)/HOMO (50%) → LUMO transitions at 477 nm (f = 0.097). As summarized in Figure 2-2, Tables 2-2, and 2-3, it is predicted that the electrons of **2c** and **2c'** in both HOMO−1 and HOMO distribute to each d-orbital of the ruthenium(II) atom and, partly to the π-orbital of each DBDE-bpy moiety. On the other hand, the LUMOs of **2c** and **2c'** distribute to p(B). These results strongly support the assignment of the lowest-energy absorption bands of **2a**–**c** and **2a'**–**c'** to the synergistic MLCT/ π(aryl)–p(B) CT transitions, which are very different from the pure MLCT transition in $[Ru(bpy)_3]^{2+}$ (see Table 2-8). As seen in Tables 2-2 and 2-3, furthermore, the MO population of the DBDE-bpy moiety in HOMO−1 of **2c** is larger than that of **2c'**, which implies that a contribution of the ππ*(durylethynyl-bpy) transition is much larger for **2c**. It is also worth noting that the LUMO of **2c** distributes to the two boron atoms in the DBDE groups, with larger contributions of the MO to the boron atoms than that of **2c'**. Such contributions of the ππ*(durylethynyl-bpy)/π(aryl)–p(B) CT to the excited states of **2c** and **2c'** enhance the dipole moments of the MLCT absorption transitions in **2c** and **2c'**, which is consistent with the experimental observations: the ε values of the MLCT/π(aryl)–p(B) CT bands of both **2a**–**c** and **2a**–**c'** increase with an increase in n as discussed in the previous section.

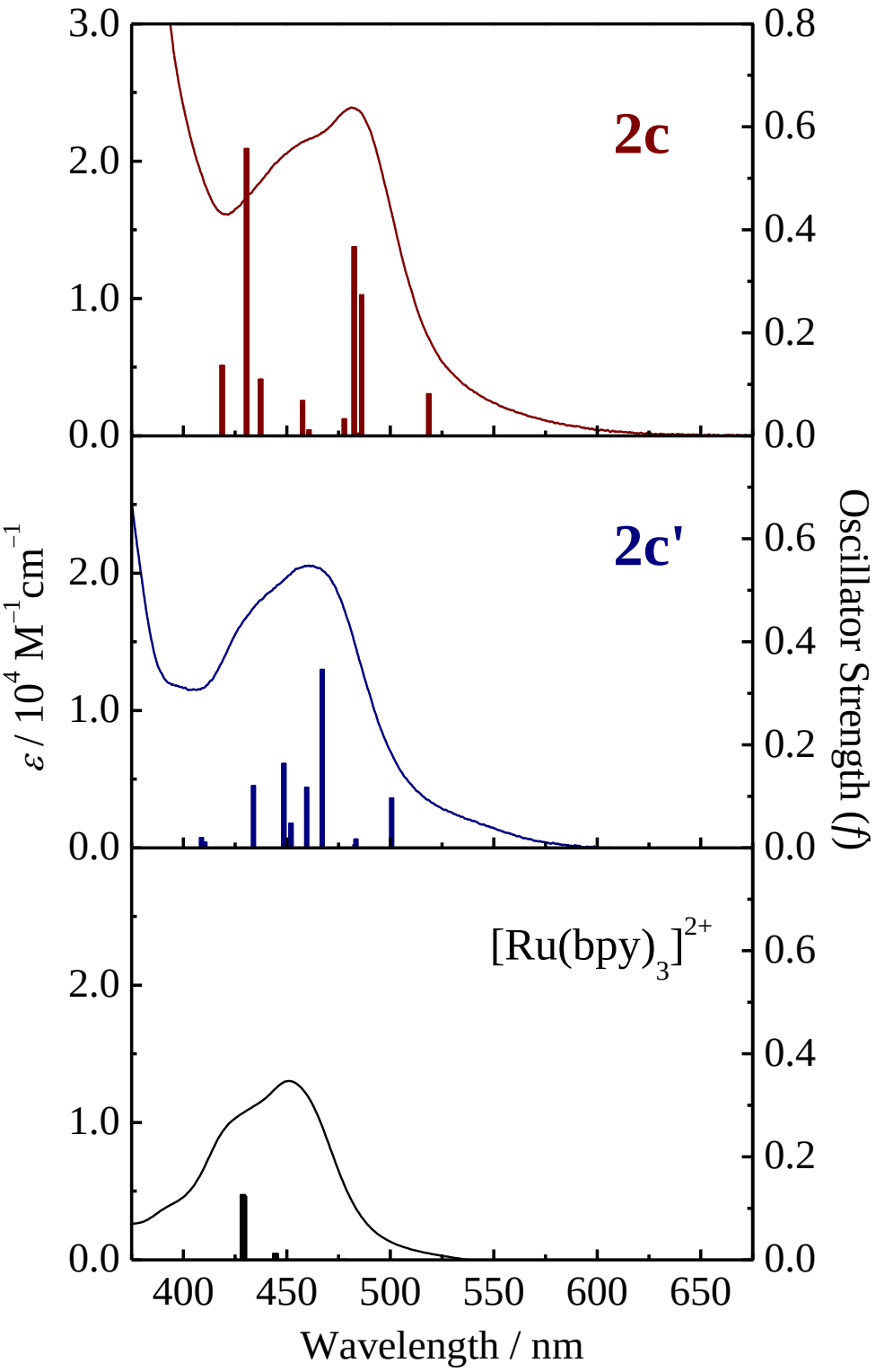

Figure 2-6. Comparison of the observed absorption spectra and oscillator strengths (perpendicular bars) estimated by the TD-DFT calculations for **2c**, **2c'**, and $[Ru(bpy)_3]^{2+}$ in CH_3CN at 298 K.

Table 2-6. Calculated excited states of **2c** in CH_3CN.

Excited State	Transition	Energy (Wavelength)	Oscillator Strength
S_1	HOMO−7 → LUMO (20%) HOMO−1 → LUMO (80%)	2.5100 eV (493.96 nm)	0.0818
S_2	HOMO−7 → LUMO+2 (31%) HOMO−1 → LUMO+2 (69%)	2.6775 eV (463.05 nm)	0.2738
S_3	HOMO−7 → LUMO+1 (19%) HOMO−1 → LUMO (17%) HOMO−1 → LUMO+1 (64%)	2.6830 eV (462.10 nm)	0.0056
S_4	HOMO−14→ LUMO (9%) HOMO−1 → LUMO (27%) HOMO−1 → LUMO+1 (10%) HOMO−1 → LUMO+2 (23%) HOMO → LUMO (31%)	2.6976 eV (459.60 nm)	0.3672
S_5	HOMO−11→ LUMO (10%) HOMO−7 → LUMO (32%) HOMO−4 → LUMO (47%) HOMO−1 → LUMO (11%)	2.7244 eV (455.08 nm)	0.0335
S_6	HOMO−14→ LUMO+2 (14%) HOMO−8 → LUMO+2 (10%) HOMO−7 → LUMO+1 (8%) HOMO−4 → LUMO (9%) HOMO−4 → LUMO+1 (11%) HOMO−1 → LUMO+2 (22%) HOMO → LUMO+2 (26%)	2.8254 eV (438.81 nm)	0.0117
S_7	HOMO−14→ LUMO+1 (13%) HOMO−8 → LUMO+1 (10%) HOMO−7 → LUMO+2 (10%) HOMO−4 → LUMO+2 (14%) HOMO−1 → LUMO+1 (25%) HOMO → LUMO+1 (28%)	2.8445 eV (435.87 nm)	0.0685
S_8	HOMO−11→ LUMO+1 (11%) HOMO−7 → LUMO+1 (33%) HOMO−4 → LUMO+1 (43%) HOMO−1 → LUMO+1 (13%)	2.9768 eV (416.51 nm)	0.1102
S_9	HOMO−11→ LUMO (27%) HOMO−7 → LUMO (55%) HOMO → LUMO (18%)	3.0236 eV (410.06 nm)	0.5579
S_{10}	HOMO−7 → LUMO+2 (27%) HOMO−4 → LUMO+2 (41%) HOMO−1 → LUMO+2 (13%) HOMO → LUMO+3 (19%)	3.1085 eV (398.85 nm)	0.1372

Table 2-7. Calculated excited states of **2c'** in CH_3CN.

Excited State	Transition	Energy (Wavelength)	Oscillator Strength
S_1	HOMO−1 → LUMO (50%) HOMO → LUMO (50%)	2.6004 eV (476.79 nm)	0.0969
S_2	HOMO−1 → LUMO+1 (40%) HOMO → LUMO (18%) HOMO → LUMO+1 (42%)	2.6928 eV (460.42 nm)	0.0172
S_3	HOMO−8 → LUMO+2 (10%) HOMO−1 → LUMO+2 (44%) HOMO → LUMO+2 (46%)	2.6957 eV (459.94 nm)	0.0064
S_4	HOMO−5 → LUMO (17%) HOMO−3 → LUMO+1 (17%) HOMO−1 → LUMO (54%) HOMO−1 → LUMO+1 (12%)	2.7871 eV (444.85 nm)	0.3467
S_5	HOMO−5 → LUMO+1 (10%) HOMO−3 → LUMO (39%) HOMO−1 → LUMO (18%) HOMO−1 → LUMO+1 (19%) HOMO−1 → LUMO+2 (14%)	2.8324 eV (437.73 nm)	0.1178
S_6	HOMO−8 → LUMO+2 (17%) HOMO−3 → LUMO (39%) HOMO−3 → LUMO+1 (18%) HOMO → LUMO+2 (26%)	2.8798 eV (430.53 nm)	0.0481
S_7	HOMO−8 → LUMO+1 (18%) HOMO−3 → LUMO+2 (42%) HOMO → LUMO+1 (40%)	2.9020 eV (427.24 nm)	0.1640
S_8	HOMO−5 → LUMO+2 (9%) HOMO−3 → LUMO (10%) HOMO−3 → LUMO+1 (53%) HOMO−1 → LUMO+2 (19%) HOMO → LUMO+1 (9%)	3.0000 eV (413.29 nm)	0.1210
S_9	HOMO−5 → LUMO (11%) HOMO−3 → LUMO+1 (14%) HOMO−3 → LUMO+2 (49%) HOMO−1 → LUMO+1 (14%) HOMO → LUMO (12%)	3.1718 eV (390.90 nm)	0.0112
S_{10}	HOMO−2 → LUMO	3.1846 eV (389.32 nm)	0.0202

Table 2-8. Calculated excited states of $[Ru(bpy)_3]^{2+}$ in CH_3CN.

Excited State	Transition	Energy (Wavelength)	Oscillator Strength
S_1	HOMO → LUMO (43%) HOMO → LUMO+1 (57%)	2.7179 eV (456.18 nm)	0.0004
S_2	HOMO → LUMO+1 (50%) HOMO → LUMO+2 (50%)	2.7194 eV (455.92 nm)	0.0001
S_3	HOMO → LUMO (63%) HOMO → LUMO+2 (37%)	2.7232 eV (455.29 nm)	0.0010
S_4	HOMO–2 → LUMO+2	2.9037 eV (426.98 nm)	0.0002
S_5	HOMO–2 → LUMO (72%) HOMO–2 → LUMO+1 (16%) HOMO–1 → LUMO (12%)	2.9265 eV (423.66 nm)	0.0109
S_6	HOMO–1 → LUMO (78%) HOMO–1 → LUMO+2 (22%)	2.9292 eV (423.28 nm)	0.0127
S_7	HOMO–2 → LUMO+1 (25%) HOMO–2 → LUMO+2 (25%) HOMO–1 → LUMO (26%) HOMO–1 → LUMO+1 (24%)	3.0323 eV (408.88 nm)	0.1235
S_8	HOMO–2 → LUMO (25%) HOMO–2 → LUMO+2 (25%) HOMO–1 → LUMO+1 (25%) HOMO–1 → LUMO+2 (25%)	3.0356 eV (408.43 nm)	0.1266
S_9	HOMO–2 → LUMO+1 (50%) HOMO–1 → LUMO+2 (50%)	3.2487 eV (381.64 nm)	0.0000
S_{10}	HOMO → LUMO+2	3.5839 eV (345.95 nm)	0.0070

2-3-3: Emission Spectra at Room Temperature

All of the complexes in CH_3CN at 298 K showed obvious emission whose spectra were characterized by the broad and structureless bands as shown in Figure 2-7. The emission maximum wavelengths (λ_{em}) are summarized in Table 2-9, together with the photophysical parameters of the complexes. The λ_{em} value of the complex was shifted to the longer wavelength with an increase in the number of the DBDE groups in a bpy ligand (e.g., λ_{em} = 620, 640, and 651 nm for $[Ru(bpy)_3]^{2+}$, **2a'**, and **2a**, respectively), in good accordance with the sequence of the longer-wavelength shift of λ_{abs}. For a **2a**–**c** or **2a'**–**c'** series, on the other hand, the λ_{em} value is shifted to the shorter wavelength with an increase in *n* with the value being varied from 659 to 651 nm for **2a**–**c** ($[Ru(B_2bpy)_n(bpy)_{3-n}]^{2+}$) and from 647 to 640 nm for **2a'**–**c'** ($[Ru(Bbpy)_n(bpy)_{3-n}]^{2+}$). The results are unexpected since the emission maximum energy of $[RuL_3]^{2+}$ (E_{em}) correlates in general proportionally to the ($E_{ox} - E_{red1}$) value of the complex, similar to E_{abs} in Figure 2-5.[47] As seen in Figure 2-8, however, the E_{em} values of **2a**–**c** or **2a'**–**c'** did not fall on the proportional relationship between the E_{em} and ($E_{ox} - E_{red1}$) values observed for ordinary polydiimine $[RuL_3]^{2+}$ complexes and showed a reverse E_{em} shift with an increase in the ($E_{ox} - E_{red1}$) value. There are two possible explanations for such the unusual emission energy shift of **2a**–**c** or **2a'**–**c'**: excited-state relaxation and intersystem crossing in **2a**–**c** or **2a'**–**c'** as discussed in detail in the followings.

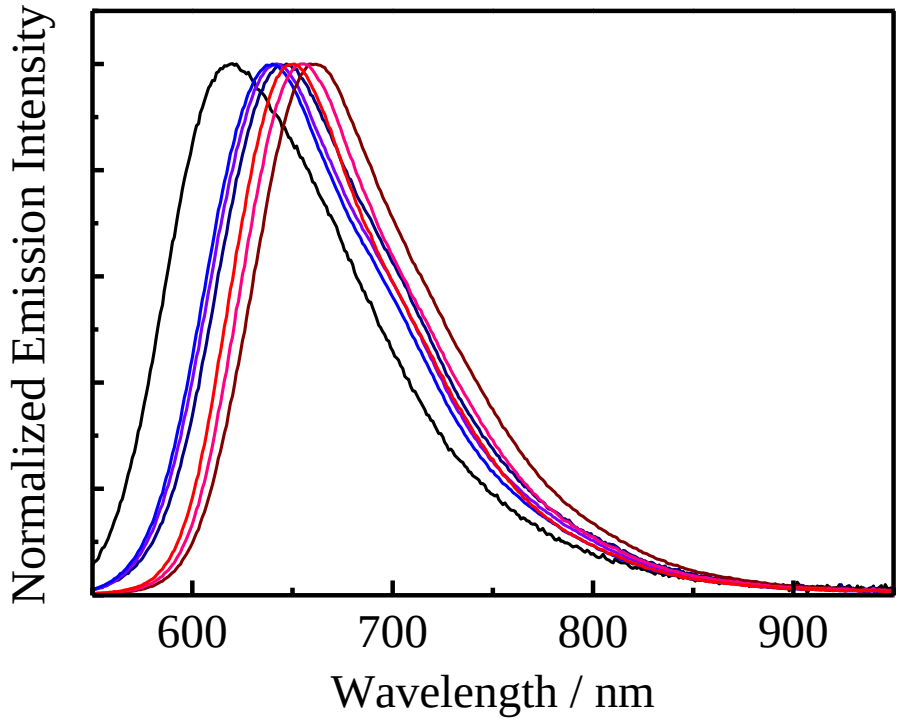

Figure 2-7. Corrected emission spectra of **2a**–**c**, **2a'**–**c'**, and $[Ru(bpy)_3]^{2+}$ in CH_3CN at 298 K. The emission intensities of the complexes are normalized to those at the maximum wavelengths. The colors of the spectra correspond to those indicated in Figure 2-1.

Table 2-9. Emission parameters of the complexes in CH_3CN at 298 K.

Complex	λ_{em} / nm	Φ_{em}	τ_{em} / μs	k_r / s^{-1}	k_{nr} / s^{-1}
2a (n = 3)	651	0.43	1.7	2.5×10^5	3.4×10^5
2b (n = 2)	656	0.36	1.7	2.1×10^5	3.8×10^5
2c (n = 1)	659	0.27	1.7	1.6×10^5	4.3×10^5
2a' (n = 3)	640	0.26	2.5	1.0×10^5	3.0×10^5
2b' (n = 2)	642	0.24	2.4	1.0×10^5	3.2×10^5
2c' (n = 1)	647	0.20	2.3	0.87×10^5	3.5×10^5
$[Ru(bpy)_3]^{2+}$	620	0.095	0.89	1.1×10^5	10×10^5

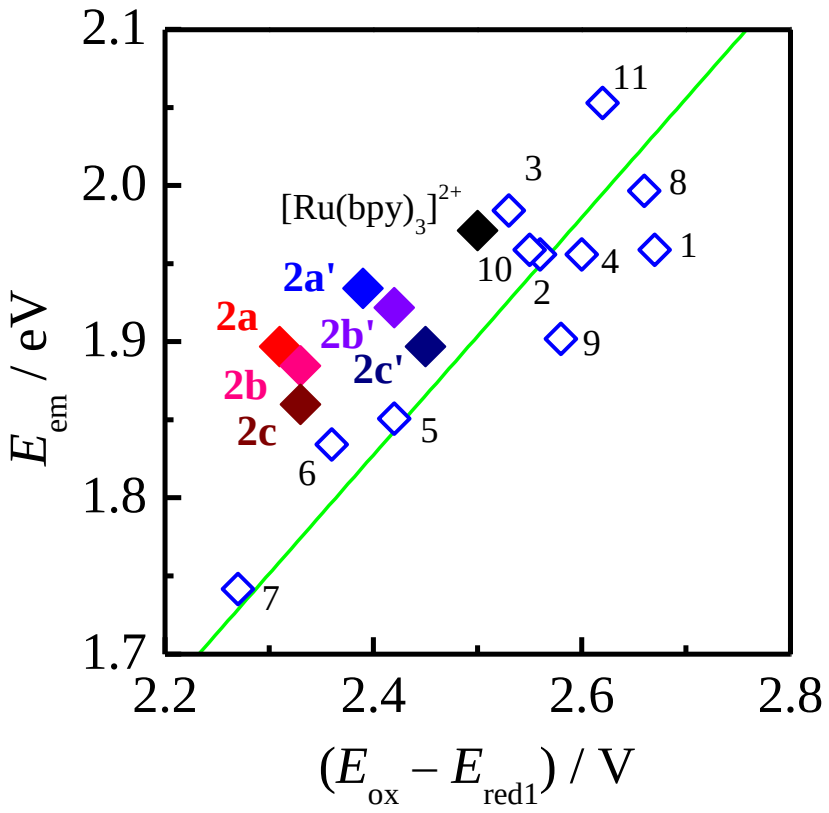

Figure 2-8. Relationship between the E_{em} and (E_{ox} − E_{red1}) values of the complexes. Blue open boxes represent the reported data for ordinary polydiimine $[RuL_3]^{2+}$ complexes (the numbers are identical to those in Figure 2-5).[47] The green line represents the linear regression, of which the intercept has been fixed at 0 eV, for the relation between E_{em} and (E_{ox} − E_{red1}) reported for $[RuL_3]^{2+}$.[47]

The radiative transition from the excited state of $[RuL_3]^{2+}$ proceeds from the thermally-equilibrated triplet MLCT excited state and, therefore, the solvent relaxation in the excited state is one of the important factors to determine the emission energy of the complex. Since an introduction of the DBDE group(s) to a bpy ligand(s) results in an increase in the molecular size of the complex, this will lead to a decrease in the solvation energy around the ^{3}MLCT excited state and, thus, the unfavorable solvation structures in the sequence $n = 1 < n = 2 < n = 3$ for **2a**–**c** or **2a'**–**c'** may render destabilization of the ^{3}MLCT excited-state energy: a shorter-wavelength shift of the

emission spectrum. The extent of the solvation energy in the excited state is in general reflected on the full width at half maximum (*fwhm*) of the emission spectrum. Nevertheless, the *fwhm* value of the emission spectrum of the present complex in CH_3CN at 298 K was almost independent of the number of the DBDE-substituted ligand with the *fwhm* value being almost constant at 2390–2420 or 2670–2680 cm^{-1} for **2a**–**c** or **2a'**–**c'**, respectively. To obtain further details on the excited states of the complexes, the Franck–Condon analysis of the emission spectra[39,40] was conducted. As shown in Figure 2-9, the emission spectra of the complexes were adequately reproduced by the one-averaged-mode approximation by eq. 2-1 using the parameters in Table 2-10. The medium-frequency vibration mode ($\hbar\omega_M$), which characterizes the emitting excited state, was almost independent of the complex, and the $\hbar\omega_M$ value (1310–1370 cm^{-1}) was simulated as the typical values reported for the ^{3}MLCT excited states of $[RuL_3]^{2+}$-type complexes.[42] The inner-sphere reorganization energy (λ_i), as a measure of the structural change in the excited-state, given by eq. 2-3 was not sensitive to *n* in $[Ru(B_2bpy)_n(bpy)_{3-n}]^{2+}$ (**2a**–**c**, ~910 cm^{-1}) or $[Ru(Bbpy)_n(bpy)_{3-n}]^{2+}$ (**2a'**–**c'**, ~1050 cm^{-1}). The solvation energy for the excited-state complex can be also estimated as an outer-sphere reorganization energy (λ_o), and those of the complexes calculated by eq. 2-2 are almost constant at 1040–1090 or 1270–1280 cm^{-1} for **2a**–**c** or **2a'**–**c'**, respectively. According to the λ_i and λ_o values of the complexes, the unusual E_{em} shift against an increase in ($E_{ox} - E_{red1}$) observed for **2a**–**c** or **2a'**–**c'** in Figure 2-8 will not be explained by the solvent relaxation in the excited state of the complex.

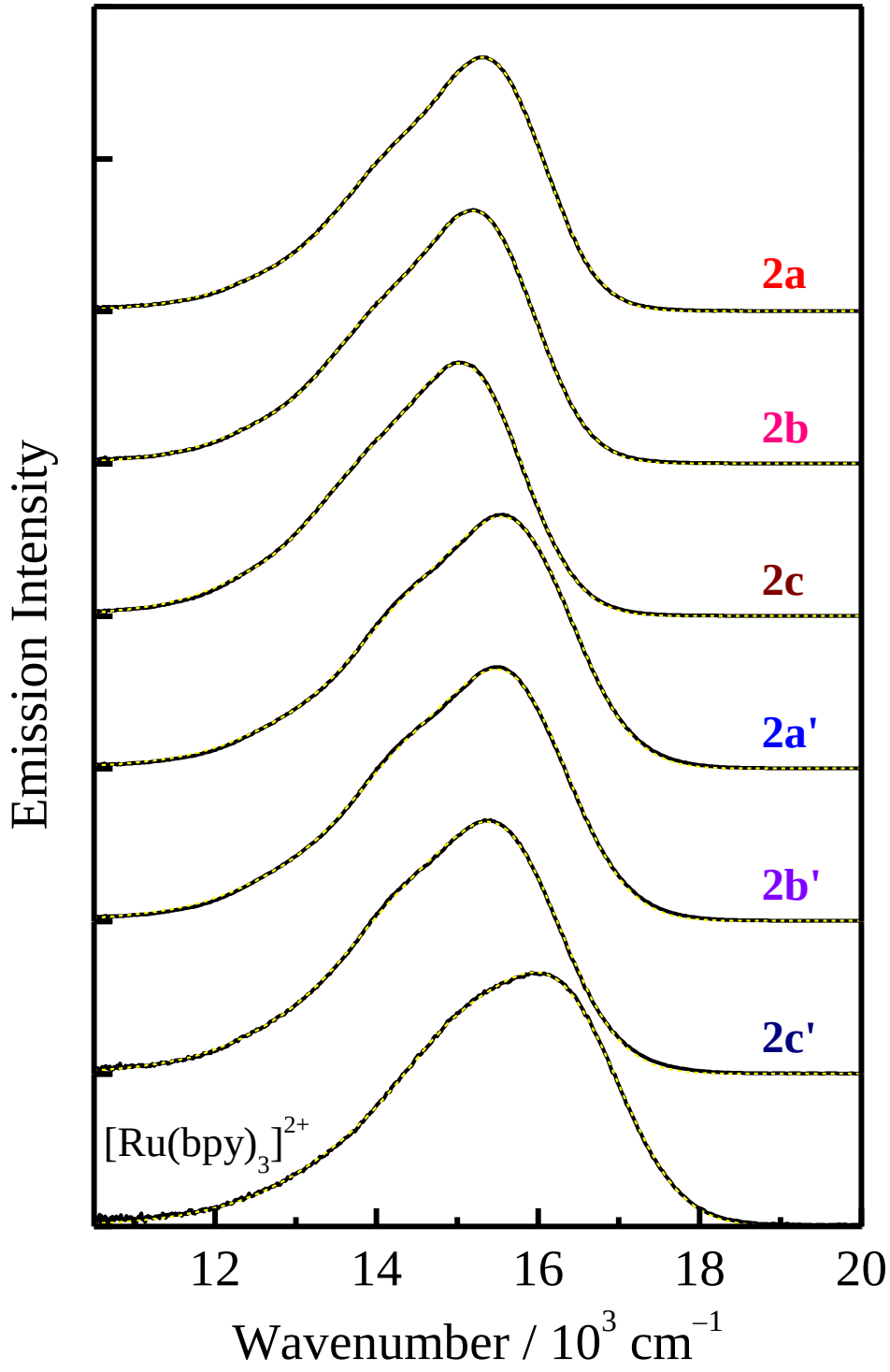

Figure. 2-9. Corrected emission spectra of the complexes in CH_3CN at 298 K (black solid curves) and the theoretical fits of the spectra by eq. 2-1 using the parameters in Table 2-10 (yellow broken curves).

Table. 2-10. Franck–Condon emission spectral fitting parameters for the complexes in CH_3CN at 298 K.[a]

Complex	E_0	$\Delta\tilde{\nu}_{1/2}$	$\hbar\omega_M$	S_M	λ_i	λ_o	ΔG_{ES}
	/ cm^{-1}				/ cm^{-1}		
2a (n = 3)	15440	1550	1310	0.69	900	1040	16480
2b (n = 2)	15320	1560	1310	0.69	900	1060	16380
2c (n = 1)	15170	1590	1310	0.70	920	1090	16260
2a' (n = 3)	15740	1710	1370	0.76	1040	1270	17010
2b' (n = 2)	15680	1720	1360	0.78	1060	1280	16960
2c' (n = 1)	15590	1720	1330	0.78	1040	1280	16870
$[Ru(bpy)_3]^{2+}$	16310	1760	1340	0.96	1290	1350	17660

[a] See also section 2-2-6.

The energy splitting between the singlet and triplet excited states (ΔE_{ST}) is another important factor to govern the emission energy of a $[RuL_3]^{2+}$ complex. The free energy content of the excited state of **2a**–**c** or **2a'**–**c'** (ΔG_{ES}) estimated by the Franck–Condon analyses increases with increasing n as seen in Table 2-10. The results indicate that the complex with a larger n value shows higher-energy emission than that expected from the ($E_{ox} - E_{red1}$) value, demonstrating that one of the factors governing E_{em} of the complex is ΔE_{ST}. An important information on the ΔE_{ST} value of the complex is also obtained by DFT calculations. On the basis of the Kohn–Sham MOs in Figure 2-2, HOMO of **2c** or **2c'** is characterized by the electron densities on the ruthenium(II) atom and the durylethynyl-bpy moiety, and the LUMO distributes partly to the boron atom(s). The participation of p(B) in LUMO will give rise to the decrease in the electron-exchange integral in the excited state of the complex and, therefore, the ΔE_{ST} value should be small in the excited state of **2c** or **2c'** relative to that of $[Ru(bpy)_3]^{2+}$. Although the data on DFT calculations are limited to those of **2c** and **2c'** alone due to the computational cost in the present stage of the investigation, it can be

easily expected that an increase in n of $[Ru(B_2bpy\}_n(bpy)_{3-n}]^{2+}$ or $[Ru(Bbpy)_n(bpy)_{3-n}]^{2+}$ enhances the contribution of p(B) to the LUMO and the resulting small ΔE_{ST} value gives rise to an increase in the emission energy of the complex.

2-3-4: Photophysical Properties at Room Temperature

Figures 2-10 and 2-11 show the emission spectra in a wavenumber scale and the emission decay profiles of the complexes in CH_3CN at 298 K, respectively. The complexes **2a**–**c** and **2a'**–**c'** showed intense emission with the quantum yield (Φ_{em}) > 0.20, and the Φ_{em} value increased with an increase in n for both **2a**–**c** and **2a'**–**c'** series. In particular, **2a** shows extremely intense emission with Φ_{em} = 0.43. To the best of my knowledge, this is the highest value among those of MLCT-type $[RuL_3]^{2+}$ complexes hitherto reported.[50] The emission decay profiles of the complexes were fitted satisfactorily by single-exponential functions. The complexes **2a**–**c** and **2a'**–**c'** showed longer-lived emission (emission lifetime (τ_{em}) > 1.7 μs) than $[Ru(bpy)_3]^{2+}$ (τ_{em} = 0.89 μs) and, surprisingly, the τ_{em} value was insensitive to n with τ_{em} being 2.3–2.5 and 1.7 μs for **2a**–**c** and **2a'**–**c'**, respectively, in contrast to the enhanced Φ_{em} with n in **2a**–**c** and **2a'**–**c'**. The results strongly suggest that an increase in n accelerates the radiative process of the complex as the radiative (k_r) and nonradiative decay rate constants (k_{nr}) of the complexes, evaluated by the relations $\tau_{em} = 1/(k_r + k_{nr})$ and $\Phi_{em} = k_r/(k_r + k_{nr})$, are included in Table 2-9. The photophysical properties of the complexes are discussed in terms of the k_r and k_{nr} values as described in the succeeding sections.

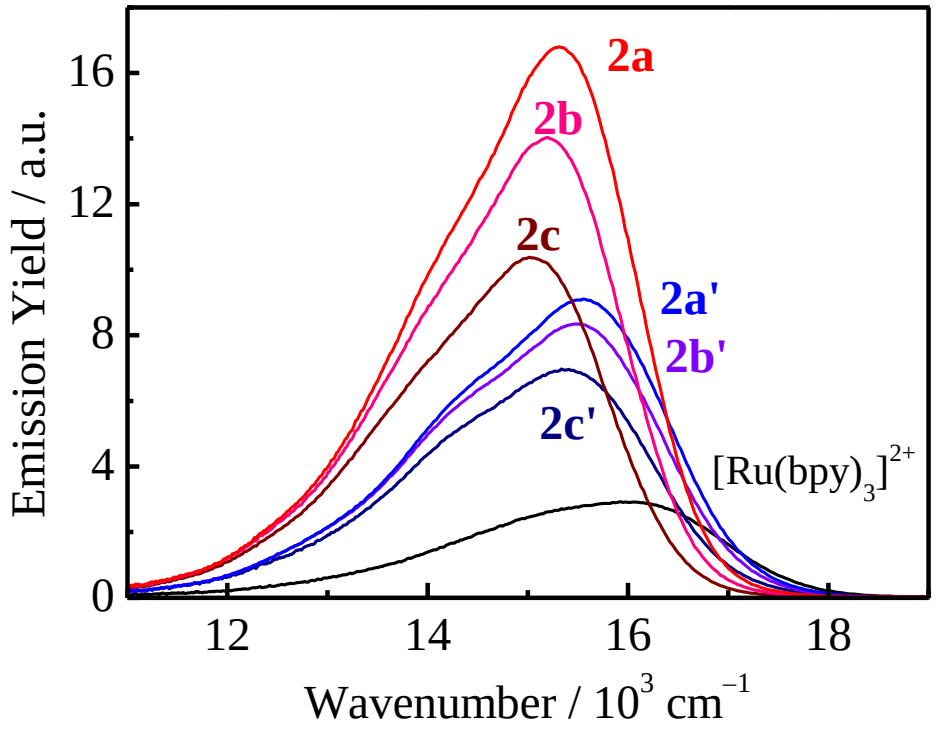

Figure 2-10. Corrected emission spectra of the complexes in CH_3CN at 298 K whose spectral integrations correspond to the relative emission quantum yields of the complexes.

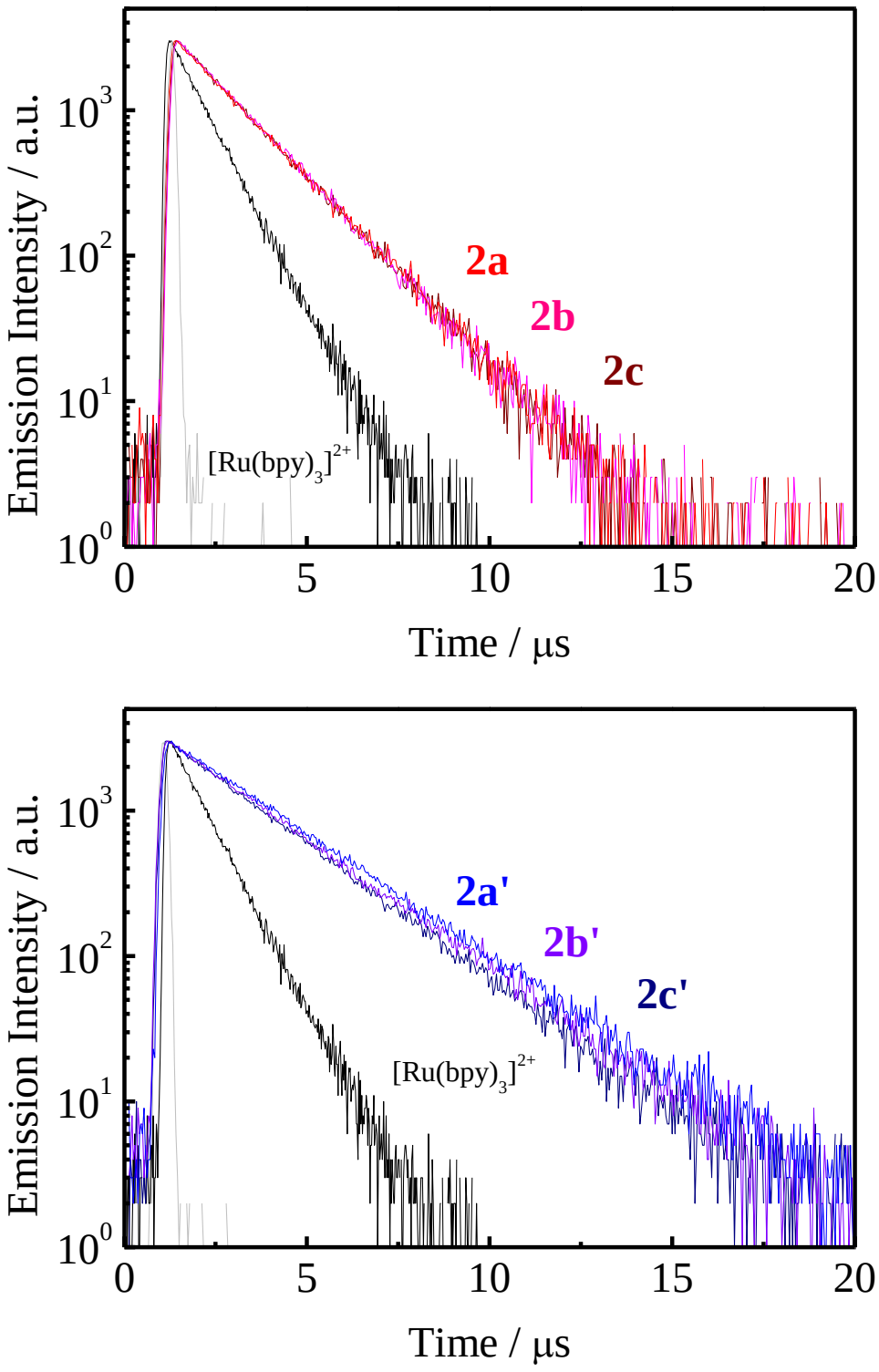

Figure 2-11. Emission decay profiles of the complexes in CH_3CN at 298 K. Gray curves represent instrumental response functions.

2-3-5: Nonradiative Decay Rate Constants

A distinguished consequence obtained for the present complexes is the smaller k_{nr} values of **2a**–**c** and **2a'**–**c'** ((3.0–4.3) × 10^5 s^{-1}) than that of $[Ru(bpy)_3]^{2+}$ (10 × 10^5 s^{-1}). Since it is well known that the k_{nr} values of the polypyridyl complexes of ruthenium(II), osmium(II), rhenium(I), and so forth follow the energy gap law,[39,42,51–54] by which the ln k_{nr} value of a complex linearly increases with decreasing E_{em}. As the energy gap plots for the present complexes and a series of diimine $[RuL_3]^{2+}$ complexes are shown in Figure 2-12, the complexes **2a**–**c** and **2a'**–**c'** show a good linear relationship between ln k_{nr} and E_{em}, though the absolute k_{nr} values of **2a**–**c** and **2a'**–**c'** are extraordinarily small compared to that of $[Ru(bpy)_3]^{2+}$ as mentioned before. The results demonstrate that the nonradiative decay mode from the MLCT excited state to the ground state of **2a**–**c** and **2a'**–**c'** is common for the complexes and differs from those of other $[RuL_3]^{2+}$ complexes. Since the excited electrons in LUMOs of **2a**–**c** and **2a'**–**c'** distribute more or less to p(B) as described in the preceding section, the large deviation of the emission data of ordinary polydiimine $[RuL_3]^{2+}$ complexes from the linear relation between ln k_{nr} and E_{em} in Figure 2-12 will be also explained by the participation of the synergistic MLCT/π(aryl)–p(B) CT interactions in the emitting excited states of **2a**–**c** and **2a'**–**c'**.[55]

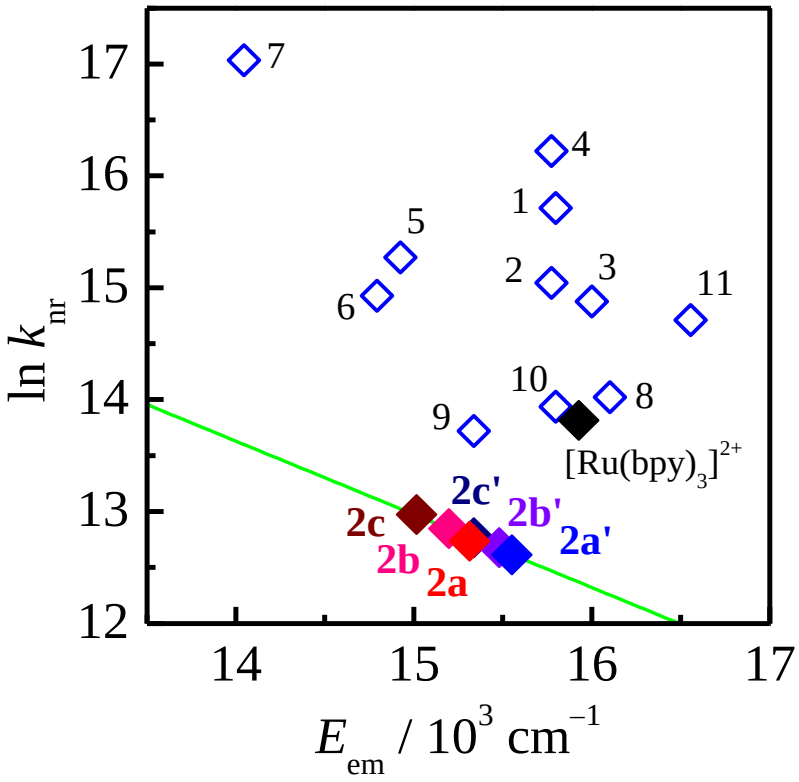

Figure 2-12. Energy gap plot for the complexes in CH_3CN at 298 K. Blue open boxes represent the data on a series of diimine $[RuL_3]^{2+}$ complexes (the numbers are identical to those in Figure 2-5).[47] Green line represents the linear regression for the data of **2a**–**c** and **2a'**–**c'** on the basis of the energy gap law.

To reveal the origin of the small k_{nr} values of **2a**–**c** and **2a'**–**c'**, temperature (T) dependences of the emission lifetimes of **2c**, **2c'**, and $[Ru(bpy)_3]^{2+}$ were investigated. The T-dependence of the emission lifetime of $[RuL_3]^{2+}$ ($\tau_{em}(T)$) is known to be analyzed by an Arrhenius-type equation, eq. 2-6,[56]

$$[\tau_{em}(T)]^{-1} = (k_r^0 + k_{nr}^0) + k'\exp(-\frac{\Delta E}{k_B T})$$

(eq. 2-6)

where k_r^0 and k_{nr}^0 are the T-independent radiative and nonradiative decay rate constants

from the emitting excited state to the ground state, respectively. The parameter k' is the frequency factor for thermal activation from the ^{3}MLCT excited state to the upper-lying nonemitting excited state (typically, triplet dd excited (^{3}dd*) state for a polypyridyl ruthenium(II) complex) with the energy barrier between the two states being ΔE. Figure 2-13 shows the T-dependences (250–330 K) of the emission decay profiles of the complexes in propylene carbonate. While the emission lifetime of $[Ru(bpy)_3]^{2+}$ decreases sharply upon T-elevation, **2c** and **2c'** show very small T-dependent emission lifetimes. The emission decay profiles of the complexes in 250–330 K were analyzed by single-exponential functions, irrespective of T, and the T-dependences of τ_{em} were adequately fitted by eq. 2-6 as shown in Figure 2-14 with the fitting parameters (ΔE, ($k_r^0 + k_{nr}^0$), and k') being summarized in Table 2-11. The ΔE values of **2c** (930 cm^{-1}) and **2c'** (2450 cm^{-1}) are smaller than that of $[Ru(bpy)_3]^{2+}$ (3780 cm^{-1}), suggesting that thermal activation from ^{3}MLCT to ^{3}dd* is supposed to be more likely for **2c** and **2c'** compared to that of $[Ru(bpy)_3]^{2+}$. On the other hand, the k' values of **2c** (1.4×10^7 s^{-1}) and **2c'** (7.3×10^9 s^{-1}) are much smaller than that of $[Ru(bpy)_3]^{2+}$ (2.9×10^{13} s^{-1}), demonstrating a minor contribution of the ^{3}dd* state to nonradiative decay from the ^{3}MLCT excited state of **2c** or **2c'**. Such small k' values have been often reported for $[RuL_3]^{2+}$-type complexes and, in such cases, the T-dependent τ_{em} has been discussed in terms of the contribution of the fourth ^{3}MLCT excited state, which locates in a higher energy by several hundreds of wavenumbers than the emitting ^{3}MLCT excited state.[57,58] Since both ΔE and k' values observed for **2c** or **2c'** are close to those for thermal activation from ^{3}MLCT to the fourth ^{3}MLCT state, the T-dependent emission lifetimes of **2c** and **2c'** are explained by the contribution of thermal activation from ^{3}MLCT to the fourth MLCT excited state to

nonradiative decay from the ^{3}MLCT excited state to the ground state.[59] While the contribution of thermal activation to the fourth ^{3}MLCT excited state to excited-state decay is generally minor for $[RuL_3]^{2+}$, it plays important roles in excited-state decay of **2c** and **2c'**, probably due to large stabilization of the emitting ^{3}MLCT state in energy by the synergistic MLCT/π(aryl)–p(B) CT interactions relative to that of the ^{3}dd* energy. Such characteristics are common for the triplet MLCT/π(aryl)–p(B) CT excited states of **2a**–**c** and **2a'**–**c'**. As described in the preceding section, the E_{ox} values assigned to the metal oxidation are almost the same for **2a**–**c**, **2a'**–**c'**, and $[Ru(bpy)_3]^{2+}$, while the E_{red1} value assigned to the ligand reduction of **2a**–**c** and **2a'**–**c'** shifts to the positive potential direction compared to that of $[Ru(bpy)_3]^{2+}$. This indicates that the ^{3}dd*-state energies of the complexes are comparable with one another, while the ^{3}MLCT excited-state energies of **2a**–**c** and **2a'**–**c'** decrease relative to the ^{3}dd*-state energies owing to the presence of the DBDE group(s) in the ligand(s). The resulting large ^{3}MLCT–^{3}dd* energy gap in **2a**–**c** and **2a'**–**c'** would suppress thermal deactivation of the ^{3}MLCT state *via* the ^{3}dd* state, which will be the origin of the small *T*-dependences of the emission lifetimes and, thus, the small k_{nr} values of **2a**–**c** and **2a'**–**c'**.

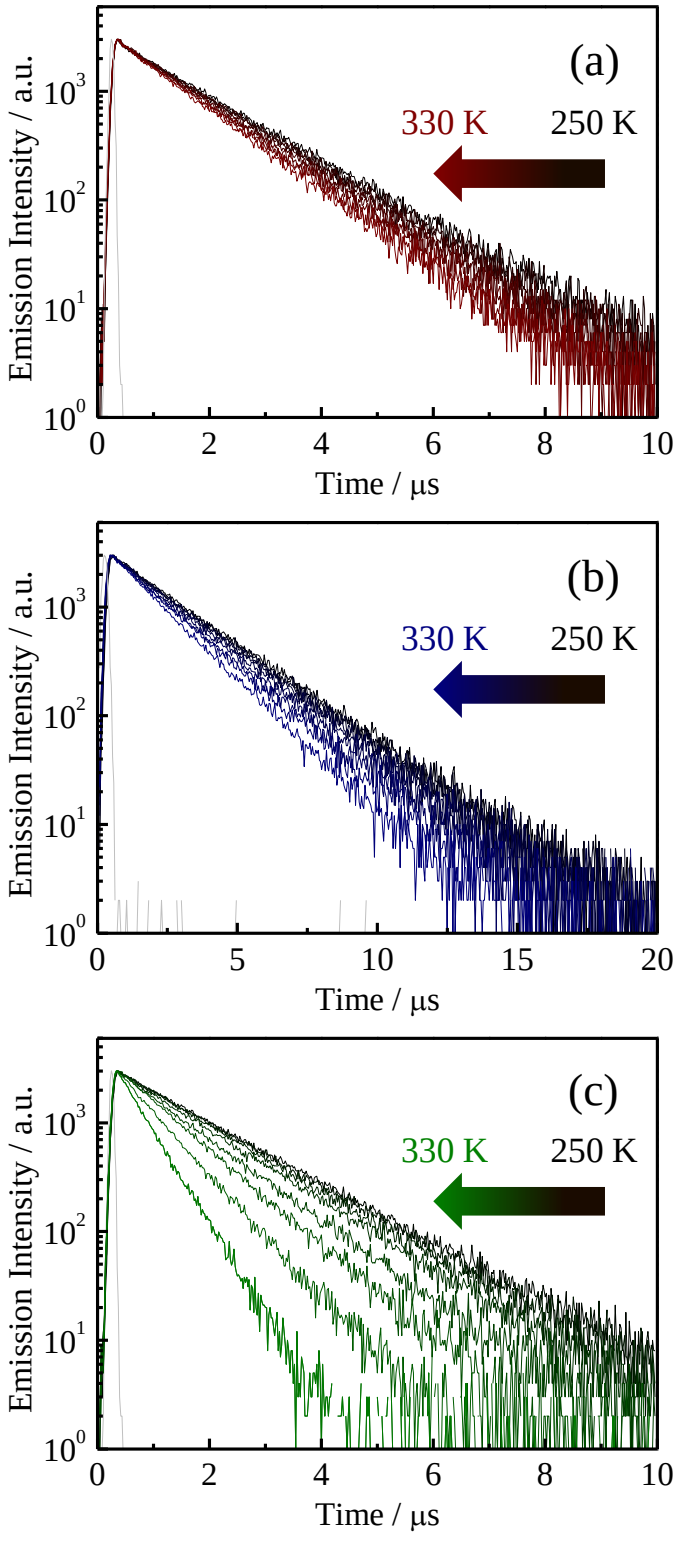

Figure 2-13. *T*-dependences (*T* = 250–330 K) of the emission decay profiles of **2c** (a), **2c'** (b), and $[Ru(bpy)_3]^{2+}$ (c) in propylene carbonate. Gray curves represent instrumental response functions.

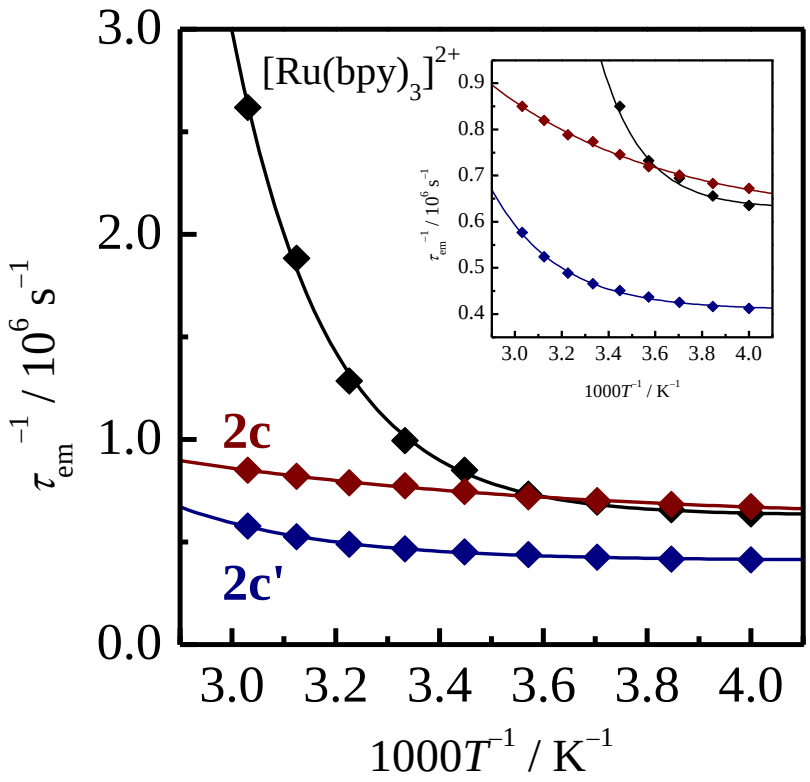

Figure 2-14. *T*-dependences (*T* = 250–330 K) of the emission lifetimes of **2c**, **2c'**, and $[Ru(bpy)_3]^{2+}$ in propylene carbonate. The curves represent the best fits of the experimental data by eq. 2-6. Inset: enlarged view.

Table 2-11. Activation parameters for the *T*-dependent emission lifetimes of **2c**, **2c'**, and $[Ru(bpy)_3]^{2+}$ in propylene carbonate.

Complex	ΔE / cm^{-1}	$(k_r^0 + k_{nr}^0)$ / s^{-1}	k' / s^{-1}
2c	930	6.0×10^5	1.4×10^7
2c'	2450	4.1×10^5	7.3×10^9
$[Ru(bpy)_3]^{2+}$	3780	6.3×10^5	2.9×10^{13}

2-3-6: Radiative Rate Constants

Characteristic emission behaviors are also observed for the k_r values of the complexes. The k_r values of **2a**–**c** ((1.6–2.5) × 10^5 s^{-1}) and **2a'**–**c'** ((0.87–1.0) × 10^5 s^{-1}) increased with an increase in *n*. It is important to emphasize that the ε_{MLCT} value of the complex also increases with an increase in *n* as mentioned before, and this might relate to the *n* dependence of the k_r value. In practice, as shown in Figure 2-15, the k_r values of **2a**–**c** correlate very well with the relevant ε_{MLCT} values. Also, one can find a positive correlation between the k_r and ε_{MLCT} values for **2a'**–**c'**, although the variation of k_r with *n* is not large enough. These correlations between k_r and ε_{MLCT} observed for **2a**–**c** and **2a'**–**c'** resemble with the Strickler–Berg relation for the fluorescence transition of a molecule given by eq. 2-7,[60]

$$k_r^0 = 2.880 \times 10^{-9} {D_s}^2 \frac{g_l}{g_u} \frac{\int I(\tilde{\nu}) d\tilde{\nu}}{\int \tilde{\nu}^{-3} I(\tilde{\nu}) d\tilde{\nu}} \int \frac{\varepsilon(\tilde{\nu})}{\tilde{\nu}} d\tilde{\nu} \qquad \text{(eq. 2-7)}$$

where k_r^0 is the intrinsic (or natural) S_1–S_0 fluorescence rate constant. $I(\tilde{\nu})$ and $\varepsilon(\tilde{\nu})$ are the fluorescence intensity and the ε value of the absorption band of a molecule responsible for the (S_1–S_0) fluorescence transition at a given wavenumber ($\tilde{\nu}$), respectively. D_s is the refractive index of a medium and, g_l and g_u are the electronic degeneracies in the ground and excited states, respectively. The Strickler–Berg relation demonstrates that the larger is the ε value (i.e., $\varepsilon(S_0–S_1)$), the larger is the relevant fluorescence rate constant (k_r^0) and, thus, the fluorescence quantum yield: $\Phi_{em} \propto \varepsilon(S_0–S_1)$. The results in Figure 2-15 suggest a Strickler–Berg-type relation is also held for the emission data of **2a**–**c** and **2a'**–**c'**, though there is no theoretical proof for the applicability of the relation to a phosphorescence transition. While a Strickler–Berg-

type relation between k_r and ε_{MLCT} for a phosphorescent transition metal complex has never been reported, the present results in Figure 2-15 for **2a**–**c** are not fortuitous, and similar positive relationship between k_r and ε_{MLCT} can be also found for a series of $[Ru(bpy)_3]^{2+}$ derivatives ($[Ru(X\text{-}bpy)_3]^{2+}$)[61,62]: see Figure 2-15.

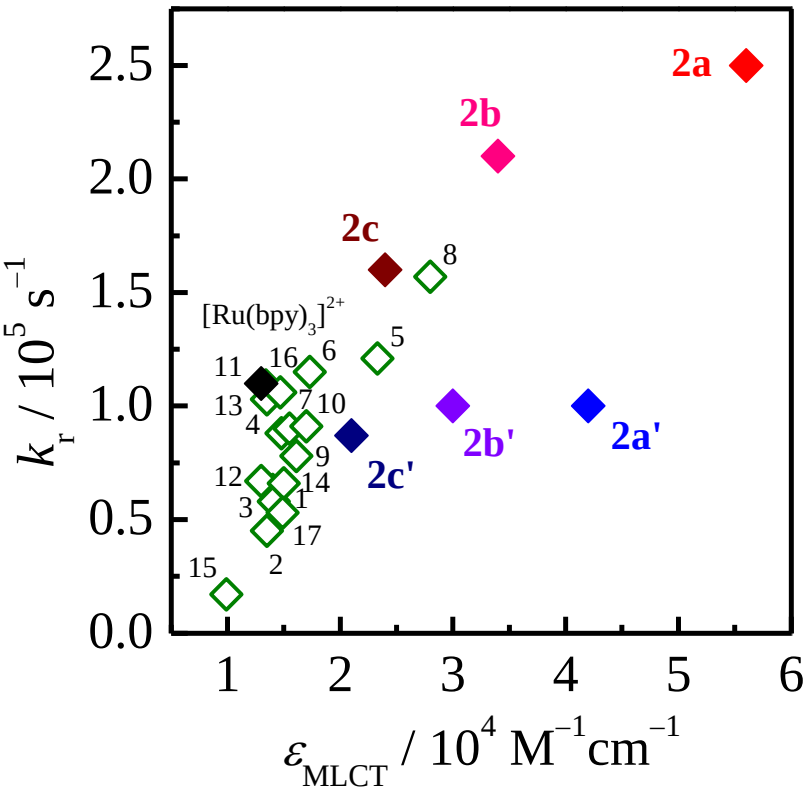

Figure 2-15. Relationship between k_r and ε_{MLCT} for the complexes in CH_3CN at 298 K. Green open boxes represent the data for a series of $[Ru(X\text{-}bpy)_3]^{2+}$ complexes (X = 4-bromo (1), 4-chloro (2), 4-methoxy (3), 4-benzyloxy (4), 4,4'-bisethoxycarbonyl (5), 4,4'-dibromo (6), 4,4'-dichloro (7), 4,4'-diphenyl (8), 4,4'-dibenzyl (9), 4,4'-dimethyl (10), 4,4'-diphenoxy (11), 4,4'-diethoxy (12), 4,4'-dibenzyloxy (13), 4,4'-bisacetamido (14), 5,5'-bisethoxycarbonyl (15), 5,5'-dimethyl (16), 5,5'-bisacetamido (17)) in EtOH–MeOH (4/1, v/v) at 293 K. The literature data were taken from ref. [61,62].

It is clear that a comparison of the k_r data with the molar absorption coefficient of the S_0–T_1 MLCT absorption band of a complex (ε_{3MLCT}) is more favorable. Unfortunately, the S_0–T_1 MLCT absorption of **2a**–**c** and **2a'**–**c'** has not been observed experimentally. However, the linear relationship between ε_{MLCT} and k_r seen in Figure 2-15 demonstrates that the S_0–T_1 ε_{3MLCT} value of the complex is proportional to the relevant S_0–S_1 ε_{MLCT} value. This is not strange since the phosphorescence transition probability of a molecule in the T_1 state is gained by mixing between S_1 and T_1 by spin–orbit coupling.[63] As reported by Nozaki *et al.*, the phosphorescence rate constant of a transition metal complex is predicted by eq. 2-8.[64]

$$k_r = \frac{16\pi \times 10^6 {E_{em}}^3 {D_s}^3}{3h\varepsilon_0} |\vec{\mu}_T|^2$$

(eq. 2-8)

In eq. 2-8, D_s is the refractive index of a medium, h is the Planck constant, and ε_0 is the permittivity in vacuum. Furthermore, the T_1–S_0 transition dipole moment ($\vec{\mu}_T$) can be estimated as a function of the relevant S_n–S_0 transition dipole moment ($\vec{\mu}_{S_n}$),

$$\vec{\mu}_T = \sum_n \frac{\langle \Psi_{T_1} | H_{SO} | \Psi_{S_n} \rangle}{E_{T_1} - E_{S_n}} \vec{\mu}_{S_n}$$

(eq. 2-9)

where Ψ_{T1} and Ψ_{Sn} (n = 1, 2, $\cdots n$) are the wavefunctions of the T_1 and S_n states having the eigenvalues of E_{T1} and E_{Sn}, respectively, and H_{SO} is the Hamiltonian for spin–orbit coupling. By assuming that the contribution of the S_n states (n > 2) can be neglected owing to the large E_{T1}–E_{Sn} gap(s), integration of eqs. 2-8 and 2-9 affords eq. 2-10.

$$k_{\mathrm{r}} = \frac{16\pi^3 \times 10^6 {E_{\mathrm{em}}}^3 {D_{\mathrm{s}}}^3}{3h\varepsilon_0} \left| \frac{\langle \Psi_{\mathrm{T}_1} | H_{\mathrm{SO}} | \Psi_{\mathrm{S}_1} \rangle}{\left| E_{\mathrm{T}_1} - E_{\mathrm{S}_1} \right|} \vec{\mu}_{\mathrm{S}_1} \right|^2$$

(eq. 2-10)

Since $\varepsilon_{\mathrm{MLCT}}$ is proportional to the square of the transition moment ($\varepsilon_{\mathrm{MLCT}} \propto \left|\vec{\mu}_{\mathrm{MLCT}}\right|^2$) and it can be assumed that the difference in the eigenvalues between the T_1 and S_1 states in eq. 2-10 is comparable with that in the MLCT emission–absorption energies difference ($|E_{\mathrm{em}} - E_{\mathrm{abs}}|$), eq. 2-10 is rewritten as in eq. 2-11.

$$k_{\mathrm{r}} \propto \frac{\varepsilon_{\mathrm{MLCT}} {E_{\mathrm{em}}}^3}{|E_{\mathrm{em}} - E_{\mathrm{abs}}|^2}$$

(eq. 2-11)

Figure 2-16 shows the relationship between k_{r} and $\varepsilon_{\mathrm{MLCT}} E_{\mathrm{em}} / |E_{\mathrm{em}} - E_{\mathrm{abs}}|^2$ for **2a–c**, **2a'–c'**, and $[\mathrm{Ru(X\text{-}bpy)_3}]^{2+}$. Although the correlation coefficient of the plot is not necessarily sufficient (r = 0.8694), Figure 2-16 demonstrates that the k_{r} values of the complexes are explained by the fundamental spectroscopic parameters (i.e., $\varepsilon_{\mathrm{MLCT}}$, E_{abs}, and E_{em}). It is worth noting that the data on **2a'**–**c'** fall moderately on the proportional regression line in Figure 2-16, while those do not fall on a single line in Figure 2-15. Since the E_{em} values of **2a'–c'** and **2a–c** are not very different, it is demonstrated that the $|E_{\mathrm{em}} - E_{\mathrm{abs}}|$ (i.e., ΔE_{ST}) and $\varepsilon_{\mathrm{MLCT}}$ values of the complexes determine primarily the k_{r} values, leading to the Strickler–Berg-type relation in Figure 2-15 or 2-16.

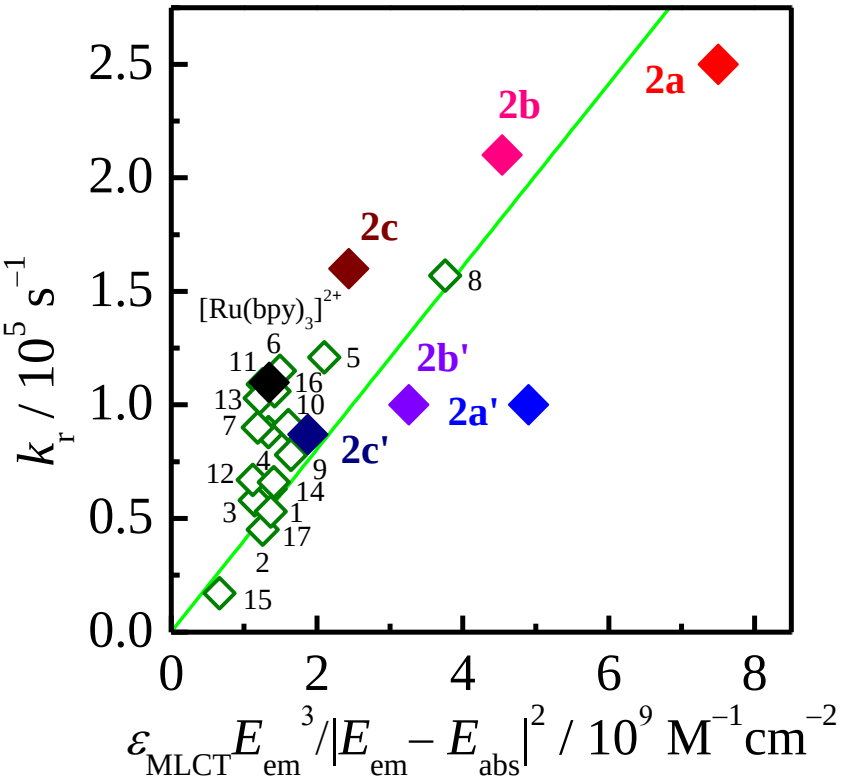

Figure. 2-16. Relationship between k_r and $\varepsilon_{MLCT}E_{em}{}^3/|E_{em} - E_{abs}|^2$ for the complexes in CH_3CN at 298 K. Green open boxes represent the data for a series of $[Ru(X\text{-}bpy)_3]^{2+}$ complexes (the numbers are identical to those in Figure 2-15) in EtOH–MeOH (4/1, v/v) at 293 K. The literature data were taken and converted from ref. [61,62]. The green line represents the linear regression, of which intercept has been fixed at 0 s^{-1}, for the data.

2-3-6: Zero-Magnetic-Field Splitting in Triplet Excited State

Although the emission from the triplet excited state of a transition metal complex is generally treated as a single-averaged photophysical process, the complex having a heavy metal atom experiences large spin–orbit coupling and, thereby, the emitting triplet excited state splits in energy to spin-sublevels by zero-magnetic-field splitting (ZFS).[63] Therefore, it is important to elucidate the contribution of ZFS to the emission from the arylborane–ruthenium(II) complexes. To determine the ZFS

parameters, *T*-dependences (*T* = 3.5–100 K) of the emission lifetimes of **2a** and $[Ru(bpy)_3]^{2+}$, which possessed O_h symmetry, were investigated. Figure 2-17 shows the emission decay profiles of the complexes in PEG-DMA550 polymerized films in 3.5–100 K.[27–30] Although the emission decay profile of $[Ru(bpy)_3]^{2+}$ was analyzed by a single-exponential function irrespective of *T*, that of **2a** was fitted by a double-exponential function. Since the long-lived emission component of **2a** was appeared only when the complex was introduced to a PEG-DMA550 film, the short-lived emission component of **2a** at given *T* was employed for the following analysis and discussions. As the *T*-dependences of the emission lifetimes of **2a** and $[Ru(bpy)_3]^{2+}$ in PEG-DMA550 films are shown in Figure 2-17, both **2a** and $[Ru(bpy)_3]^{2+}$ showed extremely long-lived emission at around 3.5 K, and the emission lifetimes decreased sharply upon *T*-elevation above 3.5 K. The contributions of the spin-sublevels are observed as an averaged lifetime ($\tau_{em}(T)$) and varied by varying *T* as in eq. 2-12.[65]

$$\tau_{em}(T) = \frac{1 + 2\exp\left(-\frac{\Delta E_2}{k_B T}\right) + \exp\left(-\frac{\Delta E_3}{k_B T}\right)}{\frac{1}{\tau_1} + \frac{2}{\tau_2}\exp\left(-\frac{\Delta E_2}{k_B T}\right) + \frac{1}{\tau_3}\exp\left(-\frac{\Delta E_3}{k_B T}\right)} \quad \text{(eq. 2-12)}$$

In eq. 2-12, τ_i is the emission lifetime of the individual spin-sublevel (i = 1, 2, or 3) in the emitting T_1 state, and ΔE_i is the energy difference between the lowest-energy spin-sublevel (i = 1) and upper-lying spin-sublevel i (2 or 3), which is given by eq. 2-13,[63]

$$E_{(i)} = E_{\mathrm{T}_1} + \sum_{n,j} \frac{\left|\left\langle \Psi_{\mathrm{T}_n(j)} \middle| H_{\mathrm{SO}} \middle| \Psi_{\mathrm{T}_1(i)} \right\rangle\right|^2}{E_{\mathrm{T}_1} - E_{\mathrm{T}_n}} + \sum_{m} \frac{\left|\left\langle \Psi_{S_m} \middle| H_{\mathrm{SO}} \middle| \Psi_{\mathrm{T}_1(i)} \right\rangle\right|^2}{E_{\mathrm{T}_1} - E_{\mathrm{S}_m}}$$

(eq. 2-13)

where $\Psi_{\mathrm{T}n(j)}$, $\Psi_{\mathrm{T}1(i)}$, and $\Psi_{\mathrm{S}m(i)}$ are the wavefunctions of $\mathrm{T}_n(j)$, $\mathrm{T}_1(i)$ and $\mathrm{S}_m(i)$ possessing the relevant non-perturbed energies $E_{\mathrm{T}n}$, $E_{\mathrm{T}1}$, and $E_{\mathrm{S}m}$, respectively. The *T*-dependences of the complexes were adequately analyzed by eq. 2-12 using the parameters (τ_i and ΔE_i) summarized in Table 2-12. The ZFS parameters of **2a** (ΔE_2 = 12 cm^{-1} and ΔE_3 = 67 cm^{-1}) were slightly smaller than those of $[Ru(bpy)_3]^{2+}$ (ΔE_2 = 14 cm^{-1} and ΔE_3 = 72 cm^{-1}). Although the third term in eq. 2-13 represents spin–orbit coupling for mixing between the singlet and triplet states as mentioned in the previous section, the second term in the equation is the most important on the ZES energy. Since the second term in eq. 2-13 represents spin–orbit coupling between $\mathrm{T}_{1(i)}$ and the energetically-proximity ^{3}MLCT excited states relating to a different d-orbital (T_n), the term dominates the ZFS energy when the ($E_{\mathrm{T}1} - E_{\mathrm{T}n}$) value is small.[63] Furthermore, there is no significant difference in the coordination geometry between **2a** and $[Ru(bpy)_3]^{2+}$ and, therefore, the ($E_{\mathrm{T}1} - E_{\mathrm{T}n}$) values of the complexes are presumably comparable. These expectations indicate that the spin–orbit coupling Hamiltonian (H_{SO}) term gives rise to the difference in ZFS between the complexes. Yersin *et al.* have reported that mixing of ^{3}LC characters with the ^{3}MLCT excited state decreases the ZFS energy in the triplet excited state of a transition metal complex.[63] As mentioned in the earlier section, theoretical calculations suggest that the ππ*(durylethynyl-bpy)/π(aryl)–p(B) CT contributes to the emitting states of **2a**–**c**, and this is expected to decrease the ZFS energy of **2a** due to the participation of the ππ*(durylethynyl-bpy)/π(aryl)–p(B) CT

characters. Although the differences in the ZFS energies between **2a** and $[Ru(bpy)_3]^{2+}$ are very small, the small ZFS energies of **2a** will be certainly advantageous for an increase in k_r of the complex through a larger contribution of the higher-energy-lying spin-sublevel(s) showing the faster radiative rate constant(s). In addition, the intrinsic lifetimes of the spin-sublevels (τ_1, τ_2 and τ_3) are shorter than those of $[Ru(bpy)_3]^{2+}$ owing to the large k_r values as mentioned in the previous section. As the results of the small ZFS energies and the accelerated radiative processes from the spin-sublevels in the emitting excited state, **2a** shows a large k_r value even at room temperature.

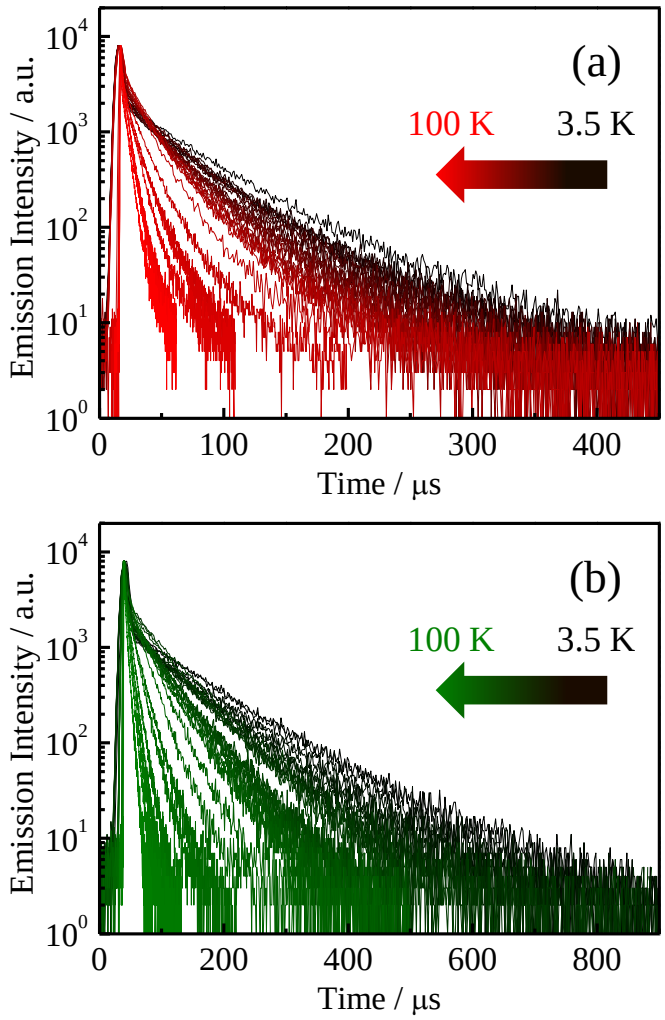

Figure 2-17. *T*-dependences (T = 3.5–100 K) of the emission decay profiles of **2a** (a) and $[Ru(bpy)_3]^{2+}$ (b) in PEG-DMA550 polymerized films.

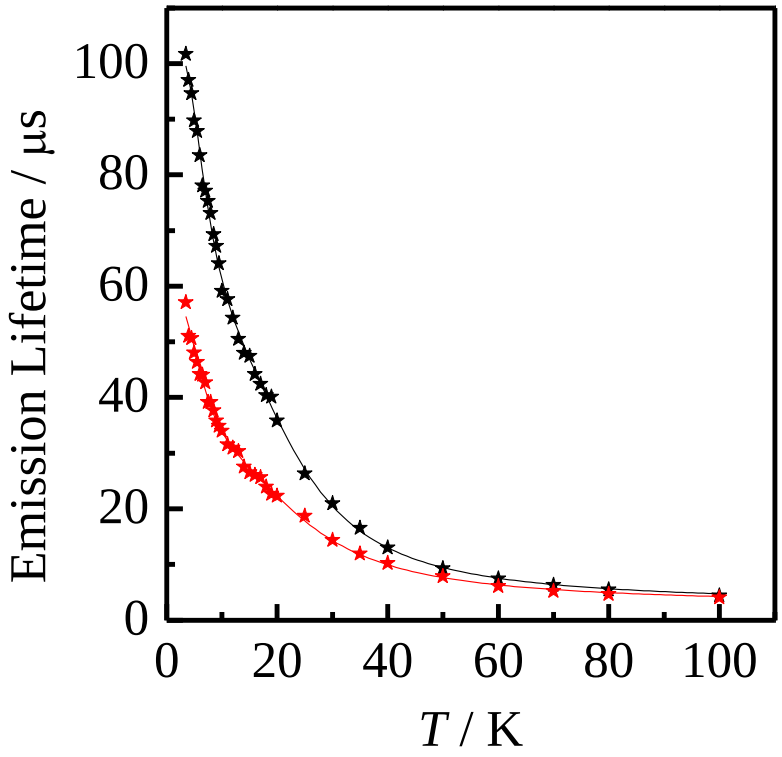

Figure 2-18. *T*-dependences (T = 3.5–100 K) of the emission lifetimes of **2a** (red) and $[Ru(bpy)_3]^{2+}$ (black) in PEG-DMA550 polymerized films. The solid curves represent the best fits of the observed data by eq. 2-12 using the parameters listed in Table 2-12.

Table 2-12. The spin-sublevel parameters of **2a** and $[Ru(bpy)_3]^{2+}$ in PEG-DMA550 films.

Complex	(τ_1)	ΔE_2 / cm^{-1} (τ_2)	ΔE_3 / cm^{-1} (τ_3)
2a	(56.6 μs)	12 (16.1 μs)	67 (0.64 μs)
$[Ru(bpy)_3]^{2+}$	(102 μs)	14 (25.1 μs)	72 (0.64 μs)

2-4: Conclusions

In this chapter, the synthesis and the electrochemical, spectroscopic, and photophysical properties of a series of the novel $[Ru(bpy)_3]^{2+}$ derivatives having multiple arylborane units ($[Ru(B_2bpy)_n(bpy)_{3-n}]^{2+}$ (**2a**: n = 3, **2b**: n = 2, **2c**: n = 1) and $[Ru(Bbpy)_n(bpy)_{3-n}]^{2+}$ (**2a'**: n = 3, **2b'**: n = 2, **2c'**: n = 1)) are described. The complexes, **2a**–**c** and **2a'**–**c'**, showed intense absorption in 290–600 nm, and the ε value of the MLCT absorption band (ε_{MLCT}) of the complex was enhanced largely by the introduction of a DBDE group(s) to the bpy ligand(s) of the complex, owing to the synergistic MLCT/π(aryl)–p(B) CT interactions. Furthermore, **2a**–**c** and **2a'**–**c'** also showed intense emission with the quantum yield (Φ_{em}) > 0.20, and the Φ_{em} value increased with an increase in n for both **2a**–**c** and **2a'**–**c'** series. In particular, **2a** showed extremely intense emission with Φ_{em} = 0.43. One of the important findings of the study is the increase in the ε_{MLCT} values of **2a**–**c** and **2a'**–**c'** with that in n, and the increase in ε_{MLCT} of the complex brings about an increase in k_r as seen in Figure 2-15. The positive correlations between k_r and ε_{MLCT} observed for **2a**–**c** and **2a'**–**c'** resemble with the Strickler–Berg relation for the fluorescence transition of a molecule. Reflecting mixing between the S_1 and T_1 states by spin–orbit coupling, it is demonstrated that the $|E_{em} - E_{abs}|$ and ε_{MLCT} values of the complex determine primarily the k_r value, leading to the Strickler–Berg-type relation between k_r and ε_{MLCT}. These results are essentially due to the synergistic MLCT/π(aryl)–p(B) CT interactions in the emitting excited states of **2a**–**c** and **2a'**–**c'**, as demonstrated by the electrochemical, spectroscopic/photophysical, and TD-DFT calculation studies. Thus, this study successfully demonstrated synthetic control/tuning of the electrochemical, spectroscopic, and photophysical properties of a $[Ru(bpy)_3]^{2+}$ derivative on the basis of

a triarylborane-appended π-chromophoric ligand(s).

2-5: References

[1] Sakuda, E.; Funahashi, A.; Kitamura, N. Synthesis and Spectroscopic Properties of Platinum(II) Terpyridine Complexes Having an Arylborane Charge Transfer Unit. *Inorg*. *Chem*. **2006**, *45*, 10670–10677.

[2] Sakuda, E.; Ando, Y.; Ito, A.; Kitamura, N. Long-Lived and Temperature-Independent Emission from a Novel Ruthenium(II) Complex Having an Arylborane Charge-Transfer Unit. *Inorg*. *Chem*. **2011**, *50*, 1603–1613

[3] Ito, A.; Hirokawa, T.; Sakuda, E.; Kitamura, N. Bright Green-Phosphorescence from Metal-to-Boron Charge-Transfer Excited State of a Novel Cyclometalated Iridium(III) Complex. *Chem*. *Lett*. **2011**, *40*, 34–36.

[4] Ito, A.; Kang, Y.; Sakuda, E.; Kitamura, N. Photophysical and Photoredox Characteristics of a Novel Tricarbonyl Rhenium(I) Complex Having an Arylborane-Appended Aromatic Diimine Ligand. *Inorg*. *Chem*. **2012**, *51*, 7722–7732.

[5] Kang, Y.; Ito, A.; Sakuda, E.; Kitamura, N. Diimine Ligand Structure Effects on Photophysical Properties of Tricarbonyl Rhenium(I) Complexes Having Arylborane Charge Transfer Units. *J*. *Photochem*. *Photobiol*. *A: Chem*. **2015**, *313*, 107–116.

[6] Kang, Y.; Ito, A.; Sakuda, E.; Kitamura, N. Characteristic Spectroscopic and Photophysical Properties of Tricarbonyl Rhenium(I) Complexes Having Multiple Arylborane Charge Transfer Units. *Bull. Chem. Soc. Jpn.* **2017**, *90*, 574–585.

[7] Sun, Y.; Ross, N.; Zhao, S.–B.; Huszarik, K.; Jia, W.–L.; Wang, R.–Y.;

Macartney, D.; Wang, S. Enhancing Electron Accepting Ability of Triarylboron via π-Conjugation with 2,2'-Bipy and Metal Chelation: 5,5'-Bis($BMes_2$)-2,2'-bipy and Its Metal Complexes. *J. Am. Chem. Soc.* **2007**, *129*, 7510–7511.

[8] Zhao, S.–B.; McCormick, T.; Wang, S. Ambient-Temperature Metal-to-Ligand Charge-Transfer Phosphorescence Facilitated by Triarylboron: Bnpa and Its Metal Complexes. *Inorg. Chem.* **2007**, *46*, 10965–10967.

[9] Sun, Y.; Wang, S. Conjugated Triarylboryl Donor–Acceptor Systems Supported by 2,2'-Bipyridine: Metal Chelation Impact on Intraligand Charger Transfer Emission, Electron Accepting Ability, and "Turn-on" Fluoride Sensing. *Inorg. Chem.* **2009**, *48*, 3755–3767.

[10] Hudson, Z. M.; Zhao, S.–B.; Wang, R. Y.; Wang, S. Switchable Ambient-Temperature Singlet-Triplet Dual Emission in Nonconjugated Donor-Acceptor Triarylboron-Pt Complexes. *Chem.–Eur. J.* **2009**, *15*, 6131–6137.

[11] Rao, Y.–L.; Wang, S. Impact of Constitutional Isomers of ($BMes_2$)phenylpyridine on Structure, Stability, Phosphorescence, and Lewis Acidity of Mononuclear and Dinuclear Pt(II) Complexes. *Inorg. Chem.* **2009**, *48*, 7698–7713.

[12] Sun, Y.; Wang, S. Extending π-Conjugation of Triarylborons with a 2,2-Bpy Core: Impact of Donor−Acceptor Geometry on Luminescence, Anion Sensing, and Metal Ion Binding *Inorg. Chem.* **2010**, *49*, 4394–4404.

[13] Zhou, G.; Ho, C.–L.; Wong, W.–Y.; Wang, Q.; Ma, D.; Wang, L.; Lin, Z.; Marder, T. B.; Beeby, A. Manipulating Charge-Transfer Character with

Electron-Withdrawing Main-Group Moieties for the Color Tuning of Iridium Electrophosphors. *Adv. Funct. Mater.* **2008**, *18*, 499–511.

[14] You, Y.; Park, S. Y. A Phosphorescent Ir(III) Complex for Selective Fluoride Ion Sensing with a High Signal-to-Noise Ratio. *Adv. Mater.* **2008**, *20*, 3820–3826.

[15] Zhao, Q.; Li, F.; Liu, S.; Yu, M.; Liu, Z.; Yi, T.; Huang, C. Highly Selective Phosphorescent Chemosensor for Fluoride Based on an Iridium(III) Complex Containing Arylborane Units. *Inorg. Chem.* **2008**, *47*, 9256–9264.

[16] Lin, W.; Tan, Q.; Liang, H.; Zhang, K. Y. Liu, S.; Jiang, R.; Hu, R.; Xu, W.; Zhao, Q.; Huang, W. Phosphorescence Switch and Logic Gate of Iridium(III) Complexes Containing a Triarylboron Moiety Triggered by Fluoride and an Electric Field. *J. Mater. Chem. C* **2015**, *3*, 1883–1887.

[17] Wade, C. R.; Gabbaï, F. P. Cyanide Anion Binding by a Triarylborane at the Outer Rim of a Cyclometalated Ruthenium(II) Cationic Complex. *Inorg. Chem.* **2010**, *49*, 714–720.

[18] Sun, Y.; Hudson, Z. M. Rao, Y.; Wang, S. Tuning and Switching MLCT Phosphorescence of $[Ru(bpy)_3]^{2+}$ Complexes with Triarylboranes and Anions *Inorg. Chem.* **2011**, *50*, 3373–3378.

[19] Smith, L. F.; Blight, B. A.; Park, H.–J.; Wang, S. Sensitizing Tb(III) and Eu(III) Emission with Triarylboron Functionalized 1,3-Diketonato Ligands. *Inorg. Chem.* **2014**, *53*, 8036–8044.

[20] Park, H.–J.; Ko, S.–B.; Wyman, I. W.; Wang, S. Selective Sensitization of Eu(III) and Tb(III) Emission with Triarylboron-Functionalized Dipicolinic Acids. *Inorg. Chem.* **2014**, *53*, 9751–9760.

[21] Doi, T.; Nagamiya, H.; Kokubo, M.; Hirabayashi, K.; Takahashi, T. Synthesis of

a Tetrabenzyl-Substituted 10-Membered Cyclic Diamide. *Tetrahedron* **2002**, *58*, 2957–2963.

[22] Kent, C. A.; Liu, D.; Ma, L.; Papanikolas, J. M.; Meyer, T. J.; Lin, W. Light Harvesting in Microscale Metal–Organic Frameworks by Energy Migration and Interfacial Electron Transfer Quenching. *J. Am. Chem. Soc.* **2011**, *133*, 12940–12943.

[23] Slattery, S. J.; Gokalda, N.; Mick, T.; Goldsby, K. A. Bis(4,4'-bis(diethylamino)-2,2'-bipyridine)dichlororuthenium(III): A New Starting Material for Ruthenium Polypyridyl Complexes Exhibiting Low Redox Potentials. *Inorg. Chem.* **1994**, *33*, 3621–3624.

[24] Suzuki, K.; Kobayashi, A.; Kaneko, S.; Takehira, K.; Yoshihara, T.; Ishida, H.; Shiina, Y.; Oishi, S.; Tobita, S. Reevaluation of Absolute Luminescence Quantum Yields of Standard Solutions Using a Spectrometer with an Integrating Sphere and a Back-Thinned CCD Detector. *Phys. Chem. Chem. Phys.* **2009**, *11*, 9850–9860.

[25] Ishida, H.; Tobita, S.; Hasegawa, Y.; Katoh R.; Nozaki, K. Recent Advances in Instrumentation for Absolute Emission Quantum Yield Measurements. *Coord. Chem. Rev.* **2010**, *254*, 2449–2458.

[26] Perrin, D. D.; Armarego, W. L. F.; Perrin, D. R. *Purification of Laboratory Chemicals, 2nd ed.*, Pergamon Press, Oxford, **1980**.

[27] Knight, T. E.; Goldstein, A. P.; Brennaman, M. K.; Cardolaccia, T.; Pandya, A.; DeSimone, J. M.; Meyer, T. J. Influence of the Fluid-to-Film Transition on Photophysical Properties of MLCT Excited States in a Polymerizable Dimethacrylate Fluid. *J. Phys. Chem. B* **2011**, *115*, 64–70.

[28] Ito, A.; Stewart, D. J.; Knight, T. E.; Fang, Z.; Brennaman, M. K.; Meyer, T. J. Excited-State Dynamics in Rigid Media: Evidence for Long-Range Energy Transfer. *J. Phys. Chem. B* **2013**, *117*, 3428–3438.

[29] Ito, A.; Fang, Z.; Brennaman, M. K.; Meyer, T. J. Long-Range Photoinduced Electron Transfer Dynamics in Rigid Media. *Phys. Chem. Chem. Phys.* **2014**, *16*, 4880–4891.

[30] Ito, A.; Knight, T. E.; Stewart, D. J.; Brennaman, M. K.; Meyer, T. J. Rigid Medium Effects on Photophysical Properties of MLCT Excited States of Polypyridyl Os(II) Complexes in Polymerized Poly(ethylene glycol)dimethacrylate Monoliths. *J. Phys. Chem. A* **2014**, *118*, 10326–10332.

[31] Frisch, M. J.; Trucks, G. W.; Schlegel, H. B.; Scuseria, G. E.; Robb, M. A.; Cheeseman, J. R.; Scalmani, G.; Barone, V.; Mennucci, B.; Petersson, G. A.; Nakatsuji, H.; Caricato, M.; Li, X.; Hratchian, H. P.; Izmaylov, A. F.; Bloino, J.; Zheng, G.; Sonnenberg, J. L.; Hada, M.; Ehara, M.; Toyota, K.; Fukuda, R.; Hasegawa, J.; Ishida, M.; Nakajima, T.; Honda, Y.; Kitao, O.; Nakai, H.; Vreven, T.; Montgomery, J. A., Jr.; Peralta, J. E.; Ogliaro, F.; Bearpark, M.; Heyd, J. J.; Brothers, E.; Kudin, K. N.; Staroverov, V. N.; Kobayashi, R.; Normand, J.; Raghavachari, K.; Rendell, A.; Burant, J. C.; Iyengar, S. S.; Tomasi, J.; Cossi, M.; Rega, N.; Millam, M. J.; Klene, M.; Knox, J. E.; Cross, J. B.; Bakken, V.; Adamo, C.; Jaramillo, J.; Gomperts, R.; Stratmann, R. E.; Yazyev, O.; Austin, A. J.; Cammi, R.; Pomelli, C.; Ochterski, J. W.; Martin, R. L.; Morokuma, K.; Zakrzewski, V. G.; Voth, G. A.; Salvador, P.; Dannenberg, J. J.; Dapprich, S.; Daniels, A. D.; Farkas, Ö.; Foresman, J. B.; Ortiz, J. V.; Cioslowski, J.; Fox, D. J. *Gaussian 09, Revision A.02*, Gaussian, Inc.: Wallingford, CT, **2009**.

[32] Frisch, M. J.; Trucks, G. W.; Schlegel, H. B.; Scuseria, G. E.; Robb, M. A.; Cheeseman, J. R.; Scalmani, G.; Barone, V.; Petersson, G. A.; Nakatsuji, H.; Li, X.; Caricato, M.; Marenich, A. V.; Bloino, J.; Janesko, B. G.; Gomperts, R.; Mennucci, B.; Hratchian, H. P.; Ortiz, J. V.; Izmaylov, A. F.; Sonnenberg, J. L.; Williams-Young, D.; Ding, F.; Lipparini, F.; Egidi, F.; Goings, J.; Peng, B.; Petrone, A.; Henderson, T.; Ranasinghe, D.; Zakrzewski, V. G.; Gao, J.; Rega, N.; Zheng, G.; Liang, W.; Hada, M.; Ehara, M.; Toyota, K.; Fukuda, R.; Hasegawa, J.; Ishida, M.; Nakajima, T.; Honda, Y.; Kitao, O.; Nakai, H.; Vreven, T.; Throssell, K.; Montgomery, J. A., Jr.; Peralta, J. E.; Ogliaro, F.; Bearpark, M. J.; Heyd, J. J.; Brothers, E. N.; Kudin, K. N.; Staroverov, V. N.; Keith, T. A.; Kobayashi, R.; Normand, J.; Raghavachari, K.; Rendell, A. P.; Burant, J. C.; Iyengar, S. S.; Tomasi, J.; Cossi, M.; Millam, J. M.; Klene, M.; Adamo, C.; Cammi, R.; Ochterski, J. W.; Martin, R. L.; Morokuma, K.; Farkas, O.; Foresman, J. B.; Fox, D. J. *Gaussian 16, Revision A.03*, Gaussian, Inc.: Wallingford, CT, **2016**.

[33] Becke, A. D. Density-Functional Thermochemistry. III. The Role of Exact Exchange. *J. Chem. Phys.* **1993**, *98*, 5648–5652.

[34] Lee, C.; Yang, W.; Parr, R. G. Development of the Colle-Salvetti Correlation-Energy Formula into a Functional of the Electron Density. *Phys. Rev. B* **1988**, *37*, 785–789.

[35] Hay, P. J.; Wadt, W. R. *Ab initio* Effective Core Potentials for Molecular Calculations. Potentials for K to Au Including the Outermost Core Orbitals. *J. Chem. Phys.* **1985**, *82*, 299–310.

[36] Petersson, G. A.; Al-Laham, M. A. A Complete Basis Set Model Chemistry. III.

The Complete Basis Set-Quadratic Configuration Interaction Family of Methods. *J. Chem. Phys*. **1991**, *94*, 6081–6090.

[37] Dennington, R.; Keith, T.; Millam, J. *GaussView, Version 5*, Semichem Inc: Shawnee Mission KS, **2009**.

[38] Dennington, R.; Keith, T.; Millam, J. *GaussView, Version 6*, Semichem Inc: Shawnee Mission KS, **2016**.

[39] Kober, E. M.; Caspar, J. V.; Lumpkin, R. S.; Meyer, T. J. Application of the Energy Gap Law to Excited-State Decay of Osmium(II)-Polypyridine Complexes: Calculation of Relative Nonradiative Decay Rates from Emission Spectral Profiles. *J. Phys. Chem*. **1986**, *90*, 3722–3734.

[40] Kestell, J. D.; Williams, Z. L.; Stultz, L. K.; Claude, J. P. Medium Dependence of Intramolecular Vibrational Modes Coupled to MLCT Transitions in Metal Polypyridyl Complexes. *J. Phys. Chem. A* **2002**, *106*, 5768–5778.

[41] Huang, K.; Rhys, A. Theory of Light Absorption and Non-Radiative Transitions in *F*-Centres. *Proc. R. Soc. London, Ser. A* **1950**, *204*, 406–423.

[42] Allen, G. H.; White, R. P.; Rillema, D. P.; Meyer, T. J. Synthetic Control of Excited-State Properties. Tris-Chelate Complexes Containing the Ligands 2,2'-Bipyrazine, 2,2'-Bipyridine, and 2,2'-Bipyrimidine. *J. Am. Chem. Soc*. **1984**, *106*, 2613–2620.

[43] Fylstra, D.; Lasdon, L.; Watson, J.; Waren, A. Design and Use of the Microsoft Excel Solver. *Interfaces*, **1998**, *28*, 29–55.

[44] Thompson, D.W.; Ito, A.; Meyer. T. J. $[Ru(bpy)_3]^{2+}$* and Other Remarkable Metal-to-Ligand Charge Transfer (MLCT) Excited States. *Pure Appl. Chem.* **2013**, 85, 1257–1305.

[45] Ito, A.; Meyer, T. J. The Golden Rule. Application for Fun and Profit in Electron Transfer, Energy Transfer, and Excited-State Decay. *Phys. Chem. Chem. Phys.* **2012**, *14*, 13731–13745.

[46] Tahara, K.; Akita, T.; Katao, S.; Kikuchi, J. Construction of Di- and Tetra-Ferrocenyl Spiroborate Complexes from Catechol Building Blocks and their Redox Behaviors. *Dalton Trans.* **2014**, *43*, 1368–1379.

[47] Kawanishi, Y.; Kitamura, N.; Tazuke, S. Dependence of Spectroscopic, Electrochemical, and Excited-State Properties of Tris Chelate Ruthenium(II) Complexes on Ligand Structure. *Inorg. Chem.* **1989**, *28*, 2968–2975.

[48] Yamaguchi, S.; Akiyama, S.; Tamao, K. Tri-9-anthrylborane and Its Derivatives: New Boron-Containing π-Electron Systems with Divergently Extended π-Conjugation through Boron. *J. Am. Chem. Soc.* **2000**, *122*, 6335–6336.

[49] Sakuda, E. Spectroscopic and Photophysical Studies on Triarylborane Derivatives. *Ph. D Thesis*, Hokkaido University, **2008**.

[50] e. g.: Montalti, M.; Credi, A.; Prodi, L.; Teresa, M. *Handbook of Photochemistry, 3rd ed.*, CRC Press, Boca Raton, **2006**.

[51] Caspar, J. V.; Meyer, T. J. Photochemistry of $Ru(bpy)_3^{2+}$. Solvent Effects. *J. Am. Chem. Soc.* **1983**, *105*, 5583–5590.

[52] Caspar, J. V.; Meyer, T. J. Photochemistry of MLCT Excited States. Effect of Nonchromophoric Ligand Variations on Photophysical Properties in the Series *cis*-$Ru(bpy)_2L_2^{2+}$. *Inorg. Chem.* **1983**, *22*, 2444–2453.

[53] Kober, E. M.; Sullivan, B. P.; Dressick, W. J.; Caspar, J. V.; Meyer, T. J. Highly Luminescent Polypyridyl Complexes of Osmium(II). *J. Am. Chem. Soc.* **1980**,

102, 7383–7385.

[54] Caspar, J. V.; Meyer, T. J. Application of the Energy Gap Law to Nonradiative, Excited-State Decay. *J. Phys. Chem.* **1983**, *87*, 952–957.

[55] Treadway, J. A.; Loeb, B.; Lopez, R.; Anderson, P. A.; Keene, F. R.; Meyer, T. J. Effect of Delocalization and Rigidity in the Acceptor Ligand on MLCT Excited-State Decay. *Inorg. Chem.* **1996**, *35*, 2242–2246.

[56] Van Houten, J.; Watts, R. J. Temperature Dependence of the Photophysical and Photochemical Properties of the Tris(2,2'-bipyridyl)ruthenium(II) Ion in Aqueous Solution. *J. Am. Chem. Soc.* **1976**, *98*, 4853–4858.

[57] Kober, E. M.; Meyer, T. J. An Electronic Structural Model for the Emitting MLCT Excited States of $Ru(bpy)_3^{2+}$ and $Os(bpy)_3^{2+}$. *Inorg. Chem.* **1984**, *23*, 3877–3886.

[58] Lumpkin, R. S.; Kober, E. M.; Worl, L. A.; Murtaza, Z.; Meyer, T. J. Metal-to-Ligand Charge-Transfer (MLCT) Photochemistry: Experimental Evidence for the Participation of a Higher Lying MLCT State in Polypyridyl Complexes of Ruthenium(II) and Osmium(II). *J. Phys. Chem.* **1990**, *94*, 239–243.

[59] Taheri, A.; Meyer, G. J. Temperature Dependent Iodide Oxidation by MLCT Excited States *Dalton Trans.* **2014**, *43*, 17856–17863.

[60] Strickler, S. J.; Berg, R. A. Relationship between Absorption Intensity and Fluorescence Lifetime of Molecules. *J. Chem. Phys.* **1962**, *37*, 814–822.

[61] Cook, M. J.; Lewis, A. P. McAuliffe, G. S. G; Skarda, V.; Thomson, A. J. Luminescent Metal Complexes. Part 1. Tris-chelates of Substituted 2,2'-Bipyridyls with Ruthenium(II) as Dyes for Luminescent Solar Collectors. *J.*

Chem. *Soc*. *Perkin Trans*. *2* **1984**, 1293–1301.

[62] Cook, M. J.; Lewis, A. P. McAuliffe, G. S. G; Skarda, V.; Thomson, A. J. A Model for the Luminescence Properties of the Tris-Chelates of Substituted 2.2'-Bipyridyls with Ruthenium(II). *J*. *Chem*. *Soc*. *Perkin Trans*. *2* **1984**, 1303–1307.

[63] Yersin, H.; Rausch, A. F.; Czerwieniec, R.; Hofbeck, T.; Fischer, T. The Triplet State of Organo-Transition Metal Compounds. Triplet Harvesting and Singlet Harvesting for Efficient OLEDs. *Coord*. *Chem*. *Rev*. **2011**, *255*, 2622–2652.

[64] Obara, S.; Itabashi, M.; Okuda, F.; Tamaki, S.; Tanabe, Y.; Ishii, Y.; Nozaki, K.; Haga, M. Highly Phosphorescent Iridium Complexes Containing Both Tridentate Bis(benzimidazolyl)-benzene or -pyridine and Bidentate Phenylpyridine: Synthesis, Photophysical Properties, and Theoretical Study of Ir-bis(benzimidazolyl)phenyl Complex. *Inorg. Chem.* **2006**, *45*, 8907–8921.

[65] Harrigan, R. W.; Crosby, G. A. Symmetry Assignments of the Lowest CT Excited States of Ruthenium (II) Complexes via a Proposed Electronic Coupling Model. *J. Chem. Phys.* **1973**, *59*, 3468–3476.

Chapter 3: Ligand-Structure Effects on the Spectroscopic and Photophysical Properties of Homoleptic Ruthenium(II) Complexes Having Arylborane-Appended Diimine Ligands: 2,2'-Bipyridine vs. 1,10-Phenanthroline

3-1: Introduction

As described in Chapter 2, a series of $[Ru(bpy)_3]^{2+}$ (bpy = 2,2'-bipyridine) derivatives having a DBDE ((dimesityl)borylduryletheynyl) group(s) at the 4- or 4,4'-position(s) of the bpy ligand(s), ($[Ru(Bbpy)_n(bpy)_{3-n}]^{2+}$ (**2a'**–**c'**) or $[Ru(B_2bpy)_n(bpy)_{3-n}]^{2+}$ (**2a**–**c**), respectively) shows intense absorption/emission in the visible region due to the synergistic interactions[1–6] between MLCT and π(aryl)–p(B) CT.[7–15] Furthermore, it has been demonstrated that the synergistic MLCT/π(aryl)–p(B) CT absorption/emission of the complex can enhance the emission quantum yield (Φ_{em}) successively with increasing the number of an arylborane-substituted ligand (*n*) and, in particular, $[Ru(B_2bpy)_3]^{2+}$ (**2a**) shows a remarkably high Φ_{em} with 0.43 in CH_3CN at 298 K. Therefore, a class of homoleptic arylborane–ruthenium(II) complexes possessing a starburst-type structure is a possible candidate for future photofunctional materials. On the other hand, it has been reported that an introduction of a DBDE group at the 4-position of a 1,10-phenanthroline (phen) ligand in $[Ru(phen)_3]^{2+}$ extensively elongates the emission lifetime (τ_{em}) of the complex: τ_{em} = 12 and 0.42 μs for 4RuB ($[Ru(Bphen)(phen)_2]^{2+}$) and $[Ru(phen)_3]^{2+}$, respectively.[2] Such elongation of the excited-state lifetime has not been observed for the $[Ru(bpy)_3]^{2+}$-based complexes (e.g., τ_{em} = 1.7 μs for **2a**–**c**) and, therefore, further understandings of the photophysical behaviors of the arylborane–ruthenium(II)

complexes are absolutely necessary. There is no doubt that a diimine-ligand structure as the core of $[RuL_3]^{2+}$ moiety plays an important role in characterizing the arylborane effects on the spectroscopic/photophysical properties of the complex. Nonetheless, the detailed information on diimine-structure effects has not been obtained in the earlier studies since the asymmetric environment around the coordination sphere in the heteroleptic complex, 4RuB, also affects its spectroscopic and photophysical characteristics.

In this chapter, the spectroscopic and photophysical properties of a novel homoleptic ruthenium(II) complex having two DBDE groups at the 4- and 7-positions of each phen ligand in $[Ru(phen)_3]^{2+}$ ($[Ru(B_2phen)_3]^{2+}$: **3a**, Chart 3-1) are discussed focusing on the diimine-ligand structure effects on the properties by comparing the data with those of **2a**.

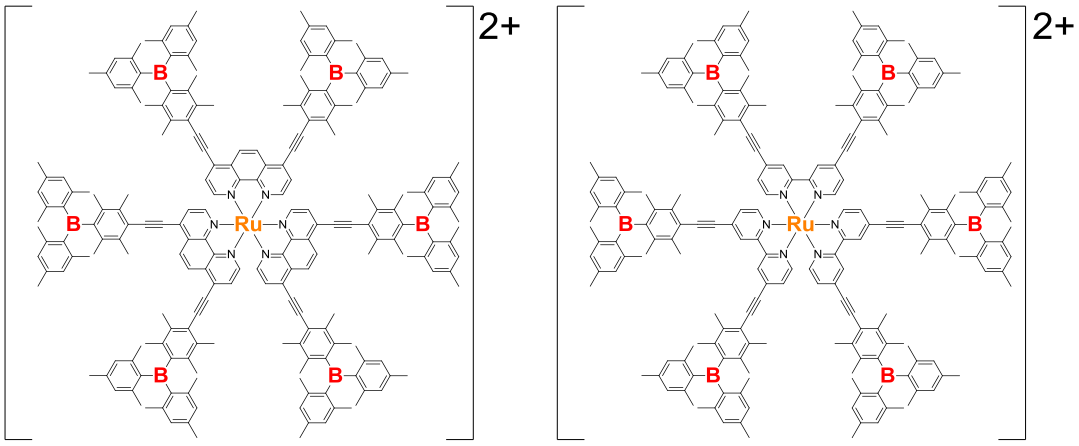

3a **2a**

Chart 3-1. Chemical structures of **3a** and **2a**.

3-2: Experiments and Methodologies

3-2-1: Synthesis

The synthetic route to **3a** is shown in Scheme 3-1. The complex was successfully synthesized as a PF_6^- salt similar to the synthetic procedures for **2a** described in Chapter 2. Although the reaction between $RuCl_3 \cdot nH_2O$ and 4,7-dibromo-1,10-phenanthroline (4,7-Br_2-phen) in ethylene glycol under microwave irradiation by using a microwave synthesizer (EYELA, Wave Magic® MWO-1000S) gave a mixture of $[Ru(4,7\text{-}Br_2\text{-}phen)_3]^{2+}$ and $[Ru(4,7\text{-}Br/Cl\text{-}phen)_3]^{2+}$ with the latter complex being produced by the reaction of 4,7-Br_2-phen and/or $[Ru(4,7\text{-}Br_2\text{-}phen)_3]^{2+}$ with a liberated Cl atom(s) from $RuCl_3 \cdot nH_2O$, the mixture was used for the next step without separation of the products. The spectroscopic and photophysical purity of **3a** was confirmed by single-exponential emission decay in CH_3CN at 298 K in addition to the typical characterization methods described in Chapter 2. 4,7-Dihydroxy-1,10-phenanthroline was prepared according to the literature,[16] and other chemicals used for the synthesis of **3a** were essentially the same with those described in Chapter 2.

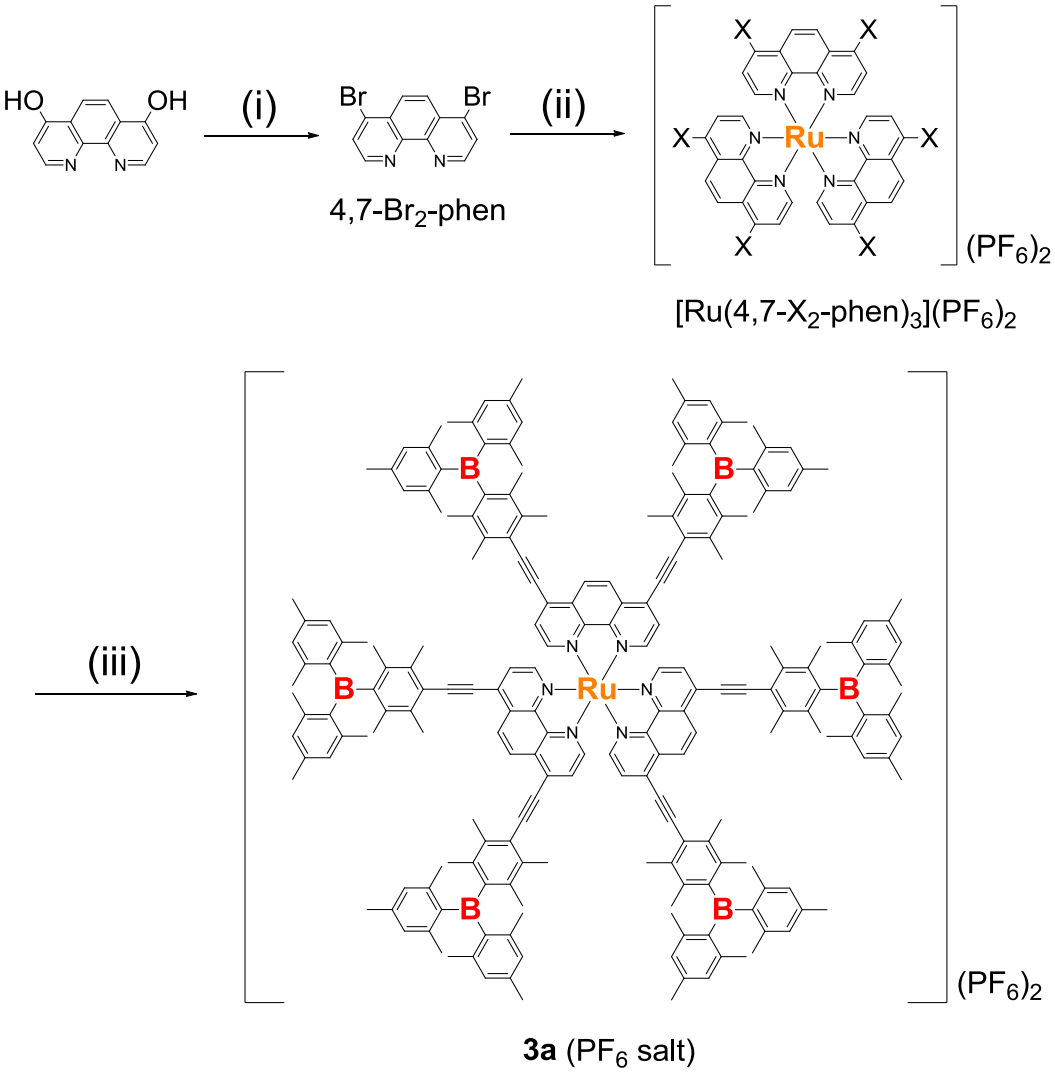

Scheme 3-1. Synthetic route to the PF_6^- salt of **3a**: (i) PBr_3, *N*,*N*-dimethylformamide (DMF), RT, 1 h; (ii) $RuCl_3 \cdot nH_2O$, ethylene glycol, microwave (200 W), 5 min; (iii) (ethynylduryl)dimesitylborane (EDDB), $Pd(PPh_3)_2Cl_2$, CuI, NEt_3, CH_3CN/THF, 50°C, 4 h.

Synthesis of 4,7-Dibromo-1,10-phenathroline (4,7-Br_2-phen). To a suspension of 4,7-dihydroxy-1,10-phenanthroline (500 mg, 1.48 mmol) in *N*,*N*-dimethylformamide (DMF) (150 mL), phosphorous tribromide (15 mL, 160 mmol) was added slowly. After stirring at room temperature for 1 h, a 4-M KOH(aq) solution was added to the reaction mixture to adjust pH~13. The solution was extracted with $CHCl_3$ (200 mL × 3) and,

then, the combined organic phase was dried over anhydrous $MgSO_4$ and concentrated under reduced pressure. The crude product was purified by column chromatography (Al_2O_3, $CHCl_3$, R_f = 0.57) and recrystallization from $CHCl_3$/*n*-hexane (1/1, v/v), giving 4,7-Br_2-phen as light-yellow powders (250 mg, 31%). ^{1}H NMR (270 MHz, $CDCl_3$, TMS): δ/ppm 8.98 (2H, d, J = 4.7 Hz, 2,9-Ar-H), 8.33 (2H, s, 5,6-Ar-H), 7.96 (2H, d, J = 4.7 Hz, 3,8-Ar-H). MS (ESI) m/z 338.8 (calcd for $[M]^+$ ($C_{12}H_6N_6Br_2$): 338.9).

Synthesis of Tris(4,7-dihalogeno-1,10-phenanthroline)ruthenium(II) Bis(hexafluorophosphate) ([Ru(4,7-X_2-phen)$_3$]$(PF_6)_2$, X = Br and/or Cl). A suspension of $RuCl_3 \cdot nH_2O$ (22 mg, 0.084 mmol) and 4,7-Br_2-phen (110 mg, 0.33 mmol) in ethylene glycol (10 mL) was irradiated by microwave (2450 MHz, 200 W) for 5 min under nitrogen-gas atmosphere. After cooling the mixture to room temperature, an excess amount of an NH_4PF_6(aq) solution was added. The resulting precipitates were collected by filtration and purified by column chromatography (Al_2O_3, CH_3CN/$CHCl_3$ (1/1, v/v)). The crude product was dissolved in a minimum amount of acetone and, then, an excess amount of *n*-hexane was added dropwise to the solution, giving [Ru(4,7-X_2-phen)$_3$]$(PF_6)_2$ (X = Br and/or Cl) as red powders (80 mg). ^{1}H NMR (270 MHz, CD_3CN, TMS): δ/ppm 8.64–8.53 (6H, *m*, 2,9-Ar-H), 8.03–7.91 (6H, *m*, 5,6-Ar-H), 7.90–7.73 (6H, *m*, 3,8-Ar-H). MS (ESI) m/z 557.7(34), 535.7(85), 513.4(100), 490.7(78), 468.9(61), 445.9(53), 423.9(45) (calcd for $[M–2PF_6]^{2+}$ ($C_{36}H_{18}N_6Br_6Ru$, $C_{36}H_{18}N_6Br_5ClRu$, $C_{36}H_{18}N_6Br_4Cl_2Ru$, $C_{36}H_{18}N_6Br_3Cl_3Ru$, $C_{36}H_{18}N_6Br_2Cl_4Ru$, $C_{36}H_{18}N_6BrCl_5Ru$, $C_{36}H_{18}N_6Cl_6Ru$): 557.5, 535.3, 513.1, 490.9, 468.6, 446.4, 424.2).

Synthesis of Tris[4,7-bis{(dimesitylboryl)durylethynyl}-1,10-phenanthroline]-

ruthenium(II) Bis(hexafluorophosphate) (3a(PF_6)$_2$). An oven-dried Schlenk tube was evacuated and filled subsequently with an argon gas. [Ru(4,7-X_2-phen)$_3$](PF_6)$_2$ (44 mg, 0.031 mmol calculated as [Ru(4,7-Br_2-phen)$_3$](PF_6)$_2$), CuI (1.7 mg, 0.0089 mmol), and Pd(PPh_3)$_2$$Cl_2$ (2.3 mg, 0.0033 mmol) were added to the tube and, then, the tube was evacuated and filled with an argon gas again. An argon-gas purged CH_3CN/ triethylamine (NEt_3) mixture (1.0 mL/0.40 mL) was added to the reaction tube, and the resulting suspension was stirred at room temperature for 20 min. A tetrahydrofuran (THF) solution (5.5 mL) of (ethynylduryl)dimesitylborane (EDDB) (110 mg, 0.27 mmol) was then added dropwise to the reaction mixture. The mixture was stirred at 50ºC for 4 h under argon-gas atmosphere and, then, allowed to cool to room temperature. The insoluble residues were removed by filtration and the filtrate was dried under reduced pressure. The crude product was dissolved in a minimum amount of acetone and the solution was added dropwise to an excess amount of *n*-hexane, giving red precipitates. After repeating the reprecipitation procedures three times, purification by preparative HPLC (GPC, chloroform) afforded **3a(PF_6)$_2$** as red powders (44 mg, 42%). ^{1}H NMR (270 MHz, $CDCl_3$, TMS) δ/ppm 8.63 (6H, s, 5,6-Ar-H of phen), 8.54 (6H, *m*, 3,8-Ar-H of phen), 7.97 (6H, d, J = 5.6 Hz, 2,9-Ar-H of phen), 6.75 (24H, s, Ar-H of mes), 2.49 (36H, s, CH_3, *m*-positions of duryl groups), 2.27 (36H, s, CH_3, *o*-positions of duryl groups), 2.03 (36H, s, CH_3, *p*-positions of mes groups), 1.97 (72H, s, CH_3, *o*-positions of mes groups). MS (ESI) m/z 1533.4 (calcd for $[M-2PF_6]^{2+}$ ($C_{216}H_{222}N_6B_6Ru$): 1533.9). Elemental analysis calcd (%) for $C_{216}H_{222}N_6B_6RuP_2F_{12}\cdot 3.6CHCl_3$: C 69.63, H 6.00, N 2.22; found: C 69.57, H 6.04, N 2.33.

3-2-2: Other Chemicals, Physical Measurements, and Theoretical Calculations

The solvents used for spectroscopic and electrochemical measurements reported in this chapter were essentially the same with those described in Chapter 2. The PF_6^- salt of tris(1,10-phenanthroline)ruthenium(II) ($[Ru(phen)_3](PF_6)_2$) as a reference complex was prepared according to the literature.[17] All of the physical measurements and theoretical calculations reported in this chapter were performed under the identical conditions to those described in Chapter 2.

3-3: Results and Discussion

3-3-1: Redox Potentials

The cyclic voltammograms (CVs) and differential pulse voltammograms (DPVs) of **3a** and $[Ru(phen)_3]^{2+}$ in DMF are shown in Figure 3-1, together with those of **2a** and $[Ru(bpy)_3]^{2+}$ for comparison. The redox potentials of the complexes determined by the peak potentials of DPVs are summarized in Table 3-1. As seen in Figure 3-1 and Table 3-1, **3a** and $[Ru(phen)_3]^{2+}$ showed quasi-reversible oxidation waves responsible for the metal oxidation (E_{ox}) at +0.86 and +0.79 V (vs. ferrocene/ ferrocenium ion redox couple (Fc/Fc^+)), respectively. The oxidation potential of **3a** was shifted to the positive direction by an introduction of the DBDE groups to the phen ligands. The observed trend is similar to that observed for **2a** in which the DBDE groups are introduced to the bpy ligands (E_{ox} = +0.85 V for **2a** and E_{ox} = +0.79 V for $[Ru(bpy)_3]^{2+}$), indicating that the electron-withdrawing effects of the DBDE groups on the ruthenium atom in $[RuL_3]^{2+}$ are independent of the nature of the diimine ligand, L. On the other hand, **3a** showed a quasi-reversible reduction wave at E_{red1} = −1.41 V. Although it is expected that **3a** exhibits the five reduction waves ($E_{red1–5}$) similar to **2a**

(see Chapter 2), additional four redox waves ($E_{red2–5}$) other than E_{red1} have not been observed experimentally, probably due to instability of the reduced species of **3a**. The E_{red1} value of **3a** (−1.41 V) is more positive than the relevant value of $[Ru(phen)_3]^{2+}$ (−1.75 V), and the difference between the E_{red1} of the two complexes (ΔE_{red1} = +0.34 V) is larger than the relevant potential difference between **2a** and $[Ru(bpy)_3]^{2+}$ (ΔE_{red1} = +0.25 V; E_{red1} = −1.46 and −1.71 V for **2a** and $[Ru(bpy)_3]^{2+}$, respectively). The results demonstrate the electron-withdrawing DBDE groups affect more strongly the π*-orbital energy of the phen ligand than that of the bpy ligand and, thus, the spectroscopic/photophysical properties of **3a** are predicted to be influenced by the presence of the DBDE groups on the phen ligands.

Table 3-1. Redox potentials of the complexes in DMF containing 0.1-M $TBAPF_6$.

Complex	Potential E / V vs. Fc/Fc^+ [a]					
	red5	red4	red3	red2	red1	ox
3a					−1.41	+0.86
$[Ru(phen)_3]^{2+}$			−2.19	−1.90	−1.75	+0.79
2a [b]	−2.50	−2.35	−1.83	−1.61	−1.46	+0.85
$[Ru(bpy)_3]^{2+}$ [b]			−2.16	−1.90	−1.71	+0.79

[a] The values were determined by the peak potentials of DPV of the complexes. [b] Data taken from Chapter 2.

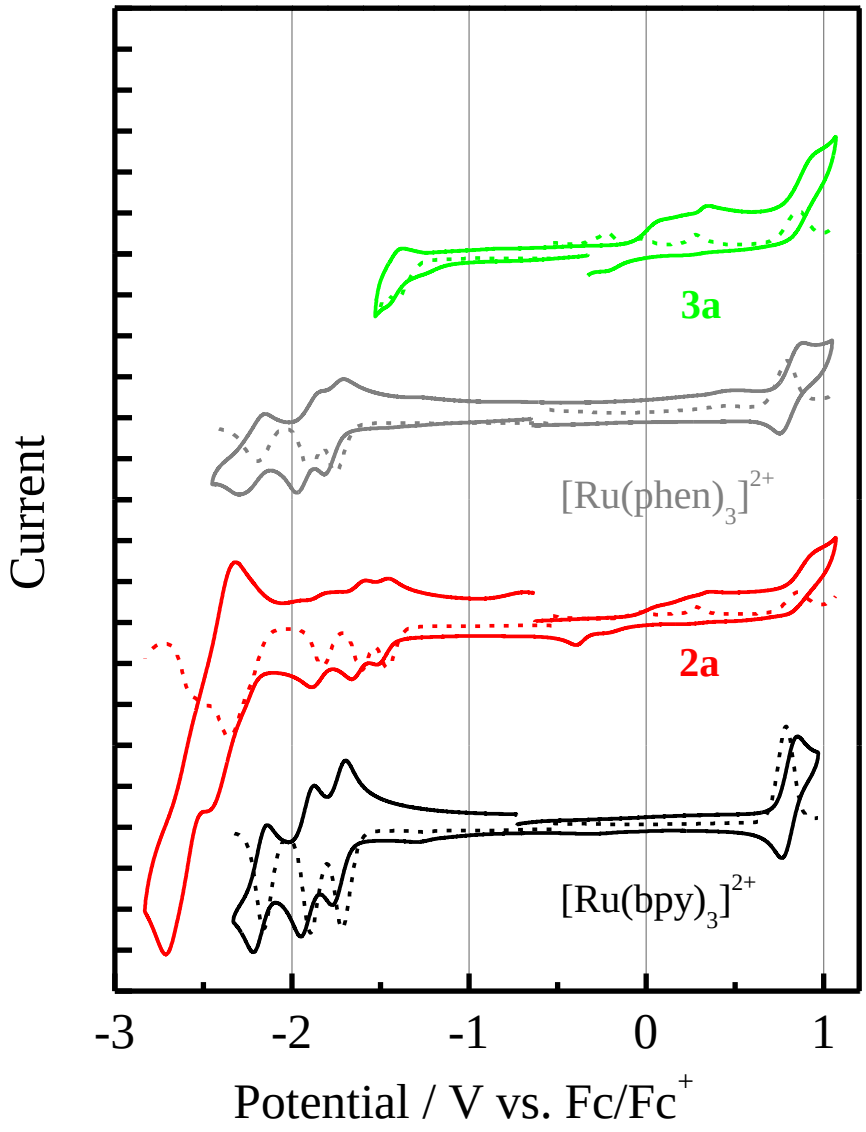

Figure 3-1. CVs (solid curves) and DPVs (broken curves) of the complexes in DMF containing 0.1-M $TBAPF_6$. The vertical axis is scaled in 5 μA per division. The data for **2a** and $[Ru(bpy)_3]^{2+}$ were taken from Chapter 2.

3-3-2: Absorption Spectra

The absorption spectra of **3a** and $[Ru(phen)_3]^{2+}$ in CH_3CN at 298 K are shown in Figure 3-2, together with those of **2a** and $[Ru(bpy)_3]^{2+}$ for comparison. The absorption maximum wavelengths (λ_{abs}) and corresponding ε values of the complexes are summarized in Table 3-2. The relatively narrow and intense $^1\pi\pi^*$ bands of the phen moieties were shifted to the longer wavelength (i.e., lower energy) by an introduction of the DBDE groups to $[Ru(phen)_3]^{2+}$ (λ_{abs} = 284 and 263 nm for **3a** and $[Ru(phen)_3]^{2+}$, respectively), indicating stabilization of the π^*-orbital energy of the ligand as suggested by the electrochemical measurements. Furthermore, **3a** exhibits an intense and characteristic absorption band in λ = 300–400 nm, which can be assigned to the superposition of the $^1\pi\pi^*$ transitions in the durylethynyl-phen moieties and the π(aryl)–p(B) CT transitions in the B_2phen ligands: LC absorption transition.[2]

The ^{1}MLCT absorption energy (E_{abs}) was also lowered by the introduction of the DBDE groups to the peripheries of the three phen ligands: E_{abs} = 21200 cm^{-1} (λ_{abs} = 471 nm) with a shoulder at around 19800 cm^{-1} ($\lambda \approx$ 505 nm) for **3a** and E_{abs} = 22500 cm^{-1} (λ_{abs} = 445 nm) for $[Ru(phen)_3]^{2+}$. The energy differences in the ^{1}MLCT and $^1\pi\pi^*$ bands between **3a** and $[Ru(phen)_3]^{2+}$ are almost comparable with each other (ΔE_{abs} = 2700 and 2800 cm^{-1}, respectively). Therefore, the low-energy shifts of the ^{1}MLCT absorption bands observed for **3a** are ascribed primarily to stabilization of the π^*-orbital energy of the ligand. The results are supported by the redox potentials of the complexes described in the previous section. The E_{red1} value responsible for the ligand reduction of **3a** (−1.41 V) was more positive than that of $[Ru(phen)_3]^{2+}$ (−1.75 V), and the energy calculated from the potential difference (0.34 eV = 2700 cm^{-1}) is comparable with the amount of the low-energy shift of the ^{1}MLCT band of **3a** relative

to that $[Ru(phen)_3]^{2+}$. In addition to the low-energy ^{1}MLCT transition, the ε_{MLCT} value observed for **3a** (7.2×10^4 $M^{-1}cm^{-1}$ at 471 nm) is enhanced significantly compared to that of $[Ru(phen)_3]^{2+}$ (1.7×10^4 $M^{-1}cm^{-1}$ at 445 nm). The enhancement of the ^{1}MLCT band intensity of **3a** can be explained by the increase in the relevant absorption transition dipole moment owing to the participation of extended intramolecular CT from the metal ion to the electron-withdrawing arylborane units: synergistic MLCT/π(aryl)–p(B) CT interactions as described in Chapter 2.

The comparison of the absorption spectrum of **3a** with that of **2a** provides further significant insights into the synergistic MLCT/π(aryl)–p(B) CT interactions. The ^{1}MLCT absorption bands of both **3a** and **2a** are shifted to the lower energy relative to those of the relevant reference complexes, and the ε_{MLCT} values of **2a** and **3a** are enhanced by the introduction of the six DBDE groups to the peripheries of the three ligands. Among the two complexes, however, more pronounced triarylborane effects on the ε_{MLCT} value are observed for **3a**, as demonstrated by the ε_{MLCT} value of **3a** (7.2×10^4 $M^{-1}cm^{-1}$ at 471 nm) being larger than that of **2a** (5.6×10^4 $M^{-1}cm^{-1}$ at 488 nm). The results demonstrate that the electronic coupling between the phen and DBDE units in **3a** is stronger than that between the bpy and DBDE units in **2a**, and such stronger electronic coupling leads to more effective synergistic MLCT/π(aryl)–p(B) CT interactions in **3a**. This could be explained by the rigid and planar π-extended structure of phen, which will be more favorable for the synergistic CT interactions compared to the more-structurally-flexible and less-π-extended bpy. As shown in Figure 3-2(b), the broader ^{1}MLCT absorption band observed for **3a** (the full width at half maximum (*fwhm*) of the spectrum is ca. 5300 cm^{-1}) relative to that of **2a** (~3500 cm^{-1}) might also indicate the effective and strong synergistic MLCT/π(aryl)–p(B) CT interactions in **3a**.

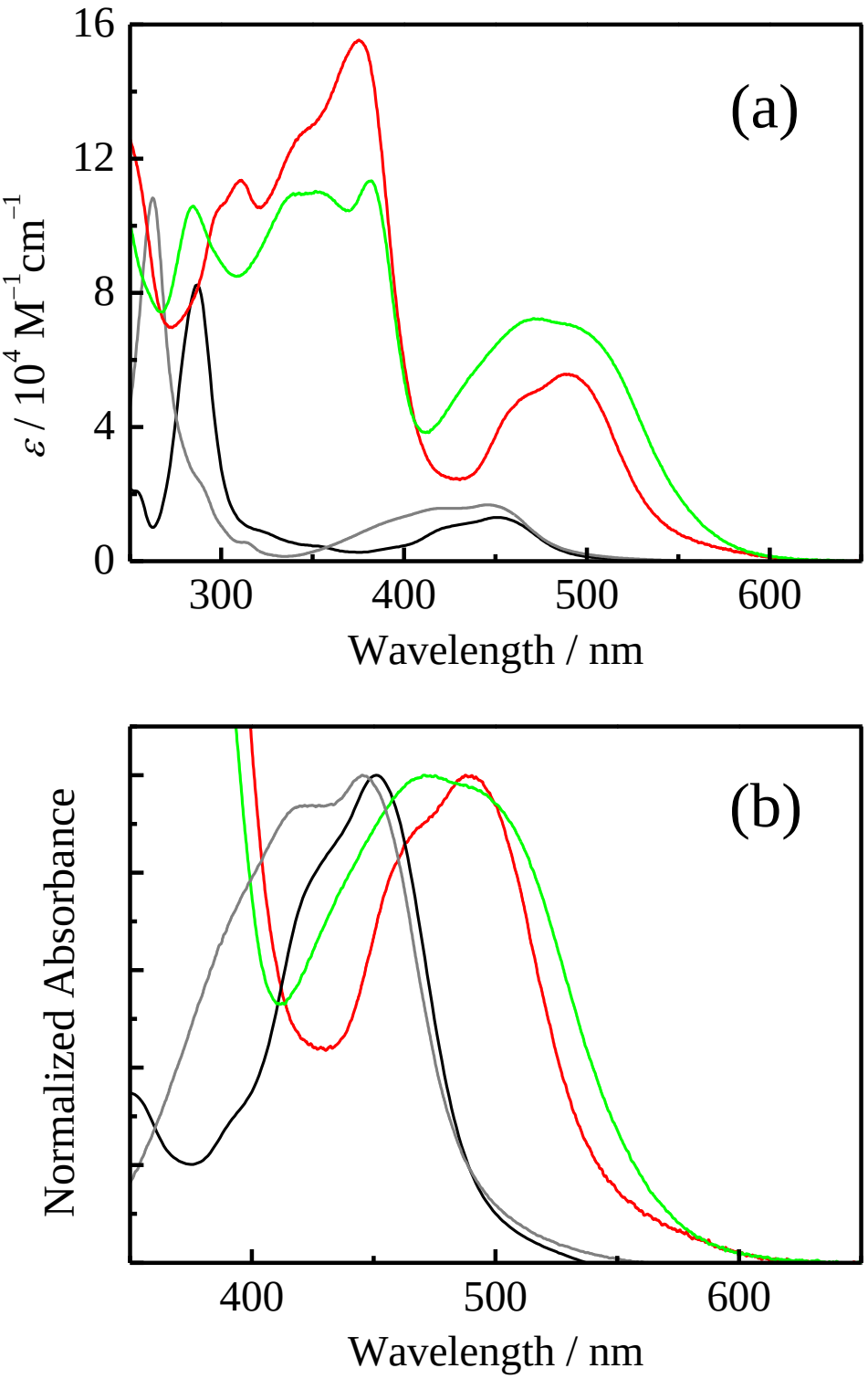

Figure 3-2. Absorption spectra of the complexes in CH_3CN at 298 K (a) and the spectra normalized to the maximum ε values of the MLCT bands (b). The colors of the spectra correspond to those indicated in Figure 3-1, and the spectra of **2a** and $[Ru(bpy)_3]^{2+}$ are taken from Chapter 2.

Table 3-2. Absorption parameters of the complexes in CH_3CN at 298 K.

Complex	λ_{abs} / nm (ε / 10^4 $M^{-1}cm^{-1}$)			
3a	284 (10.6)	382 (11.3)	471 (7.2)	505sh (6.6)
$[Ru(phen)_3]^{2+}$	263 (10.6)		416sh (1.6)	445 (1.7)
2a [a]	311 (11.4)	375 (15.5)	460sh (4.6)	488 (5.6)
$[Ru(bpy)_3]^{2+}$ [a]	287 (8.2)		424sh (1.1)	451 (1.3)

[a] Data taken from Chapter 2.

3-3-3: Time-Dependent Density Functional Theory (TD-DFT) Calculations

More details about the differences in the MLCT/π(aryl)–p(B) CT interactions between the complexes **3a** and **2a** are obtained by TD-DFT calculations. To reduce the computational cost, heteroleptic complexes $[Ru(B_2phen)(phen)_2]^{2+}$ (**3c**) and $[Ru(B_2bpy)(bpy)_2]^{2+}$ (**2c**) shown in Chart 3-2 were employed as model complexes for **3a** and **2a**, respectively. The calculated absorption transitions (energy and oscillator strength (*f*)) of **3c** and $[Ru(phen)_3]^{2+}$ are summarized in Tables 3-3 and 3-4. In Table 3-3, the absorption transitions related mainly to the unsubstituted bpy ligand are shown in a gray color since they do not contribute to the observed spectrum of **3a** and, thus, these data are not discussed here. The calculated absorption transitions are compared with the observed absorption spectra in Figure 3-3, in which the calculated transitions are shifted to the lower energy by 5% to correct the overestimation of the transition energies calculated by TD-DFT.[18] The Kohn–Sham MOs of **3c** and $[Ru(phen)_3]^{2+}$ are shown in Figure 3-4, whose details are also summarized in Tables 3-5 and 3-6. The relevant data for **2c** and $[Ru(bpy)_3]^{2+}$ can be found in Chapter 2.

As shown in Figure 3-3, the TD-DFT calculations demonstrated the lower-energy and more intense singlet–singlet (S_0–S_n) transitions in **3c** and **2c** relative to those of the reference complexes, $[Ru(phen)_3]^{2+}$ and $[Ru(bpy)_3]^{2+}$, respectively.

Hence, the calculations on **3c** and **2c** reproduce properly the absorption spectra of **3a** and **2a**, despite the calculations on the model complexes, **3c** and **2c**. The lowest-energy singlet excited states (S_1) of **3c** and **2c** are ascribed mainly to the HOMO−1→LUMO transitions at λ = 487 (f = 0.054) and 494 nm (f = 0.082), respectively. The LUMOs of both complexes are distributed over the entire arylborane-substituted ligand (i.e., B_2phen or B_2bpy), whose MO distributions are very similar with each other as shown in Figures 3-4 and 2-2. Although the HOMO−1 levels of both **3c** and **2c** also range from the ruthenium(II) atom to the DBDE groups in similar fashions with one another, that of **3c** populates on the ruthenium(II) atom more largely (~51%) than that of **2c** (~38%). It is worth pointing out, furthermore, that HOMO−1 of **3c** distributes to the two DBDE groups, while that of **2c** localizes on one DBDE group. Therefore, these results demonstrate that the lowest-energy excited state of **3c** is best characterized by synergistic MLCT/π(aryl)–p(B) CT, and that the excited state possesses a relatively larger charge-separated character than that of **2c**.

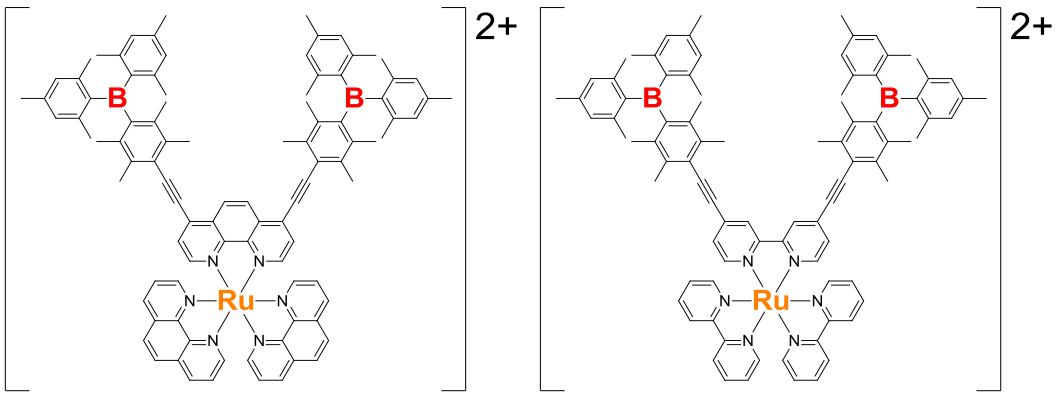

3c **2c**

Chart 3-2. Chemical structures of **3c** and **2c**.

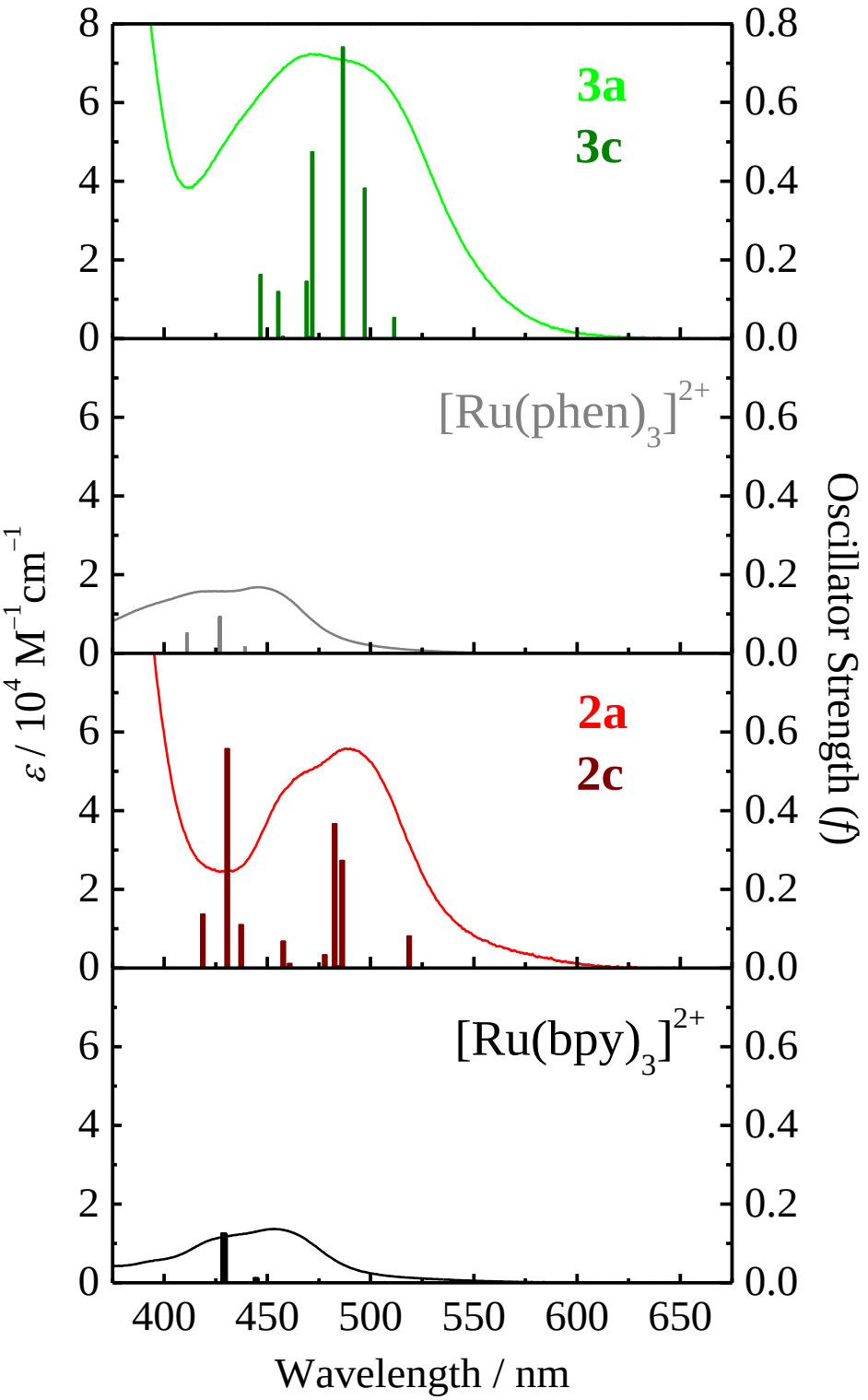

Figure 3-3. Comparison of the observed absorption spectra and oscillator strengths (perpendicular bars) estimated by the TD-DFT calculations for the complexes in CH_3CN at 298 K. **3c** and **2c** were used as model complexes for **3a** and **2a**, respectively.

Table 3-3. Calculated excited states for **3c** in CH_3CN.

Excited State	Transition	Energy (Wavelength)	Oscillator Strength
S_1	HOMO−7 → LUMO (15%) HOMO−4 → LUMO (25%) HOMO−1 → LUMO (60%)	2.5452 eV (487.13 nm)	0.0536
S_2	HOMO−14→ LUMO (16%) HOMO → LUMO (84%)	2.6185 eV (473.50 nm)	0.3823
S_3	HOMO → LUMO+1	2.6755 eV (463.40 nm)	0.7410
S_4	HOMO−4 → LUMO (85%) HOMO−4 → LUMO+2 (15%)	2.7162 eV (456.46 nm)	0.0011
S_5	HOMO−4 → LUMO+1 (12%) HOMO−4 → LUMO+3 (15%) HOMO−1 → LUMO+1 (37%) HOMO−1 → LUMO+3 (20%) HOMO → LUMO (16%)	2.7594 eV (449.31 nm)	0.4753
S_6	HOMO−11→ LUMO+2 (10%) HOMO−7 → LUMO+2 (16%) HOMO−4 → LUMO+2 (23%) HOMO−1 → LUMO+2 (51%)	2.7697 eV (447.64 nm)	0.0047
S_7	HOMO−11→ LUMO+3 (11%) HOMO−7 → LUMO+3 (18%) HOMO−4 → LUMO+3 (19%) HOMO−1 → LUMO+3 (52%)	2.7755 eV (446.71 nm)	0.1457
S_8	HOMO−14→ LUMO+3 (19%) HOMO−8 → LUMO+3 (14%) HOMO−4 → LUMO+2 (16%) HOMO → LUMO+3 (51%)	2.8453 eV (435.76 nm)	0.0059
S_9	HOMO−14→ LUMO+2 (11%) HOMO−8 → LUMO+2 (8%) HOMO−4 → LUMO+1 (12%) HOMO−4 → LUMO+3 (16%) HOMO−1 → LUMO+1 (9%) HOMO → LUMO (7%) HOMO → LUMO+2 (37%)	2.8593 eV (433.61 nm)	0.1200
S_{10}	HOMO−4 → LUMO+1	2.9143 eV (425.43 nm)	0.1632

Table 3-4. Calculated excited states for $[Ru(phen)_3]^{2+}$ in CH_3CN.

Excited State	Transition	Energy (Wavelength)	Oscillator Strength
S_1	HOMO → LUMO (71%) HOMO → LUMO+1 (29%)	2.8017 eV (442.53 nm)	0.0008
S_2	HOMO → LUMO (16%) HOMO → LUMO+2 (84%)	2.8058 eV (441.88 nm)	0.0000
S_3	HOMO → LUMO+1 (75%) HOMO → LUMO+2 (25%)	2.8063 eV (441.80 nm)	0.0001
S_4	HOMO−2 → LUMO+2 (49%) HOMO−1 → LUMO+1 (51%)	2.9463 eV (420.82 nm)	0.0001
S_5	HOMO−2 → LUMO (56%) HOMO−2 → LUMO+1 (21%) HOMO−1 → LUMO+2 (23%)	2.9635 eV (418.37 nm)	0.0152
S_6	HOMO−2 → LUMO (37%) HOMO−2 → LUMO+2 (18%) HOMO−1 → LUMO (45%)	2.9643 eV (418.26 nm)	0.0164
S_7	HOMO−2 → LUMO+2 (68%) HOMO → LUMO+5 (32%)	3.0478 eV (406.79 nm)	0.0935
S_8	HOMO−2 → LUMO+1 (36%) HOMO−1 → LUMO+2 (44%) HOMO → LUMO+4 (20%)	3.0502 eV (406.48 nm)	0.0928
S_9	HOMO−2 → LUMO+1 (29%) HOMO−2 → LUMO+2 (11%) HOMO → LUMO+3 (60%)	3.0534 eV (406.06 nm)	0.0058
S_{10}	HOMO−1 → LUMO (11%) HOMO → LUMO+4 (33%) HOMO → LUMO+5 (56%)	3.1670 eV (391.48 nm)	0.0520

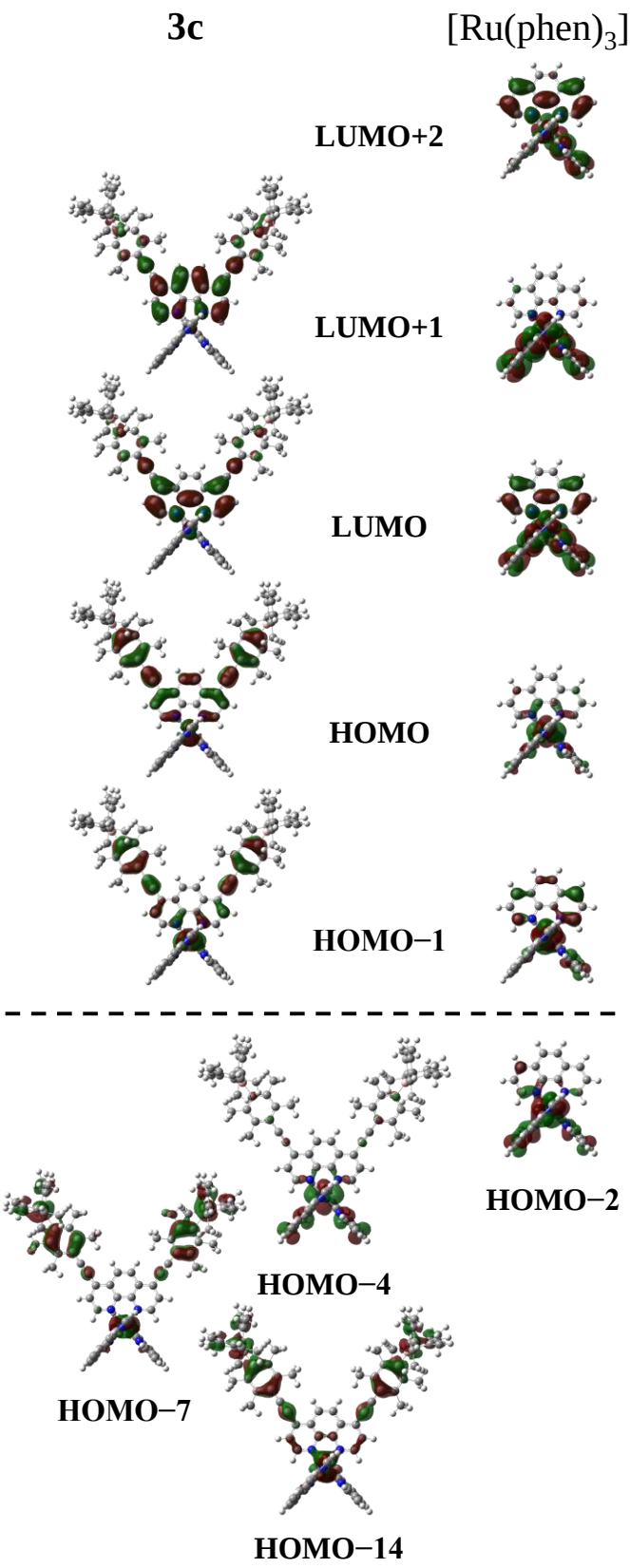

Figure 3-4. The Kohn–Sham MOs of **3c** and $[Ru(phen)_3]^{2+}$ (contour = 0.02 eÅ^{-3}).

Table 3-5. Calculated molecular orbitals of **3c** in CH_3CN.

Molecular Orbital	Eigenvalue / Hartrees	MO Population / %						
		ruthenium	B_2phen					phen
			phen	ethynyl	duryl	boron	mesityl	
LUMO+3	−0.08921	7.70	1.04	0.01	0.01	0.00	0.00	91.24
LUMO+2	−0.09113	5.01	2.77	0.22	0.26	0.05	0.06	91.63
LUMO+1	−0.09974	1.07	72.06	10.83	12.22	1.39	1.94	0.49
LUMO	−0.10194	5.08	70.11	8.58	8.80	1.01	1.43	4.99
HOMO	−0.21670	30.63	19.27	13.75	26.94	0.47	4.33	4.61
HOMO−1	−0.22100	50.86	10.56	8.58	19.39	0.34	3.77	6.50
HOMO−2	−0.22765	0.01	0.01	0.05	11.06	1.07	87.80	0.00
HOMO−3	−0.22771	0.01	0.01	0.05	10.86	1.06	88.01	0.00

Table 3-6. Calculated molecular orbitals of $[Ru(phen)_3]^{2+}$ in CH_3CN.

Molecular Orbital	Eigenvalue / Hartrees	MO Population / %						
		ruthenium						phen
LUMO+3	−0.08607	1.59						98.41
LUMO+2	−0.08939	7.82						92.18
LUMO+1	−0.08947	7.74						92.26
LUMO	−0.09293	2.01						97.99
HOMO	−0.22653	83.30						16.70
HOMO−1	−0.23040	74.48						25.52
HOMO−2	−0.23051	74.62						25.38
HOMO−3	−0.26386	0.33						99.67

3-3-4: Emission Properties

Figure 3-5 shows the corrected emission spectra of the complexes in CH_3CN at 298 K, in which the integrations of the spectra in a wavenumber scale correspond to the relative emission quantum yields (Φ_{em}) of the complexes, and Table 3-7 summarizes the emission properties of the complexes. The structureless emission spectrum of **3a** indicates that the emitting excited state of the complex is MLCT in character, and the emission maximum of **3a** (λ_{em} = 671 nm, E_{em} = 14800 cm^{-1}) is shifted to a longer wavelength compared to that of $[Ru(phen)_3]^{2+}$ (λ_{em} = 599 nm, E_{em} = 16600 cm^{-1}). The results demonstrate that the triplet MLCT/π(aryl)–p(B) CT excited state of **3a** is largely stabilized in energy compared to that of $[Ru(phen)_3]^{2+}$. Since the difference in the emission energy between **3a** and $[Ru(phen)_3]^{2+}$ (1800 cm^{-1}) is much larger than the relevant value between **2a** and $[Ru(bpy)_3]^{2+}$ (700 cm^{-1}), the effects of the arylborane substituents on the emission spectrum are more obvious in **3a** than **2a**. Furthermore, **3a** shows intense emission with Φ_{em} = 0.29 (in CH_3CN at 298 K), which is 6.4-times higher than that of $[Ru(phen)_3]^{2+}$ (Φ_{em} = 0.045). As described in Chapter 2, the introduction of the DBDE group(s) to $[Ru(bpy)_3]^{2+}$ enhances the emission efficiency, and the Φ_{em} value of **2a** (0.43 in CH_3CN at 298 K) is the largest among the polypyridyl ruthenium(II) complexes hitherto reported.[19] The present results demonstrate that the introduction of six DBDE groups to the peripheries of the three ligands in $[Ru(phen)_3]^{2+}$ also enhances Φ_{em} of the complex, and the enhancement factor of 6.4 is larger than that obtained for **2a**: Φ_{em}(**2a**)/Φ_{em}($[Ru(bpy)_3]^{2+}$) = 0.43/0.095 = 4.5. It is also worth emphasizing that enhancements of both ε_{MLCT} and Φ_{em} observed for **3a** (ε_{MLCT} = 7.2 × 10^4 $M^{-1}cm^{-1}$ at 471 nm and Φ_{em} = 0.29 in CH_3CN at 298 K) relative to the relevant values of $[Ru(phen)_3]^{2+}$ demonstrate brighter emission from **3a** than that from

$[Ru(phen)_3]^{2+}$ (ε_{MLCT} = 1.7 × 10^4 $M^{-1}cm^{-1}$ at 445 nm and Φ_{em} = 0.045).

Complex **3a** also exhibits long-lived emission as the decay profile is shown in Figure 3-6 together with that of $[Ru(phen)_3]^{2+}$. The emission lifetime (τ_{em}) value of **3a** (8.7 μs) is 21-times longer than that of $[Ru(phen)_3]^{2+}$ (0.42 μs) and, thus, **3a** shows simultaneously intense (Φ_{em} = 0.29) and long-lived emission (τ_{em} = 8.7 μs) in CH_3CN at 298 K. Since the phosphorescence transition of a molecule is a spin-forbidden process, the radiative rate constant (k_r) is generally very small. This leads to long τ_{em} ($\propto 1/k_r$) and small Φ_{em} ($\propto k_r$) values. Therefore, an achievement of both high Φ_{em} and long τ_{em} is generally difficult for an ordinary ruthenium(II) complex and, thus, the photophysical properties of **3a** are worth discussing in detailed as described in the followings.

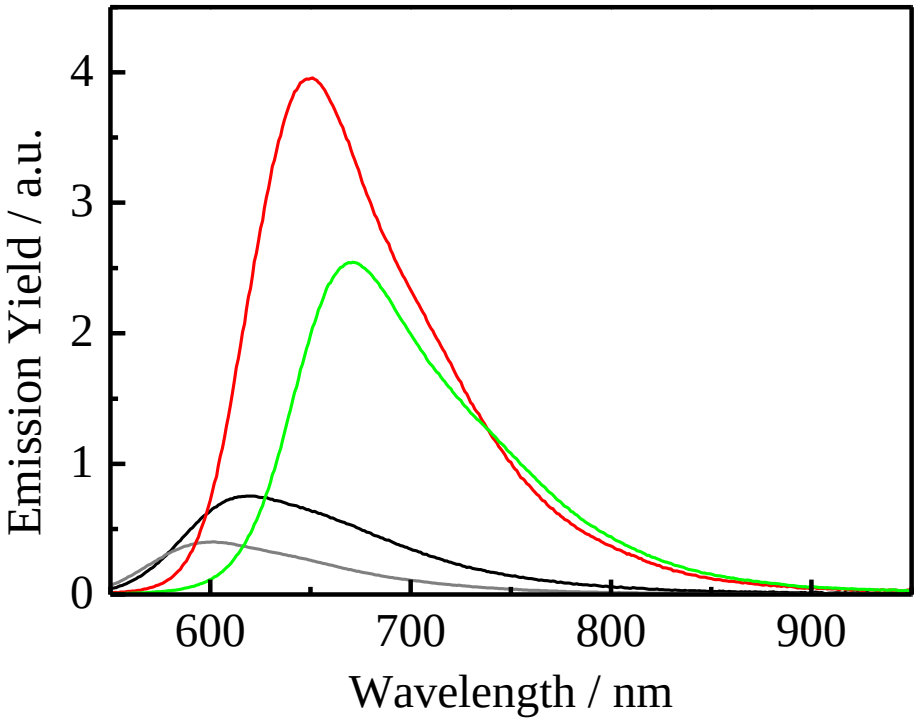

Figure 3-5. Corrected emission spectra of the complexes in CH_3CN at 298 K. The colors of the spectra correspond to those indicated in Figure 3-1, and the spectra of **2a** and $[Ru(bpy)_3]^{2+}$ are taken and modified from Chapter 2.

Table 3-7. Emission properties of the complexes in CH_3CN at 298 K.

complex	λ_{em} / nm	Φ_{em}	τ_{em} / μs	k_r [b] / s^{-1}	k_{nr} [b] / s^{-1}
3a	671	0.29	8.7	0.33×10^5	0.82×10^5
$[Ru(phen)_3]^{2+}$	599	0.045	0.42	1.1×10^5	23×10^5
2a [a]	651	0.43	1.7	2.5×10^5	3.4×10^5
$[Ru(bpy)_3]^{2+}$ [a]	620	0.095	0.89	1.1×10^5	10×10^5

[a] Data taken from Chapter 2. [b] Calculated by the equation, $\Phi_{em} = k_r/(k_r + k_{nr}) = k_r\tau_{em}$, where k_r and k_{nr} are the radiative and nonradiative decay rate constants, respectively.

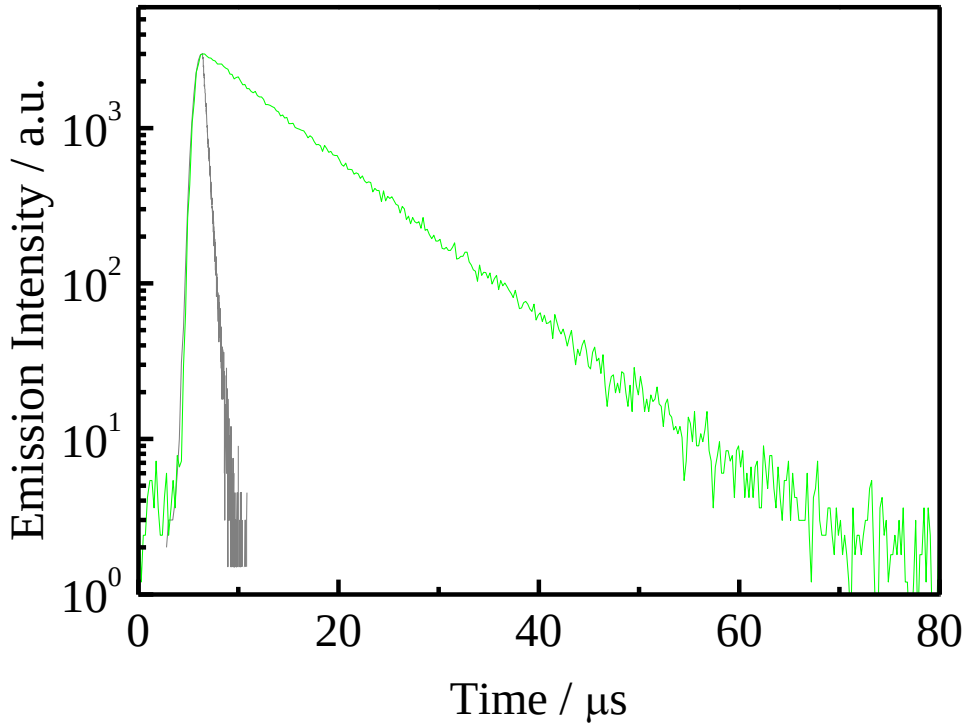

Figure 3-6. Emission decay profiles of **3a** (green) and $[Ru(phen)_3]^{2+}$ (gray) in CH_3CN at 298 K.

3-3-5: Nonradiative Decay Rate Constants

Owing to the large k_{nr} nature, the photophysical properties of a $[Ru(phen)_3]^{2+}$ derivative are controlled primarily by k_{nr} as predicted by the relation $\Phi_{em} = k_r\tau_{em} \approx k_r/k_{nr}$, where k_r and k_{nr} are the radiative and nonradiative decay rate constants, respectively. In practice, the extremely small k_{nr} value of **3a** (8.2×10^4 s^{-1}) compared to that of $[Ru(phen)_3]^{2+}$ (2.3×10^6 s^{-1}) dominates the simultaneous enhancements of Φ_{em} and τ_{em} for **3a**. To reveal the origin of the small k_{nr} value of **3a**, temperature (T)-dependent emission of the complex was studied in detail. Figure 3-7 shows the T-dependences (250–330 K) of the emission decay profiles of **3a** and **2a** in propylene carbonate. The emission decay profiles of **3a** and **2a** in 250–330 K were analyzed by single-exponential functions irrespective of T, and the T-dependences of τ_{em} for the complexes including

$[Ru(phen)_3]^{2+}$ and $[Ru(bpy)_3]^{2+}$ were analyzed by eq. 3-1,[20]

$$[\tau_{em}(T)]^{-1} = (k_r^0 + k_{nr}^0) + k'\exp(-\frac{\Delta E}{k_B T}) \quad \text{(eq. 3-1)}$$

where k_r^0 and k_{nr}^0 are the *T*-independent radiative and nonradiative decay rate constants from the emitting excited state to the ground state, respectively. The parameter *k*' is the frequency factor for thermal activation from the ^{3}MLCT excited state to the upper-lying nonemitting excited state (typically, triplet dd excited (^{3}dd*) state for a polypyridyl ruthenium(II) complex) with the energy barrier between the two states being ΔE. The *T*-dependences of τ_{em} were fitted adequately by eq. 3-1 as shown in Figure 3-8 with the fitting parameters (ΔE, (k_r^0 + k_{nr}^0), and *k*') being summarized in Table 3-8. Since nonradiative decay from the ^{3}MLCT excited state of a polypyridyl ruthenium(II) complex proceeds in general *via* the ^{3}dd* state as described in Chapter 2, the emission lifetime of the complex decreases upon *T*-elevation. The τ_{em} values of **3a** and **2a**, however, are almost independent of *T*, similar to those of other DBDE-appended polypyridyl ruthenium(II) and rhenium(I) complexes.[2,4,5] The parameter *k*' of **3a** (1.0×10^6 s^{-1}) or **2a** (2.9×10^9 s^{-1}) is much smaller than that of $[Ru(phen)_3]^{2+}$ or $[Ru(bpy)_3]^{2+}$ (~10^{13} s^{-1}), respectively, indicating the contribution of the fourth ^{3}MLCT excited state to excited-state decay of **3a** and **2a** as described in Chapter 2. Although the contributions of the ^{3}dd* state and the fourth ^{3}MLCT excited state to the observed *T*-dependent emission lifetime of **3a** cannot be separated in the present data, the observed ΔE and *k*' values of **3a** (ΔE = 930 cm^{-1} and *k*' = 1.0×10^6 s^{-1}) suggest that the fourth ^{3}MLCT excited state largely contributes to the nonradiative decay process of the complex due to close similarities of the data to the relevant values for $[Ru(bpy)_3]^{2+}$ in a

cellulose acetate film (ΔE = 810 cm^{-1} and k' = 1.7 × 10^7 s^{-1}).[21] It is worth emphasizing that the comparable metal oxidation potentials of the present four complexes (**2a**, **3a**, $[Ru(bpy)_3]^{2+}$, and, $[Ru(phen)_3]^{2+}$: +0.79–+0.86 V) suggest comparable ^{3}dd* energies of the complexes. On the other hand, the energy of the emitting state of **3a** (E_{em} = 14800 cm^{-1} (1.83 eV)) is lower than those of the other complexes: E_{em} = 16600 cm^{-1} (2.06 eV), 15300 cm^{-1} (1.90 eV), and 15900 cm^{-1} (1.97 eV) for $[Ru(phen)_3]^{2+}$, **2a**, and $[Ru(bpy)_3]^{2+}$, respectively. The resulting large ^{3}MLCT–^{3}dd* energy gap in **3a** extinguishes nonradiative decay pathway *via* the ^{3}dd* state and, thus, **3a** shows the extremely small k_{nr} value.

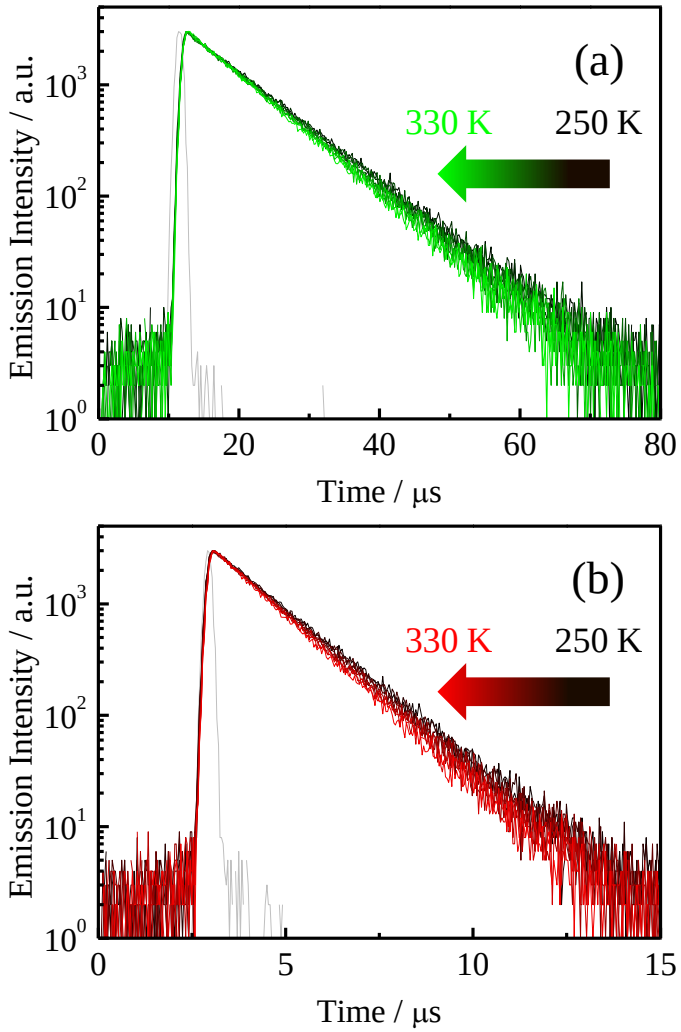

Figure 3-7. *T*-dependences (*T* = 250–330 K) of the emission decay profiles of **3a** (a) and **2a** (b) in propylene carbonate. Gray curves represent instrumental response functions.

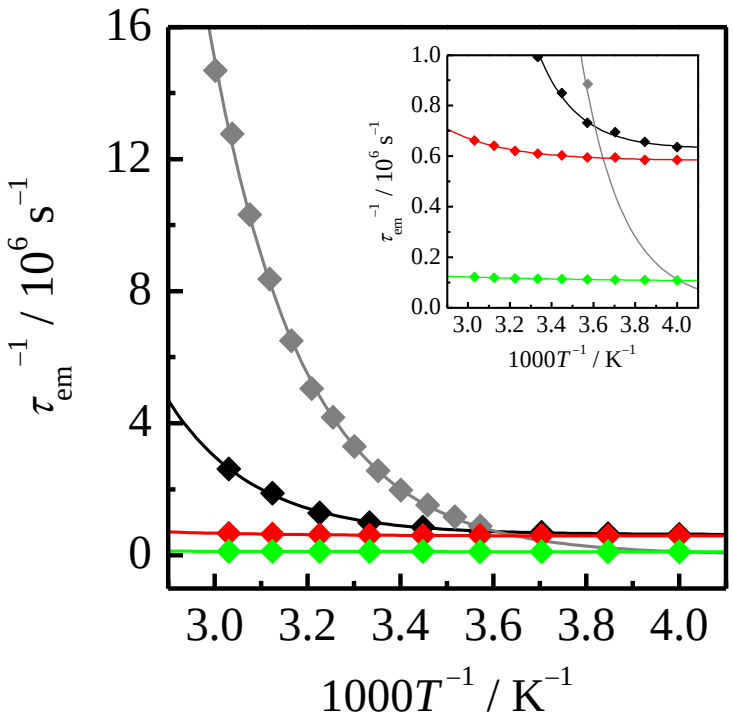

Figure 3-8. *T*-dependences (T = 250–330 K) of τ_{em} of the complexes in propylene carbonate. The colors of the data points correspond to those indicated in Figure 3-1. The curves represent the best fits of the experimental data by eq. 3-1. Inset: enlarged view. The data on $[Ru(phen)_3]^{2+}$ and $[Ru(bpy)_3]^{2+}$ are taken from ref. [2] and Figure 2-14 in Chapter 2, respectively.

Table 3-8. Activation parameters for the *T*-dependent emission lifetimes of the complexes in propylene carbonate.

Complex	ΔE / cm^{-1}	$(k_r^0 + k_{nr}^0)$ / s^{-1}	k' / s^{-1}
3a	930	1.0×10^5	1.0×10^6
$[Ru(phen)_3]^{2+}$ [a]	3500	1.5×10^5	5.7×10^{13}
2a	2410	5.8×10^5	2.9×10^9
$[Ru(bpy)_3]^{2+}$ [b]	3780	6.3×10^5	2.9×10^{13}

[a] Data taken from ref. [2]. [b] Data taken from Chapter 2.

3-3-6: Radiative Rate Constants

The radiative rate constant (k_r) of the complex is another important factor in determining the photophysical properties, especially Φ_{em}, of the complex. A huge difference in k_r between **3a** and **2a** is observed as the data are summarized in Table 3-7: smaller k_r for **3a** (3.3×10^4 s^{-1}) and larger k_r for **2a** (2.5×10^5 s^{-1}) compared to those of $[Ru(phen)_3]^{2+}$ and $[Ru(bpy)_3]^{2+}$ (1.1×10^5 s^{-1}). As described in Chapter 2, the k_r values of a series of **2a**–**c** and **2a'**–**c'** correlate positively with $\varepsilon_{MLCT}E_{em}/|E_{em} - E_{abs}|^2$ on the basis of the Strickler–Berg-type relation. However, the small k_r value of **3a** is not explained by a Strickler–Berg-type model since the spectroscopic data for **3a** show a larger $\varepsilon_{MLCT}E_{em}/|E_{em} - E_{abs}|^2$ value (8.6×10^9 $M^{-1}cm^{-2}$) than $[Ru(phen)_3]^{2+}$ (2.3×10^9 $M^{-1}cm^{-2}$). A possible explanation for small k_r of **3a** is the structural differences between the excited and ground states. Large differences in the emitting- and ground-state structures typically decreases the overlap integral of the wavefunctions between the two states, and it reduces the phosphorescence transition probability (i.e., k_r). As the TD-DFT calculations have indicated, the synergistic MLCT/π(aryl)–p(B) CT excited state of **3a** possesses a larger charge-separated character than that of **2a**. Owing to the elongated charge-transfer distance upon photoexcitation, the excited state of **3a** is stabilized by vibrational relaxation and, thus, resulting large structural differences between the thermally-equilibrated excited and ground states decrease k_r. In the case of **3a**, such effects may prevail a Strickler–Berg-type behavior.

3-4: Conclusions

In this chapter, the spectroscopic and photophysical properties of a novel homoleptic ruthenium(II) complex having the DBDE groups at the 4- and 7-positions of

the phen ligands in $[Ru(phen)_3]^{2+}$ ($[Ru(B_2phen)_3]^{2+}$: **3a**, Chart 3-1) were described in special references to the diimine ligand structure effects by comparing the data on **3a** with those on **2a**. The ε_{MLCT} value of **3a** (7.2×10^4 $M^{-1}cm^{-1}$ at 471 nm) is larger than that of **2a** (5.6×10^4 $M^{-1}cm^{-1}$ at 488 nm). The results demonstrate that the electronic coupling between the phen and DBDE units in **3a** is stronger than that between the bpy and DBDE units in **2a**, and this stronger electronic coupling leads to more effective synergistic MLCT/π(aryl)–p(B) CT interactions in **3a** relative to that in **2a**. On the basis of TD-DFT calculations, furthermore, it has been shown that the lowest-energy excited state of **3c** is best characterized by synergistic MLCT/π(aryl)–p(B) CT and the excited state possesses a relatively larger charge-separated character than that of **2c**. It is also worth emphasizing that enhancements of both ε_{MLCT} and Φ_{em} values observed for **3a** (ε_{MLCT} = 7.2×10^4 $M^{-1}cm^{-1}$ at 471 nm and Φ_{em} = 0.29 in CH_3CN at 298 K) represent bright emission from **3a**. The complex, **3a**, also exhibits long-lived emission owing to the large ^{3}MLCT–^{3}dd* energy gap in **3a** and this extinguishes the nonradiative decay pathway *via* the ^{3}dd* state: very small k_{nr} for **3a**. Thus, **3a** shows simultaneously intense (Φ_{em} = 0.29) and long-lived emission (τ_{em} = 8.7 μs). Since **3a** possesses simultaneously intense visible absorption, high Φ_{em}, and long τ_{em}, the complex is a promising candidate for a visible-light driven photo/redox sensitizer, a phosphorescence sensor, an emitting material, and so forth.

3-5: References

[1] Sakuda, E.; Funahashi, A.; Kitamura, N. Synthesis and Spectroscopic Properties of Platinum(II) Terpyridine Complexes Having an Arylborane Charge Transfer Unit. *Inorg. Chem.* **2006**, *45*, 10670–10677.

[2] Sakuda, E.; Ando, Y.; Ito, A.; Kitamura, N. Long-Lived and Temperature-Independent Emission from a Novel Ruthenium(II) Complex Having an Arylborane Charge-Transfer Unit. *Inorg. Chem.* **2011**, *50*, 1603–1613.

[3] Ito, A.; Hirokawa, T.; Sakuda, E.; Kitamura, N. Bright Green-Phosphorescence from Metal-to-Boron Charge-Transfer Excited State of a Novel Cyclometalated Iridium(III) Complex. *Chem. Lett.* **2011**, *40*, 34–36.

[4] Ito, A.; Kang, Y.; Sakuda, E.; Kitamura, N. Photophysical and Photoredox Characteristics of a Novel Tricarbonyl Rhenium(I) Complex Having an Arylborane-Appended Aromatic Diimine Ligand. *Inorg. Chem.* **2012**, *51*, 7722–7732.

[5] Kang, Y.; Ito, A.; Sakuda, E.; Kitamura, N. Diimine Ligand Structure Effects on Photophysical Properties of Tricarbonyl Rhenium(I) Complexes Having Arylborane Charge Transfer Units. *J. Photochem. Photobiol. A: Chem.* **2015**, 313, 107–116.

[6] Kang, Y.; Ito, A.; Sakuda, E.; Kitamura, N. Characteristic Spectroscopic and Photophysical Properties of Tricarbonyl Rhenium(I) Complexes Having Multiple Arylborane Charge Transfer Units. *Bull. Chem. Soc. Jpn.* **2017**, *90*, 574–585.

[7] Yamaguchi, S.; Akiyama, S.; Tamao, K. Tri-9-anthrylborane and Its Derivatives: New Boron-Containing π-Electron Systems with Divergently Extended π-Conjugation through Boron. *J. Am. Chem. Soc.* **2000**, *122*, 6335–6336.

[8] Yamaguchi, S.; Shirasaka, T.; Tamao, K. Tridurylboranes Extended by Three Arylethynyl Groups as a New Family of Boron-Based π-Electron Systems. *Org. Lett.* **2000**, *2*, 4129–4132.

[9] Kitamura, N.; Sakuda, E. Spectroscopic and Excited-State Properties of

Tri-9-anthrylborane I: Solvent Polarity Effects. *J. Phys. Chem. A* **2005**, *109*, 7429–7434.

[10] Kitamura, N.; Sakuda, E.; Yoshizawa, T.; Iimori, T.; Ohta, N. Spectroscopic and Excited-State Properties of Tri-9-anthrylborane II: Electroabsorption and Electrofluorescence Spectra. *J. Phys. Chem. A* **2005**, *109*, 7435–7441.

[11] Sakuda, E.; Tsuge, K.; Sasaki, Y.; Kitamura, N. Spectroscopic and Excited-State Properties of Tri-9-anthrylborane III: Crystal and Spectroscopic Polymorphisms. *J. Phys. Chem. B* **2005**, *109*, 22326–22331.

[12] Kitamura, N.; Sakuda, E.; Iwahashi, Y.; Tsuge, K.; Sasaki, Y.; Ishizaka, S. Linkage-Structure Dependences of the Spectroscopic and Photophysical Properties of Anthracene Derivatives: Tri(9-anthryl)benzene and Tri(9-anthryl)borane. *J. Photochem. Photobiol. A: Chem.* **2009**, *207*, 102–108.

[13] Kitamura, N.; Sakuda, E.; Ando, Y. Spectroscopic and Excited-State Properties of Triarylboranes and their Transition-Metal Complexes. *Chem. Lett.* **2009**, *38*, 938–943.

[14] Sakuda, E.; Ando, Y.; Ito, A.; Kitamura, N. Extremely Large Dipole Moment in the Excited Singlet State of Tris{[*p*-(*N*,*N*-dimethylamino)-phenylethynyl]duryl}borane. *J. Phys. Chem. A* **2010**, *114*, 9144–9150.

[15] Ito, A.; Kawanishi, K.; Sakuda, E.; Kitamura, N. Synthetic Control of Spectroscopic and Photophysical Properties of Triarylborane Derivatives Having Peripheral Electron-Donating Groups. *Chem.–Eur. J.* **2014**, *20*, 3940–3953.

[16] Altman, R. A.; Buchwald, A. L. 4,7-Dimethoxy-1,10-phenanthroline: An Excellent Ligand for the Cu-Catalyzed *N*-Arylation of Imidazoles. *Org. Lett.* **2006**, *8*, 2779–2782.

[17] Matsumura-Inoue, T.; Tanabe, M.; Minami, T.; Ohashi, T. A Remarkably Rapid Synthesis of Ruthenium(II) Polypyridine Complexes by Microwave Irradiation. *Chem. Lett.* **1994**, *12*, 2443–2446.

[18] Petersson, G. A.; Al-Laham, M. A. A Complete Basis Set Model Chemistry. III. The Complete Basis Set-Quadratic Configuration Interaction Family of Methods. *J. Chem. Phys.* **1991**, *94*, 6081–6090.

[19] Lumpkin, R. S.; Kober, E. M.; Worl, L. A.; Murtaza, Z.; Meyer, T. J. Metal-to-Ligand Charge-Transfer (MLCT) Photochemistry: Experimental Evidence for the Participation of a Higher Lying MLCT State in Polypyridyl Complexes of Ruthenium(II) and Osmium(II). *J. Phys. Chem.* **1990**, *94*, 239–243.

[20] Van Houten, J.; Watts, R. J. Temperature Dependence of the Photophysical and Photochemical Properties of the Tris(2,2'-bipyridyl)ruthenium(II) Ion in Aqueous Solution. *J. Am. Chem. Soc.* **1976**, *98*, 4853–4858.

[21] e. g.: Montalti, M.; Credi, A.; Prodi, L.; Teresa, M. *Handbook of Photochemistry, 3rd ed.*, CRC Press, Boca Raton, **2006**.

Chapter 4: Ancillary-Ligand Effects on the Spectroscopic and Photophysical Properties of Heteroleptic Arylborane–Ruthenium(II) Complexes

4-1: Introduction

In Chapter 3, the spectroscopic and photophysical properties of a homoleptic arylborane–ruthenium(II) complex (**3a**), in which six (dimesityl)borylduryletheynyl (DBDE) groups are introduced to $[Ru(phen)_3]^{2+}$ (phen = 1,10-phenanthroline) at the 4,7-positions of the three phen ligands, were described and compared with those of the relevant $[Ru(bpy)_3]^{2+}$ (bpy = 2,2'-bipyridine) derivative (**2a**). In CH_3CN at 298 K, **3a** showed simultaneously intense and long-lived emission (emission quantum yield (Φ_{em}) = 0.29 and emission lifetime (τ_{em}) = 8.7 μs), while **2a** exhibited extremely intense emission (Φ_{em} = 0.43 and τ_{em} = 1.7 μs). The results demonstrate that the DBDE group is a useful functional group for a development of highly-emissive transition metal complexes and that the diimine-ligand structure is one of the important factors to characterize the synergistic MLCT/π(aryl)–p(B) CT interactions. Furthermore, the emission spectral features of the arylborane–ruthenium(II) complexes were independent of the number of an arylborane-appended ligand as described in Chapter 2 and, therefore, it could be expected that the excited electron in the emissive triplet excited state is localized primarily on one arylborane-appended ligand in the complex. This indicates that the two ligands other than the arylborane-appended ligand in a heteroleptic tris-diimine ruthenium(II) complex can be utilized as ancillary ligands to control the electronic structures of an arylborane–ruthenium(II) complex in the ground and excited states.

In this chapter, the synthesis and spectroscopic/photophysical properties of novel

heteroleptic arylborane–ruthenium(II) complexes having a series of ancillary ligands L' ([Ru(B_2bpy)L'$_2$]$^{2+}$ (B_2bpy = 4,4'-(DBDE)$_2$-bpy): **4dpbpy** (L' = 4,4'-diphenyl-bpy (4,4'-ph_2-bpy)), **4dmbpy** (L' = 4,4'-dimethyl-bpy (4,4'-me_2-bpy)), **4dpphen** (L' = 4,7-diphenyl-phen (4,7-ph_2-phen)), **4dmphen** (L' = 4,7-dimethyl-phen (4,7-me_2-phen)), **4phen** (L' = phen), Chart 4-1) are described and discuss the properties in terms of the ancillary-ligand effects. The ligand, B_2bpy, has been employed as the common ligand in these five new complexes, since it is expected that the B_2bpy ligand can enhance Φ_{em} of the complex more largely than a 4-DBDE-bpy (Bbpy) or 4,7-(DBDE)$_2$-phen (B_2phen) ligand. The phenyl and methyl groups in the ancillary bpy or phen ligand were used as π- and σ-type electron-donating groups, respectively.

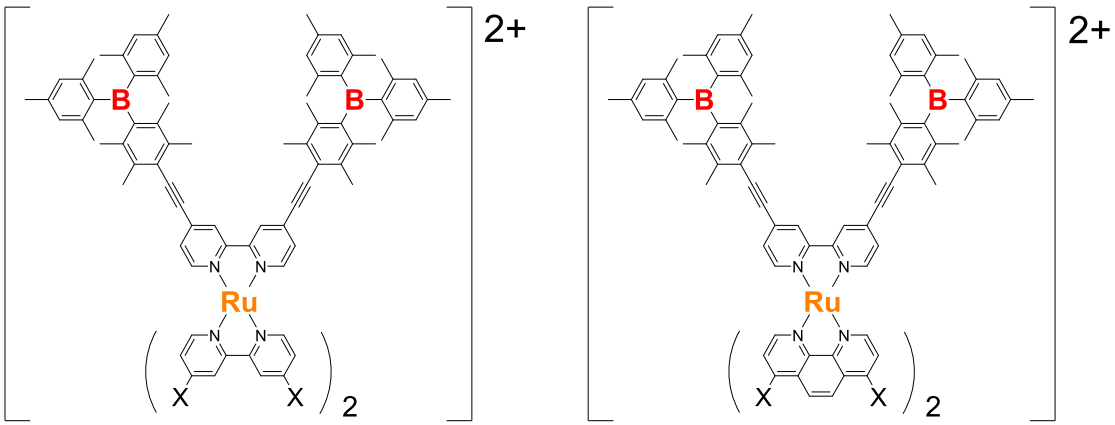

4dpbpy (-X = -C_6H_5),
4dmbpy (-X = -CH_3)

4dpphen (-X = -C_6H_5),
4dmphen (-X = -CH_3),
4phen (-X = -H)

Chart 4-1. Chemical structures of heteroleptic arylborane–ruthenium(II) complexes.

4-2: Experiments and Methodologies

4-2-1: Synthesis

The synthetic routes to **4dpbpy**, **4dmbpy**, **4dpphen**, **4dmphen**, and **4phen** are

shown in Scheme 4-1. The complexes were successfully synthesized as the hexafluoro-phosphate (PF_6^-) salts similar to the synthetic procedures for **2a**. The PF_6^- salt of a reference complex, $[Ru(bpy)(phen)_2]^{2+}$, was also prepared similar to the synthetic procedures for **2a**. The spectroscopic and photophysical purities of the complexes were confirmed by single-exponential emission decay in CH_3CN at 298 K in addition to the typical characterization methods described in Chapter 2. The ligand, 4,4'-ph_2-bpy, was prepared according to the literature,[1] and other chemicals used for the syntheses of $[Ru(B_2bpy)L'_2]^{2+}$ and $[Ru(bpy)(phen)_2]^{2+}$ were essentially the same with those described in Chapter 2.

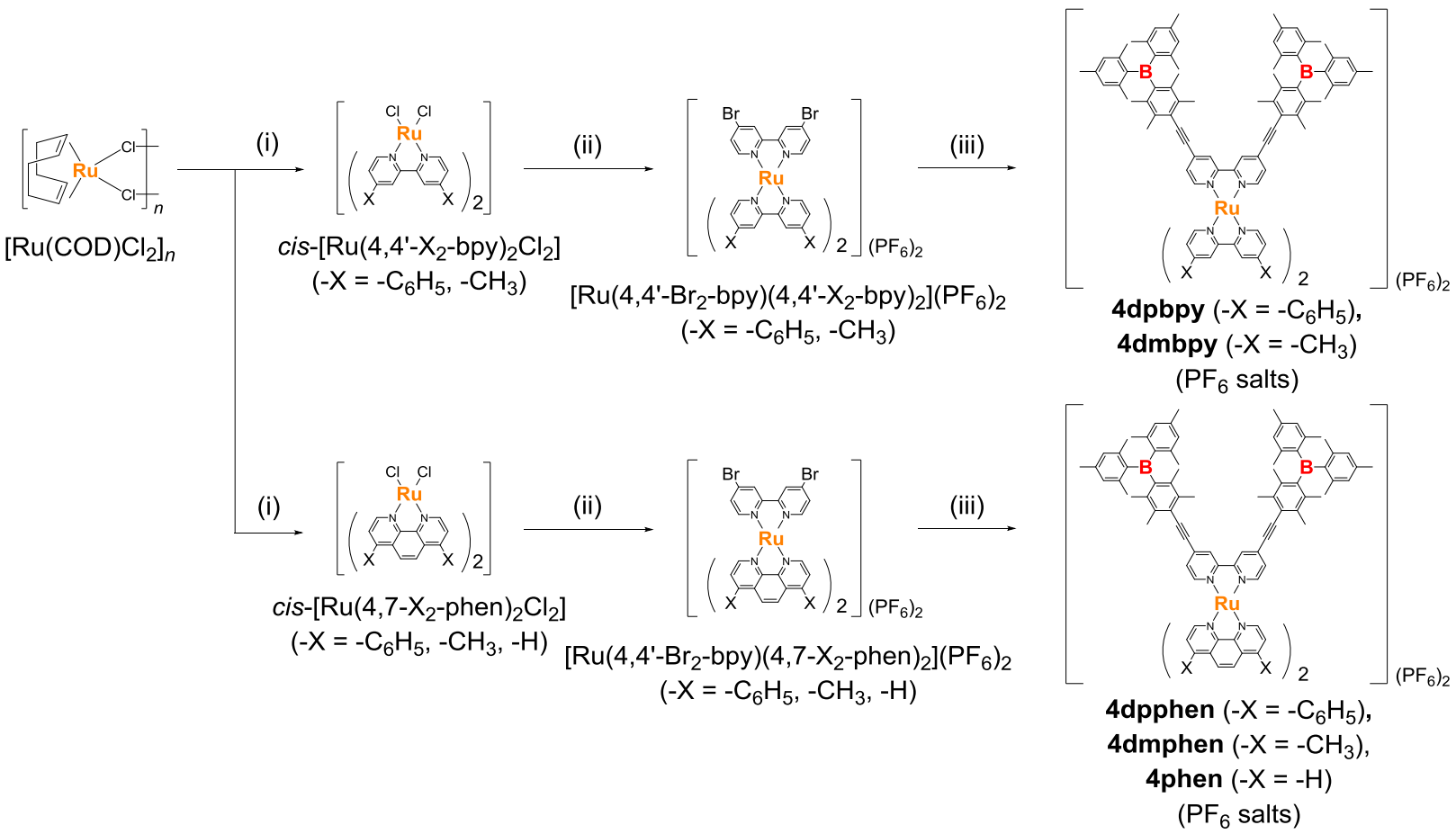

Scheme 4-1. Synthetic routes for the PF_6^- salts of $[Ru(B_2bpy)L'_2]^{2+}$: (i) L', *o*-dichlorobenzene, 160ºC, 2 h, (ii) 4,4'-Br_2-bpy, ethanol/water, 80ºC, 5 h, (iii) (ethynylduryl)dimesitylborane (EDDB), $Pd(PPh_3)_2Cl_2$, CuI, NEt_3, CH_3CN/THF, 50ºC, 4 h.

Synthesis of *cis*-Dichloridobis(4,4'-diphenyl-2,2'-bipyridine)ruthenium(II) (*cis*-[Ru(4,4'-ph$_2$-bpy)$_2$Cl$_2$]). The synthesis was performed by the reported procedures with some modifications.[2] A suspension of [Ru(COD)Cl$_2$]$_n$ (COD = 1,5-cyclooctadiene, 70 mg, 0.25 mmol on the basis of the ruthenium atom) and 4,4'-ph$_2$-bpy (150 mg, 0.49 mmol) in *o*-dichlorobenzene (6 mL) was heated at reflux temperature (160ºC) for 2 h. After cooling the suspension, the reaction mixture was added into diethyl ether (40 mL) and stirred for 30 min. The resulting precipitates were collected by filtration, affording *cis*-[Ru(4,4'-ph$_2$-bpy)$_2$Cl$_2$] as black powders (170 mg, 88%). This compound was used in the following step without any purification and identification.

Synthesis of *cis*-Dichloridobis(4,4'-dimethyl-2,2'-bipyridine)ruthenium(II) (*cis*-[Ru(4,4'-me$_2$-bpy)$_2$Cl$_2$]). The complex was synthesized similar to the synthesis of *cis*-[Ru(4,4'-ph$_2$-bpy)$_2$Cl$_2$] by heating a suspension of [Ru(COD)Cl$_2$]$_n$ (100 mg, 0.36 mmol) and 4,4'-me$_2$-bpy (130 mg, 0.71 mmol) in *o*-dichlorobenzene (10 mL), giving *cis*-[Ru(4,4'-me$_2$-bpy)$_2$Cl$_2$] as black powders (180 mg, 92%). This compound was used in the following step without any purification and identification.

Synthesis of *cis*-Dichloridobis(4,7-diphenyl-1,10-phenanthroline)ruthenium(II) (*cis*-[Ru(4,7-ph$_2$-phen)$_2$Cl$_2$]). The complex was synthesized similar to the synthesis of *cis*-[Ru(4,4'-ph$_2$-bpy)$_2$Cl$_2$] by heating a suspension of [Ru(COD)Cl$_2$]$_n$ (100 mg, 0.36 mmol) and 4,7-ph$_2$-phen (240 mg, 0.72 mmol) in *o*-dichlorobenzene (10 mL), giving *cis*-[Ru(4,7-ph$_2$-phen)$_2$Cl$_2$] as black powders (170 mg, 56%) after washing the products by a small amount of ethanol to remove [Ru(4,4'-ph$_2$-phen)$_3$]Cl$_2$ as a byproduct. This compound was used in the following step without identification.

Synthesis of *cis*-Dichloridobis(4,7-dimethyl-1,10-phenanthroline)ruthenium(II) (*cis*-[Ru(4,7-me$_2$-phen)$_2$Cl$_2$]). The complex was synthesized similar to the synthesis of *cis*-[Ru(4,4'-ph$_2$-bpy)$_2$Cl$_2$] by heating a suspension of [Ru(COD)Cl$_2$]$_n$ (67 mg, 0.24 mmol) and 4,7-me$_2$-phen (100 mg, 0.48 mmol) in *o*-dichlorobenzene (10 mL), giving *cis*-[Ru(4,7-me$_2$-phen)$_2$Cl$_2$] as black powders (97 mg, 67%) after washing the products by a small amount of ethanol to remove [Ru(4,4'-me$_2$-phen)$_3$]Cl$_2$ as a byproduct. This compound was used in the following step without identification.

Synthesis of *cis*-Dichloridobis(1,10-phenanthroline)ruthenium(II) (*cis*-[Ru(phen)$_2$-Cl$_2$]). The complex was synthesized similar to the synthesis of *cis*-[Ru(4,4'-ph$_2$-bpy)$_2$Cl$_2$] by reacting [Ru(COD)Cl$_2$]$_n$ (1.5 g, 5.4 mmol) and phen (1.9 g, 11 mmol) in *o*-dichlorobenzene (140 mL), giving *cis*-[Ru(phen)$_2$Cl$_2$] as black powders (2.7 g, 94%). This compound was used in the following step without any purification and identification.

Synthesis of (4,4'-Dibromo-2,2'-bipyridine)bis(4,4'-diphenyl-2,2'-bipyridine)-ruthenium(II) Bis(hexafluorophosphate) ([Ru(4,4'-Br$_2$-bpy)(4,4'-ph$_2$-bpy)$_2$](PF$_6$)$_2$). The synthesis was performed by the reported procedures with some modifications.[3] A suspension of *cis*-[Ru(4,4'-ph$_2$-bpy)$_2$Cl$_2$] (60 mg, 0.076 mmol) and 4,4'-Br$_2$-bpy (71 mg, 0.23 mmol) in 70 mL of an ethanol/water mixture (1/1, v/v) was heated at 80°C for 5 h. After cooling to room temperature, ethanol was removed under reduced pressure. The insoluble residues were removed by filtration, and an excess amount of an NH_4PF_6(aq) solution was added to the filtrate. The resulting precipitates were collected and purified by column chromatography (Al_2O_3, $CH_3CN/CHCl_3$ (1/1, v/v)). The crude product was dissolved in a minimum amount of acetone and, then, an excess amount of *n*-hexane was

added dropwise to the solution, giving [Ru(4,4'-Br_2-bpy)(4,4'-ph_2-bpy)$_2$](PF_6)$_2$ as red powders (55 mg, 55%). ^{1}H NMR (270 MHz, CD_3CN) δ/ppm 8.93 (4H, s, 3,3'-Ar-H of 4,4'-ph_2-bpy), 8.80 (2H, d, J = 2.2 Hz, 3,3'-Ar-H of 4,4'-Br_2-bpy), 7.98–7.89 (8H, *m*, 5,5',6,6'-Ar-H of 4,4'-Br_2-bpy and 6,6'-Ar-H of 4,4'-ph_2-bpy), 7.85 (4H, d, J = 6.0 Hz, 5,5'-Ar-H of 4,4'-ph_2-bpy), 7.75–7.55 (20H, *m*, Ar-H of phenyl); MS (ESI) m/z 516.1 (calcd for $[M-2PF_6]^{2+}$ ($C_{54}H_{38}N_6Br_2Ru$): 515.9).

Synthesis of (4,4'-Dibromo-2,2'-bipyridine)bis(4,4'-dimethyl-2,2'-bipyridine)-ruthenium(II) Bis(hexafluorophosphate) ([Ru(4,4'-Br_2-bpy)(4,4'-me_2-bpy)$_2$](PF_6)$_2$). The complex was synthesized similar to the synthesis of [Ru(4,4'-Br_2-bpy)(4,4'-ph_2-bpy)$_2$](PF_6)$_2$ by heating a suspension of *cis*-[Ru(4,4'-me_2-bpy)$_2Cl_2$] (110 mg, 0.20 mmol) and 4,4'-Br_2-bpy (190 mg, 0.61 mmol) in 200 mL of an ethanol/water mixture (1/1, v/v). The work-up and purification procedures similar to those mentioned above gave [Ru(4,4'-Br_2-bpy)(4,4'-me_2-bpy)$_2$](PF_6)$_2$ as red powders (140 mg, 65%). ^{1}H NMR (270 MHz, CD_3CN, TMS) δ/ppm 8.71 (2H, s, 3,3'-Ar-H of 4,4'-Br_2-bpy), 8.33 (4H, s, 3,3'-Ar-H of 4,4'-me_2-bpy), 7.58–7.52 (6H, *m*, 6,6'-Ar-H of 4,4'-Br_2-bpy and 6,6'-Ar-H of 4,4'-me_2-bpy), 7.47 (2H, d, J = 5.8 Hz, 5,5'-Ar-H of 4,4'-Br_2-bpy), 7.26–7.19 (4H, *m*, 5,5'-Ar-H of 4,4'-me_2-bpy), 2.53 (6H, s, CH_3 of 4,4'-me_2-bpy), 2.52 (6H, s, CH_3 of 4,4'-me_2-bpy); MS (ESI) m/z 392.0 (calcd for $[M-2PF_6]^{2+}$ ($C_{34}H_{30}N_6Br_2Ru$): 391.8).

Synthesis of (4,4'-Dibromo-2,2'-bipyridine)bis(4,7-diphenyl-1,10-phenanthroline)-ruthenium(II) Bis(hexafluorophosphate) ([Ru(4,4'-Br_2-bpy)(4,7-ph_2-phen)$_2$](PF_6)$_2$). The complex was synthesized similar to the synthesis of [Ru(4,4'-Br_2-bpy)(4,4'-ph_2-bpy)$_2$](PF_6)$_2$ by heating a suspension of *cis*-[Ru(4,7-ph_2-phen)$_2Cl_2$] (100 mg, 0.12 mmol)

and 4,4'-Br_2-bpy (110 mg, 0.36 mmol) in 120 mL of an ethanol/water mixture (1/1, v/v). The work-up and purification procedures similar to those mentioned above gave [Ru(4,4'-Br_2-bpy)(4,7-ph_2-phen)$_2$](PF_6)$_2$ as red powders (100 mg, 62%). ^{1}H NMR (270 MHz, CD_3CN) δ/ppm 8.84 (2H, d, J = 2.0 Hz, 3,3'-Ar-H of 4,4'-Br_2-bpy), 8.50 (2H, d, J = 5.5 Hz, 2,9-Ar-H of 4,7-ph_2-phen), 8.20 (4H, d, J = 2.5 Hz, 5,6-Ar-H of 4,7-ph_2-phen), 8.07 (2H, d, J = 5.5 Hz, 2,9-Ar-H of 4,7-ph_2-phen), 7.78 (2H, d, J = 5.5 Hz, 6,6'-Ar-H of 4,4'-Br_2-bpy), 7.73–7.54 (26H, *m*, 5,5'-Ar-H of 4,4'-Br_2-bpy, 2,9-Ar-H of 4,7-ph_2-phen and Ar-H of phenyl); MS (ESI) m/z 539.5 (calcd for $[M-2PF_6]^{2+}$ ($C_{58}H_{38}N_6Br_2Ru$): 540.0).

Synthesis of (4,4'-Dibromo-2,2'-bipyridine)bis(4,7-dimethyl-1,10-phenanthroline)-ruthenium(II) Bis(hexafluorophosphate) ([Ru(4,4'-Br_2-bpy)(4,7-me_2-phen)$_2$](PF_6)$_2$). The complex was synthesized similar to the synthesis of [Ru(4,4'-Br_2-bpy)(4,4'-ph_2-bpy)$_2$](PF_6)$_2$ by heating a suspension of *cis*-[Ru(4,7-me_2-phen)$_2Cl_2$] (50 mg, 0.09 mmol) and 4,4'-Br_2-bpy (85 mg, 0.27 mmol) in 100 mL of an ethanol/water mixture (1/1, v/v). The work-up and purification procedures similar to those mentioned above gave [Ru(4,4'-Br_2-bpy)(4,7-me_2-phen)$_2$](PF_6)$_2$ as red powders (61 mg, 60%). ^{1}H NMR (270 MHz, CD_3CN) δ/ppm 8.72 (2H, s, 3,3'-Ar-H of 4,4'-Br_2-bpy), 8.38 (4H, d, J = 4.3 Hz, 5,6-Ar-H of 4,7-me_2-phen), 8.06 (2H, d, J =5.3 Hz, 2,9-Ar-H of 4,7-me_2-phen), 7.67 (2H, d, J = 5.4 Hz, 2,9-Ar-H of 4,7-me_2-phen), 7.63 (2H, d, J = 5.4 Hz, 3,8-Ar-H of 4,7-me_2-phen), 7.54–7.43 (4H, *m*, 5,5',6,6'-Ar-H of 4,4'-Br_2-bpy), 7.38 (2H, d, J = 5.4 Hz, 3,8-Ar-H of 4,7-me_2-phen), 2.95 (6H, s, CH_3 of 4,7-me_2-phen), 2.85 (6H, s, CH_3 of 4,7-me_2-phen); MS (ESI) m/z 415.9 (calcd for $[M-2PF_6]^{2+}$ ($C_{38}H_{30}N_6Br_2Ru$): 415.8).

Synthesis of (4,4'-Dibromo-2,2'-bipyridine)bis(1,10-phenanthroline)ruthenium(II)

Bis(hexafluorophosphate) ([Ru(4,4'-Br_2-bpy)(phen)$_2$](PF_6)$_2$). The complex was synthesized similar to the synthesis of [Ru(4,4'-Br_2-bpy)(4,4'-ph_2-bpy)$_2$](PF_6)$_2$ by heating a suspension of *cis*-[Ru(phen)$_2Cl_2$] (36 mg, 0.068 mmol) and 4,4'-Br_2-bpy (64 mg, 0.20 mmol) in 60 mL of an ethanol/water mixture (1/1, v/v). The work-up and purification procedures similar to those mentioned above gave [Ru(4,4'-Br_2-bpy)(phen)$_2$](PF_6)$_2$ as red powders (42 mg, 57%). ^{1}H NMR (270 MHz, CD_3CN) δ/ppm 8.77 (2H, d, J = 1.9 Hz, 3,3'-Ar-H of 4,4'-Br_2-bpy), 8.69 (2H, dd, J = 1.4, 8.1 Hz, 4,7-Ar-H of phen), 8.55 (2H, dd, J = 1.4, 8.1 Hz, 4,7-Ar-H of phen), 8.26 (2H, s, 5,6-Ar-H of phen), 8.24 (2H, s, 5,6-Ar-H of phen), 7.86–7.78 (6H, *m*, 2,9-Ar-H of phen and 6,6'-Ar-H of 4,4'-Br_2-bpy), 7.58–7.52 (2H, *m*, 5,5'-Ar-H of 4,4'-Br_2-bpy), 7.50–7.47 (4H, *m*, 3,8-Ar-H of phen); MS (ESI) m/z 388.0 (calcd for [M−2PF_6]$^{2+}$ ($C_{34}H_{22}N_6Br_2Ru$): 387.7).

Synthesis of [4,4'-Bis{(dimesitylboryl)durylethynyl}-2,2'-bipyridine]bis(4,4'-diphenyl-2,2'-bipyridine)ruthenium(II) Bis(hexafluorophosphate) (4dpbpy(PF_6)$_2$). An oven-dried Schlenk tube was evacuated and filled subsequently with an argon gas. [Ru(4,4'-Br_2-bpy)(4,4'-ph_2-bpy)$_2$](PF_6)$_2$ (50 mg, 0.038 mmol), CuI (2.9 mg, 0.011 mmol), and Pd(PPh_3)$_2Cl_2$ (1.9 mg, 0.0027 mmol) were added to the tube and, then, the tube was evacuated and filled with an argon gas again. An argon-gas purged CH_3CN/triethylamine (NEt_3) mixture (1.2 mL/0.50 mL) was added to the reaction tube, and the resulting suspension was stirred at room temperature for 20 min. A tetrahydrofuran (THF) solution (3.5 mL) of (ethynylduryl)dimesitylborane (EDDB) (45 mg, 0.11 mmol) was then added dropwise to the reaction mixture. The mixture was stirred at 50ºC for 4 h under argon-gas atmosphere and, then, allowed to cool to room temperature. The insoluble residues were removed by filtration through Celite® (No. 500), and the filtrate was evaporated to

dryness. The crude product was dissolved in a minimum amount of acetone and the solution was added dropwise to an excess amount of *n*-hexane, giving red precipitates. After repeating the reprecipitation procedures three times, purifications by column chromatography (LH-20, CH_3CN/ethanol, (1/1, v/v)) followed by preparative HPLC (GPC, chloroform) afforded **4dpbpy**$(PF_6)_2$ as red powders (30 mg, 50%). ^{1}H NMR (270 MHz, CD_3CN, TMS) δ/ppm 8.96 (4H, s, 3,3'-Ar-H of 4,4'-ph_2-bpy), 8.74 (2H, s, 3,3'-Ar-H of B_2bpy), 7.95–7.88 (12H, *m*, 6,6'-Ar-H of 4,4'-ph_2-bpy and B_2bpy and Ar-H of phenyl), 7.75–7.54 (14H, *m*, 5,5'-Ar-H of B_2bpy and Ar-H of phenyl), 6.80 (8H, s, Ar-H of mes), 2.44(12H, s, CH_3, *m*-positions of duryl groups), 2.24 (12H, s, CH_3, *o*-positions of duryl groups), 2.02 (12H, s, CH_3, *p*-positions of mes groups), 1.94 (24H, s, CH_3, *o*-positions of mes groups); MS (ESI) m/z 841.2 (calcd for $[M-2PF_6]^{2+}$ ($C_{114}H_{106}N_6B_2Ru$): 841.4). Elemental analysis calcd (%) for $C_{114}H_{106}N_6B_2RuP_2F_{12}\cdot 2.5CHCl_3$: C 61.34, H 4.79, N 3.68; found: C 61.57, H 4.77, N 3.65.

Synthesis of [4,4'-Bis{(dimesitylboryl)durylethynyl}-2,2'-bipyridine]bis(4,4'-dimethyl-2,2'-bipyridine)ruthenium(II) Bis(hexafluorophosphate) (4dmbpy$(PF_6)_2$). The complex was synthesized similar to the synthesis of **4dpbpy**$(PF_6)_2$ by reacting [Ru(4,4'-Br_2-bpy)$_2$(4,4'-me_2-bpy)]$(PF_6)_2$ (62 mg, 0.057 mmol), CuI (1.5 mg, 0.0080 mmol), $Pd(PPh_3)_2Cl_2$ (2.8 mg, 0.0040 mmol) in CH_3CN/NEt_3 (1.8 mL/0.70 mL) and a THF (3.5 mL) solution of EDDB (70 mg, 0.17 mmol), giving **4dmbpy**$(PF_6)_2$ as red powders (52 mg, 53%). ^{1}H NMR (270 MHz, CD_3CN) δ/ppm 8.65 (2H, s, 3,3'-Ar-H of B_2bpy), 8.36 (4H, s, 3,3'-Ar-H of 4,4'-me_2-bpy), 7.74–7.68 (2H, *m*, 6,6'-Ar-H of B_2bpy), 7.63–7.56 (2H, *m*, 6,6'-Ar-H of 4,4'-me_2-bpy), 7.55–7.48 (2H, *m*, 6,6'-Ar-H of 4,4'-me_2-bpy), 7.47–7.41 (2H, *m*, 5,5'-Ar-H of 5,5'-Ar-H of B_2bpy), 7.32–7.18 (4H, *m*, 5,5'-Ar-H

of 4,4'-me_2-bpy), 6.80 (8H, s, Ar-H of mes), 2.53 (12H, s, CH_3 of 4,4'-me_2-bpy), 2.44(12H, s, CH_3, *m*-positions of duryl groups), 2.25 (12H, s, CH_3, *o*-positions of duryl groups), 2.02 (12H, s, CH_3, *p*-positions of mes groups), 1.94 (24H, s, CH_3, *o*-positions of mes groups); MS (ESI) m/z 717.2 (calcd for $[M-2PF_6]^{2+}$ ($C_{94}H_{98}N_6B_2Ru$): 717.4). Elemental analysis calcd (%) for $C_{94}H_{98}N_6B_2RuP_2F_{12}\cdot 0.3CHCl_3$: C 64.34, H 5.40, N 4.77; found: C 64.19, H 5.56, N 4.72.

Synthesis of [4,4'-Bis{(dimesitylboryl)durylethynyl}-2,2'-bipyridine]bis(4,7-diphenyl-1,10-phenanthroline)ruthenium(II) Bis(hexafluorophosphate) (4dpphen(PF_6)$_2$). The complex was synthesized similar to the synthesis of **4dpbbpy**(PF_6)$_2$ by reacting [Ru(4,4'-Br_2-bpy)(4,7-ph_2-phen)$_2$](PF_6)$_2$ (150 mg, 0.11 mmol), CuI (2.7 mg, 0.014 mmol)), $Pd(PPh_3)_2Cl_2$ (5.5 mg, 0.0078 mmol) in CH_3CN/NEt_3 (3.3 mL/1.6 mL) and a THF (2.6 mL) solution of EDDB (200 mg, 0.50 mmol), giving **4dpphen**(PF_6)$_2$ as red powders (17 mg, 7.6%). ^{1}H NMR (270 MHz, CD_3CN, TMS) δ/ppm 8.78 (2H, s, 3,3'-Ar-H of B_2bpy), 8.40 (2H, d, J = 5.7 Hz, 2,9-Ar-H of 4,7-ph_2-phen), 8.22 (2H, s, 5,6-Ar-H of 4,7-ph_2-phen), 8.21 (2H, s, 5,6-Ar-H of 4,7-ph_2-phen), 8.11 (2H, d, J = 5.7 Hz, 2,9-Ar-H of 4,7-ph_2-phen), 7.86 (2H, d, J = 5.7 Hz, 3,8-Ar-H of 4,7-ph_2-phen), 7.80 (2H, d, J = 5.7 Hz, 3,8-Ar-H of 4,7-ph_2-phen), 7.66–7.60 (22H, *m*, 6,6'-Ar-H of B_2bpy and Ar-H of phenyl), 7.45 (2H, d, J = 5.9 Hz, 5,5'-Ar-H of B_2bpy), 6.80 (8H, s, Ar-H of mes), 2.44 (12H, s, CH_3, *m*-positions of duryl groups), 2.24 (12H, s, CH_3, *o*-positions of duryl groups), 2.01 (12H, s, CH_3, *p*-positions of mes groups), 1.93 (24H, s, CH_3, *o*-positions of mes groups); MS (ESI) m/z 865.1 (calcd for $[M-2PF_6]^{2+}$ ($C_{118}H_{106}N_6B_2Ru$): 865.4). Elemental analysis calcd (%) for $C_{118}H_{106}N_6B_2RuP_2F_{12}\cdot 1.1CHCl_3$: C 66.47, H 5.02, N 3.91; found: C 66.36, H 4.98, N 3.87.

Synthesis of [4,4'-Bis{(dimesitylboryl)durylethynyl}-2,2'-bipyridine]bis(4,7-dimethyl-1,10-phenanthroline)ruthenium(II) Bis(hexafluorophosphate) (4dmphen(PF_6)$_2$). The complex was synthesized similar to the synthesis of **4dpbpy**(PF_6)$_2$ by reacting [Ru(4,4'-Br_2-bpy)$_2$(4,7-me_2-phen)](PF_6)$_2$ (100 mg, 0.089 mmol), CuI (4.9 mg, 0.026 mmol), Pd(PPh_3)$_2Cl_2$ (4.38 mg, 0.0063 mmol) in CH_3CN/NEt_3 (2.8 mL/1.2 mL) and a THF (2.0 mL) solution of EDDB (150 mg, 0.38 mmol), giving **4dmphen**(PF_6)$_2$ as red powders (25 mg, 16%). ^{1}H NMR (270 MHz, CD_3CN, TMS) δ/ppm 8.71–8.68 (2H, *m*, 3,3'-Ar-H of B_2bpy), 8.39 (4H, d, J = 3.8 Hz, 2,9-Ar-H of 4,7-me_2-phen), 8.12 (2H, d, J = 5.4 Hz, 5,6-Ar-H of 4,7-me_2-phen), 7.70 (2H, d, J = 5.4 Hz, 5,6-Ar-H of 4,7-me_2-phen), 7.68–7.63 (4H, *m*, 3,8-Ar-H of 4,7-me_2-phen), 7.40 (2H, d, J = 6.3 Hz, 6,6'-Ar-H of B_2bpy), 7.35 (2H, *m*, 5,5'-Ar-H of B_2bpy), 6.80 (8H, s, Ar-H of mes), 2.96 (6H, s, CH_3 of 4,7-me_2-phen), 2.86 (6H, s, CH_3 of 4,7-me_2-phen), 2.42 (12H, s, CH_3, *m*-positions of duryl groups), 2.24 (12H, s, CH_3, *o*-positions of duryl groups), 2.01 (12H, s, CH_3, *p*-positions of mes groups), 1.93 (24H, s, CH_3, *o*-positions of mes groups); MS (ESI) m/z 741.3 (calcd for [M−2PF_6]$^{2+}$ ($C_{98}H_{98}N_6B_2Ru$): 741.2). Elemental analysis calcd (%) for $C_{98}H_{98}N_6B_2RuP_2F_{12}$·1.2$CHCl_3$: C 62.19, H 5.22 N 4.39; found: C 62.16, H 5.26, N 4.34.

Synthesis of [4,4'-Bis{(dimesitylboryl)durylethynyl}-2,2'-bipyridine]bis(1,10-phenanthroline)ruthenium(II) Bis(hexafluorophosphate) (4phen(PF_6)$_2$). The complex was synthesized similar to the synthesis of **4dpbpy**(PF_6)$_2$ by reacting [Ru(4,4'-Br_2-bpy)$_2$(phen)](PF_6)$_2$ (100 mg, 0.094 mmol), CuI (2.3 mg, 0.012 mmol), Pd(PPh_3)$_2Cl_2$ (4.6 mg, 0.0066 mmol) in CH_3CN/NEt_3 (3.2 mL/1.5 mL) and a THF (2.4 mL) solution of

EDDB (170 mg, 0.42 mmol), giving **4phen**$(PF_6)_2$ as red powders (77 mg, 48%). ^{1}H NMR (270 MHz, CD_3CN, TMS) δ/ppm 8.71–8.68 (4H, *m*, 3,3'-Ar-H of B_2bpy and 4,7-Ar-H of phen), 8.57 (2H, d, J = 8.0 Hz, 4,7-Ar-H of phen), 8.31–8.29 (2H, *m*, 2,9-Ar-H of phen), 8.27 (2H, s, 5,6-Ar-H of phen), 8.25 (2H, s, 5,6-Ar-H of phen), 7.89–7.81 (4H, *m*, 2,3,8,9-Ar-H of phen), 7.66 (2H, d, J = 5.9 Hz, 6,6'-Ar-H of B_2bpy), 7.57 (2H, dd, J = 5.4, 8.4 Hz, 3,8-Ar-H of phen), 7.35 (2H, dd, J =1.6, 6.2 Hz, 5,5'-Ar-H of B_2bpy), 6.80 (8H, s, Ar-H of mes), 2.42 (12H, s, CH_3, *m*-positions of duryl groups), 2.24 (12H, s, CH_3, *o*-positions of duryl groups), 2.01 (12H, s, CH_3, *p*-positions of mes groups), 1.93 (24H, s, CH_3, *o*-positions of mes groups); MS (ESI) m/z 713.2 (calcd for $[M-2PF_6]^{2+}$ ($C_{94}H_{90}N_6B_2Ru$): 713.2). Elemental analysis calcd (%) for $C_{94}H_{90}N_6B_2RuP_2F_{12}\cdot 1.2CHCl_3$: C 61.49, H 4.52, N 4.90; found: C 61.34, H 4.93, N 4.44.

Synthesis of (2,2'-bipyridine)bis(1,10-phenanthroline)ruthenium(II) Bis(hexafluorophosphate) ([Ru(bpy)(phen)$_2$](PF$_6$)$_2$). The complex was synthesized similar to the synthesis of [Ru(4,4'-Br_2-bpy)(4,4'-ph_2-bpy)$_2$]$(PF_6)_2$ by heating a suspension of *cis*-[Ru(phen)$_2Cl_2$] (64 mg, 0.12 mmol) and bpy (37 mg, 0.24 mmol) in 120 mL of an ethanol/water mixture (1/1, v/v), giving [Ru(bpy)(phen)$_2$]$(PF_6)_2$ as red powders (78 mg, 72%). ^{1}H NMR (270 MHz, CD_3CN, TMS) δ/ppm 8.66 (2H, dd, J = 1.1, 8.1 Hz, 3,3'-Ar-H of bpy), 8.57–8.50 (4H, *m*, 2,9-Ar-H of phen), 8.25 (2H, s, 5,6-Ar-H of phen), 8.24 (2H, s, 5,6-Ar-H of phen), 8.20 (2H, dd, J = 1.1, 5.4 Hz, 4,7-Ar-H of phen), 8.03 (2H, td, J = 1.6, 8.1 Hz, 4,4'-Ar-H of bpy), 7.89 (2H, dd, J = 1.1, 5.4 Hz, 4,7-Ar-H of phen), 7.79 (2H, dd, J = 5.1, 8.6 Hz, 3,8-Ar-H of phen), 7.68 (2H, d, J = 5.6 Hz, 6,6'-Ar-H of bpy), 7.56 (2H, dd, J = 5.1, 8.6 Hz, 3,8-Ar-H of phen), 7.28 (2H, ddd, J = 1.4, 5.9, 8.4 Hz, 5,5'-Ar-H of bpy); MS (ESI) m/z 309.1 (calcd for $[M-2PF_6]^{2+}$ ($C_{34}H_{24}N_6Ru$): 308.8). Elemental

analysis calcd (%) for $C_{34}H_{24}N_6RuP_2F_{12}\cdot 0.3H_2O$: C 44.73, H 2.72, N 9.20; found C 44.50, H 2.50, N 8.96.

4-2-2: Other Chemicals, Physical Measurements, and Theoretical Calculations

The solvents used for spectroscopic and electrochemical measurements reported in this chapter were essentially the same with those described in Chapter 2. All of the physical measurements and theoretical calculations reported in this chapter were performed under the identical conditions to those described in Chapter 2.

4-3: Results and Discussion

4-3-1: Redox Potentials

The ancillary-ligand effects on the electronic structures of $[Ru(B_2bpy)L'_2]^{2+}$ including **2c** (L' = bpy) were evaluated by electrochemical measurements. The cyclic (CVs) and differential pulse voltammograms (DPVs) of the complexes in *N*,*N*-dimethylformamide (DMF) are shown in Figures 4-1 and 4-2, and the redox potentials of the complexes determined by the peak potentials of DPVs are summarized in Table 4-1. $[Ru(B_2bpy)L'_2]^{2+}$ showed quasi-reversible oxidation waves responsible for the metal oxidation (E_{ox}) at +0.72–+0.81 V vs. a ferrocene/ferrocenium ion redox couple (Fc/Fc^+). The E_{ox} value of **4dpbpy** (+0.76 V) was shifted to the negative direction compared to that of **2c** (+0.81 V), indicating the increase in the electron density on the ruthenium atom through the π-electron donation effects of the phenyl groups in the 4,4'-ph_2-bpy ligands. The E_{ox} value of **4dmbpy** (+0.72 V) was shifted to the more negative potential region than that of **dpbpy** owing to the stronger electron donating ability of the methyl group originated from the hyperconjugation of the groups in the 4,4'-me_2-bpy ligands. The effect

of the methyl groups in L' on E_{ox} was almost independent of the diimine-ligand structure as suggested by the comparable E_{ox} values of **4dmbpy** and **4dmphen** (+0.73 V). On the other hand, the E_{ox} value of **4dpphen** (+0.80 V) was more positive than that of **4dpbpy**. The difference in E_{ox} between **4dpphen** and **4dpbpy** is explainable by the weaker electron donating ability of **4dpphen** relative to that of **4dpbpy** owing to the larger dihedral angle between the phen and phenyl moieties (~52º estimated by the optimized geometry by DFT calculation) than that between the bpy and phenyl moieties in **4dpbpy** (~34º).

Similar to **2a** or **3a**, $[Ru(B_2bpy)L'_2]^{2+}$ also exhibited multiple reversible or quasi-reversible reduction waves ($E_{red1–5}$) originated from the ligand reductions. The first (E_{red1}), second (E_{red2}), and third reduction waves (E_{red3}) correspond to the sequential reductions of the three diimine moieties in a complex, and the fourth (E_{red4}) and fifth reduction waves (E_{red5}) are ascribed to the reduction of one and another DBDE groups in B_2bpy, respectively, as described in Chapter 2. The E_{red1} value of $[Ru(B_2bpy)L'_2]^{2+}$ (−1.52 to −1.56 V) are almost independent of L' and observed at a more positive potential region compared to $[Ru(bpy)_3]^{2+}$ (−1.71 V) or $[Ru(bpy)(phen)_2]^{2+}$ (−1.72 V). The results demonstrate that E_{red1} of the complexes are assigned to the reduction of B_2bpy, irrespective of L', and that the π*-orbital energy of the bpy moiety in B_2bpy is controlled primarily by the electron-withdrawing ability of the DBDE group. The reduction waves for E_{red2} and E_{red3} of the complexes are assigned to the reductions of L'. In practice, the $E_{red2/3}$ values of the complexes were dependent on L' while E_{red1} was comparable with each other, irrespective of L'.

Since the first oxidation and reduction potentials are related to the highest-energy occupied molecular orbital (HOMO) and lowest-energy unoccupied molecular orbital (LUMO) of a complex, respectively, the ancillary-ligand effects on HOMO and LUMO

of $[Ru(B_2bpy)L'_2]^{2+}$ were evaluated by DFT calculations. The Kohn–Sham MOs of the complexes are shown in Figures 4-3–4-8, and the details of the calculated MOs are summarized in Tables 4-2–4-7. The HOMO of the complex distributes primarily to the ruthenium atom and B_2bpy ligand irrespective of the complexes. The HOMO is localized on the ruthenium atom of the complex more largely in the presence of the stronger electron-donating groups in L' and, furthermore, the HOMO energy of $[Ru(B_2bpy)L'_2]^{2+}$ increases with an increase in the HOMO population on the ruthenium atom: **4dmbpy** (~59%, −5.90 eV) > **4dmphen** (~56%, −5.90 eV) > **4dpbpy** (~52%, −5.93 eV) > **4dpphen** (~44%, −5.94 eV) > **2c** (~41%, −5.97 eV) > **4phen** (~36%, −5.97 eV). The sequence of the HOMO energy mentioned above agrees with that of E_{ox} as confirmed by Scheme 4-2. Since the HOMO of $[Ru(B_2bpy)L'_2]^{2+}$ is characterized by the contributions from both d-orbital of the ruthenium(II) atom and π-orbital of the B_2bpy ligand, destabilization of the d-orbital energy by electron donation from the ancillary ligands is expected to increase the HOMO energy and the contribution of the ruthenium atom to HOMO. On the other hand, the LUMOs of $[Ru(B_2bpy)L'_2]^{2+}$ are localized on the B_2bpy ligand, irrespective of L', and the LUMO distributions and energies (−2.73 to −2.77 eV) of the complexes are comparable with one another. These results indicate that the LUMO of $[Ru(B_2bpy)L'_2]^{2+}$ is insensitive to L' similar to the results on E_{red1}. These redox potentials and MOs of the complexes suggest that the spectroscopic and photophysical properties of $[Ru(B_2bpy)L'_2]^{2+}$ are characterized by the electronic structures of the ancillary ligand and the main ligand (i.e., B_2bpy).

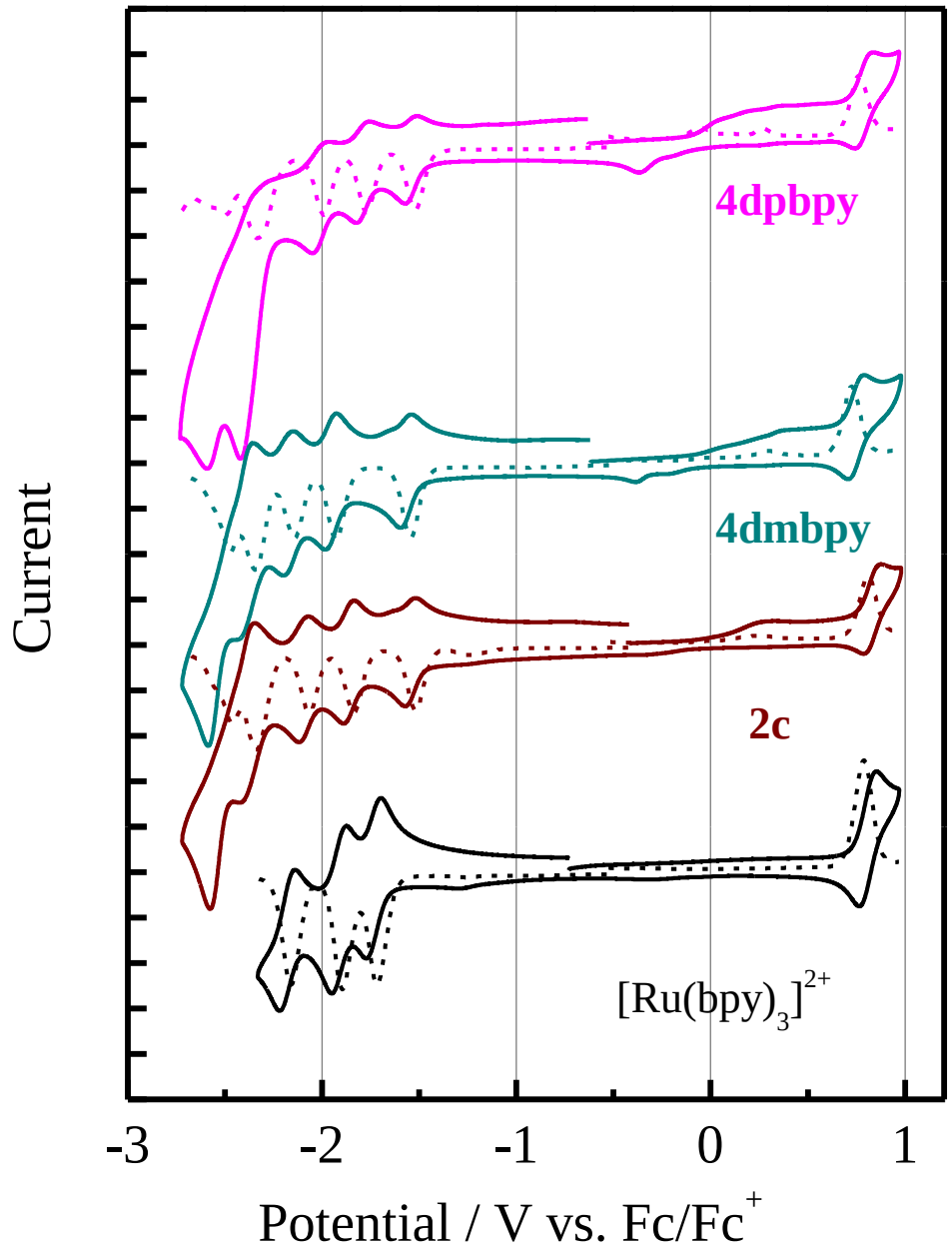

Figure 4-1. CVs (solid curves) and DPVs (broken curves) of **4dpbpy**, **4dmbpy**, **2c**, and $[Ru(bpy)_3]^{2+}$ in DMF containing 0.1-M $TBAPF_6$. The vertical-axis scale is 5 μA per division. The data for **2c** and $[Ru(bpy)_3]^{2+}$ were taken from Chapter 2.

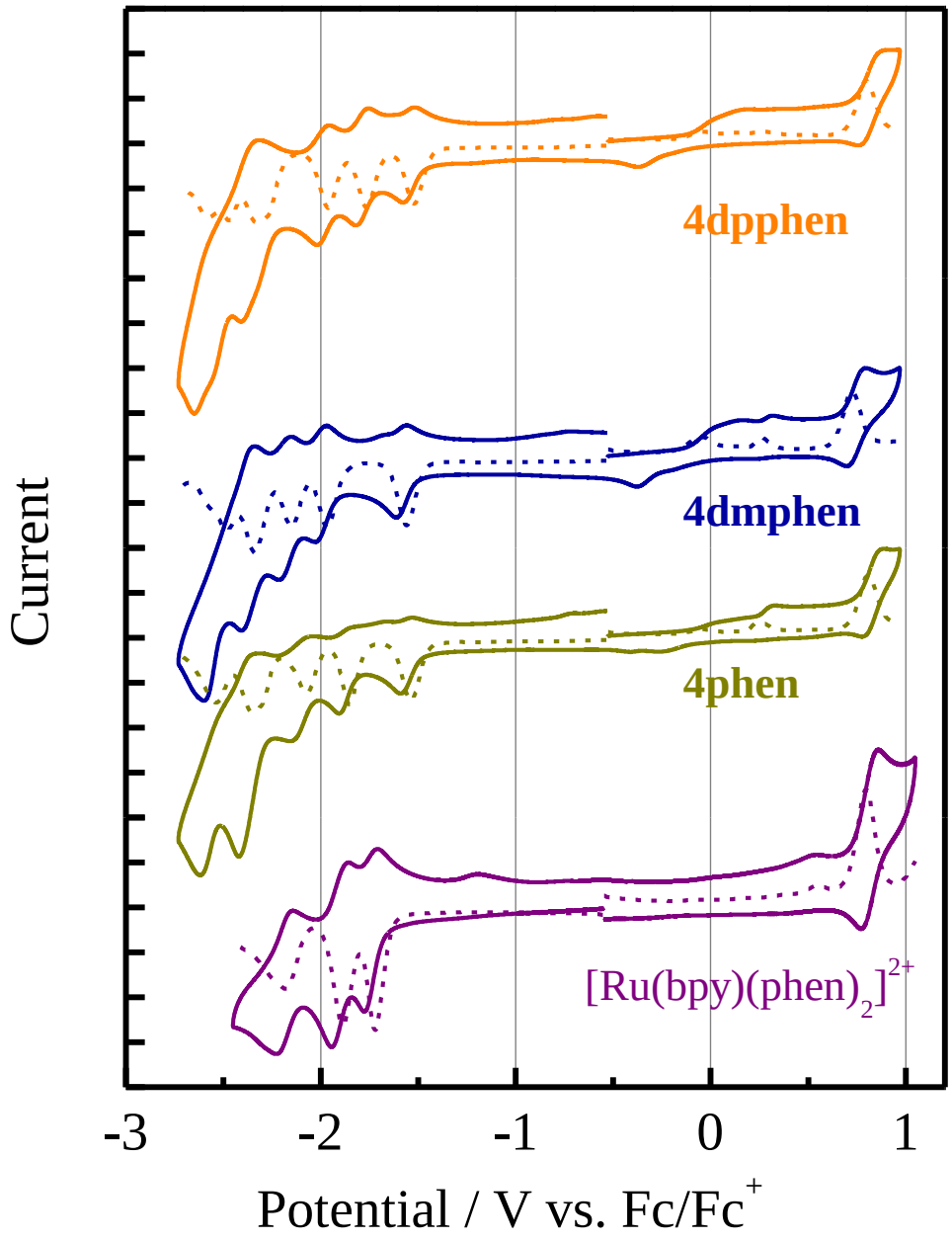

Figure 4-2. CVs (solid curves) and DPVs (broken curves) of **4dpphen**, **4dmphen**, **4phen**, and $[Ru(bpy)(phen)_2]^{2+}$ in DMF containing 0.1-M $TBAPF_6$. The vertical-axis scale is 5 μA per division.

Table 4-1. Redox potentials of the complexes in DMF containing 0.1-M $TBAPF_6$.

Complex	Potential E / V vs. Fc/Fc^+ [a]					
	red5	red4	red3	red2	red1	ox
4dpbpy	−2.49	−2.33	−1.99	−1.77	−1.52	+0.76
4dmbpy	−2.47	−2.34	−2.14	−1.93	−1.54	+0.72
2c [b]	−2.46	−2.34	−2.06	−1.83	−1.52	+0.81
$[Ru(bpy)_3]^{2+}$ [b]			−2.16	−1.90	−1.71	+0.79
4dpphen	−2.47	−2.33	−1.96	−1.76	−1.52	+0.80
4dmphen	−2.48	−2.34	−2.15	−1.97	−1.56	+0.73
4phen	−2.53	−2.35	−2.07	−1.85	−1.54	+0.81
$[Ru(bpy)(phen)_2]^{2+}$			−2.18	−1.89	−1.72	+0.80

[a] The values were determined by the peak potentials of DPV of the complexes.

[b] Data taken from Chapter 2.

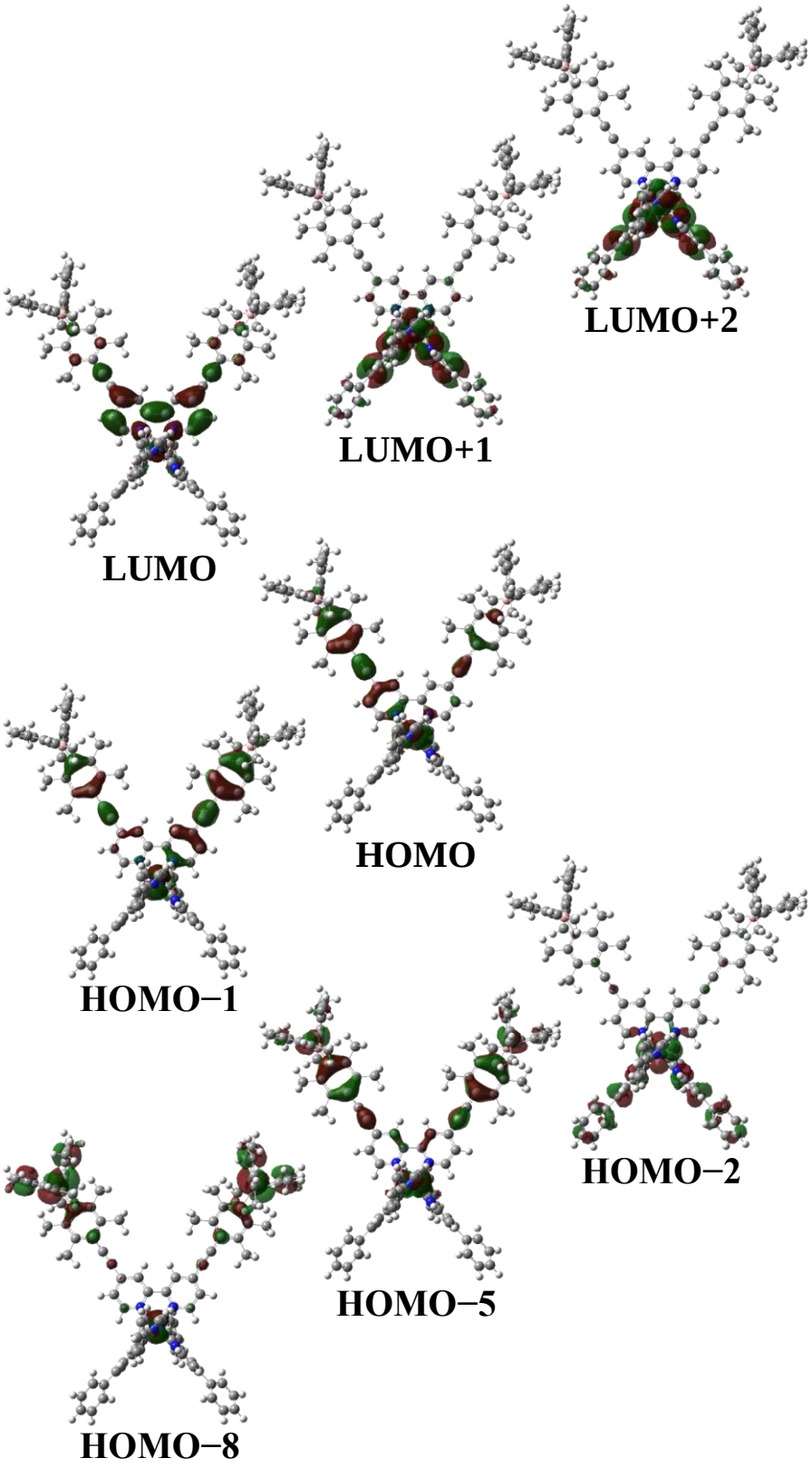

Figure 4-3. The Kohn–Sham MOs of **4dpbpy** (contour = 0.02 eÅ^{-3}).

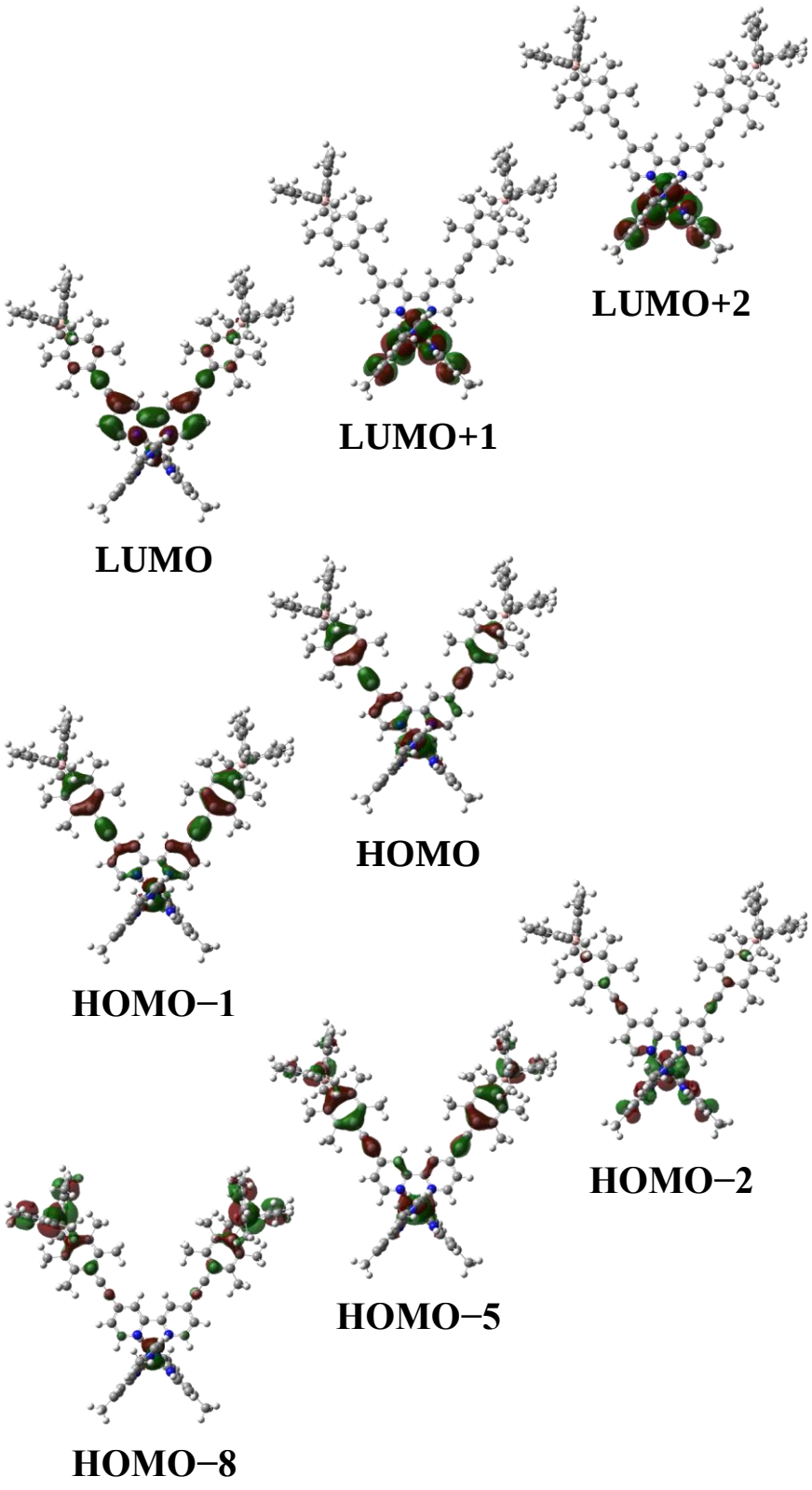

Figure 4-4. The Kohn–Sham MOs of **4dmbpy** (contour = 0.02 eÅ^{-3}).

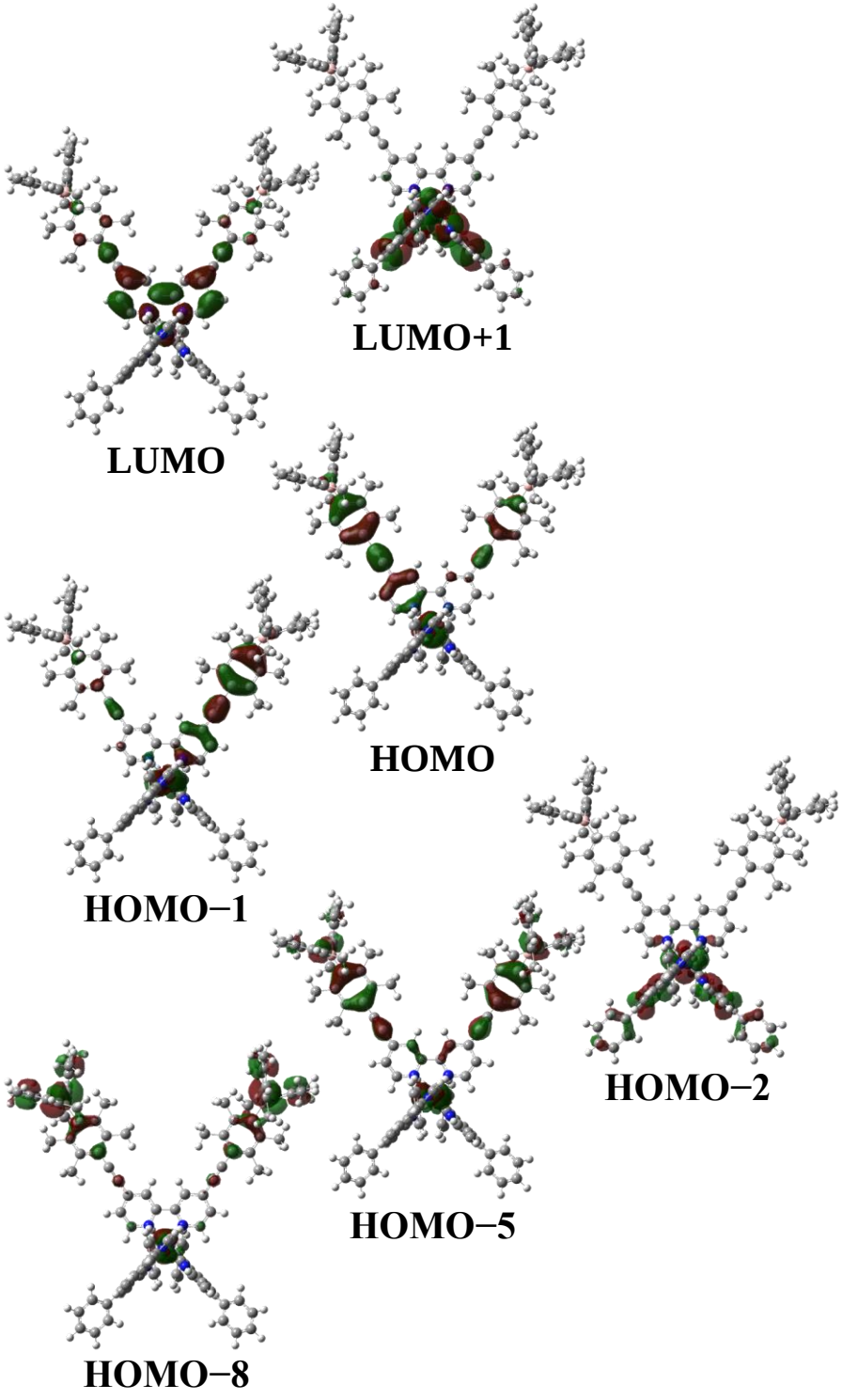

Figure 4-5. The Kohn–Sham MOs of **4dpphen** (contour = 0.02 eÅ^{-3}).

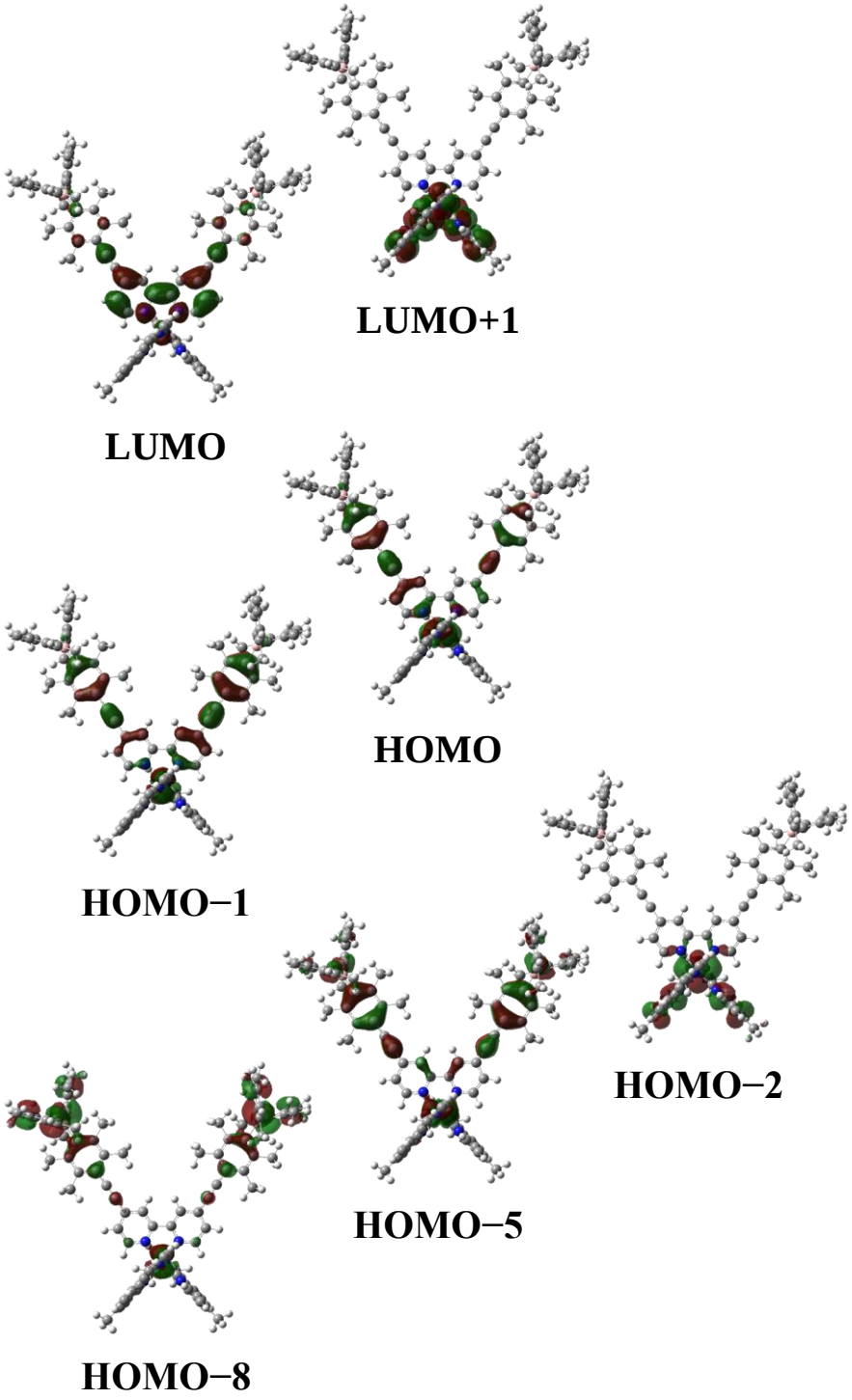

Figure 4-6. The Kohn–Sham MOs of **4dmphen** (contour = 0.02 eÅ^{-3}).

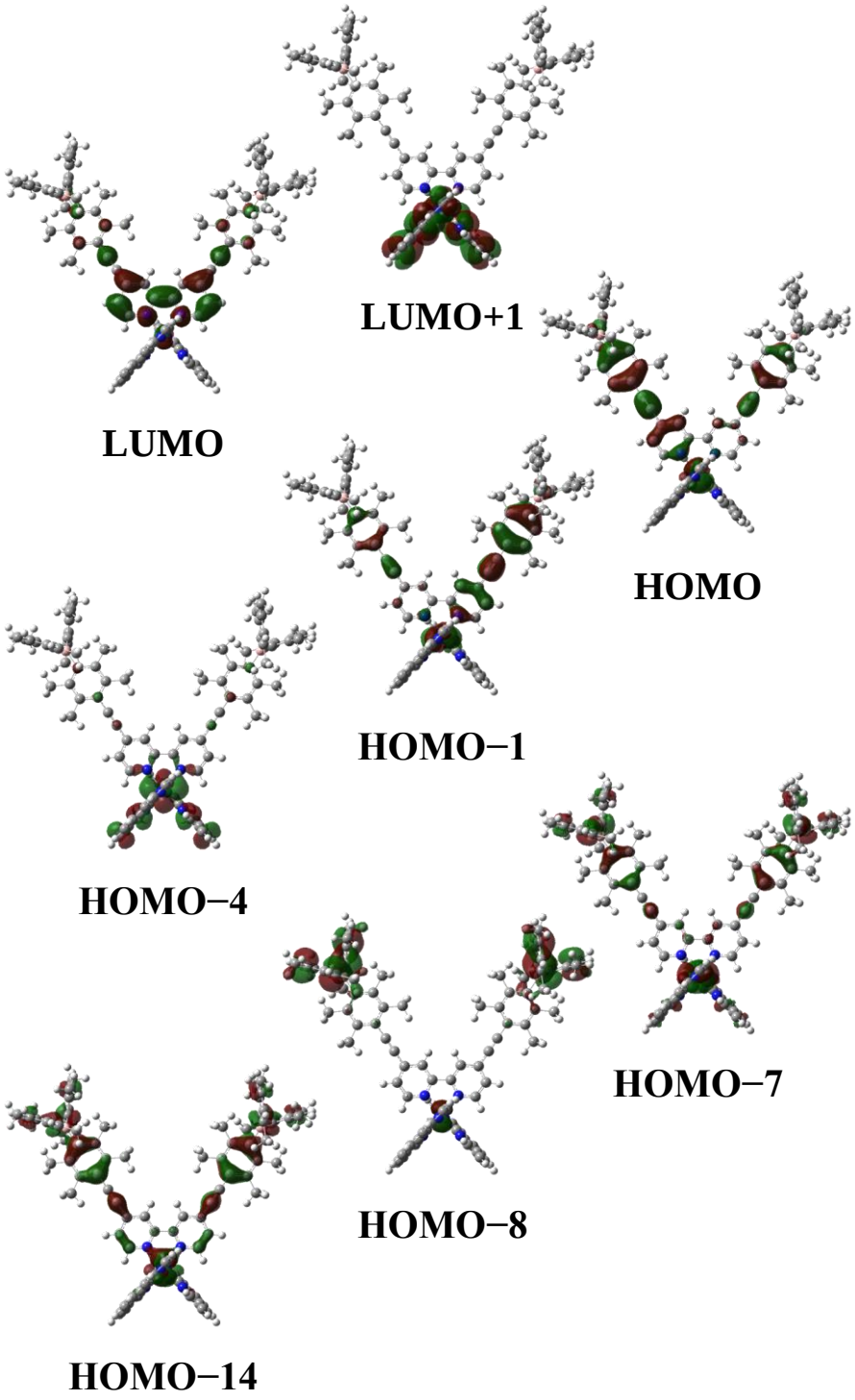

Figure 4-7. The Kohn–Sham MOs of **4phen** (contour = 0.02 eÅ^{-3}).

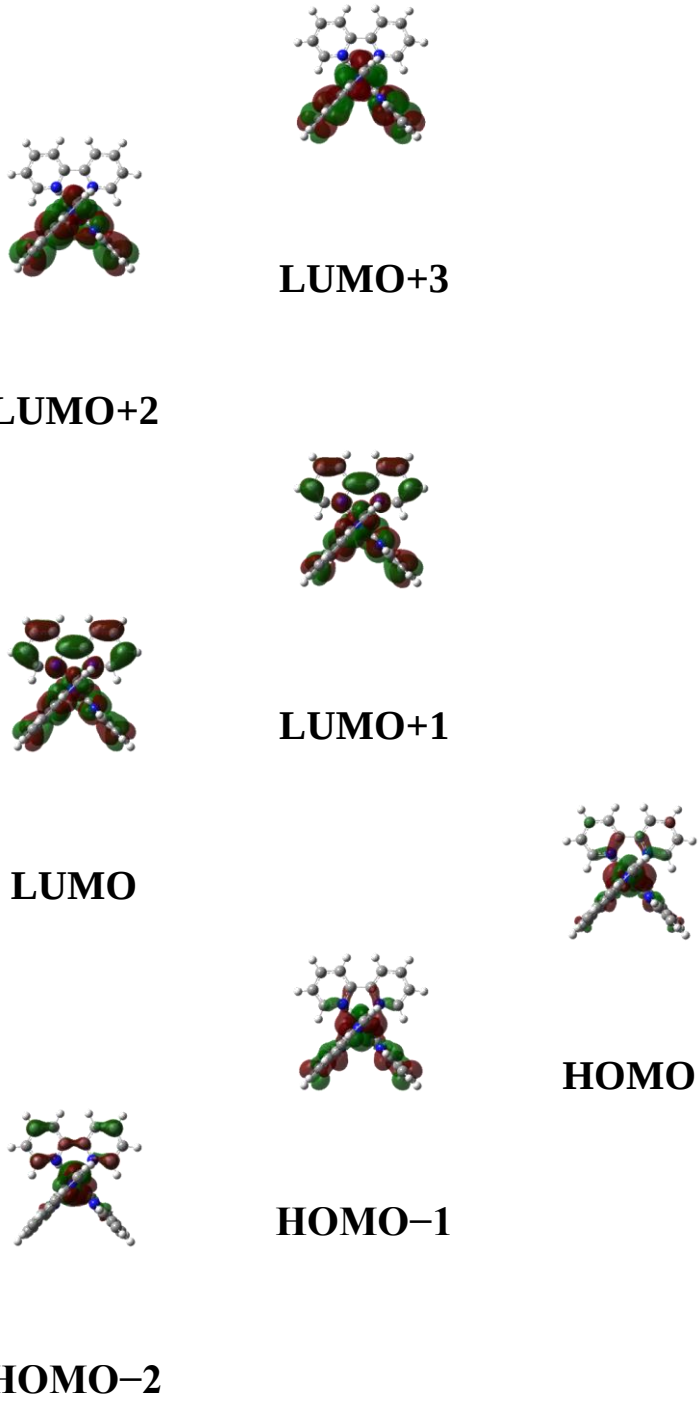

Figure 4-8. The Kohn–Sham MOs of $[Ru(bpy)(phen)_2]^{2+}$ (contour = 0.02 eÅ^{-3}).

Table 4-2. Calculated molecular orbitals of **4dpbpy** in CH_3CN.

Molecular Orbital	Eigenvalue / Hartrees	MO Population / %								
		ruthenium	B_2bpy					4,4'-ph_2-bpy	
			bpy	ethynyl	duryl	boron	mesityl	bpy	ph
LUMO+3	−0.08157	1.16	46.22	14.26	21.19	7.18	9.25	0.68	0.06
LUMO+2	−0.09314	7.64	1.00	0.03	0.02	0.00	0.01	79.81	11.49
LUMO+1	−0.09485	5.59	5.89	0.59	0.65	0.11	0.14	76.14	10.89
LUMO	−0.10148	4.63	67.38	7.59	7.71	0.95	1.36	9.26	1.12
HOMO	−0.21805	52.44	9.36	8.50	17.49	0.31	3.06	7.24	1.60
HOMO−1	−0.21819	41.73	10.18	11.61	24.03	0.42	4.20	6.32	1.51
HOMO−2	−0.22464	68.37	4.46	1.12	2.85	0.05	0.74	14.84	7.57
HOMO−3	−0.22748	0.00	0.00	0.05	11.48	1.07	87.40	0.00	0.00

Table 4-3. Calculated molecular orbitals of **4dmbpy** in CH_3CN.

Molecular Orbital	Eigenvalue / Hartrees	MO Population / %							
		ruthenium	B_2bpy					4,4'-me_2-bpy	
			bpy	ethynyl	duryl	boron	mesityl	bpy	me
LUMO+3	−0.08116	1.19	45.51	14.22	21.43	7.48	9.65	0.52	0.00
LUMO+2	−0.08712	6.67	0.96	0.04	0.02	0.00	0.00	88.31	4.00
LUMO+1	−0.08909	4.28	2.27	0.23	0.28	0.06	0.07	88.79	4.02
LUMO	−0.10052	5.67	70.92	8.01	8.22	1.06	1.49	4.49	0.14
HOMO	−0.21683	58.67	8.98	7.33	14.52	0.25	2.43	7.53	0.29
HOMO−1	−0.21731	44.30	10.32	11.40	22.93	0.40	3.89	6.49	0.27
HOMO−2	−0.22474	71.32	5.07	1.97	5.15	0.09	1.35	14.04	1.01
HOMO−3	−0.22745	0.00	0.00	0.05	11.57	1.07	87.31	0.00	0.00

Table 4-4. Calculated molecular orbitals of **4dpphen** in CH_3CN.

Molecular Orbital	Eigenvalue / Hartrees	MO Population / %							
		ruthenium	B_2bpy					4,7-ph_2-phen	
			bpy	ethynyl	duryl	boron	mesityl	phen	ph
LUMO+3	−0.08821	1.11	0.31	0.00	0.01	0.00	0.00	87.56	11.01
LUMO+2	−0.09049	7.69	1.12	0.04	0.04	0.01	0.01	82.03	9.06
LUMO+1	−0.09257	5.50	4.26	0.34	0.40	0.07	0.09	80.39	8.95
LUMO	−0.10136	5.00	69.13	7.83	7.95	0.99	1.41	7.08	0.61
HOMO	−0.21836	41.03	10.23	11.61	24.09	0.42	4.26	7.09	1.27
HOMO−1	−0.21848	49.02	9.82	9.40	19.60	0.34	3.46	7.21	1.15
HOMO−2	−0.22439	67.21	3.81	0.20	0.43	0.01	0.11	21.35	6.88
HOMO−3	−0.22748	0.00	0.00	0.05	11.46	1.07	87.42	0.00	0.00

Table 4-5. Calculated molecular orbitals of **4dmphen** in CH_3CN.

Molecular Orbital	Eigenvalue / Hartrees	MO Population / %								
		ruthenium	B_2bpy					4,7-me_2-phen	
			bpy	ethynyl	duryl	boron	mesityl	phen	me
LUMO+3	−0.08319	0.23	1.01	0.09	0.13	0.04	0.05	90.93	7.52
LUMO+2	−0.08432	1.61	0.50	0.02	0.01	0.00	0.01	90.64	7.21
LUMO+1	−0.08462	4.73	1.75	0.06	0.07	0.02	0.03	90.90	2.44
LUMO	−0.10029	5.93	71.44	8.12	8.36	1.08	1.53	3.48	0.06
HOMO	−0.21698	56.27	9.34	7.86	15.65	0.27	2.63	7.64	0.34
HOMO−1	−0.21727	44.17	10.27	11.27	22.63	0.39	3.84	7.09	0.34
HOMO−2	−0.22367	72.57	4.34	0.58	1.42	0.02	0.34	19.31	1.42
HOMO−3	−0.22744	0.00	0.00	0.05	11.56	1.07	87.32	0.00	0.00

Table 4-6. Calculated molecular orbitals of **4phen** in CH_3CN.

Molecular Orbital	Eigenvalue / Hartrees	MO Population / %							
		ruthenium	B_2bpy					phen	
			bpy	ethynyl	duryl	boron	mesityl	phen	
LUMO+3	−0.08539	1.13	0.43	0.00	0.00	0.00	0.00	98.44	
LUMO+2	−0.08944	7.59	1.12	0.05	0.05	0.01	0.02	91.16	
LUMO+1	−0.09129	5.12	2.97	0.21	0.25	0.05	0.06	91.34	
LUMO	−0.10164	5.28	70.89	7.98	8.09	1.00	1.43	5.33	
HOMO	−0.21950	36.45	10.87	13.14	28.37	0.49	5.27	5.41	
HOMO−1	−0.21965	43.40	10.72	11.14	24.18	0.42	4.49	5.65	
HOMO−2	−0.22751	0.00	0.00	0.05	11.45	1.07	87.43	0.00	
HOMO−3	−0.22770	0.00	0.01	0.05	11.78	1.07	87.09	0.00	

Table 4-7. Calculated molecular orbitals of $[Ru(bpy)(phen)_2]^{2+}$ in CH_3CN.

Molecular Orbital	Eigenvalue / Hartrees	MO Population / %							
		ruthenium	bpy					phen	
			bpy					phen	
LUMO+3	−0.08548	1.14	0.39					98.47	
LUMO+2	−0.08955	7.70	1.30					91.00	
LUMO+1	−0.09034	7.25	38.62					54.13	
LUMO	−0.09361	2.16	54.21					43.63	
HOMO	−0.22610	83.43	5.66					10.91	
HOMO−1	−0.23020	74.77	4.51					20.72	
HOMO−2	−0.23165	77.81	8.56					13.63	
HOMO−3	−0.26461	4.37	1.42					94.21	

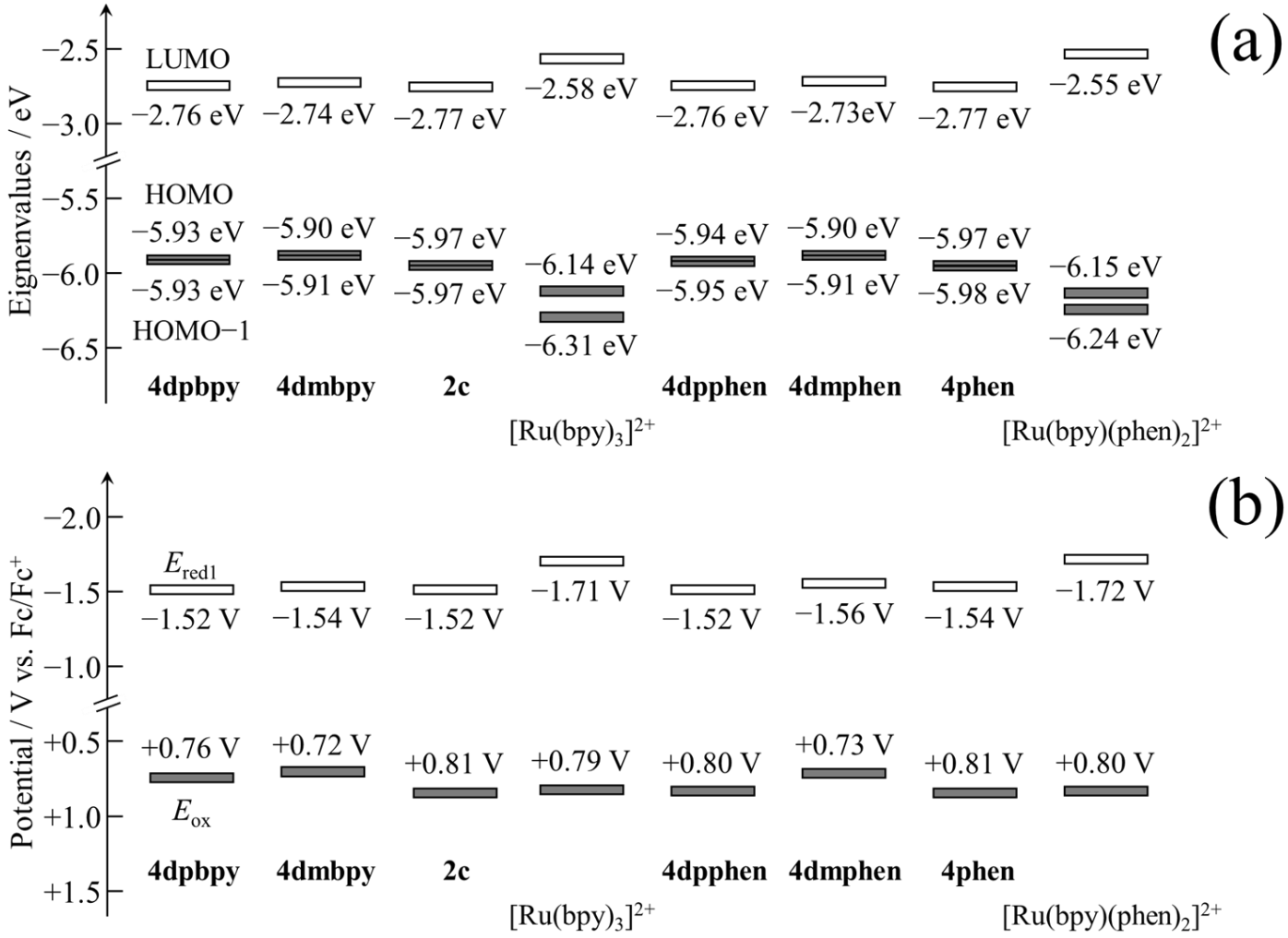

Scheme 4-2. Calculated HOMO/LUMO energies (a) and redox potentials (b) of the complexes.

4-3-2: Absorption Spectra

Figure 4-9 shows the absorption spectra of the complexes in CH_3CN at 298 K. The absorption maximum wavelength (λ_{abs}) and corresponding molar absorption coefficients (ε) are summarized in Table 4-8. All of the complexes show the intense absorption bands in <340 nm, and they are assigned to the $^1\pi\pi^*$ transitions of the diimine ligands. Although the methyl groups in L' did not affect the λ_{abs} value of the $^1\pi\pi^*$ band, the absorption band of **4dpbpy** (λ_{abs} = 309 nm) or **4dpphen** (λ_{abs} = 279 nm) was shifted to the longer wavelength compared to that of **2c** (λ_{abs} = 289 nm) or **4phen** (λ_{abs} = 263 nm), respectively. Since the energy difference in the absorption bands (in a wavenumber scale) between these complexes is almost independent of the diimine-ligand structure (~2200 cm^{-1}), the lower-energy shift of the band observed for **4dpbpy** relative to **2c** is explainable by stabilization of the π^*-orbital energy of L' by the introduction of the phenyl groups to L'. Furthermore, $[Ru(B_2bpy)L'_2]^{2+}$ exhibits a characteristic absorption band in 300–400 nm, which is the superposition of the $^1\pi\pi^*$ band in the durylethynyl-bpy moiety and the π(aryl)–p(B) CT band in the triarylborane moieties as described in Chapter 2.

$[Ru(B_2bpy)L'_2]^{2+}$ showed the longer-wavelength shifted (i.e., lower-energy shift) and intense ^{1}MLCT absorption band (λ_{abs} = 480–493 nm) compared to $[Ru(bpy)_3]^{2+}$ (λ_{abs} = 451 nm) or $[Ru(bpy)(phen)_2]^{2+}$ (λ_{abs} = 446 nm). The lower-energy shifts of the ^{1}MLCT bands of these complexes would be originated primarily from the low-energy π^*-orbital of the B_2bpy ligand as described above. Furthermore, the phenyl or methyl groups in L' of the complex gave a further lower-energy shift of the ^{1}MLCT band by 300–500 cm^{-1}, presumably due to destabilization of the ground state of the complex as suggested by the electrochemical data. To evaluate the ancillary-ligand effects on the ^{1}MLCT absorption, the ^{1}MLCT absorption maximum energies (E_{abs}) of $[Ru(B_2bpy)L'_2]^{2+}$ were plotted against

the difference in the redox potentials ($E_{ox} - E_{red}$) in Figure 4-10, together with the relevant data of the reference complexes[4] including the complexes described in Chapter 2 (i.e., $[Ru(B_2bpy)_3]^{2+}$ (**2a**), $[Ru(B_2bpy)_2(bpy)]^{2+}$ (**2b**) and $[Ru\{4\text{-DBDE-bpy}\}_n(bpy)_{3-n}]^{2+}$ (**2a'**–**c'**)). A good proportional relationship between E_{abs} and ($E_{ox} - E_{red}$) with the slope of 1.09 eV/V (r = 0.9998) demonstrates that the ^{1}MLCT absorption energy of $[Ru(B_2bpy)L'_2]^{2+}$ is manipulated synthetically by the electron-donating ability of the ancillary ligand(s) through the control of the redox potentials of the complex.

The molar absorption coefficient of the ^{1}MLCT band (ε_{MLCT}) of $[Ru(B_2bpy)L'_2]^{2+}$ (ε_{MLCT} = (2.2–3.3) × 10^4 $M^{-1}cm^{-1}$) was larger than that of the relevant reference complex $[Ru(bpy)_3]^{2+}$ (ε_{MLCT} = 1.3 × 10^4 $M^{-1}cm^{-1}$) or $[Ru(bpy)(phen)_2]^{2+}$ (ε_{MLCT} = 1.7 × 10^4 $M^{-1}cm^{-1}$). Such enhancement of ε_{MLCT} is explainable by the synergistic MLCT/π(aryl)–p(B) CT interactions as described in Chapter 2. Furthermore, the larger ε_{MLCT} values relative to those of **2c** and **4phen** (ε_{MLCT} = 2.4 × 10^4 $M^{-1}cm^{-1}$) were observed for **4dpbpy** (ε_{MLCT} = 3.3 × 10^4 $M^{-1}cm^{-1}$) and **4dpphen** (ε_{MLCT} = 3.1 × 10^4 $M^{-1}cm^{-1}$). The large ε_{MLCT} values of the complexes suggest an increase in the MLCT absorption transition dipole moment by introduction of the phenyl groups to L'.

To reveal more details about the ancillary-ligand effects on the absorption spectrum, TD-DFT calculations were performed for $[Ru(B_2bpy)L'_2]^{2+}$. The absorption transition energies and the relevant oscillator strengths (f) for the singlet excited states of $[Ru(B_2bpy)L'_2]^{2+}$ and $[Ru(bpy)(phen)_2]^{2+}$ are summarized in Tables 4-9–4-14, and the relevant data on **2c** and $[Ru(bpy)_3]^{2+}$ have been reported in Chapter 2. The calculated results are compared with the observed absorption spectra in Figure 4-11, in which the calculated transitions are shifted to the lower-energy by 5% to correct the overestimation of the transition energy by TD-DFT.[5] As clearly seen in Figure 4-11, TD-DFT

calculations explain very well the low-energy and intense ^{1}MLCT absorption observed for $[Ru(B_2bpy)L'_2]^{2+}$. The HOMO−5, HOMO−1, and HOMO of **4dpbpy**, **4dmbpy**, **4dpphen** and **4dmphen** or HOMO−7, HOMO−1, and HOMO of **2c** and **4phen** distribute to the relevant ruthenium–B_2bpy moiety, and LUMO is localized on the respective B_2bpy ligand. Therefore, the lowest-energy singlet excited state (S_1) of $[Ru(B_2bpy)L'_2]^{2+}$ is ascribed primarily to the synergistic MLCT/π(aryl)–p(B) CT/ππ*(durylethynyl-bpy) transition (100% for **2c** and 77–80% for the other complexes). Furthermore, the partial contributions of the HOMO−2→LUMO transitions in **4dpbpy**, **4dmbpy**, **4dpphen**, and **4dmphen** or HOMO−4→LUMO transition in **4phen** to S_1 (20–23%) suggest mixing between the MLCT and Ligand-to-Ligand Charge Transfer (LLCT) transitions in the excited states of these complexes, since the HOMO−2 of **4dpbpy**, **4dmbpy**, **4dpphen** and **4dmphen** or HOMO−4 of **4phen** distribute to the relevant ruthenium atoms and ancillary ligands. In particular, the HOMO−2 of **4dpbpy** or **4dpphen** is populated on the phenyl groups in L' (7–8%) and, therefore, the resulting larger absorption transition dipole moment relative to that of **2c** or **4phen** would results in the larger ε_{MLCT} value of **4dpbpy** or **4dpphen**, respectively, than that of **2c** or **4phen**. As the results, the low-energy and intense ^{1}MLCT absorption observed for $[Ru(B_2bpy)L'_2]^{2+}$ including its ancillary-ligand effects can be explained successfully by the results on the TD-DFT calculations.

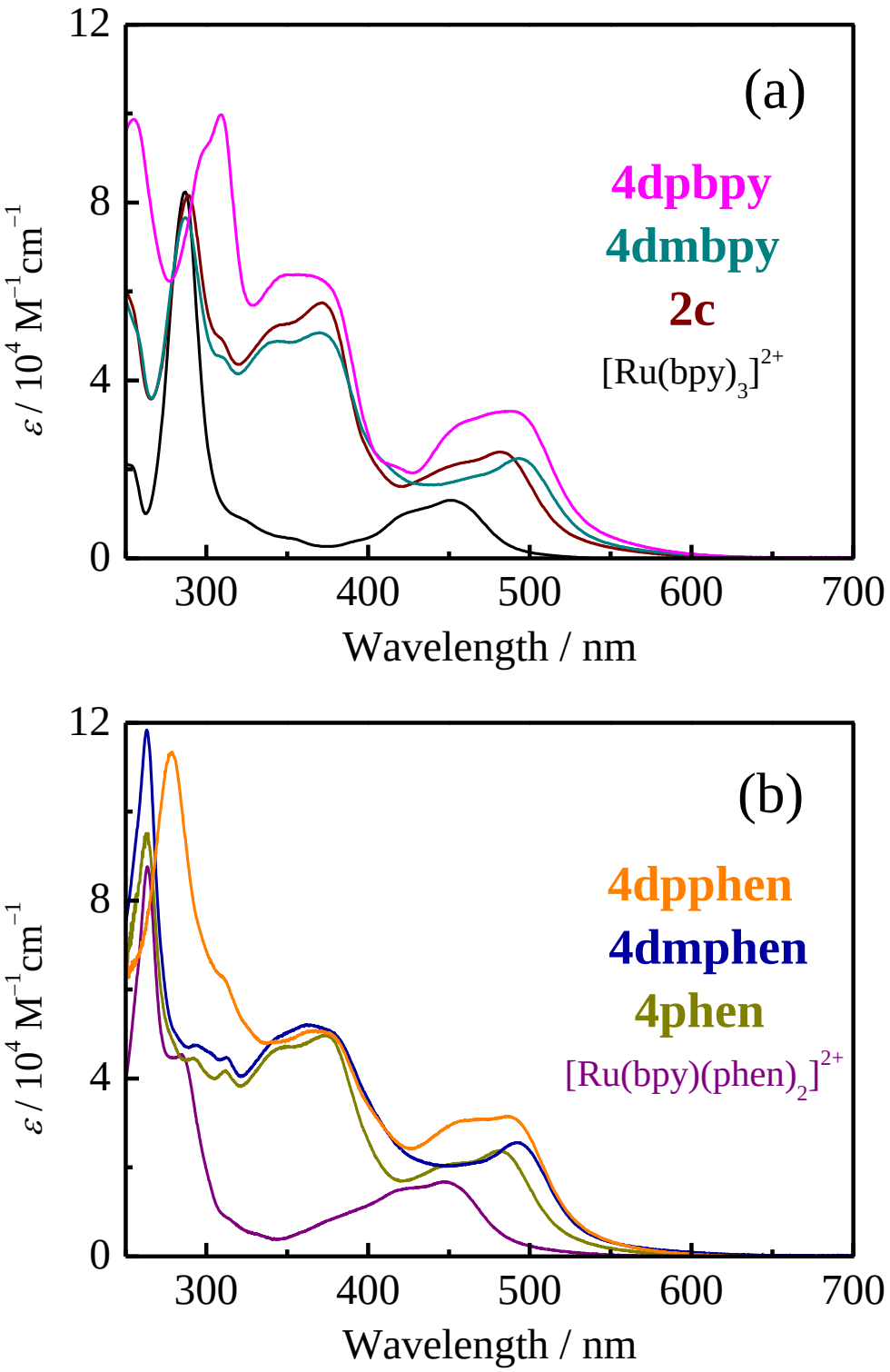

Figure 4-9. Absorption spectra of the complexes (**4dpbpy**, **4dmbpy**, **2c**, and $[Ru(bpy)_3]^{2+}$ (a) and **4dpphen**, **4dmphen**, **4phen**, and $[Ru(bpy)(phen)_2]^{2+}$ (b)) in CH_3CN at 298 K. The data for **2c** and $[Ru(bpy)_3]^{2+}$ were taken from Chapter 2.

Table 4-8. Absorption parameters of the complexes in CH_3CN at 298 K.

Complex	λ_{abs} / nm (ε / 10^4 $M^{-1}cm^{-1}$)		
4dpbpy	309 (10)	374sh (6.2)	490 (3.3)
4dmbpy	287 (7.7)	371 (5.1)	493 (2.2)
2c [a]	289 (8.2)	371 (5.7)	481 (2.4)
$[Ru(bpy)_3]^{2+}$ [a]	287 (8.2)		451 (1.3)
4dpphen	279 (11)	378sh (5.0)	487 (3.1)
4dmphen	263 (12)	377sh (5.1)	491 (2.5)
4phen	263 (9.5)	374 (5.0)	480 (2.4)
$[Ru(bpy)(phen)_2]^{2+}$	264 (8.7)		446 (1.7)

[a] Data taken from Chapter 2.

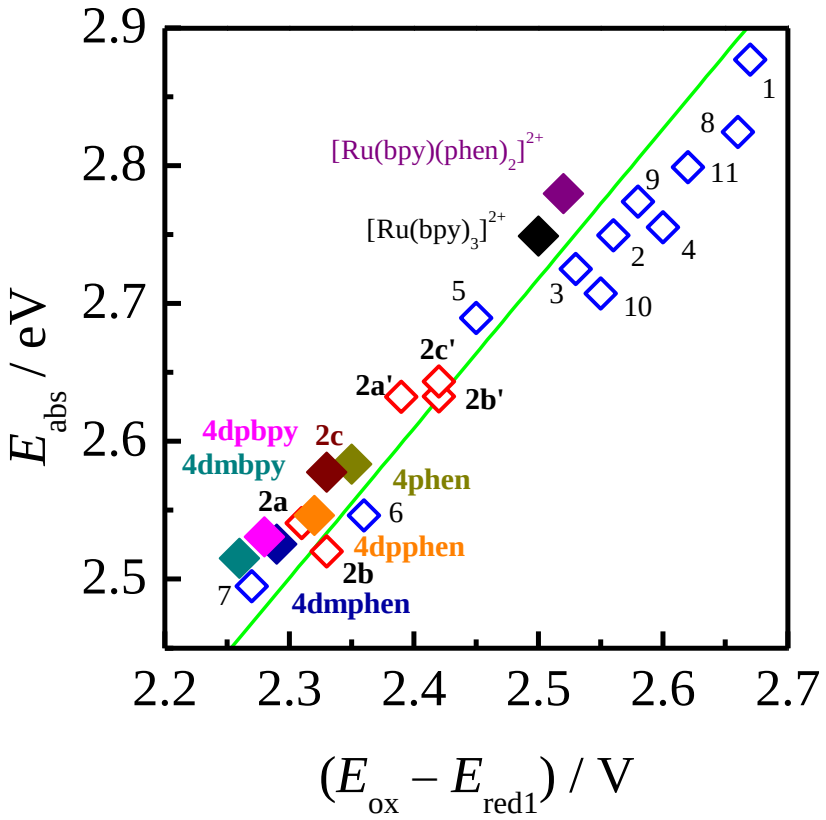

Figure 4-10. Relationship between the E_{abs} and (E_{ox} − E_{red1}) values of ruthenium(II) complexes. Red open boxes represent the data on the arylborane–ruthenium(II) complexes described in Chapter 2. Blue open boxes represent the data on the $[RuL_3]^{2+}$ complexes reported by Tazuke *et al.* (L = 2-(2-pyridyl)pyrimidine (1), 4-methyl-2-(2-pyridyl)pyrimidine (2), 5-phenyl-2-(2-pyridyl)pyrimidine (3), 2,2'-bipyrimidine (4), 6-methyl-4-(2-pyridyl)pyrimidine (5), 6-phenyl-4-(2-pyridyl)pyrimidine (6), 6,6'-dimethyl-4,4'-bipyrimidine (7), 2,2'-bipyrazine (8), 3,3'-bipyridazine (9), 4,4'-dimethyl-bpy (10), phen (11)) in CH_3CN at 298 K whose data were taken from [4]. The data on $[Ru(B_2bpy)L'_2]^{2+}$ are taken from Tables 4-1 and 4-8. The green line represents the linear regression between E_{abs} and (E_{ox} − E_{red1}), in which the intercept has been fixed at 0 eV.

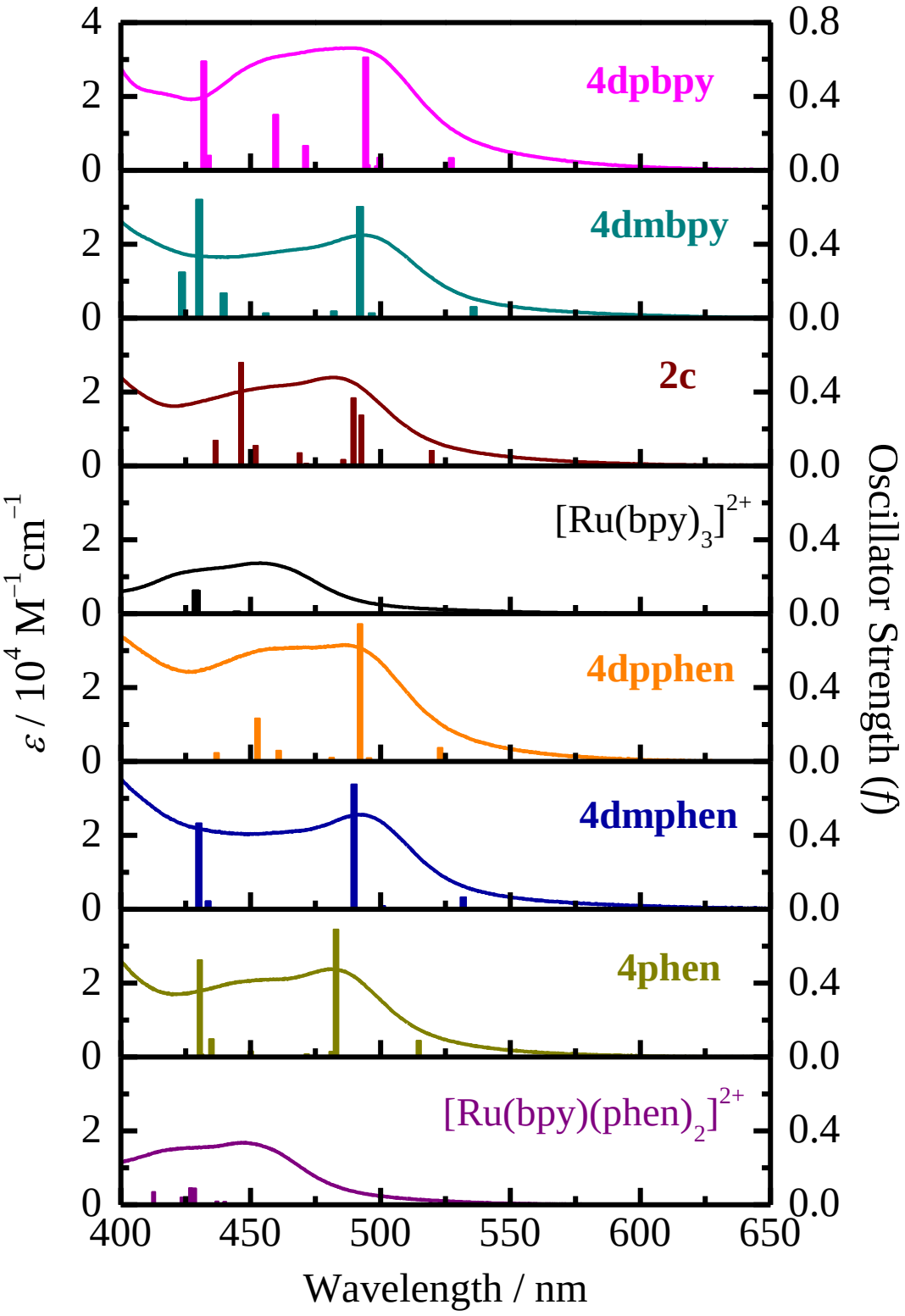

Figure 4-11. Comparison of the observed absorption spectra and oscillator strengths (perpendicular bars) estimated by TD-DFT calculations for the complexes in CH_3CN at 298 K. The data for **2c** and $[Ru(bpy)_3]^{2+}$ were taken from Chapter 2.

Table 4-9. Calculated excited states of **4dpbpy** in CH_3CN.

Excited State	Transition	Energy (Wavelength)	Oscillator Strength
S_1	HOMO−5 → LUMO (18%) HOMO−2 → LUMO (23%) HOMO → LUMO (59%)	2.4689 eV (502.18 nm)	0.0671
S_2	HOMO−5 → LUMO+2 (23%) HOMO−2 → LUMO+2 (19%) HOMO → LUMO+2 (58%)	2.6050 eV (475.95 nm)	0.0690
S_3	HOMO−5 → LUMO+1 (15%) HOMO−2 → LUMO+1 (22%) HOMO → LUMO (18%) HOMO → LUMO+1 (45%)	2.6097 eV (475.09 nm)	0.0234
S_4	HOMO−2 → LUMO (57%) HOMO−1 → LUMO (12%) HOMO−1 → LUMO+2 (12%) HOMO → LUMO+1 (19%)	2.6301 eV (471.40 nm)	0.0286
S_5	HOMO−8 → LUMO (9%) HOMO−2 → LUMO+2 (12%) HOMO−1 → LUMO (43%) HOMO−1 → LUMO+1 (12%) HOMO → LUMO (11%) HOMO → LUMO+2 (13%)	2.6334 eV (470.81 nm)	0.6115
S_6	HOMO−14→ LUMO+2 (15%) HOMO−8 → LUMO+2 (19%) HOMO−1 → LUMO+2 (54%) HOMO → LUMO+2 (12%)	2.7338 eV (453.52 nm)	0.0036
S_7	HOMO−14→ LUMO+1 (13%) HOMO−8 → LUMO+1 (17%) HOMO−1 → LUMO+1 (57%) HOMO → LUMO+1 (13%)	2.7633 eV (448.69 nm)	0.1322
S_8	HOMO−2 → LUMO+1 (66%) HOMO−1 → LUMO+2 (34%)	2.8325 eV (437.72 nm)	0.3013
S_9	HOMO−2 → LUMO+2 (67%) HOMO−1 → LUMO+1 (33%)	3.0009 eV (413.16 nm)	0.0793
S_{10}	HOMO−11→ LUMO (13%) HOMO−5 → LUMO (58%) HOMO−2 → LUMO (11%) HOMO−1 → LUMO+3 (18%)	3.0141 eV (411.35 nm)	0.5903

Table 4-10. Calculated excited states of **4dmbpy** in CH_3CN.

Excited State	Transition	Energy (Wavelength)	Oscillator Strength
S_1	HOMO−5 → LUMO (15%) HOMO−2 → LUMO (23%) HOMO → LUMO (62%)	2.4297 eV (510.29 nm)	0.0596
S_2	HOMO−2 → LUMO	2.6214 eV (472.98 nm)	0.0260
S_3	HOMO−8 → LUMO (14%) HOMO−1 → LUMO (74%) HOMO−1 → LUMO+1 (12%)	2.6454 eV (468.68 nm)	0.6031
S_4	HOMO−5 → LUMO+1 (15%) HOMO−2 → LUMO+1 (19%) HOMO → LUMO+1 (53%) HOMO → LUMO+2 (13%)	2.6972 eV (459.68 nm)	0.0039
S_5	HOMO−5 → LUMO+2 (15%) HOMO−2 → LUMO+2 (20%) HOMO−1 → LUMO (13%) HOMO → LUMO+2 (52%)	2.7005 eV (459.11 nm)	0.0372
S_6	HOMO−14→ LUMO+2 (16%) HOMO−8 → LUMO+2 (18%) HOMO−5 → LUMO+1 (10%) HOMO−1 → LUMO+2 (56%)	2.8387 eV (436.77 nm)	0.0043
S_7	HOMO−14→ LUMO+1 (15%) HOMO−8 → LUMO+1 (17%) HOMO−5 → LUMO+2 (10%) HOMO−1 → LUMO+1 (58%)	2.8558 eV (434.15 nm)	0.0256
S_8	HOMO−2 → LUMO+1 (68%) HOMO−1 → LUMO+2 (32%)	2.9610 eV (418.72 nm)	0.1357
S_9	HOMO−11→ LUMO (12%) HOMO−5 → LUMO (53%) HOMO−2 → LUMO (15%) HOMO−1 → LUMO+3 (20%)	3.0256 eV (409.78 nm)	0.6425
S_{10}	HOMO−2 → LUMO+2 (73%) HOMO−1 → LUMO+1 (27%)	3.0734 eV (403.42 nm)	0.2488

Table 4-11. Calculated excited states of **4dpphen** in CH_3CN.

Excited State	Transition	Energy (Wavelength)	Oscillator Strength
S_1	HOMO−5 → LUMO (18%) HOMO−2 → LUMO (20%) HOMO−1 → LUMO (47%) HOMO → LUMO (15%)	2.4892 eV (498.08 nm)	0.0733
S_2	HOMO−2 → LUMO (84%) HOMO−2 → LUMO+1 (16%)	2.6270 eV (471.95 nm)	0.0173
S_3	HOMO−8 → LUMO (18%) HOMO → LUMO (82%)	2.6457 eV (468.63 nm)	0.7441
S_4	HOMO−5 → LUMO+1 (21%) HOMO−2 → LUMO+1 (19%) HOMO−1 → LUMO+1 (45%) HOMO → LUMO+1 (15%)	2.6938 eV (460.26 nm)	0.0076
S_5	HOMO−5 → LUMO+2 (21%) HOMO−2 → LUMO+2 (20%) HOMO−1 → LUMO+2 (44%) HOMO → LUMO+2 (15%)	2.7053 eV (458.31 nm)	0.0197
S_6	HOMO−12→ LUMO+2 (10%) HOMO−8 → LUMO+2 (16%) HOMO−2 → LUMO+1 (30%) HOMO → LUMO+2 (44%)	2.8079 eV (441.55 nm)	0.0009
S_7	HOMO−12→ LUMO+1 (10%) HOMO−8 → LUMO+1 (15%) HOMO−2 → LUMO+2 (26%) HOMO → LUMO+1 (49%)	2.8251 eV (438.87 nm)	0.0578
S_8	HOMO−2 → LUMO+1 (83%) HOMO−1 → LUMO+2 (17%)	2.8763 eV (431.05 nm)	0.2323
S_9	HOMO−5 → LUMO+3 (17%) HOMO−2 → LUMO+3 (19%) HOMO−1 → LUMO+2 (9%) HOMO−1 → LUMO+3 (41%) HOMO → LUMO+3 (14%)	2.9164 eV (425.13 nm)	0.0072
S_{10}	HOMO−5 → LUMO+4 (18%) HOMO−2 → LUMO+1 (9%) HOMO−2 → LUMO+4 (12%) HOMO−1 → LUMO+4 (45%) HOMO → LUMO+4 (16%)	2.9795 eV (416.12 nm)	0.0448

Table 4-12. Calculated excited states of **4dmphen** in CH_3CN.

Excited State	Transition	Energy (Wavelength)	Oscillator Strength
S_1	HOMO−5 → LUMO (18%) HOMO−2 → LUMO (22%) HOMO → LUMO (60%)	2.4473 eV (506.62 nm)	0.0644
S_2	HOMO−2 → LUMO	2.6000 eV (476.86 nm)	0.0191
S_3	HOMO−8 → LUMO (16%) HOMO−1 → LUMO (84%)	2.6577 eV (466.50 nm)	0.6756
S_4	HOMO−5 → LUMO+4 (21%) HOMO−2 → LUMO+4 (21%) HOMO → LUMO+4 (58%)	2.8364 eV (437.12 nm)	0.0042
S_5	HOMO−5 → LUMO+1 (20%) HOMO−2 → LUMO+1 (22%) HOMO → LUMO+1 (58%)	2.8379 eV (436.88 nm)	0.0063
S_6	HOMO−8 → LUMO+1 (11%) HOMO−5 → LUMO+2 (9%) HOMO−2 → LUMO+2 (11%) HOMO−1 → LUMO+1 (32%) HOMO → LUMO+2 (29%) HOMO → LUMO+4 (8%)	2.9575 eV (419.22 nm)	0.0001
S_7	HOMO−14→ LUMO+4 (13%) HOMO−8 → LUMO+4 (22%) HOMO−1 → LUMO+4 (65%)	2.9586 eV (419.06 nm)	0.0019
S_8	HOMO−5 → LUMO+2 (15%) HOMO−2 → LUMO+4 (42%) HOMO → LUMO+2 (43%)	2.9876 eV (415.00 nm)	0.0105
S_9	HOMO−5 → LUMO+3 (21%) HOMO−2 → LUMO+3 (15%) HOMO → LUMO+3 (64%)	3.0020 eV (413.00 nm)	0.0441
S_{10}	HOMO−11→ LUMO (11%) HOMO−5 → LUMO (53%) HOMO−2 → LUMO+1 (17%) HOMO−1 → LUMO+5 (19%)	3.0271 eV (409.59 nm)	0.4656

Table 4-13. Calculated excited states of **4phen** in CH_3CN.

Excited State	Transition	Energy (Wavelength)	Oscillator Strength
S_1	HOMO−7 → LUMO (15%) HOMO−4 → LUMO (23%) HOMO−1 → LUMO (48%) HOMO → LUMO (14%)	2.5294 eV (490.17 nm)	0.0889
S_2	HOMO−14→ LUMO (16%) HOMO−8 → LUMO (12%) HOMO → LUMO (72%)	2.6961 eV (459.86 nm)	0.6913
S_3	HOMO−4 → LUMO (83%) HOMO−4 → LUMO+1 (17%)	2.7056 eV (458.25 nm)	0.0282
S_4	HOMO−7 → LUMO+1 (14%) HOMO−4 → LUMO+1 (19%) HOMO−4 → LUMO+2 (8%) HOMO−1 → LUMO+1 (36%) HOMO−1 → LUMO+2 (15%) HOMO → LUMO+1 (8%)	2.7584 eV (449.48 nm)	0.0049
S_5	HOMO−7 → LUMO+2 (16%) HOMO−4 → LUMO+2 (23%) HOMO−1 → LUMO+2 (39%) HOMO → LUMO (8%) HOMO → LUMO+2 (14%)	2.7602 eV (449.18 nm)	0.0156
S_6	HOMO−14→ LUMO+2 (19%) HOMO−8 → LUMO+2 (15%) HOMO−4 → LUMO+1 (20%) HOMO → LUMO+2 (46%)	2.8774 eV (430.89 nm)	0.0048
S_7	HOMO−14→ LUMO+1 (18%) HOMO−8 → LUMO+1 (13%) HOMO−4 → LUMO+2 (21%) HOMO → LUMO+1 (48%)	2.8925 eV (428.65 nm)	0.0308
S_8	HOMO−4 → LUMO+1	2.9929 eV (414.25 nm)	0.0977
S_9	HOMO−7 → LUMO+2 (12%) HOMO−7 → LUMO+3 (12%) HOMO−4 → LUMO+3 (20%) HOMO−1 → LUMO+2 (8%) HOMO−1 → LUMO+3 (37%) HOMO → LUMO+3 (11%)	3.0206 eV (410.46 nm)	0.0132
S_{10}	HOMO−11→ LUMO (20%) HOMO−7 → LUMO (50%) HOMO−4 → LUMO (15%) HOMO → LUMO+5 (15%)	3.0241 eV (409.99 nm)	0.5246

Table 4-14. Calculated excited states of $[Ru(bpy)(phen)_2]^{2+}$ in CH_3CN.

Excited State	Transition	Energy (Wavelength)	Oscillator Strength
S_1	HOMO → LUMO (54%) HOMO → LUMO+1 (46%)	2.7398 eV (452.52 nm)	0.0005
S_2	HOMO → LUMO+2	2.7895 eV (444.46 nm)	0.0000
S_3	HOMO → LUMO+1	2.7934 eV (443.84 nm)	0.0008
S_4	HOMO−1 → LUMO (55%) HOMO−1 → LUMO+1 (45%)	2.8998 eV (427.56 nm)	0.0020
S_5	HOMO−2 → LUMO+2 (53%) HOMO−1 → LUMO (47%)	2.9583 eV (419.11 nm)	0.0152
S_6	HOMO−2 → LUMO (74%) HOMO−1 → LUMO+2 (26%)	2.9788 eV (416.22 nm)	0.0183
S_7	HOMO−1 → LUMO+2 (64%) HOMO → LUMO+3 (36%)	3.0388 eV (408.00 nm)	0.0879
S_8	HOMO−2 → LUMO+2 (56%) HOMO−1 → LUMO+1 (44%)	3.0490 eV (406.63 nm)	0.0899
S_9	HOMO−2 → LUMO (18%) HOMO−2 → LUMO+1 (31%) HOMO → LUMO+3 (51%)	3.0731 eV (403.45 nm)	0.0388
S_{10}	HOMO−2 → LUMO+2 (15%) HOMO−1 → LUMO+1 (15%) HOMO → LUMO+4 (70%)	3.1542 eV (393.08 nm)	0.0696

4-3-3: Emission Properties

The $[Ru(B_2bpy)L'_2]^{2+}$ complexes exhibit the emissions from the MLCT-type excited states as the broad and structureless spectra in CH_3CN at 298 K are shown in Figure 4-12. Figure 4-13 shows the emission decay profiles and Table 4-15 summarizes the emission properties of the complexes. The emission maximum (λ_{em}) of $[Ru(B_2bpy)L'_2]^{2+}$ (λ_{em} = 654–684 nm) was shifted to a longer wavelength compared to that of $[Ru(bpy)_3]^{2+}$ (λ_{em} = 620 nm) or $[Ru(bpy)(phen)_2]^{2+}$ (λ_{em} = 611 nm) owing to the synergistic MLCT/π(aryl)–p(B) CT interactions as described in Chapter 2. Furthermore, the phenyl or methyl groups in L' of the complex gave rise to a further decrease in the emission maximum energy and the extent of the emission energy (E_{em}) change by the introduction of the methyl groups to bpy or phen (500–520 cm^{-1}) was larger than that of the phenyl groups (100–120 cm^{-1}). Figure 4-14 shows a relationship between the E_{em} and ($E_{ox} - E_{red1}$) values of the complexes including the arylborane–ruthenium(II) complexes described in Chapter 2 and reported $[RuL_3]^{2+}$ complexes.[4] The arylborane–ruthenium(II) complexes exhibit a good proportional relationship between E_{em} and ($E_{ox} - E_{red1}$) as seen in Figure 4-14, and the slope of the plot with 0.801 eV/V is larger than that of the reported $[RuL_3]^{2+}$ complexes without an arylborane group (0.766 eV/V) in spite of comparable slopes of the E_{abs} vs. ($E_{ox} - E_{red1}$) plots as described above. The results demonstrate that the arylborane–ruthenium(II) complexes show higher-energy emissions compared to that expected from the redox potentials, which can be explained by the small energy splitting between the singlet (S_1) and triplet excited (T_1) states (ΔE_{ST}) of the arylborane–ruthenium(II) complexes. Since the mixed MLCT/π(aryl)–p(B) CT character of the arylborane–ruthenium(II) complex in the excited state would give rise to the decrease in the electron-exchange integral between the S_1 and T_1 states, the resulting small ΔE_{ST} of

the complex increases E_{em} by decreasing energy loss upon intersystem crossing from S_1 to T_1. However, such effects on E_{em} is expected to be minor and, therefore, the arylborane–ruthenium(II) complexes show low-energy ^{3}MLCT emission owing to the low-energy unoccupied MOs as revealed by the electrochemical measurements. In addition, the phenyl or methyl groups in L' lower the excited-state energy of $[Ru(B_2bpy)L'_2]^{2+}$ by destabilization of the occupied MOs.

$[Ru(B_2bpy)L'_2]^{2+}$ shows more intense and longer-lived emission (Φ_{em} = 0.18–0.33 and τ_{em} = 1.1–2.1 μs) than $[Ru(bpy)_3]^{2+}$ (Φ_{em} = 0.095 and τ_{em} = 0.89 μs) or $[Ru(bpy)(phen)_2]^{2+}$ (Φ_{em} = 0.078 and τ_{em} = 0.74 μs). Furthermore, the phenyl groups in L' of the complex enhance the Φ_{em} value (Φ_{em} = 0.33 or 0.29 for **4dpbpy** or **4dpphen**, respectiely), while the methyl groups weaken the emission (Φ_{em} = 0.18 or 0.22 for **4dmbpy** or **4dmphen**, respectively). On the other hand, both phenyl and methyl groups in L' of the complex shorten the τ_{em} value compared to that of **2c** (τ_{em} = 1.7 μs) or **4phen** (2.1 μs), and the τ_{em} value of **4dmbpy** (τ_{em} = 1.1 μs) or **4dmphen** (τ_{em} = 1.2 μs) is shorter than that of **4dpbpy** (τ_{em} = 1.4 μs) or **4dpphen** (τ_{em} = 1.9 μs). Since the electron-donating phenyl and methyl groups in L' of the complex affect the Φ_{em} and τ_{em} values in different manners, the complicated ancillary-ligand effects on the photophysical properties of $[Ru(B_2bpy)L'_2]^{2+}$ should be discussed in terms of the radiative (k_r) and nonradiative decay rate constants (k_{nr}) summarized in Table 4-15. The k_r value of **4dpbpy** (2.4×10^5 s^{-1}) is larger than those of other $[Ru(B_2bpy)L'_2]^{2+}$ ($(1.3–1.8) \times 10^5$ s^{-1}), and these values are slightly larger than that of $[Ru(bpy)_3]^{2+}$ or $[Ru(bpy)(phen)_2]^{2+}$ (1.1×10^5 s^{-1}). On the other hand, the k_{nr} values of $[Ru(B_2bpy)L'_2]^{2+}$ ($(3.5–7.5) \times 10^5$ s^{-1}) are significantly smaller than those of the reference complexes ($(1.0–1.2) \times 10^6$ s^{-1}), and the value increases with an increase in the electron-donating ability of the functional group in L'. Such large k_r and

small k_{nr} values, whose details are described in the following sections, give rise to the intense and long-lived emission from $[Ru(B_2bpy)L'_2]^{2+}$.

Table 4-15. Emission properties of the complexes in CH_3CN at 298 K.

Complex	λ_{em} / nm	Φ_{em}	τ_{em} / μs	k_r [b] / s^{-1}	k_{nr} [b] / s^{-1}
4dpbpy	668	0.33	1.4	2.4×10^5	4.8×10^5
4dmbpy	684	0.18	1.1	1.6×10^5	7.5×10^5
2c [a]	659	0.27	1.7	1.6×10^5	4.3×10^5
$[Ru(bpy)_3]^{2+}$ [a]	620	0.095	0.89	1.1×10^5	10×10^5
4dpphen	658	0.29	1.9	1.5×10^5	3.7×10^5
4dmphen	678	0.22	1.2	1.8×10^5	6.5×10^5
4phen	654	0.27	2.1	1.3×10^5	3.5×10^5
$[Ru(bpy)(phen)_2]^{2+}$	611	0.078	0.74	1.1×10^5	12×10^5

[a] Data taken from Chapter 2. [b] Calculated by $\Phi_{em} = k_r/(k_r + k_{nr}) = k_r\tau_{em}$.

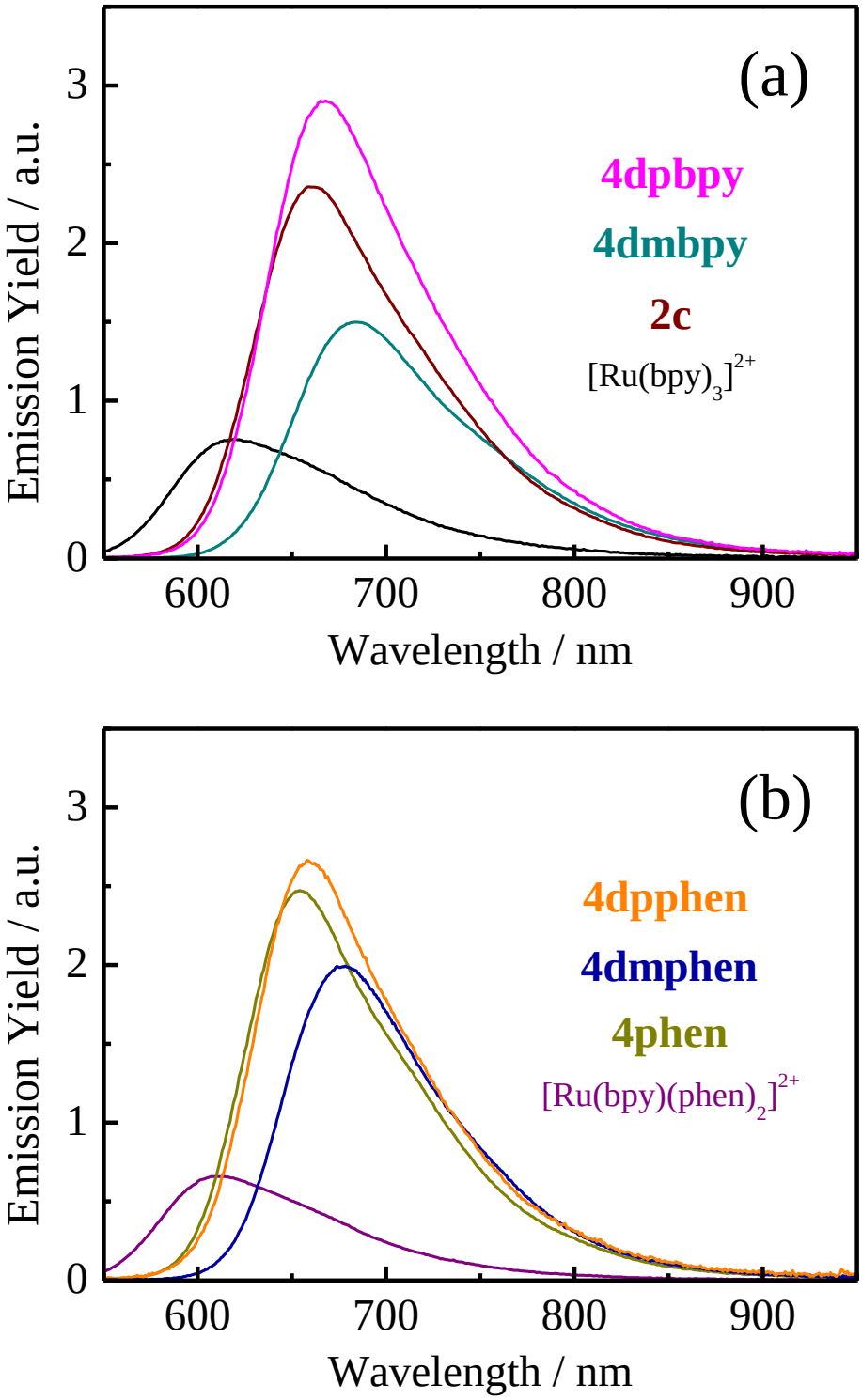

Figure 4-12. Corrected emission spectra of the complexes in CH_3CN at 298 K. The spectral integrations in a wavenumber scale correspond to the relative Φ_{em} values of the complexes.

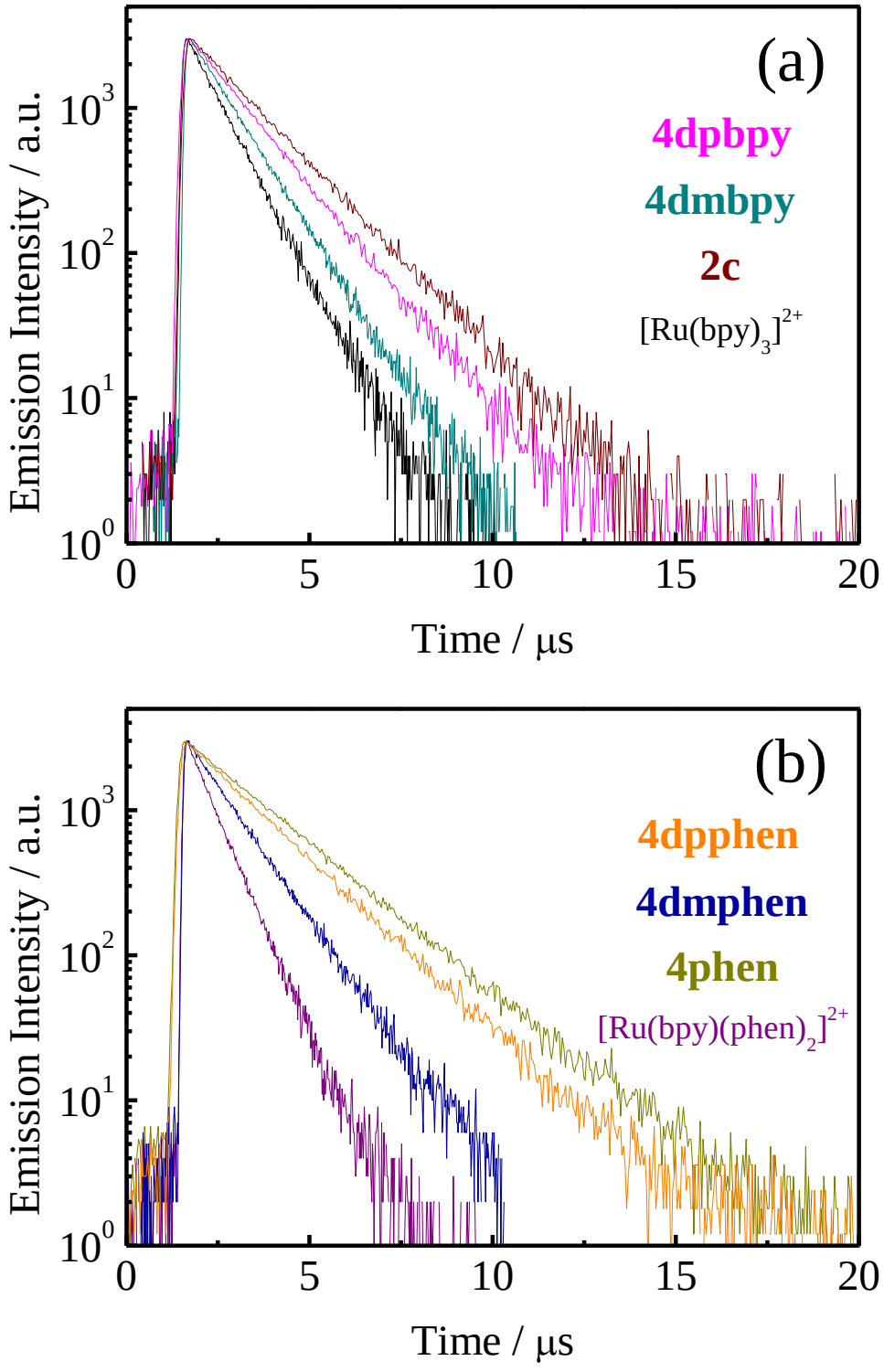

Figure 4-13. Emission decay profiles of the complexes in CH_3CN at 298 K.

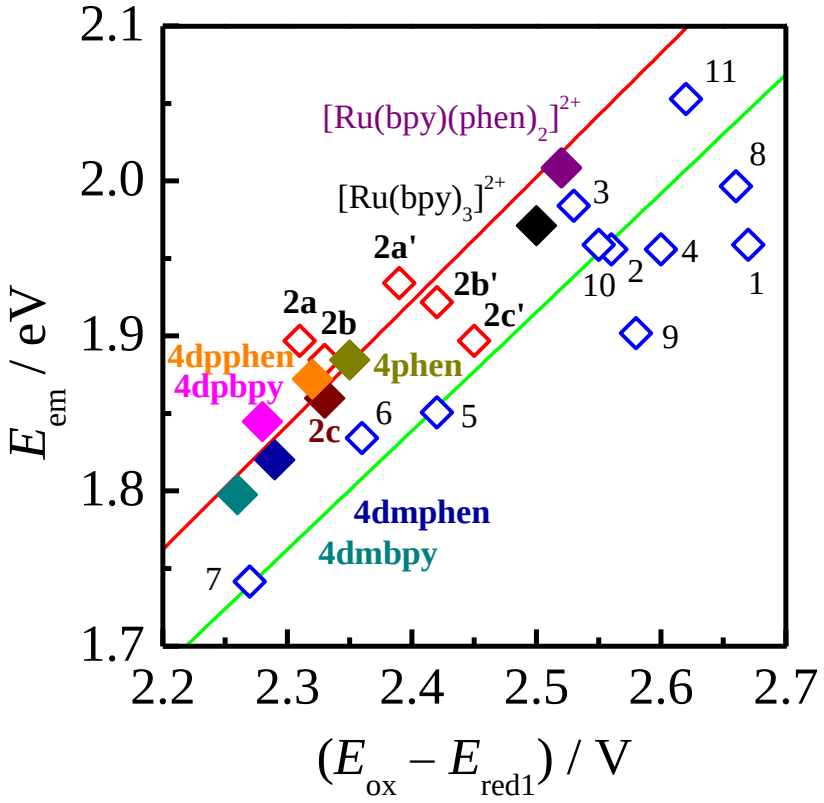

Figure 4-14. Relationships between the E_{em} and (E_{ox} − E_{red1}) values of the complexes. The plot styles are identical to those in Figure 4-10. The red or green line represents the linear regression for the relation between E_{em} and (E_{ox} − E_{red1}) for arylborane–ruthenium(II) complexes or the conventional ruthenium(II) complexes, respectively, in which the intercept has been fixed at 0 eV.

4-3-4: Nonradiative Decay Rate Constants

Figure 4-15 shows the energy gap plot for a series of the complexes (i.e., [Ru(B$_2$bpy)L'$_2$]$^{2+}$, **2a**, **2b**, **2a'**–**c'** and reported [RuL$_3$]$^{2+}$ complexes[4]). The arylborane–ruthenium(II) complexes including [Ru(B$_2$bpy)L'$_2$]$^{2+}$ show a good linear relationship between ln k_{nr} and E_{em}, suggesting the energy gap dependence of k_{nr}. However, the trend of the arylborane–ruthenium(II) complexes in Figure 4-15 hugely deviates from that of the reference complexes. The results demonstrate that the nonradiative decay modes from the emitting excited states to the ground states of the arylborane–ruthenium(II) complexes

are common, and the k_{nr} value of $[Ru(B_2bpy)L'_2]^{2+}$ varies by the excited-state energy (i.e., E_{em}) of the complex, which can be controlled primarily by the ancillary-ligand effect on the oxidation potential (E_{ox}) of the complex. The significantly small k_{nr} value of $[Ru(B_2bpy)L'_2]^{2+}$ is expected to be originated from suppressed thermal deactivation of the excited state *via* the triplet dd excited (^{3}dd*) state owing to the large ^{3}MLCT–^{3}dd* energy gap as described in Chapters 2 and 3. The thermal transition from the ^{3}MLCT state to the ^{3}dd* state and subsequent deactivation to the ground state is predominant for nonradiative decay from the emitting excited state of a conventional polypyridyl ruthenium(II) complex and is almost independent of the ligand structure, since the ^{3}MLCT- and ^{3}dd*-energies vary synchronously through the change in the ligand-field splitting and π*-orbital energies. Therefore, such decrease in the contribution of the ^{3}dd* state to nonradiative decay in the arylborane–ruthenium(II) complexes is extraordinary and resulted by the low-energy emitting excited state and the insensitive ^{3}dd* state upon an introduction of the DBDE group(s). Although the electrochemical data indicate that the electron-donating groups in L' affect the ligand-field splitting of the complex, the relevant effects on the ^{3}MLCT–^{3}dd* energy gap would be minor and, therefore, the k_{nr} values of the arylborane–ruthenium(II) complexes follows the energy gap law.[6–12]

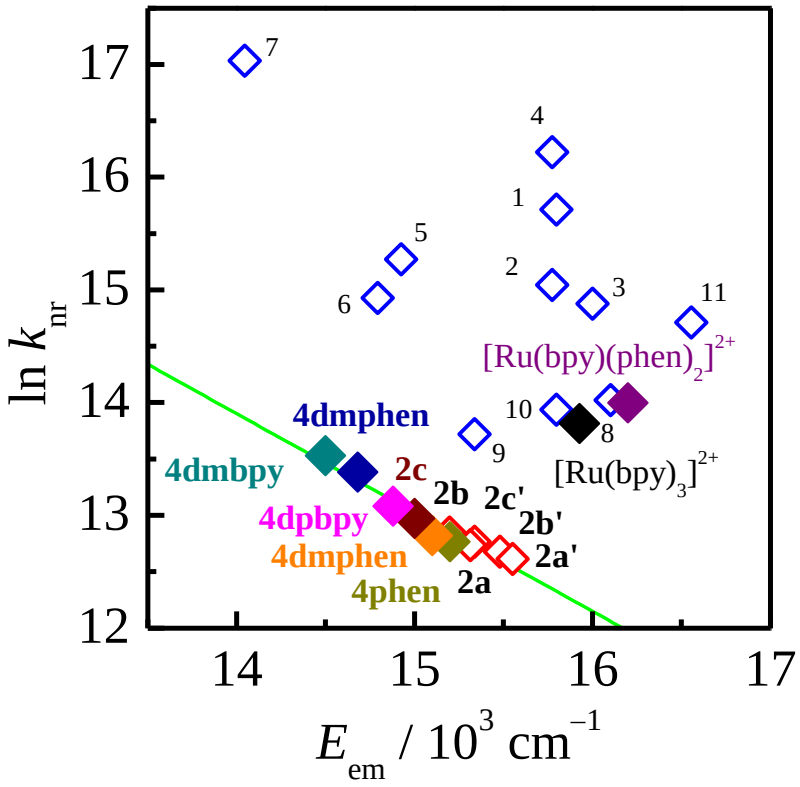

Figure 4-15. Energy gap plot for the complexes in CH_3CN at 298 K. The plot styles are identical to those in Figure 4-10. The green line represents the linear regression for the data of the arylborane–ruthenium(II) complexes.

The details of the nonradiative decay process of $[Ru(B_2bpy)L'_2]^{2+}$ were investigated by temperature (T) dependences of the emission lifetime. Figure 4-16 shows the T-dependences (250–330 K) of the emission decay profiles of the complexes in propylene carbonate. The decay profiles of the complexes were analyzed by single-exponential decay functions, irrespective of T, and the τ_{em} values of $[Ru(B_2bpy)L'_2]^{2+}$ were almost independent of T while those of the reference complexes (i.e., $[Ru(bpy)_3]^{2+}$ and $[Ru(bpy)(phen)_2]^{2+}$) hugely decreased upon T-elevation. The T-dependences of τ_{em} for the complexes were adequately fitted by eq. 4-1[13] using the parameters (ΔE, (k_r^0 + k_{nr}^0), and k') in Table 4-16.

$$[\tau_{em}(T)]^{-1} = (k_r^0 + k_{nr}^0) + k' \exp(-\frac{\Delta E}{k_B T}) \quad \text{(eq. 4-1)}$$

In eq. 4-1, k_r^0 and k_{nr}^0 are the T-independent radiative and nonradiative decay rate constants from the emitting excited state to the ground state, respectively. The parameter k' is the frequency factor for thermal activation from the ^{3}MLCT excited state to the upper-lying nonemitting excited state (typically, ^{3}dd* state for a polypyridyl ruthenium(II) complex) with the energy barrier between the two states being ΔE. The parameters ΔE (870–1190 cm^{-1}) and k' ((0.47–2.7) × 10^7 s^{-1}) of $[Ru(B_2bpy)L'_2]^{2+}$ are almost independent of L', and significantly differ from those of $[Ru(bpy)_3]^{2+}$ and $[Ru(bpy)(phen)_2]^{2+}$ (ΔE = 3600–3780 cm^{-1} and k' = (2.9–3.4) × 10^{13} s^{-1}). The k' values of $[Ru(B_2bpy)L'_2]^{2+}$ suggest a contribution of the fourth ^{3}MLCT excited state to the nonradiative decay process as described in Chapters 2 and 3. Therefore, the parameter ΔE of $[Ru(B_2bpy)L'_2]^{2+}$ represents the energy barrier to the fourth ^{3}MLCT excited state[14,15] rather than the ^{3}dd*

state presumably due to the large ^{3}MLCT–^{3}dd* energy gap of the complex which is not obtainable under the present experimental conditions.

To obtain further insights into the activation parameters of the complexes, they were plotted against E_{em} in Figure 4-18, together with the data for the complexes described in Chapters 2 and 3 (i.e., **2a**, **2c**, **2c'**, **3a** and $[Ru(phen)_3]^{2+}$). Drastic changes in the ΔE and k' parameters were observed at $E_{em} \approx 15300$ cm^{-1}. The trends indicate that an introduction of the DBDE group(s) to a diimine ruthenium(II) complex does not affect the ligand-field splitting energy largely and the emitting excited states of the complexes exhibiting the high-energy emission deactivate thermally *via* ^{3}dd* state in contrast to nonradiative decay *via* the fourth ^{3}MLCT excited state for the complex showing the lower-energy emission. On the other hand, the ($k_r^0 + k_{nr}^0$) values of a series of the complexes except for **3a** decreased exponentially with an increase in E_{em}, suggesting that the parameter was dominated by the energy gap law and the presence of the DBDE group does not affect the nonradiative decay mode from the emitting excited state of the complex to the relevant excited state. The extraordinarily small ($k_r^0 + k_{nr}^0$) value observed for **3a** is presumably due to the rigid structure of the phen moiety in the main ligand. These total analysis for the activation parameters revealed that the k_{nr} value of the arylborane–ruthenium(II) complex is controllable by the energy of the emitting excited state and, thus, that of $[Ru(B_2bpy)L'_2]^{2+}$ can be manipulated synthetically by the ancillary-ligand.

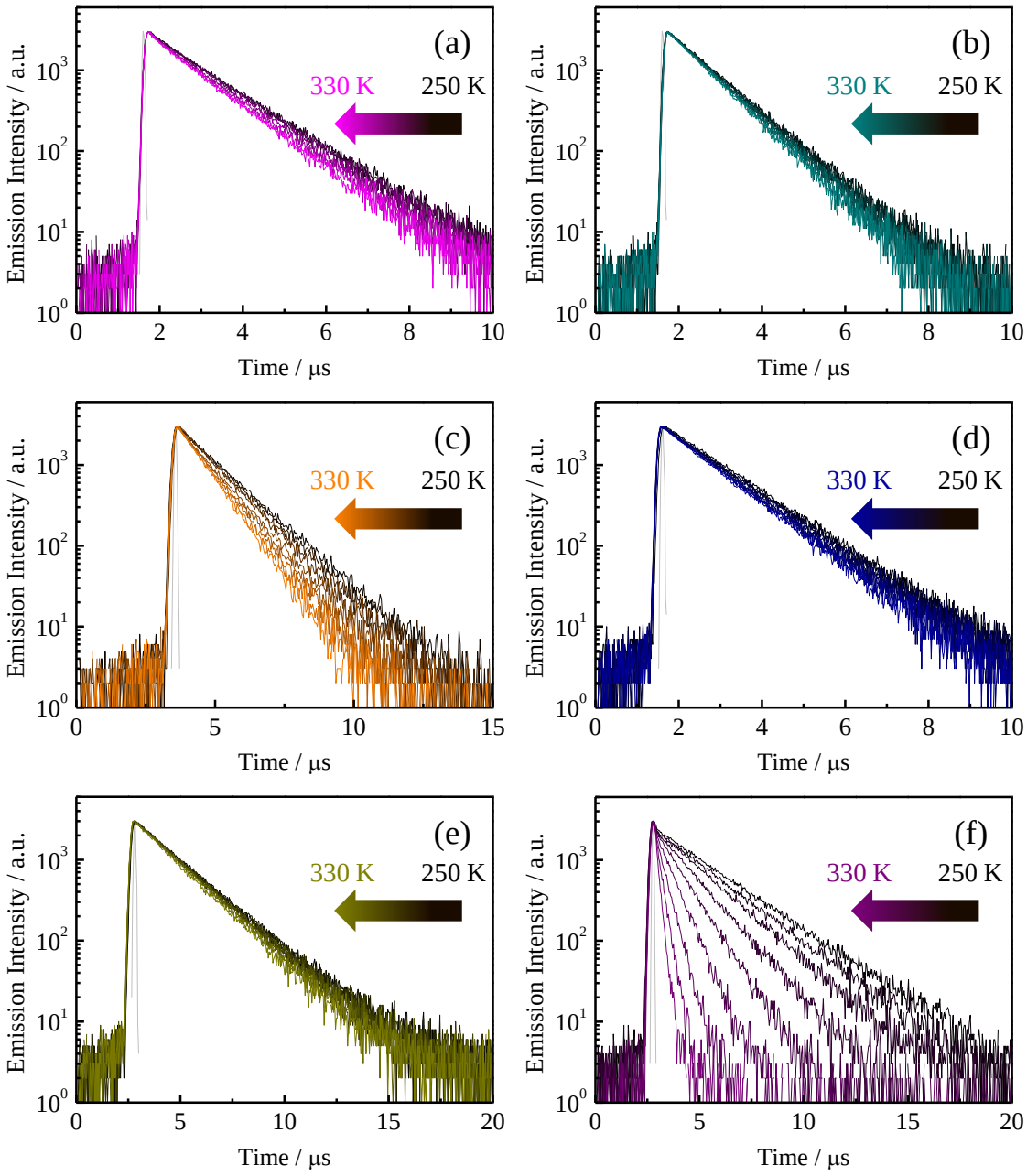

Figure 4-16. *T*-dependences (*T* = 250–330 K) of the emission decay profiles of **4dpbpy** (a), **4dmbpy** (b), **4dpphen** (c), **4dmphen** (d), **4phen** (e) and $[Ru(bpy)(phen)_2]^{2+}$ (f) in propylene carbonate. Gray curves represent instrumental response functions.

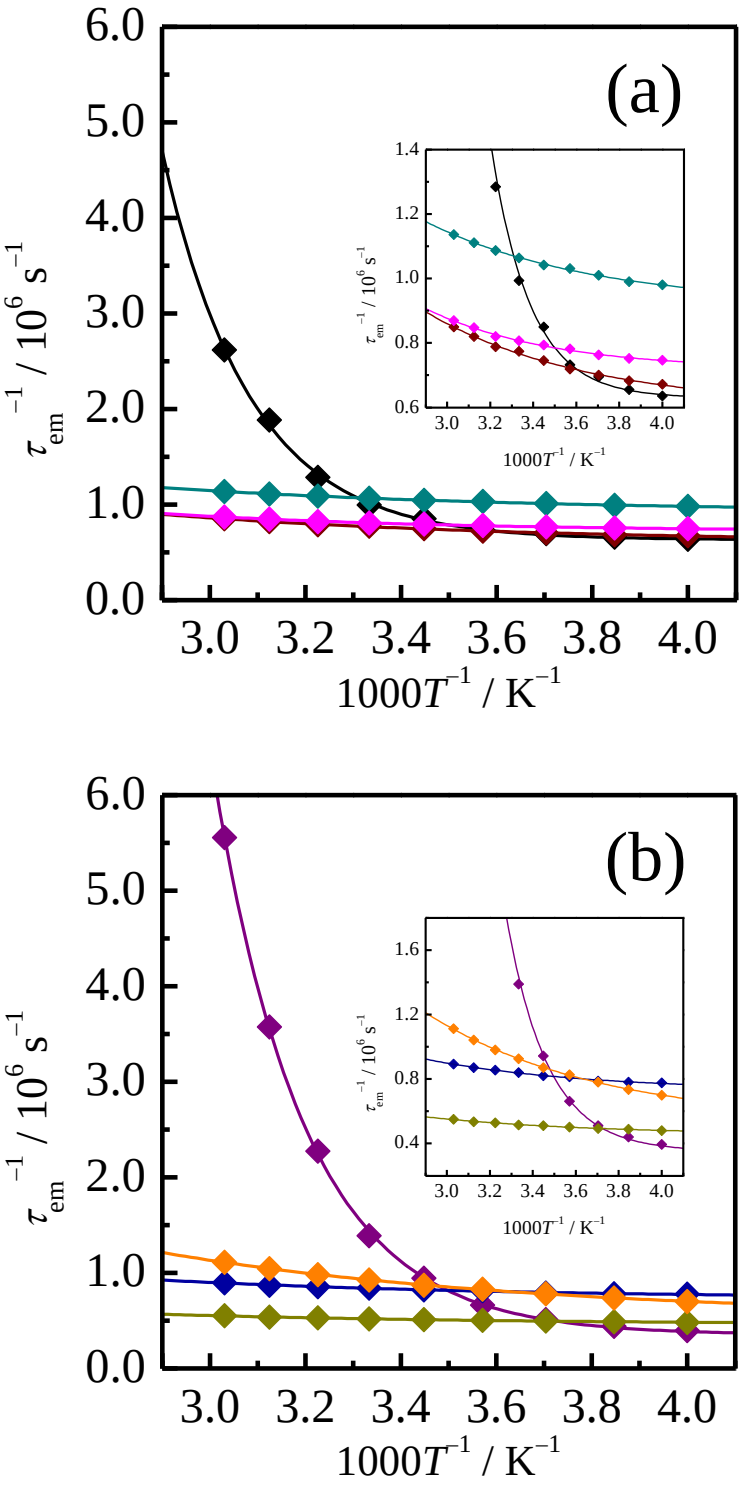

Figure 4-17. *T*-dependences (T = 250–330 K) of the τ_{em} values of the complexes in propylene carbonate. The colors of the data points and the relevant curves correspond to those indicated in Figures 4-1 and 4-2. The curves represent the best fits of the experimental data by eq. 4-1. Inset: enlarged view.

Table 4-16. Activation parameters for the *T*-dependent emission lifetimes of the complexes in propylene carbonate.

Complex	ΔE / cm^{-1}	$(k_r^0 + k_{nr}^0)$ / s^{-1}	k' / s^{-1}
4dpbpy	1190	7.2×10^5	2.7×10^7
4dmbpy	900	9.1×10^5	1.1×10^7
2c [a]	930	6.0×10^5	1.4×10^7
$[Ru(bpy)_3]^{2+}$ [a]	3780	6.3×10^5	2.9×10^{13}
4dpphen	870	5.3×10^5	2.6×10^7
4dmphen	920	7.3×10^5	0.93×10^7
4phen	900	4.6×10^5	0.47×10^7
$[Ru(bpy)(phen)_2]^{2+}$	3600	3.5×10^5	3.4×10^{13}

[a] Data taken from Chapter 2.

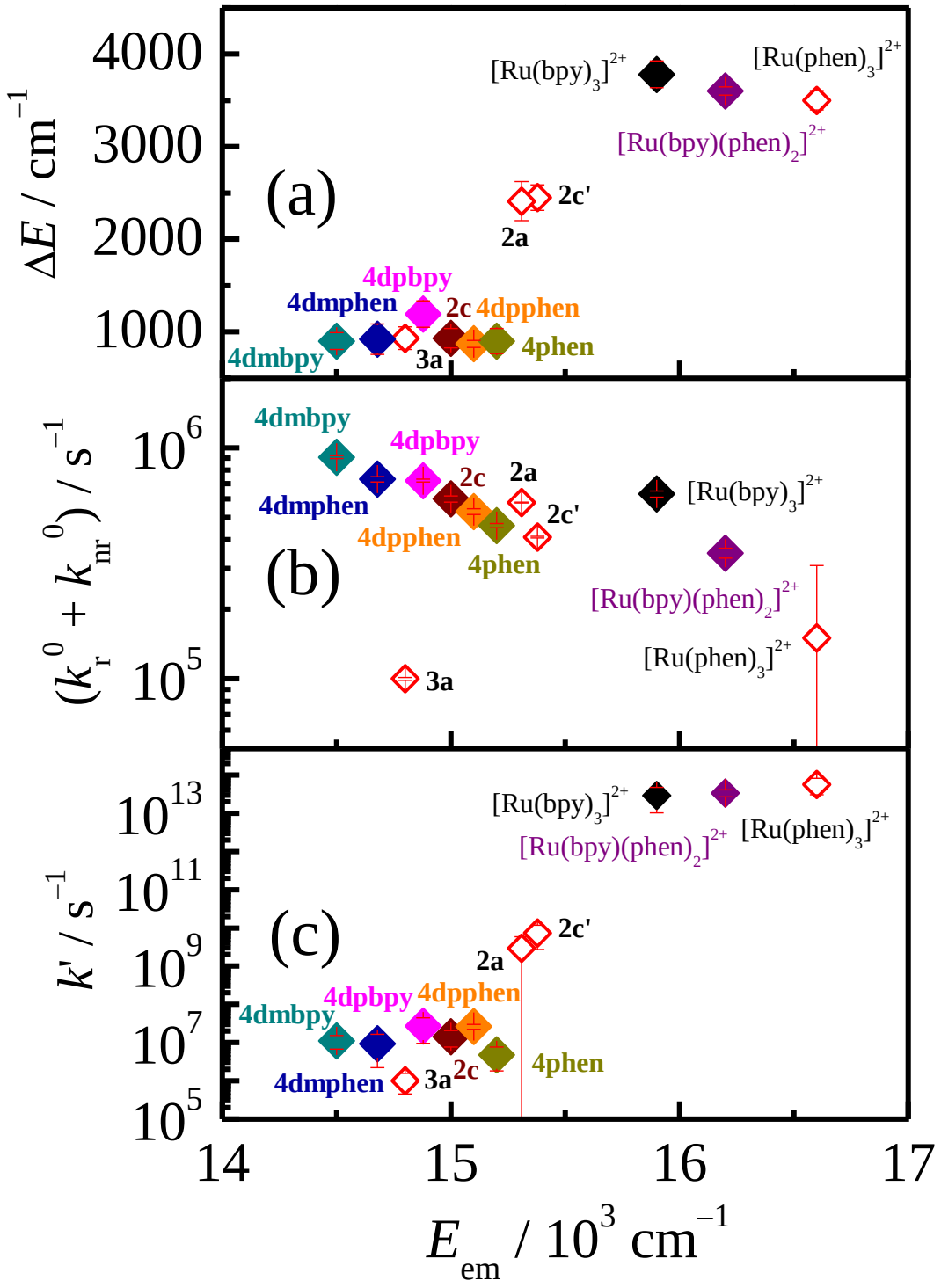

Figure. 4-18. E_{em} dependences of the activation parameters for the *T*-dependent emission lifetimes of the complexes (ΔE (a), ($k_r^0 + k_{nr}^0$) (b) and k' (c)). Error bars represent standard errors for the data fittings.

4-3-4: Radiative Rate Constants

$[Ru(B_2bpy)L'_2]^{2+}$ exhibited larger k_r than the reference complex (i.e., $[Ru(bpy)_3]^{2+}$ or $[Ru(bpy)(phen)_2]^{2+}$), and further enhancement of k_r was observed by the introduction of the phenyl groups in L' of the complex. The radiative transition from the triplet excited state of a transition metal complex should gain a probability by singlet–triplet mixing in the excited state through spin–orbit coupling and, therefore, the k_r value of the ruthenium(II) complex correlates positively with $\varepsilon_{MLCT}E_{em}^3/|E_{em} - E_{abs}|^2$ on the basis of the Strickler–Berg-type relation[16] as demonstrated in Chapter 2. Figure 4-19 shows a k_r vs. $\varepsilon_{MLCT}E_{em}^3/|E_{em} - E_{abs}|^2$ plot of the complexes including the data on a series of $[Ru(bpy)_3]^{2+}$ derivatives[17,18]. A good proportional relationship between the parameters (r = 0.9210) indicates that large k_r of $[Ru(B_2bpy)L'_2]^{2+}$ is dominated by the Strickler–Berg-type relation. Since the E_{em} value of a polypyridyl ruthenium(II) complex does not vary by the ligand structure largely, the E_{em} value should be less effective to the $\varepsilon_{MLCT}E_{em}^3/|E_{em} - E_{abs}|^2$ value than ε_{MLCT} and $|E_{em} - E_{abs}|$. Thus, the large k_r values of $[Ru(B_2bpy)L'_2]^{2+}$ are explainable by the large ε_{MLCT} and small $|E_{em} - E_{abs}|$ (i.e., ΔE_{ST}) values of $[Ru(B_2bpy)L'_2]^{2+}$, which coincides nicely with the experimental observation on the absorption and emission spectra. As discussed in the preceding sections, the ε_{MLCT} value of $[Ru(B_2bpy)L'_2]^{2+}$ is enhanced by the mixed MLCT/π(aryl)–p(B) CT character in the excited state, and the effects are also expected to reduce the ΔE_{ST} by decreasing the electron-exchange integral between the singlet and triplet excited states. Therefore, the resulting large ε_{MLCT} and small ΔE_{ST} values of $[Ru(B_2bpy)L'_2]^{2+}$ accelerate the radiative process of the complex. Further enhancement of k_r observed for **4dpbpy** or **4dpphen** is also explained by mixing between the LLCT and MLCT characters in the emitting excited state of the complex. These results demonstrate that the ancillary ligand certainly

contributes to an increase in the k_r value of the complex, and it could be a useful approach for the development of emissive transition metal complexes.

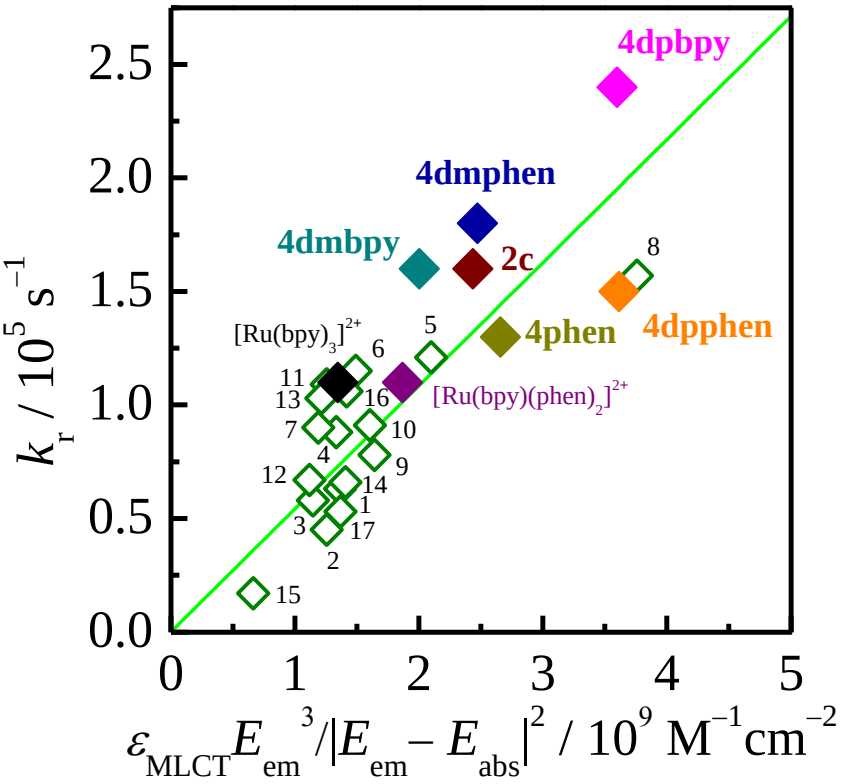

Figure 4-19. Relationship between k_r and $\varepsilon_{MLCT}E_{em}{}^3/|E_{em} - E_{abs}|^2$ for the complexes in CH_3CN at 298 K. Green open boxes represent the data for a series of $[Ru(X\text{-}bpy)_3]^{2+}$ complexes (X = 4-bromo (1), 4-chloro (2), 4-methoxy (3), 4-benzyloxy (4), 4,4'-bisethoxycarbonyl (5), 4,4'-dibromo (6), 4,4'-dichloro (7), 4,4'-diphenyl (8), 4,4'-dibenzyl (9), 4,4'-dimethyl (10), 4,4'-diphenoxy (11), 4,4'-diethoxy (12), 4,4'-dibenzyloxy (13), 4,4'-bisacetamido (14), 5,5'-bisethoxycarbonyl (15), 5,5'-dimethyl (16), 5,5'-bisacetamido (17)) in EtOH–MeOH (4/1, v/v) at 293 K. The literature data were taken from ref. [17,18]. The green line represents the linear regression for the data, in which the intercept has been fixed at 0 s^{-1} for the fitting.

4-4: Conclusions

In this chapter, the spectroscopic and photophysical properties of novel heteroleptic arylborane–ruthenium(II) complexes having a series of ancillary ligands L' ($[Ru(B_2bpy)L'_2]^{2+}$: **4dpbpy** (L' =4,4'-ph_2-bpy), **4dmbpy** (L' = 4,4'-me_2-bpy), **4dpphen** (L' = 4,7-ph_2-phen), **4dmphen** (L' = 4,7-me_2-phen), **4phen** (L' = phen), Chart 4-1) were described in terms of the ancillary-ligand effects on the properties. $[Ru(B_2bpy)L'_2]^{2+}$ showed the lower-energy and intense ^{1}MLCT absorption band (λ_{abs} = 480–493 nm and ε_{MLCT} = (2.2–3.3) × 10^4 $M^{-1}cm^{-1}$). The electrochemical data of the complexes and the relationship between E_{abs} and ($E_{ox} - E_{red}$) demonstrate that the ^{1}MLCT absorption energy of $[Ru(B_2bpy)L'_2]^{2+}$ is manipulated synthetically by the electron-donating ability of the ancillary ligand(s). Furthermore, the ε_{MLCT} value of $[Ru(B_2bpy)L'_2]^{2+}$ (ε_{MLCT} = (2.2–3.3) × 10^4 $M^{-1}cm^{-1}$) is also affected by the ancillary-ligand effects, as the TD-DFT calculations suggest an increase in the MLCT absorption transition dipole moment by mixing between MLCT and LLCT transitions in the MLCT/π(aryl)–p(B) CT excited state in the complex. On the other hand, $[Ru(B_2bpy)L'_2]^{2+}$ showed intense and long-lived emission (Φ_{em} = 0.18–0.33 and τ_{em} = 1.1–2.1 μs). The *T*-dependences of the emission lifetimes have revealed the k_{nr} value of the arylborane–ruthenium(II) complex is controllable by the energy of the emitting excited state and, can be also manipulated through the ancillary-ligand(s) in $[Ru(B_2bpy)L'_2]^{2+}$. Furthermore, the large k_r value of $[Ru(B_2bpy)L'_2]^{2+}$ is shown to be explained in the framework of the Strickler–Berg-type relation. These results demonstrate that synthetic modulation of an ancillary ligand could be a useful approach for the development of emissive transition metal complexes.

4-5: Reference

[1] Han, W.; Han, J.; Kim, H.; Choi, M. J.; Kang, Y.; Pac, C.; Kang, S. O. Electronic Optimization of Heteroleptic Ru(II) Bipyridine Complexes by Remote Substituents: Synthesis, Characterization, and Application to Dye-Sensitized Solar Cells. *Inorg*. *Chem*. **2011**, *50*, 3271–3280.

[2] Kent, C. A.; Liu, D.; Ma, L.; Papanikolas, J. M.; Meyer, T. J.; Lin, W. Light Harvesting in Microscale Metal–Organic Frameworks by Energy Migration and Interfacial Electron Transfer Quenching. *J*. *Am*. *Chem*. *Soc*. **2011**, *133*, 12940–12943.

[3] Slattery, S. J.; Gokalda, N.; Mick, T.; Goldsby, K. A. Bis(4,4'-bis(diethylamino)-2,2'-bipyridine)dichlororuthenium(III): A New Starting Material for Ruthenium Polypyridyl Complexes Exhibiting Low Redox Potentials. *Inorg*. *Chem*. **1994**, *33*, 3621–3624.

[4] Kawanishi, Y.; Kitamura, N.; Tazuke, S. Dependence of Spectroscopic, Electrochemical, and Excited-State Properties of Tris Chelate Ruthenium(II) Complexes on Ligand Structure. *Inorg*. *Chem*. **1989**, *28*, 2968–2975.

[5] Petersson, G. A.; Al-Laham, M. A. A Complete Basis Set Model Chemistry. III. The Complete Basis Set-Quadratic Configuration Interaction Family of Methods. *J*. *Chem*. *Phys*. **1991**, *94*, 6081–6090.

[6] Kober, E. M.; Caspar, J. V.; Lumpkin, R. S.; Meyer, T. J. Application of the Energy Gap Law to Excited-State Decay of Osmium(II)-Polypyridine Complexes: Calculation of Relative Nonradiative Decay Rates from Emission Spectral Profiles. *J*. *Phys*. *Chem*. **1986**, *90*, 3722–3734.

[7] Kober, E. M.; Sullivan, B. P.; Dressick, W. J.; Caspar, J. V.; Meyer, T. J. Highly

Luminescent Polypyridyl Complexes of Osmium(II). *J. Am. Chem. Soc.* **1980**, *102*, 7383–7385.

[8] Caspar, J. V.; Meyer, T. J. Photochemistry of $Ru(bpy)_3^{2+}$. Solvent Effects. *J. Am. Chem. Soc.* **1983**, *105*, 5583–5590.

[9] Caspar, J. V.; Meyer, T. J. Photochemistry of MLCT Excited States. Effect of Nonchromophoric Ligand Variations on Photophysical Properties in the Series *cis*-$Ru(bpy)_2L_2^{2+}$. *Inorg. Chem.* **1983**, *22*, 2444–2453.

[10] Caspar, J. V.; Meyer, T. J. Application of the Energy Gap Law to Nonradiative, Excited-State Decay. *J. Phys. Chem.* **1983**, *87*, 952–957.

[11] Allen, G. H.; White, R. P.; Rillema, D. P.; Meyer, T. J. Synthetic Control of Excited-State Properties. Tris-Chelate Complexes Containing the Ligands 2,2'-Bipyrazine, 2,2'-Bipyridine, and 2,2'-Bipyrimidine. *J. Am. Chem. Soc.* **1984**, *106*, 2613–2620.

[12] Kober, E. M.; Caspar, J. V.; Lumpkin, R. S.; Meyer, T. J. Application of the Energy Gap Law to Excited-State Decay of Osmium(II)-Polypyridine Complexes: Calculation of Relative Nonradiative Decay Rates from Emission Spectral Profiles. *J. Phys. Chem.* **1986**, *90*, 3722–3734.

[13] Van Houten, J.; Watts, R. J. Temperature Dependence of the Photophysical and Photochemical Properties of the Tris(2,2'-bipyridyl)ruthenium(II) Ion in Aqueous Solution. *J. Am. Chem. Soc.* **1976**, *98*, 4853–4858.

[14] Kober, E. M.; Meyer, T. J. An Electronic Structural Model for the Emitting MLCT Excited States of $Ru(bpy)_3^{2+}$ and $Os(bpy)_3^{2+}$. *Inorg. Chem.* **1984**, *23*, 3877–3886.

[15] Lumpkin, R. S.; Kober, E. M.; Worl, L. A.; Murtaza, Z.; Meyer, T. J. Metal-to-Ligand Charge-Transfer (MLCT) Photochemistry: Experimental Evidence for the

Participation of a Higher Lying MLCT State in Polypyridyl Complexes of Ruthenium(II) and Osmium(II). *J. Phys. Chem.* **1990**, *94*, 239–243.

[16] Strickler, S. J.; Berg, R. A. Relationship between Absorption Intensity and Fluorescence Lifetime of Molecules. *J. Chem. Phys.* **1962**, *37*, 814–822.

[17] Cook, M. J.; Lewis, A. P. McAuliffe, G. S. G; Skarda, V.; Thomson, A. J. Luminescent Metal Complexes. Part 1. Tris-chelates of Substituted 2,2'-Bipyridyls with Ruthenium(II) as Dyes for Luminescent Solar Collectors. *J. Chem. Soc. Perkin Trans. 2* **1984**, 1293–1301.

[18] Cook, M. J.; Lewis, A. P. McAuliffe, G. S. G; Skarda, V.; Thomson, A. J. A Model for the Luminescence Properties of the Tris-Chelates of Substituted 2.2'-Bipyridyls with Ruthenium(II). *J. Chem. Soc. Perkin Trans. 2* **1984**, 1303–1307.

Chapter 5: Conclusions

In the present thesis, twelve novel arylborane–ruthenium(II) complexes were synthesized, in which the number of the arylborane unit in the diimine ligand(s) and the diimine-/ancillary-ligand structures in the complexes were varied systematically as shown in Chart 5-1. The spectroscopic and photophysical properties of the complexes were then studied in detail. Although various attractive emissive transition metal complexes have been hitherto reported, a study on the theoretical aspects into the photophysical properties of phosphorescent transition metal complexes is not sufficient enough in the present stage of the investigation and, polypyridyl ruthenium(II) complexes are ideal targets on the present researches. However, the emission quantum yields of the complexes are not high enough and, therefore, the development of highly-emissive polypyridyl ruthenium(II) complexes is of primary importance. Owing to the presence of the vacant p-orbital on the boron atom (p(B)) in a triarylborane, a class of transition metal complexes having a triarylborane group(s) in the periphery of the ligand(s) shows fascinating excited-state properties, characterized by the synergistic interactions between MLCT in the metal-complex moiety and π(aryl)–p(B) CT in the triarylborane group: synergistic MLCT/π(aryl)–p(B) CT. Therefore, further understanding of the arylborane effects on the spectroscopic and photophysical properties of the arylborane–ruthenium(II) complexes are of primary importance. Thus, the present study targets the systematic synthetic modulation of the spectroscopic and photophysical properties of arylborane–ruthenium(II) complexes.

The principal experimental results and conclusions are as follows.

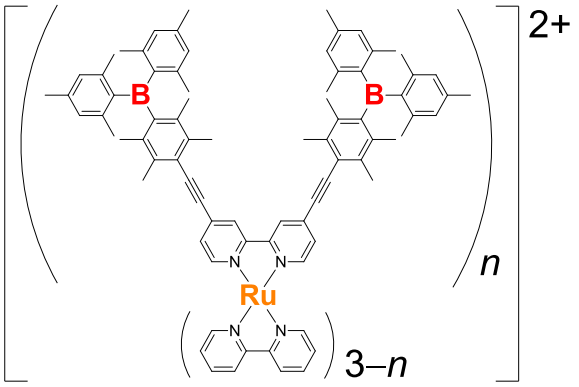

2a–**c** (*n* = 3–1)

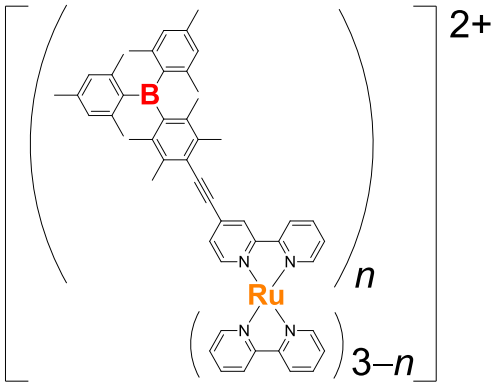

2a'–**c'** (*n* = 3–1)

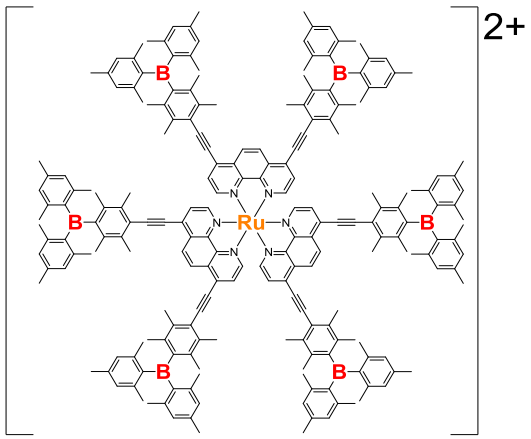

3a

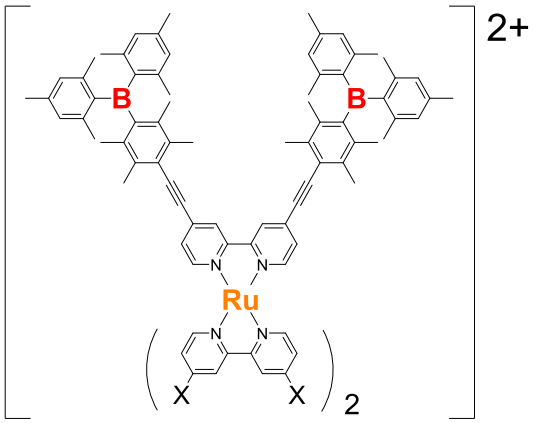

4dpbpy (-X = -C_6H_5),
4dmbpy (-X = -CH_3)

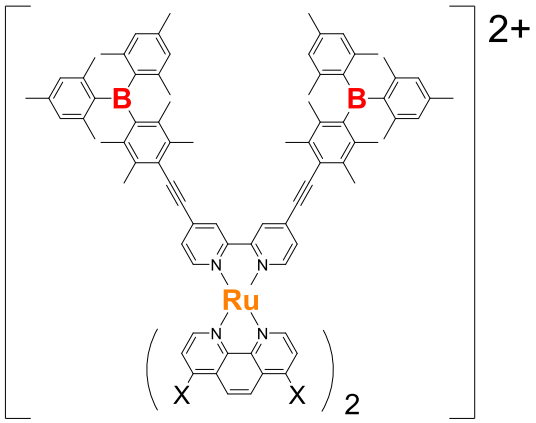

4dpphen (-X = -C_6H_5),
4dmphen (-X = -CH_3),
4phen (-X = -H)

Chart 5-1. Chemical structures and abbreviations of the arylborane–ruthenium(II) complexes developed in this thesis.

In Chapter 2, the synthesis and spectroscopic/photophysical properties of a series of the novel $[Ru(bpy)_3]^{2+}$ derivatives having multiple arylborane units ($[Ru(B_2bpy)_n(bpy)_{3-n}]^{2+}$ (**2a**: n = 3, **2b**: n = 2, **2c**: n = 1) and $[Ru(Bbpy)_n(bpy)_{3-n}]^{2+}$ (**2a'**: n = 3, **2b'**: n = 2, **2c'**: n = 1)) were described. The complexes, **2a**–**c** and **2a'**–**c'**, showed intense absorption in 290–600 nm, and the molar absorption coefficient of the MLCT absorption band (ε_{MLCT}) of the complex was largely enhanced by the introduction of a DBDE group(s) to the bpy ligand(s) of the complex, owing to the synergistic MLCT/π(aryl)–p(B) CT interactions. Furthermore, **2a**–**c** and **2a'**–**c'** also showed intense emission with the quantum yield (Φ_{em}) > 0.20, and the Φ_{em} value increased with an increase in n for both **2a**–**c** and **2a'**–**c'** series. In particular, **2a** showed extremely intense emission with Φ_{em} = 0.43. One of the important findings of the study is the increase in the ε_{MLCT} values of **2a**–**c** and **2a'**–**c'** with that in n, and the increase in ε_{MLCT} of the complex brings about an increase in the radiative rate constant of the complex (k_r). The positive correlations between k_r and ε_{MLCT} observed for **2a**–**c** and **2a'**–**c'** resemble with the Strickler–Berg relation for the fluorescence transition of a molecule. Reflecting mixing between the S_1 and T_1 states by spin–orbit coupling, it is demonstrated that the $|E_{em} - E_{abs}|$ and ε_{MLCT} values of the complex determine primarily the k_r value, leading to the Strickler–Berg-type relation between k_r and ε_{MLCT}. These results are essentially due to the synergistic MLCT/π(aryl)–p(B) CT interactions in the emitting excited states of **2a**–**c** and **2a'**–**c'**, as demonstrated by the electrochemical, spectroscopic/photophysical, and time-dependent density functional theory (TD-DFT) calculation studies.

As demonstrated in Chapter 2, **2a** shows remarkably high Φ_{em} (0.43) in CH_3CN at 298 K. Therefore, a class of homoleptic arylborane–ruthenium(II) complexes possessing a starburst-type structure is a possible candidate for future photofunctional

materials. In Chapter 3, the synthesis and spectroscopic/photophysical properties of a novel homoleptic ruthenium(II) complex having DBDE groups at the 4- and 7-positions of the phen ligands in $[Ru(phen)_3]^{2+}$ ($[Ru(B_2phen)_3]^{2+}$: **3a**) were described in special references to the diimine ligand structure effects on the properties by comparing the data on **3a** with those on **2a**. The ε_{MLCT} value of **3a** (7.2×10^4 $M^{-1}cm^{-1}$ at 471 nm) is larger than that of **2a** (5.6×10^4 $M^{-1}cm^{-1}$ at 488 nm). The results demonstrate that the electronic coupling between the phen and DBDE units in **3a** is stronger than that between the bpy and DBDE units in **2a**, and this stronger electronic coupling leads to more effective synergistic MLCT/π(aryl)–p(B) CT interactions in **3a** relative to that in **2a**. On the basis of TD-DFT calculations, furthermore, it has been shown that the lowest-energy excited state of **3c** ($[Ru(B_2phen)(phen)_2]^{2+}$) as the model complex for **3a** is best characterized by synergistic MLCT/π(aryl)–p(B) CT and the excited state possesses a relatively larger charge-separated character than that of **2c**. It is also worth emphasizing that enhancements of both ε_{MLCT} and Φ_{em} values observed for **3a** (ε_{MLCT} = 7.2×10^4 $M^{-1}cm^{-1}$ at 471 nm and Φ_{em} = 0.29 in CH_3CN at 298 K) give rise to bright emission from **3a**. The complex, **3a**, also exhibits long-lived emission owing to the large ^{3}MLCT–^{3}dd* energy gap and this extinguishes the nonradiative decay pathway *via* ^{3}dd* state: very small k_{nr} for **3a**. Thus, **3a** shows simultaneously intense (Φ_{em} = 0.29) and long-lived emission (emission lifetime (τ_{em}) = 8.7 μs). As a result, **3a** possesses simultaneously intense visible absorption, high Φ_{em}, and long τ_{em}, whose characteristics is very extraordinary as a transition metal complex.

The results of Chapters 2 and 3 demonstrate that a DBDE group is a useful functional group for a development of highly-emissive transition metal complexes and that a diimine-ligand structure is one of the important factors to characterize the

synergistic MLCT/π(aryl)–p(B) CT interactions. Furthermore, the emission spectral features of the arylborane–ruthenium(II) complexes were independent of the number of an arylborane-appended ligand as described in Chapter 2 and, therefore, it could be expected that the excited electron in the emissive triplet excited state is localized primarily on one arylborane-appended ligand in the complex. This indicates that the two ligands other than the arylborane-appended ligand in a heteroleptic tris-diimine ruthenium(II) complex can be utilized as ancillary ligands to control the electronic structures of an arylborane–ruthenium(II) complex in the ground and excited states.

Under the research background mentioned above, in Chapter 4, the synthesis and spectroscopic/photophysical properties of novel heteroleptic arylborane–ruthenium(II) complexes having a series of ancillary ligands L' ($[Ru(B_2bpy)L'_2]^{2+}$: **4dpbpy** (L' =4,4'-ph_2-bpy), **4dmbpy** (L' = 4,4'-me_2-bpy), **4dpphen** (L' = 4,7-ph_2-phen), **4dmphen** (L' = 4,7-me_2-phen), **4phen** (L' = phen)) were described focusing the study on ancillary-ligand effects on the properties. $[Ru(B_2bpy)L'_2]^{2+}$ showed a lower-energy and intense ^{1}MLCT absorption band (λ_{abs} = 480–493 nm and ε_{MLCT} = (2.2–3.3) × 10^4 $M^{-1}cm^{-1}$). The electrochemical data of the complexes and the relationship between E_{abs} and ($E_{ox} - E_{red}$) demonstrate that the ^{1}MLCT absorption energy of $[Ru(B_2bpy)L'_2]^{2+}$ is manipulated synthetically by the electron donating ability of the ancillary ligand(s). Furthermore, the ε_{MLCT} value of $[Ru(B_2bpy)L'_2]^{2+}$ (ε_{MLCT} = (2.2–3.3) × 10^4 $M^{-1}cm^{-1}$) is also affected by the ancillary-ligand, as the TD-DFT calculations suggest an increase in the MLCT absorption transition dipole moment by mixing between the MLCT and LLCT transitions in the MLCT/π(aryl)–p(B) CT excited state of the complex. On the other hand, $[Ru(B_2bpy)L'_2]^{2+}$ showed intense and long-lived emission (Φ_{em} = 0.18–0.33 and τ_{em} = 1.1–2.1 μs). The *T*-dependences of the emission lifetimes have revealed that

the k_{nr} value of the arylborane–ruthenium(II) complex is controllable by the energy of the emitting excited state and, can be also manipulated through nature of the ancillary-ligand in $[Ru(B_2bpy)L'_2]^{2+}$. Furthermore, the large k_r value observed for $[Ru(B_2bpy)L'_2]^{2+}$ is shown to be explained in the framework of a Strickler–Berg-type relation.

In the present study, synthetic tuning of the spectroscopic and photophysical properties of a polydiimine ruthenium(II) complex was successfully realized based on the introduction of an arylborane group(s) in the periphery of the diimine ligand(s). With an increase in the number of the arylborane units in the complex, the absorption and emission efficiencies are enhanced and, thus, a Strickler–Berg-type relation on the phosphorescent transition in arylborane–ruthenium(II) complexes has been demonstrated. On the other hand, a phen-ligand structure in an arylborane–ruthenium(II) complex gave arise to extremely long-lived emission due to the larger charge-separated MLCT/π(aryl)–p(B) CT excited state relative to that in the relevant bpy complex. Furthermore, it has been shown that an ancillary ligand(s) also influences the electronic structures of the complexes in the ground and excited states by the electron-donating ability of an ancillary ligand and, thus, the photophysical properties of the complexes can be manipulated by nature of an ancillary ligand as well. On the basis of such synthetic approaches, a new class of highly-emissive ruthenium(II) complexes has been developed and, it is convinced that the present ideas are also applicable to other transition metal complexes. Thus, the present researches were very successful to provide new and novel approaches to develop phosphorescent transition metal complexes. Furthermore, it is expected strongly that arylborane–ruthenium(II)

complexes showing intense/broad absorption and intense/long-lived emission will play important roles in future photofunctional materials such as visible-light driven photo/redox sensitizer, a phosphorescence sensor, and an emitting material.

Acknowledgement

I would like to express my sincere gratitude to Professor Noboru Kitamura for his continuous guidance and encouragement throughout the works of this thesis.

I wish to express my sincere gratitude to Assistant Professor Akitaka Ito (Kochi University of Technology), Associate Professor Eri Sakuda (Nagasaki University), Assistant Professor Sho Fujii, and Associate Professor Atsushi Miura for helpful suggestions and discussions.

I am deeply grateful to Professor Masako Kato, Associate Professor Atsushi Kobayashi, and Assistant Professor Masaki Yoshida for their kind help to ^{1}H-NMR measurements and invaluable discussion.

I am deeply grateful to Professor Masako Kato, Professor Yasuchika Hasegawa, Professor Kei Murakoshi, Associate Professor Atsushi Kobayashi, and Associate Professor Atsushi Miura for reviewing this thesis.

I wish to thank all the members of the Analytical Chemistry Laboratory (Kitamura Laboratory), Graduate School of Chemical Science and Engineering, Hokkaido University for their collaborations in the researches.

Finally, I would like to express my special thanks to my family and friends for their supports and encouragement.

Sapporo, Hokkaido (2018)

Atsushi Nakagawa

Publication List

Related Publications for this Thesis

[1] Atsushi Nakagawa, Akitaka Ito, Eri Sakuda, Sho Fujii and Noboru Kitamura "Bright and Long-Lived Emission from a Starburst-Type Arylborane-Appended Polypyridyl Ruthenium(II) Complex" *European Journal of Inorganic Chemistry* **2017**, Vol. 2017, 3794–3798.

[2] Atsushi Nakagawa, Eri Sakuda, Akitaka Ito, Eri Sakuda and Noboru Kitamura "Remarkably Intense Emission from Ruthenium(II) Complexes with Multiple Borane Centers" *Inorganic Chemistry* **2015**, Vol. 54, 10287–10295.

[3] Atsushi Nakagawa, Akitaka Ito, Eri Sakuda, Sho Fujii and Noboru Kitamura "Ancillary-Ligand Effects on the Spectroscopic and Photophysical Properties of Heteroleptic Arylborane–Ruthenium(II) Complexes" *in preparation* (to be submitted in 2008).

Other Publications

[1] Sho Fujii, Ryo Ishimura, Atsushi Nakagawa and Noboru Kitamura "A Novel Multimode Sensor Showing Cation-Dependent Fluorescence Colour" *Physical Chemistry Chemical Physics* **2017**, Vol. 19, 28943–28949.

[2] Eri Sakuda, Chiaki Matsumoto, Yuki Ando, Akitaka Ito, Kousuke Mochida, Atsushi Nakagawa and Noboru Kitamura "Dual Emissions from Ruthenium(II) Complexes Having 4-Arylethynyl-1,10-phenanthroline at Low Temperature" *Inorganic Chemistry* **2015**, Vol. 54, 3245–3252.